MESOSCALE SIMULATION OF BLOCK COPOLYMER PHASE SEPARATION AND DIRECTED SELF-ASSEMBLY PROCESSES: APPLICATIONS FOR SEMICONDUCTOR MANUFACTURING

A Dissertation
Presented to
The Academic Faculty

By

Andrew J. Peters

In Partial Fulfillment
of the Requirements for the Degree
Doctor of Philosophy in the
School of Chemical & Biomolecular Engineering

Georgia Institute of Technology
August 2015

Copyright © 2015 by Andrew J. Peters

MESOSCALE SIMULATION OF BLOCK COPOLYMER PHASE SEPARATION AND DIRECTED SELF-ASSEMBLY PROCESSES: APPLICATIONS FOR SEMICONDUCTOR MANUFACTURING

Approved by:

Dr. Clifford L. Henderson, Advisor
School of Chemical & Biomolecular Engineering
Georgia Institute of Technology

Dr. Peter. J Ludovice
School of Chemical & Biomolecular Engineering
Georgia Institute of Technology

Dr. Martha A. Grover
School of Chemical & Biomolecular Engineering
Georgia Institute of Technology

Dr. J. Carson Meredith
School of Chemical & Biomolecular Engineering
Georgia Institute of Technology

Dr. Laren M. Tolbert
School of Chemistry and Biochemistry
Georgia Institute of Technology

Dr. David Bucknall
School of Materials Science and Engineering
Georgia Institute of Technology

Date Approved: April 30th, 2015

ACKNOWLEDGEMENTS

First and foremost I want to thank my Lord and Savior Jesus Christ. "O wretched man that I am! Who will deliver me from this body of death? I thank God—through Jesus Christ our Lord!" He has given me strength and purpose so that I might work and produce.

I would like to give preeminent thanks to my advisor Dr. Clifford Henderson. He has been behind me thoroughly and supported me through all my years here and truly provided me with the tools and guidance I need to succeed. He has been what is most necessary in an advisor from day one.

I would like to give special thanks to Professor Peter Ludovice. He has often been like a co-advisor though this process and has provided me with great encouragement. It is easy to be discouraged at some result, or when a paper is rejected, but he constantly encouraged me and kept me positive. I would also like to thank Dr. Martha Grover, Dr. Laren Tolbert, Dr. Carson Meredith, and Dr. David Bucknall for serving on my committee and for their useful suggestions.

I would like to thank all the Henderson group members with whom I have had the pleasure to work with over the past few years. Dr. Richard Lawson and Benjamin Nation have been of immense help throughout this process. Richard has helped me from the beginning to better understand research and this field and my work would not be close to the same without him. Ben has provided great insight into a number of studies. Both Richard and Ben have pushed me to improve beyond my own inclinations and I

owe them great thanks for that. Both have been good friends throughout this process. I would like to thank Caleb Breaux for his ability to keep the office lighthearted and encouraged. It will be a good day the day he is named Dr. Breaux. I would like to thank Dr. Nathan Jarnagin for allowing me to collaborate on his PS-PHOST work. I would like to thank Dr. Jing Cheng and Dr. Wei-Ming Yeh for their support in the Intel work and teleconferences. They helped me get my feet wet in my first months as a researcher. I would also like to thank Mason Risely, Dr. Jose Baltazar, Hannah Narcross, and Brandon Sharp for their help and support as well. I would like to thank Daniel Nicoloso and Austin Ballie for their contributions as undergraduates.

I would like to especially thank my study group, MATLAB ME. Matt Mistilis, Dr. Oluwatimilehin Fadiran, Dr. Lindsay Arnold, Abiola Shitta, Dr. Brennen Mueller, and Maria Elena Casas. They were phenomenal in helping me study and get through all those classes in that first year and they have been excellent friends and supporters throughout my entire doctoral journey. I thank them for all they did, and for remaining great friends even after I was especially busy after getting married and after having my first child. I am sad that all our journeys are coming to an end and that we will all move on so soon.

I would like to thank Garry Williams, Nicole Williams, Howard Liles, Iyanna Liles, Dan Settles, Lauren Settle, Marcus Bellamy, Anna Kate Auten, and the rest of Lampstand. They were wonderful friends and brothers and sisters in Christ. They encouraged me, supported me, challenged me, and taught me like no others have.

I would also like to thank those members of FCGS that I knew while I was here. I would like to the rest of the students in my first year as they all helped support me and challenge me in one way or another. I would like to thank the professors that taught my classes her, especially Dr. Michael Filler and Dr. Mohan Srinivasarao from whom I learned much.

Lastly, I want to extend a big thank you to my family. To my mother who helped me get through all of elementary, middle, and high school without whose help I would not be here today. You trained me for this. To my father who showed me how to be a man and what life is about. Thank you dad. To my daughter Sarah: I was terrified when you first came into the world, but you have proven to be a greater blessing than I could have imagined. And finally an enormous thank you to my wife, who has allowed me to spend late nights at Tech so that I could get the work done that I needed to, and when time got short, took care of Sarah so that I could work. Thank you for your love and for talking with me about my work when you did not feel like it, and for walking with me through everything. Your love has been greater than you know.

TABLE OF CONTENTS

ACKNOWLEDGEMENTS **iii**

LIST OF TABLES **xii**

LIST OF FIGURES **xiii**

SUMMARY **xxx**

CHAPTER 1 BACKGROUND **1**

- 1.1. Integrated Circuit Fabrication and Lithography 1
- 1.2. Block Copolymers and Directed Self-Assembly 5
  - 1.2.1. Block Copolymer Basics 5
  - 1.2.2. Directing BCP Self-Assembly 9
- 1.3. Challenges in BCP-DSA 12
  - 1.3.1. Line Roughness 12
  - 1.3.2. Defectivity 13
- 1.4. Modeling of BCPs and BCP-DSA 15
- 1.5. References 20

CHAPTER 2 COARSE-GRAINED MODEL **27**

- 2.1. Coarse Grained Model 29
  - 2.1.1. Parameterization of Coarse Grained Model 36
- 2.2. Measuring Pitch 38
- 2.3. Measuring χ 41
- 2.4. Measuring ODT 49
- 2.5. Comparison with Mean-Field Theory 55
- 2.6. References 59

CHAPTER 3 IMPACT OF PERIODIC CELL DIMENSIONS ON ALLOWABLE LAMELLAR DOMAIN SIZES: APPLICATION TO BLOCK COPOLYMER MICRO-PHASE SEPARATION 65

3.1. Introduction 65

3.2. Calculation of Allowed Lamellar Domain Size 70

3.3. Block Copolymer Simulations 85

3.4. Results and Discussion 88

3.5. Conclusions 92

3.6. References 93

CHAPTER 4 EFFECT OF GUIDING LAYER PROPERTIES ON LINE ROUGHNESS 95

4.1. Introduction 95

4.2. Modeling 98

4.2.1. Coarse Grained Model 98

4.2.2. Measurement of line edge roughness (LER) and line width roughness (LWR) 101

4.3. Results and Discussion 104

4.3.1. Effect of Guiding Pattern Pitch Mismatch 104

4.3.2. Effect of Sinusoidal and Peristaltic Guiding Lines 106

4.4. Conclusions 110

4.5. References 110

CHAPTER 5 EFFECT OF POLYDISPERSITY ON LINE ROUGHNESS 113

5.1. Introduction 114

5.2. Models and Methods 115

5.2.1. Coarse-Grained Model 115

5.2.2. Measurement of line edge roughness (LER) and line width roughness (LWR) 122

5.2.3. Measurement of chain pair distribution function 125

5.2.4. Measurement of line width as a function of local number averaged degree of polymerization 126

5.3. Results and Discussion 127

5.4. Conclusions 147

5.5. References 148

CHAPTER 6 EFFECT OF χ AND N ON LINE ROUGHNESS 151

6.1. Introduction 152

6.2. Modeling 154

6.2.1. Coarse-Grained Model 154

6.2.2. Measurement of line edge roughness (LER) and line width roughness (LWR) 157

6.3. Results and Discussion 161

6.3.1. Effect of χN on LER and LWR 161

6.3.2. Effect of χN on LER with sinusoidal guiding patterns 165

6.3.3. Comparison to other models 167

6.4. Conclusions 172

6.5. References 173

CHAPTER 7 FREE ENERGY DIFFERENCE OF PITCH VARIATION AND CALCULATION OF THE ODT USING THERMODYNAMIC INTEGRATION 175

7.1. Introduction 176

7.2. Thermodynamic Integration 177

7.2.1. Thermodynamic Integration: Pitch Variations 178

7.2.2. Thermodynamic Integration: Order-Disorder Transition 185

7.3. Results and Discussion 188

7.3.1. Free Energy of Extension or Compression 188

7.3.2. ODT Calculation and the Effect of Pitch 191

7.4. Conclusions 194

7.5. References 195

CHAPTER 8 FREE ENERGY OF DEFECTS USING THERMODYNAMIC INTEGRATION 197

8.1. Introduction 198

8.2. Model and Methods 201

8.2.1. Thermodynamic Integration 201

8.3. Results and Discussion 209

8.3.1. Free energy of dislocation pair defects 209

8.4. Conclusions 220

8.5. References 221

CHAPTER 9 THE KINETICS OF LAMELLAR BCP DEFECT ANNEALING 224

9.1. Introduction 225

9.2. Methods 226

9.2.1. Defect Annealing Simulations 226

9.2.2. Calculation of Defect Heal Rate 231

9.3. Results and Discussion 235

9.3.1. Fully Periodic Simulation 235

9.3.2. Thin Film Simulations 245

9.4. Conclusions 251

9.5. References 252

CHAPTER 10 PROTRACTED COLORED NOISE DYNAMICS FOR POLYMER SYSTEMS 255

10.1. Introduction 255

10.1.1. PCND and Langevin Dynamics 257

10.2. Protracted colored noise for polymer systems 263

10.3. Applications of PCND for polymer systems 267

10.3.1. Increased Diffusion 267

10.3.2. Increased defect heal rate 270

10.3.3. Efficiency of the PCND algorithm 275

10.4. Limits of PCND parameters 276

10.5. Conclusions 285

10.6. References 286

CHAPTER 11 STUDY ON LINEAR A-B MULTIBLOCK PITCH, ODT, AND CHAIN CONFORMATIONS 289

11.1. Introduction 289

11.2. Model 291

11.2.1. Coarse Grained Model 291

11.2.2. Measurment of ODT 293

11.2.3. Calculation of Chain Orientation and Statistics 296

11.3. Results and Discussion 298

11.3.1. Multiblock BCP domain size 298

11.3.2. Effect of Multiplicity of blocks on ODT 299

11.3.3. Chain Conformations 302

11.4. Conclusions 308

11.5. References 309

CHAPTER 12 CONCLUSIONS AND RECOMMENDATIONS 311

12.1. Conclusions 311

12.2. Recommendations for future work 317

12.3. References 321

LIST OF TABLES

Table 2.1.Table of fit parameters of Equation 2.1 to the data in Figure 2.2. 31

Table 2.2. Potentials used for generic, symmetric, BCP. 38

Table 3.1. Allowable pitches for three different simulation sizes between 10 and 14 nm. 89

LIST OF FIGURES

Figure 1.1. Moore's law demonstrated by data from Intel Corporation. The black line corresponds to a doubling of the transistor count every two years. 2

Figure 1.2. Depiction of the lithographic process. Light is exposed to a photoresist which undergoes a solubility change and is selectively removed using a solvent. 4

Figure 1.3. Mean-field block copolymer phase diagram and images of various possible morphologies: Close Packed Spheres (CPS), Body Centered Cubic Spheres (S), Hexagonally Close Packed Cylinders (C), Gyroid (G), and Lamellae (L). Adapted from Bates and Fredrickson.[27] 7

Figure 1.4. Minimum pitch as a function of χ assuming polystyrene like stiffness. Different curves refer to assuming a different minimum χN value for effective DSA processes. 9

Figure 1.5. Image of fingerprint in a simulated BCP. 10

Figure 1.6. Example schematic of a chemoepitaxial process. 10

Figure 1.7. Example schematic of a graphoepitaxial process. 10

Figure 1.8. Top–down schematic of (a) LER and (b) LWR. LER is the deviation from a straight line edge, and LWR is the deviation from a uniform line width. 13

Figure 1.9. Plot of defect density over time for an IMEC process from March 2013 to February 2014. Defect density is slow to improve. 15

Figure 1.10. Mean-field theory models focus on a single molecule and models the interactions by two static fields, one for the A blocks, and one for the B blocks. 16

Figure 2.1. Description of coarse graining of polymer. Some number of monomers, corresponding to the statistical segment length, are modeled as a single bead and linked tougher. 28

Figure 2.2. Plot of $cos\theta$ as a function of monomeric separation. θ is the angle between the vector defining the direction of the polymer chain at any given monomer and the vector defining the direction of the polymer chain k monomers away. 30

Figure 2.3. The three potentials used in this model. E_{str} corresponds to the energy of bond stretching, E_{ang} corresponds to the energy of angle bending, and $E_{non\text{-}bonded}$ refers to the energy of the non-bonded interactions. 32

Figure 2.4. Density as a function of depth through the simulation. Different spacing of the tethered points in the underlayer give different density profiles. When the spacing is too low, density waves propagate from the interface before leveling off to bulk density. 34

Figure 2.5. Images of simulation with various underlayer chain spacings. The film is colored blue and the underlayer brush (with artifical wafer) is colored red. The film is a homopolymer film. a) 25 Å spacings result in a very low density underlayer and penetration of the film beyond the bottom of the underlayer. b) 15 Å spacings result in some penetration, but it does not penetrate through the entire brush. c) 10 Å spacings result in a poor interface and no interpenetration. For this work, and intermediate spacing of 15 Å was used. 35

Figure 2.6. Bond and angle distributions for atomistic and mesoscale simulations of PS. 37

Figure 2.7. Representative plot of *S(q)*. The location of the largest peak corresponds to the pitch of the BCP system. 39

Figure 2.8. Representative plot comparing the raw S(q) calculation to that including the Lorch window function. 40

Figure 2.9. Plot of the measurement error vs. measured dimension / integration length. This calculated error is used to correct measurements of unknown natural pitches in BCP systems. 41

Figure 2.10. Representative fit of Liebler's theory to our simulation results. 46

Figure 2.11. Representative plot of χ vs. $\varepsilon_0 - \varepsilon_{AB}$ for $N = 128$ and $\varphi_A = 0.25$. 46

Figure 2.12. Plot of z values found for $f_A = 0.5$ as a function of N. For $N < 115$, the shown fit is used. Above this value, z is constant at 6. 48

Figure 2.13. Plot of z values found as a function of volume fraction for $N \geq 128$. 48

Figure 2.14. Bulk BCP structure after 100 ns simulation time for increasing ε_{AB} (decreasing χ), (a) $\varepsilon_{AB} = 0.2$, (b) $\varepsilon_{AB} = 0.3$, (c) $\varepsilon_{AB} = 0.36$, (d) $\varepsilon_{AB} = 0.37$, (e) $\varepsilon_{AB} = 0.4$, (f) $\varepsilon_{AB} = 0.5$, $\chi = 0$. 50

Figure 2.15. Changes in the scattering peak height for poly(oxyethylene)-poly(oxybutylene) diblock copolymers. A sharp increase in peak height is seen at the ODT. Data from Mai et al. 52

Figure 2.16. Changes in the structure factor for a BCP with N = 32 for different values of the AB interaction strength ε_{AB} (a) the full structure factor; (b) the peak intensity of the structure factor $S(q^*)$. 54

Figure 2.17. Effect of system size on structure factor peak intensity, closed symbols are for cubic simulation with 20 nm per dimension, open symbols are for simulation with 45 nm per dimension. 55

Figure 2.18. Comparison of our simulation results with the mean field phase diagram from Bates and Fredrickson[42] 56

Figure 2.19. Comparison of average volume fraction through a single domain for SCFT and our model. The results match well. 57

Figure 2.20. Comparison of the interfacial width (w) as a function of χN with SCFT and strong segregation theory (SST) calculations.[43] There is good agreement throughout with SCFT, while SST agrees until χN is low, at which the assumptions in SST fail. 58

Figure 2.21. Comparison of pitches from our symmetric BCP model, Shull's mean-field calculation of pitch,[44] and experimental measurements of PS-b-PMMA[45-60]. Good agreement is found at low, medium, and high χN. 59

Figure 3.1 Schematic of the division of a simulation volume along the x dimension into multiple lamellae, though a similar image could be made for the division of a simulation along the y or z dimension. n corresponds to the number of divisions. The blue and red areas correspond to the subdomains of the lamellae. 72

Figure 3.2. Diagram demonstrating allowed (local minima in free energy) and disallowed tilts (not local maxima in free energy). Some tilt angles result in continuous domain at the boundaries (local minima) while others produce discontinuous domains. The tilt angles that produce a defect will be significantly higher in energy than those without a defect. A simulation will converge to a local minima, and these local minima occur when there are continuous domains across the periodic boundary, and so only those tilts that produce continuous domains will be considered allowed. 74

Figure 3.3. Diagram demonstrating allowed tilts in one dimension. In order to produce an allowed pitch: 1) The lamellar vertices (yellow dots) must be at the same positions along both the top and bottom boundaries. 2) The lamellar interfaces (yellow lines) must connect two vertices on opposites boundaries. 3) The interfaces must all be parallel. i corresponds to the difference between the indices of the vertexes connected by an interface and can range from 0 to ∞. A larger i results in a smaller pitch. 75

Figure 3.4. Diagram demonstrating allowed tilts in two dimensions for $n = 3$ and $i = 1$. Tilts in the second dimension are independent of tilts in the first dimension. The same requirements exist for this tilt as the first dimensional tilt in order to assume defect free and continuous lamellae. j corresponds to the differences between the indices of the vertexes connected by an interface between the front and back ($z = 0$ to $z = D_z$) of the simulation volume and can range from 0 to ∞. A larger j results in a smaller pitch. 76

Figure 3.5. Resulting pitches for the 18 nm cube (volume = 5832 nm3) simulation. The only two pitches measured (blue diamonds) are the two pitches calculated in Table 3.1 (red dotted lines). The green line corresponds to the calculation of natural pitches for a BCP with a = 0.761 nm using Shull's theory.[18] This simulation size causes the resulting pitches to deviate from this theory and adopt only the discrete allowed pitches. 90

Figure 3.6. Resulting pitches from the 36.6 nm by 13.3 nm by 12 nm simulation volume (volume = 5841 nm^3) which has a very similar volume as the used in generating Figure 3.5. Again the measured pitches (blue diamonds) align well with the allowed pitches from Table 3.1. Allowable pitches for three different simulation sizes between 10 and 14 nm.(shown as red dotted lines). However, the existence of many more allowable pitches from this rectangular simulation volume produces a curve that better matches, as compared to the result shown in Figure 3.5, Shull's theory (green line) which describes the relationship between block copolymer lamellae pitch and polymer χN value. 91

Figure 4.1. Top–down schematic of (a) LER and (b) LWR. LER is the deviation from a straight line edge, and LWR is the deviation from a uniform line width. 98

Figure 4.2. Density as a function of depth through the simulation. Different spacing of the tethered points in the underlayer give different density profiles. When the spacing is too low, density waves propagate from the interface before leveling off to bulk density. 102

Figure 4.3. Images of simulation with various underlayer chain spacings. The film is colored blue and the underlayer brush (with artificial wafer) is colored red. The film is a homopolymer film. a) 25 Å spacings result in a very low density underlayer and penetration of the film beyond the bottom of the underlayer. b) 15 Å spacings result in some penetration, but it does not penetrate through the entire brush. c) 10 Å spacings result in a poor interface and no interpenetration. For this work, and intermediate spacing of 15 Å was used. 103

Figure 4.4. Depiction of pinned and unpinned lines. Lines appearing above guiding stripes are considered pinned, while lines over neutral stripes are considered unpinned. 104

Figure 4.5. Line edge roughness as a function of pitch for both pitch replicating guiding layers and pitch halving guiding layers. Between 18 nm and 21 nm, there is little change in roughness, and above 22nm the BCP does not align to the pitch of the guiding pattern. Below 18nm, there seems to be a confinement effect due to simulation specifics. 105

Figure 4.6. Both images show 24 nm guiding pitch pattern with 20 nm natural pitch BCP. When the guiding layer pitch is too large, the BCP force themselves into their natural pitch in the bulk of the film while being pinned at the underlayer. a) All beads shown. b) Only A beads shown. 106

Figure 4.7. LER and LWR through depth for sinusoidal guiding lines. The film surface is located at a depth of 0 nm, and the film-underlayer interface is located at 15 nm. A refers to the amplitude and WL the wavelength of the underlayer sine wave. LER and LWR as shown are 3 σ. In most cases, roughness in the underlayer is mitigated in the first ~5nm. a) LER of pitch replicating simulation. When the amplitude and wavelength of the guiding stripe are very high relative to the line width (in this case the amplitude=35% of line width while the wavelength is 4 times the line width) then there is some roughness that persists through thickness. b) LWR of pitch replicating simulation. LWR is unaffected except perhaps right at the underlayer. c) LER of pitch halving simulation. Effects of underlayer are more damped. d) LWR of pitch halving simulation. 108

Figure 4.8 LER and LWR through depth for peristaltic guiding lines. The film surface is located at a depth of 0 nm, and the film-underlayer interface is located at 15 nm. In all cases the roughness is damped out within 5 nm of the underlayer. LER and LWR as shown are 3 σ. a) LER of pitch replicating simulation. b) LWR of pitch replicating simulation. c) LER of pitch halving simulation. d) LWR of pitch halving simulation. 109

Figure 5.1. Images of various simulation types used in this work. A beads are shown in white while B beads are shown in cyan. A) Cubic bulk simulation. These simulations are 45 nm cubes, periodic in all three dimensions, and are used to find the natural pitch of polymer systems. B) High aspect ratio bulk simulation. These simulations are 100 nm by 100 nm by 15 nm, fully periodic simulation box, and are used to view large cross sections of polymer systems at a low computational cost compared to a cubic simulation. C) Short length of a patterned underlayer film simulation. These simulations are at least 100 nm long and 15 nm thick on average. A 4 pitch wide simulation is shown, but various multiples of the natural pitch were used. This simulation is periodic in the x and y dimensions, but not in the z dimension, modeling a thin film. The underlayer (shown in red and blue instead of white and cyan for clarity) is patterned to produce alignment in the overlying polymer system. 120

Figure 5.2 Images of BCP aligned to a patterned underlayer for a PDI of 1.54 with X_N=120 monomers. The entire line was 300 nm long, but only 150 nm is shown here for clarity. A) A top-down view of the simulation in VMD. B) The line transformed using a 0.3 nm Gaussian blur with a pixel size of 0.1 nm for only A beads. C) The same Gaussian blurred image with a threshold highlighted in yellow denoting the line edge used in the calculation of LER and LWR. 124

Figure 5.3. LWR measured at individual timesteps as the simulation runs in a patterned underlayer simulation. Roughness levels off after a short time. High PDI take longer to equilibrate, but still equilibrate well within the simulation time. The jump at very short time occurs because the external ordering potential has just been turned off. 125

Figure 5.4. Pitch normalized to the monodisperse pitch. The PEP-b-PLA experimental results were obtained by Lynd and Hillmyer by varying the polydispersity in the PLA block at a χN value of ~80. Simulation results shown here use a Wesslau distribution and are at a χN of 144. Both data sets show that the scaled pitch increases with PDI at similar rates. 128

Figure 5.5. LER (A) and LWR (B) as a function of PDI and simulation size with a X_n of 120 and a χN of 144. Both LER and LWR increase at a similar rate as PDI increases. 130

Figure 5.6. A-A LER as a function of PDI and simulation size. 131

Figure 5.7. Different mechanisms to compensate an for increase in A-A and B-B roughness. A) Increasing A-B roughness. B) Correlating short and long chains. C) Deforming chains. 132

Figure 5.8. Pair distribution function for PDI = 1.53 $4L_0$ wide simulation. A) Pair distribution function for a variety of ΔN. The PDF is the # of pairs of the given ΔN over the total number of pairs of that distance. There is no clear dependence of the PDF on distance for any ΔN. B) shows the total number of pairs as a function of ΔN. This variations explains the offset for each ΔN shown in A) (i.e. there are a greater number of interactions with a ΔN of 10 than of 5 and therefore the line for ΔN = 10 is higher in A)). 133

Figure 5.9. Chain size in the x dimension as a function of chain length and PDI. The PDI = 1 line is half the natural pitch of a monodisperse system at the given N determined for the χ value used here. The longer chains are clearly perturbed from their natural state. 135

Figure 5.10. Line edge correlation coefficient (CC_{LE}) examples. 138

Figure 5.11. A) Correlation coefficient (CC_{LE}) as a function of PDI for patterned thin film simulations. B) CC_{LE} as a function of the number of interfaces separating the two lines being compared. 139

Figure 5.12. Top down views of high aspect ratio bulk simulations. A)-C) show images at PDIs of 1, 1.3, and 1.5 respectively. As PDI increases, local swelling and pinching of lines due to local variations in chain length is apparent. Run length is also decreased as PDI increases. D) and E) show the PDI = 1.5 simulation (C) showing only large chains ($X > X_n$) and small chains ($X < X_n$) respectively. 141

Figure 5.13. Analysis of line width and weight averaged degree of polymerization (X_n'). Data for simulations that are 12 pitches wide on a patterned underlayer are shown along with the high aspect ratio bulk simulation (no patterned underlayer). 143

Figure 5.14. Images of a BCP with block PDI = 2.26 and a system PDI = 1.53, showing A) A beads and B) B beads. The large numbers of very small chains and chains who volume fractions are extremely small or large results in a large number of beads in the wrong domain and in a wetting layer of short chains. 145

Figure 5.15. LER (A) , LWR (B) , and A-A LER (C) including results from simulations that have variations in volume fraction for each chain. The green 5 point stars plot the data using the PDI of the entire chain. The blue 8 point stars plot that data using the PDI of the blocks only. PDI calculated either way for the simulations whose chains are all at a volume fraction of 0.5 is equal. Using the PDI of the blocks only, the roughness of the simulations that allow volume fractions to vary on each chain matches the roughness of the simulations where chains are all 50% A. 146

Figure 6.1 LER as a function of inspection length. Above ~ 100 nm, LER becomes inspection length independent. 157

Figure 6.2 Images of bead density histograms at various binning depths. All images show the same simulation at the same time step. N = 96 χN = 20. All bins are centered in the z dimension of the film. 159

Figure 6.3 LER and normalized LER as a function of χN at various binning depths for *N* = 96. (a) 3σ LER. Increasing the binning depth decreases the measured roughness because of the smoothing due to the averaging through depth that occurs. (b) LER is normalized by LER at χN ~180. Though a different binning depth shifts the measured roughness, it does not change the sharp increase at low χN. 160

Figure 6.4 LER and LWR as a function of *χN*. There is a sharp increase in roughness as *χN* approaches the ODT. 162

Figure 6.5 Top down images of lines at a fairly high χN and at a low χN. The low χN system shows large deviations in the location of the line edges. 163

Figure 6.6 A) LER as a function of χN for various N. All N show a sharp decrease as χN approaches the ODT. Smaller N yield slightly smaller roughnesses. B) LER is plotted as a function of χ. This collapses the data to a single curve. 164

Figure 6.7 A) 3σ LER for sine wave guiding stripes and straight guiding stripes. A corresponds to the amplitude of the sine wave guiding function, and WL corresponds to the wavelength of that same function. B) LER normalized to value at χN = 125 for sine wave guiding stripes and straight guiding stripes. When A=3.5nm and WL=40 nm, there is a persistent increase in the roughness through the film. However, this effect is proportionally the same for all χN, as can be seen when the data is normalized. 166

Figure 6.8 Cutoff between high and low frequency regime from Semenov's theory. 169

Figure 6.9 Simulation LER data plotted Semenov low frequency roughness theory results at a depth of 7.5 nm, the middle of the film. For relatively high *χN* (>60) there is good agreement between our results and Semenov with a gentle increase in LER. However, when *χN* is small, our simulation predicts a much higher LER. 171

Figure 6.10 Comparison of calculation from Gallatin et al. model and the model used in this work. The Gallatin et al. model does not capture the dependence on *χN* for low *χN*, showing only a very slight increase at low *χN* values. 172

Figure 7.1. Schematic of the 3 branch method for calculating the free energy between the mixed state and demixed state. The first branch increases the external potential and phase separates the system. The second branch increases χ. Little morphological change occurs during this branch. The third branch removes the external potential and achieves the final state. Each branch is reversible and so the free energy can be calculated over each of them. The total free energy difference is the sum of the free energy differences of each branch. 179

Figure 7.2. Compositional profile of simulation results and the external potential. 180

Figure 7.3. Plot of the integrand and free energy of the first branch for N = 120 and a pitch of 16 nm as a function of the external potential strength, *A*. 182

Figure 7.4. Plot of the integrand and free energy of the second branch for N = 120, an external potential strength *A* = 2.63 kcal/mol, and a pitch of 16 nm as a function of the unlike bead interaction strength, $\varepsilon_{AB.}$ The integral is performed from $\varepsilon_{AB} = 0.5$ ($\chi N = 0$) to $\varepsilon_{AB} = 0.3$ ($\chi N = 84.5$). 184

Figure 7.5. Plot of the integrand and free energy of the third branch for N = 120, $\chi N = 84.5$, and a pitch of 16 nm as a function of the external potential strength. The integral is performed from a value of *A* = 2.63 to *A* = 0. 185

Figure 7.6. Plot of free energy compared to the $\chi = 0$ mixed state. The red line corresponds to the free energy as calculated from the $\chi = 0$ mixed state to large χN in the mixed state. The blue line corresponds to the free energy calculated from the phase separated state (determined the three branch calculation described before) to low χN in the phase separated state. The extrapolation of the two lines is shown in dashed lines. The intersection of these lines corresponds to the calculated ODT. 187

Figure 7.7. Difference in free energy between the final state and a mixed state with $\chi = 0$ as a function of pitch and χN for $N = 120$. 189

Figure 7.8. Comparison of measured natural pitch using the scattering method described in Chapter 2 and the thermodynamic integration method used here. Excellent agreement is found. 189

Figure 7.9. Free energy penalty normalized by χ plotted as a function of L/L_0. 191

Figure 7.10. Free energy compared to the mixed $\chi = 0$ case. The Mixed to ODT curve is identical to that shown in Figure 7.6. The other curves correspond to free energy calculation in the phase separated state at 26 and 20 nm pitches . 193

Figure 7.11. χN_{ODT} as a function of pitch for N = 120. 194

Figure 8.1. Top down image of the defect type studied in this paper. This is a common defect found in literature.$^{-}$ 200

Figure 8.2. Schematic of the method used to calculate the defect free energy. Two simulations are run: one from the mixed to the defective state, and one from the mixed to the defect free state. Each of these simulations yields the free energy difference between the mixed state and the corresponding final state. The difference between the free energies calculated in each simulation is the free energy difference between the defect and the defect free state. Each simulation contains three branches over which a free energy difference is calculated. The first branch orders the system from the mixed state using an external potential, the second changes χ, and the third turns off the external potential. 202

Figure 8.3 External potential used to make defect in branch 1 of the thermodynamic integration simulation. The potential is the same as the well aligned lamellae, except that a region in the center $1.5L_0$ by $0.75L_0$ is rotated 45 degrees. This rotation gives a good matching to spontaneously formed dislocation pair defects and is easily formed. The B potential is the negative of the A potential. 205

Figure 8.4. Plot of the Integrand of Equation 8.9 as A is increased. As the number of timesteps per step in A is increased, the curves converge. A value of 320,000 was used to ensure accuracy and reasonable simulation times. 205

Figure 8.5 Plot of the Integrand of Equations 8.10 and 8.11 as ε_{AB} is increased. All values of timesteps per step in ε_{AB} yield the same integrand. 207

Figure 8.6. Plot of the Integrand of Equation 8.12 as A is decreased. Values of 20,000 timesteps per step in A and higher yielded the same integrand. 208

Figure 8.7. Free energy of dislocation pair defect as a function of simulation size. Smaller simulation sizes resulted in deformed defects and made it impossible to calculate defect free energy. As long as the box size was at least $5L_0$ by $3L_0$ (area = 2160 nm^2), the defect free energy did not seem to differ greatly. 210

Figure 8.8 The defect free energy as a function of χN. Overall, ΔF increases with χN, but there is a significant change with N. Defect free energy approaches 0 as χN approaches the ODT. 212

Figure 8.9. The defect free energy as a function of χ. Defect free energy scales very well with χ with little dependence on N. 212

Figure 8.10. Image of the three possible defect locations on a 1-3 guiding pattern. 214

Figure 8.11. Defect free energy as a function of background composition and defect location relative to the underlayer for N = 64, χN = 35, and a film thickness of L_0. 215

Figure 8.12. Defect free energy as a function of PDI for N = 64 and χN = 35. The "B" defect location was used. 216

Figure 8.13. Distribution of chain lengths for PDI = 1.5, N =64, and χN = 35. The long chains tend to congregate near the defect. 218

Figure 8.14. Image of locations where long chains (N > X_N) were built. When initialized near the defect they are placed within the red rectangle. When initialized away from the defect they are placed within the yellow region outside the red rectangle. 219

Figure 8.15. Defect free energy as a function of PDI and long chain placement. When the long chains are placed near the defect the defect free energy is equal to or lower than the simulations where they were randomly placed. When the chains are placed far away from the defect, defect free energy is generally higher. 220

Figure 9.1. Views of a representative periodic simulation. Periodic simulations were periodic in all three dimensions. The defect was built using the external potential described by Equations 9.1 – 9.3. 228

Figure 9.2. Views of a representative thin film simulation. Thin film simulations were periodic in the *x* and *y* dimensions, but not in the *z* dimension. A) A film is built above an underlayer. This film is then made to form a defect using the external potential described by Equations 9.1 through 9.3. The dotted line shows the location of the wall potential used to help the film adhere to initially adhere to the underlayer and to keep the film flat during the initial stages. B) and C) show the film adhered to the underlayer in the defective state. 230

Figure 9.3. Representative plot of the fraction aligned (F) as the defect heals. Only the region in the middle of the simulation designated by the dotted line was used in the calculation. A cutoff value was assigned for each set of N and χN and the defect was deemed annealed when the fraction aligned exceeded that value. 232

Figure 9.4. Fraction defective (F_d) over time for χN = 35, N = 64 for a film thickness of 20 nm. 235

Figure 9.5. Defect heal rates as a function of χN and N for the periodic simulations. A) plots the raw rates. B) plots rates normalized by D/L_0^2. 238

Figure 9.6 Comparison of the characteristic timescales τ1 and τk. Values above 1 indicate that transport has a greater impact on the overall time to defect annihilation, whiles values less than 1 indicate that the energy barrier has a greater impact. 240

Figure 9.7. Rates calculated using exponential fit with exponential fits shown. Exponential fit for N = 64 excludes $\chi N = 16.6$. 242

Figure 9.8. Views of a representative defect through time as the defect anneals (N = 64 and $\chi N = 31.6$). Only the A domain in the center region is shown for clarity. First a branch forms across one side of the defect, and then as that line propagates outward the other side forms a branch and soon after a hole forms in the center region. The branches thicken as the hole widens until the defect is healed. 245

Figure 9.9. A) Defect healing rates for the thin film simulations plotted alongside the periodic simulation rates. Rate are calculated using an exponential fit as in Figure 9.4. B) Average τ_1 values (time to heal defect once the transition state has occurred) as a function of film thickness. 247

Figure 9.10. Views of a representative defect through time as the defect anneals in a thin film (N = 64 and $\chi N = 45$ with a thickness of 20 nm). Only the A beads in the center region are shown for clarity. The pathway is similar to that of the periodic simulation, except that the branches that initialize the healing in each domain always occur at either the free interface or the BCP-underlayer interface. 249

Figure 9.11. Images of the formation of the initial branch in a thin film simulation (N = 96, $\chi N = 45$, and thickness = 20 nm). A) and B) are included to give the viewer a clear idea of the view used in C). A) Uses the same rotation and C), while B) gives a better view of the defect as a whole. Only the A domains are shown, and the portions highlighted in red are excluded from C) in order to make the formation of the branch clearer. 250

Figure 10.1. From Jenkins[7]. Plot of reduced potential energy vs. reduced time for two simulations with different PCND parameters and one simulation run without PCND. The simulations with PCND reach the equilibrium state significantly faster than the simulation without. 263

Figure 10.2. Visualization of how the stochastic forces are applied in polymer PCND. The forces are applied along the backbone of the chain, that is, the force on an interior bead is applied along the vector between the two adjacent beads. The magnitude of the force is the same for every bead on the chain and can change sign with time. 265

Figure 10.3. Representative plot of the magnitude of the force over time for a single chain at various values of τ. As τ increases, the force magnitude is correlated over longer times. The various τ series are offset for clarity. 266

Figure 10.4. Histogram of the potential energy of beads with and without PCND at 500K and 600K. The inclusion of PCND slightly widens the energy distribution. 267

Figure 10.5. Plot of diffusion constant as a function of τ for various Ω/τ for N = 64. Diffusion appears to scale with $\tau^{0.29}$ at various values for Ω/τ. 268

Figure 10.6. Plot of the fit coefficients from Figure 10.5 as a function of Ω/τ. The coefficients, and thus diffusion, appears to scale linearly with Ω/τ. 269

Figure 10.7 Plots of the simulated rate of defect healing as a function of χN and PCND parameters for N = 64. A) shows defect heal rates as a function of χN without PCND alongside rates using PCND at various Ω/τ values for τ = 500 ps and maximum rates at elevated temperatures. All PCND sets show a massive increase in rate, ~200 times faster than the extrapolated rates that do not use PCND. Increasing temperature does not increase the rate as much as PCND does. No defect healed in the given time frame for the elevated temperatures and the rate shown is likely higher than the real rate. B) shows the defect heal rates as a function of τ and Ω/τ. Rate is not sensitive to PCND parameters, though they do look to drop as τ nears zero, as would be expected. 272

Figure 10.8. Images of end states of representative simulations. The elevated temperatures cause a decrease in pitch which results in a tilt in the lamellae. At T = 1000K the tilt is so extreme the lines buckle. At 500K under PCND (Ω/τ = 0.1 kcal/mol, τ = 500 ps) there is no tilting because the natural pitch remains unchanged. There is increased interfacial roughness due to the increased fluctuations. 274

Figure 10.9. Time spent for various calculations during MD simulation in HOOMD. PCND account for approximately 5% of the overall calculation time when N = 1000. Smaller N will result in an increase in the relative time spent calculating the PCND force. 276

Figure 10.10. Representative plot of the structure factor (S(q)) for various values of τ for Ω/τ for N = 64. At low τ values, the size and location of the peak changes little with τ. However, the small jump from τ = 15,000 ps to τ = 15,250 ps results in a sharp decrease in peak height. This sudden drop is associated with the ODT and means the BCP is now mixing. 279

Figure 10.11. Images of the simulations for which the structure factor was calculated in Figure 10.10. Rotations and increases in interfacial roughness can be seen as τ increases for $\tau \leq 15{,}000$ ps, but when τ reaches 15,250 ps the simulation has started to mix. 279

Figure 10.12. Plot of the disorder transition (but not ordered to mixed transition) of a polymer as a function of τ and A) Ω/τ or B) $N \cdot \Omega/\tau$ for various N. Parameters above and to the right of the curves, the BCP simulation mixes, while parameters below and to the left of the curves the BCP simulation phase separated. 281

Figure 10.13. Plot of measured natural pitch as a function of τ and Ω/τ for $N = 64$. At low values of τ, PCND does not perturb the natural pitch. Higher values yield a slight perturbation in pitch. 282

Figure 10.14. Histograms of A) radius of gyration (R_g), B) bond length, C) end to end distance (r_0), and D) bond angle for $N = 64$. PCND makes little difference on these statistics for the parameters shown here. 284

Figure 11.1. Types of block copolymers simulated in this work. Diblock copolymers are typically used in BCP-DSA, but other polymers may allow smaller domain sizes by depressed in the effective ODT. 291

Figure 11.2. Changes in the scattering peak height for poly(oxyethylene)-poly(oxybutylene) diblock copolymers. A sharp increase in peak height is seen at the ODT. Data from Mai et al. 294

Figure 11.3. Changes in the structure factor for a BCP with $N = 32$ for different values of the AB interaction strength ε_{AB} (A) the full structure factor; (B) the peak intensity of the structure factor $S(q^*)$. 296

Figure 11.4. Bulk BCP structure after 100 ns simulation time for increasing ε_{AB} (decreasing χ), (a) $\varepsilon_{AB} = 0.2$, (b) $\varepsilon_{AB} = 0.3$, (c) $\varepsilon_{AB} = 0.36$, (d) $\varepsilon_{AB} = 0.37$, (e) $\varepsilon_{AB} = 0.4$, (f) $\varepsilon_{AB} = 0.5$, $\chi = 0$. 296

Figure 11.5. Diagram of the X and Y components of the radius of gyration. 298

Figure 11.6. Plot of measured natural pitch (L_0) as a function of ε_{AB} and number of blocks. (A) shows the results using a diblock of 32 monomers and polymers composed of linked $N = 32$ diblocks. (B) shows the same for a diblock of 64 monomers. 299

Figure 11.7. A) Plot of χN_{ODT} (χN at the ODT) as a function of N and blocks per chain. B) Plot of χN_{Eq} (N_{eq} is the diblock equivalent N) as a function of blocks per chain. 301

Figure 11.8. Diagram of conformations of Diblock and Triblock copolymers. The Diblock only has one conformation, while the Triblock has two, an extended and a loop conformation. 303

Figure 11.9. Histograms of chain shape for both Diblock and Triblock copolymers based on a diblock of 32 monomers (N_{Eq} = 32) at an ε_{AB} of 0.3 kcal/mol. A) plots probability as a function of end to end distance (r_0) over L_0 while B) plots probability as a function of X/L_0. 304

Figure 11.10. Diagram of the possible conformation of tetra and pentablock copolymers. 307

Figure 11.11. Histogram of X/L_0 for di, tri, tetra, and pentablock copolymers for N_{Eq} = 32 and ε_{AB} = 0.3 kcal/mol. Each plot has a peak corresponding to the possible conformations in Figure 11.10. 307

Figure 11.12. Comparison of the calculated fraction of each conformation with the measured fraction in simulation for N_{Eq} = 32 and ε_{AB} = 0.3 kcal/mol. 308

LIST OF SYMBOLS AND ABBREVIATIONS

Å	Angstrom
AFM	Atomic Force Microscope
BCP	Block Copolymer
CC	Correlation Coefficient
CD	Critical Dimension
CED	Cohesive Energy Density
DFT	Density Functional Theory
DSA	Directed Self Assembly
EUV	Extreme Ultraviolet
f_A or φ_A	Volume fraction of A
g(r)	Pair distribution function
GPU	Graphic Processing Unit
H	Hamiltonian
HOOMD	Highly Optimized Object-oriented Many-particle Dynamics -- Blue Edition
IC	Integrated Circuit
k	Boltzmann constant
L_0	Natural repeat distance (pitch) of a BCP system
LER	Line Edge Roughness
LWR	Line Width Roughness
MC	Monte Carlo
MD	Molecular Dynamics
MGI	Materials Genome Initiative
M_N	Number averaged molecular weight
MOE	Molecular Operating Environment^{TM}
M_W	Weight averaged molecular weight
N	Degree of polymerization
NPT	Isothermal-Isobaric ensemble
NVE	Micro-canonical ensemble
NVT	Canonical Ensemble
ODT	Order-disorder transition
PCND	Protracted Colored Noise Dynamics
PDI	Polydispersity Index
PHOST	Polyhydroxystyrene
Pitch	repeat distance of a BCP system or lithographic pattern
PMMA	Poly(methyl methacrylate)
PS	Polystyrene
q	Scattering vector
q*	Scattering vector that yields the maximum structure factor value
r_0	End to end distance of a polymer chain

R_g	Radius of gyration
RPA	Random phase approximation
S(q)	Structure factor
SANS	Small angle neutron scattering
SAXS	Small angle x-ray scattering
SCFT	Self-consistent Field Theory
SEM	Scanning Electron Microscope
SST	Strong segregation Theory
T_g	Glass transition temperature
U_{ext}	External field potential
UV	Ultraviolet
V	System Volume
VMD	Visual Molecular Dynamics
X_N	Number averaged degree of polymerization
X_W	Weight averaged degree of polymerization
z	slope of χ - ε_{AB} relation
ΔF	Free energy difference
Δw	Exchange energy in Flory Theory
ε_0	Difference between ε_{AB} and the average of ε_{AA} and ε_{BB}
ε_{ij}	Strength of non-bonded potential between an *i* type bead and a *j* type bead
σ_{ij}	Minimum energy distance in the non-bonded interaction between an *i* type bead and a *j* type bead
τ	Time correlation for colored noise
χ	Flory-Huggins interaction parameter
Ω/τ	Root mean squared average of PCND force

SUMMARY

Block copolymer (BCP) directed self-assembly (DSA) is a process widely studied for the patterning processes in the coming generations of integrated circuit (IC) fabrication. BCP-DSA takes advantage of a BCPs natural ability to phase separate at the nanometer length scale and aligns them to lower resolution patterns created by traditional lithographic techniques such that the desired IC patterns can be created. A coarse-grained polymer model was created to investigate BCP-DSA. By using a coarse-grained model and treating multiple monomers as a point particle simulation time can be significantly reduced without sacrificing as much accuracy as older mean field models. In chapters 2 and 3 this model, and methods that are necessary to its use, are described.

Two of the major hurdles to BCP-DSA implementation are line roughness and defect density. Chapter 4 considered the effect of guiding layer properties. Guiding lines with various correlated and anti-correlated roughnesses showed that very significant guiding roughness is required to have any effect on the BCP film. In chapter 5 it was found that both line edge roughness (LER) and line width roughness (LWR) increase approximately linearly with increasing PDI, up to ~ 45% of the monodisperse value at PDI = 1.5. Mechanisms of compensation for increase A-A and B-B roughness were considered, and when the volume fraction of individual chains was allowed to vary, similar results were found when considering the PDI of the block as opposed to the PDI of the entire system. In chapter 6, a sharp increase in LER and LWR in aligned BCP

patterns was found for low χN values compared to older models. This sharp increase will likely preclude the use of low χN materials in BCP-DSA processes.

Defect density in a BCP-DSA sample can be explained due to either a small free energy difference between the defective and the defect free state, or by kinetic trapping of defects. Both aspects were considered. Chapter 7 introduces a method to calculated free energy differences and applies it to changes in BCP domain size and to measurements of the ODT. Chapter 8 applied thermodynamic integration to measure the free energy of a common defective state relative to the defect free state under various material and guiding layer conditions. It is found that χ, not χN as some previously thought, is the best determiner of defect free energy. Chapter 9 considered the kinetic aspects of defect healing as a function of χ and N and delves into the pathways of healing a common defect. An exponential increase in the energy barrier to defect formation was found with χN.

In chapter 10, a method for increasing the efficiency of sampling activated states in molecular dynamics simulations of polymer systems called protracted colored noise dynamics (PCND) is described. By applying a time correlated random force along the backbone of the polymer chain, chain movement was encouraged without significant perturbation of the free energy of the system. An increase in defect heal rate of 4 orders of magnitude was found as compared to the results from chapter 9 without PCND, and littler perturbation of the properties of a given state was found.

Finally, chapter 11 considered the effect that linking together diblock copolymers to form tri, tetra, or penta block copolymers has on domain size and the ODT. A depression in the minimum pitch possible could be achieved using multiblocks, but the effect was small. The distribution of chain conformations of multiblocks through a lamellar morphology was also studied.

CHAPTER 1

BACKGROUND

1.1. Integrated Circuit Fabrication and Lithography

Integrated circuits (ICs), and the microelectronic devices that are based on them are ubiquitous all over the world today. Though the transistor was first created by Bell Labs in 1947,[1] and the first IC was produced in the late 50's by both Jack Kilby at Texas Instruments and Robert Noyce at Fairchild Semiconductor, the information age did not truly take hold until the late 1960's and 1970's when ICs left the realm of military and government use only and entered the commercial realm with the introduction of devices such as the home computer. The reason that microelectronic devices changed the world was because of the exponential increase in computing power over time along with the exponential decrease in the cost for such devices. Gordon Moore, co-founder of the Intel Corporation, forecasted that the number of transistors per area in an integrated circuit would double every two years (plotted in Figure 1.1[2]), and his prediction has held true since he made the prediction in 1975.[3-5] The critical advancements that made such a scaling, and such an impact, possible are primarily advancements in micro and nanolithography, that is, the technique used to define the circuit features in silicon wafers.[6] The pace at which the lithographic community has advanced IC fabrication is staggering, but new challenges have arisen that threaten to slow or end such progress. In order to pack so many transistors onto a single chip, the dimensions of the smallest parts of the transistors must shrink, requiring the smallest feature that can be patterned via lithographic techniques to shrink with it.

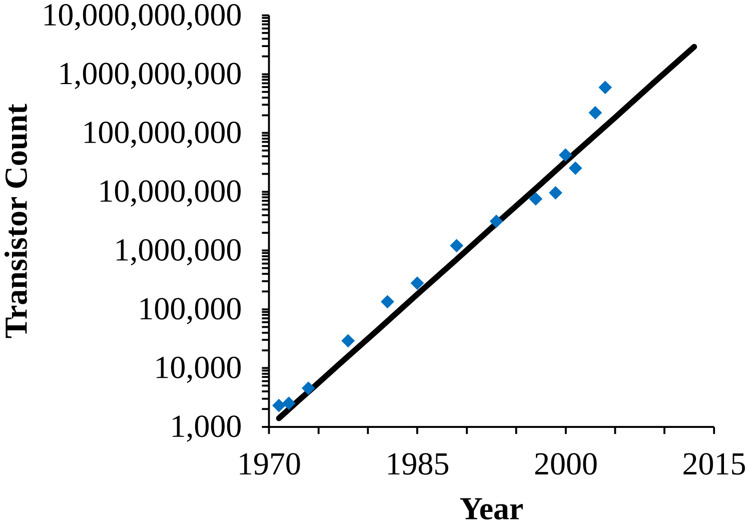

Figure 1.1. Moore’s law demonstrated by data from Intel Corporation. The black line corresponds to a doubling of the transistor count every two years.[2]

The lithographic techniques, namely optical lithographic techniques, that made early progress in increasing computing power possible are the same fundamental techniques that are still used today in IC fabrication. In optical lithography a layer of photoresist, a photosensitive polymer, is coated on top of a silicon wafer coated with a film of functional material. A photomask is used to selectively expose light to the photoresist. The photoresist reacts to the light and undergoes a solubility change in the exposed regions, and a solvent is used to selectively remove either the exposed or unexposed regions. This process is described in Figure 1.2. The minimum feature size (critical dimension or CD) of this process is determined by[7]:

$$CD = k_1 \frac{\lambda}{NA} \qquad 1.1$$

where λ is the exposure wavelength, k_1 is a process dependent factor theoretically limited at 0.25, but usually practically limited at ~ 0.4,[8] and NA is the numerical aperture of the final lens. Equation 1.1 indicates that the critical dimension of such a process can be reduced by either reducing the wavelength of light used to expose the photoresist, or by increasing the numerical aperture; however, the depth of focus degrades much more rapidly by increasing the numerical aperture than by reducing wavelength which has caused the industry to focus on reducing CD by decreasing wavelength. Feature size has been steadily reduced by decreasing the wavelength of exposure since the 1970's starting with "g-line" (436 nm) and then followed by "h-line" (405 nm), "i-line" (365 nm), KrF laser (248 nm), and ArF laser (193 nm).[7,9] After the 193 nm exposure wavelength had run its course, the next logical step was projected to use 157 nm light, but these techniques ultimately failed.[10] To compensate, immersion lithography, where the air gap between the lens and the silicon wafer is replaced by a high refractive index liquid was used.[11] This worked by increasing the numerical aperture.[7] When this technique reached the end of its life cycle, a technique called double patterning was introduced. In this technique, two exposures are made on the same wafer, patterning twice the number of lines in the same area.[11] As traditional techniques have failed, new techniques have risen up to take their place. But what is next? What is the new technology that will take the place of the older methods?

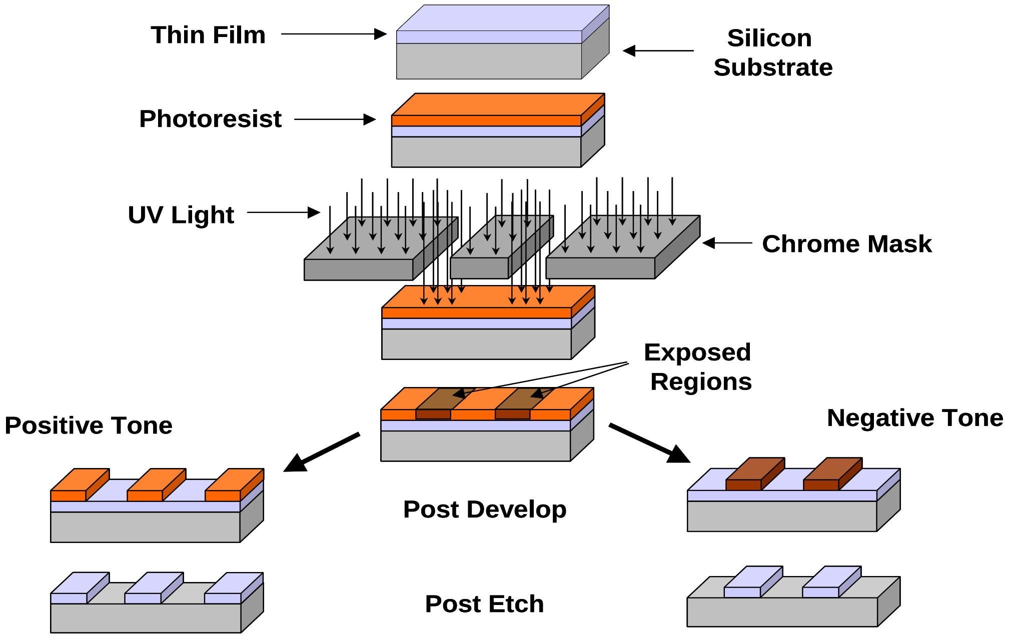
Thin Film
Silicon Substrate
Photoresist
UV Light
Chrome Mask
Exposed Regions
Positive Tone
Negative Tone
Post Develop
Post Etch

Figure 1.2. Depiction of the lithographic process. Light is exposed to a photoresist which undergoes a solubility change and is selectively removed using a solvent.[12]

The first thought someone might have is to try to reduce the wavelength, and this is what many in the community are trying to do. The next reduction in wavelength that is commonly worked on is a reduction to 13.5 nm, known as extreme ultraviolet (EUV). EUV lithography was originally intended for use in 2009[13], but it has been plagued with difficulties and is still not used in an industrial process. The primary difficulty that EUV has faced is the difficulty of delivering enough power to the wafer to achieve efficient throughput.[14] This difficulty is multifaceted. 13.5 nm wavelength light is a relatively high power wavelength, meaning that each photon that is generated requires are large amount of energy, and improved throughput in optical lithography requires more photons, so more energy is required to achieve acceptable throughput. In addition, the methods used to produce EUV radiation emit the radiation in all directions and so require more focusing which results in lost photons.[15] Finally, 13.5 nm wavelength light cannot be focused using a traditional lens but must instead be focused using mirrors. These mirrors must be made of layers of molybdenum and silicon or other similar layered materials, all of which are only ~ 70% reflective of EUV wavelengths.[16-19] When tools require ~ 10 mirrors to focus light and each of those mirrors is only 70% reflective, only about 3% of the light originally collected from the source actually reaches the wafer. All of these troubles combined amount to serious issues with EUV throughput.

A number of alternative lithographic techniques have emerged in response to the problems that EUV lithography continuous to face. Such methods include: multiple e-beam direct write,[20] nanoimprint,[21] and block copolymer directed self assembly. This last technique has been shown to be very promising and will be the focus of this work.

1.2. Block Copolymers and Directed Self-Assembly

1.2.1. Block Copolymer Basics

Block copolymers are composed of chemically dissimilar polymer chains that are covalently linked. Because of the low entropy of mixing, polymer blends are generally immiscible and macroscopically phase separate, but block copolymers are limited by the copolymer chain dimensions. They cannot macroscopically phase separate because each block of one polymer type is covalently linked to a block of a different polymer type. The length scale of this phase separation is determined by the size of the chain, typically ~ 5 – 20 nm in size, ideal for the coming generations of integrated circuits.[22] While a variety of block copolymers with a number of different combinations of monomer types are possible, linear diblock copolymers, which contains two types of polymers connected at a single junction, is the most commonly studied and the most likely candidate for use in IC fabrication. Such diblock copolymers will self-assemble into arrays of nanometer sized domains when heated above their glass transition temperature. The bulk phase behavior of such polymer has been extensively studied by multiple groups, both experimentally and theoretically.[23-26] Morphologies from spherical to cylindrical to gyroidal to lamellar are obtainable and are generally understood to depend on the volume fraction of the blocks of the BCP and the product of the degree of polymerization (N) and the Flory-Huggins interaction parameter (χ). The Flory-Huggins χ parameter describes the strength of interactions between the two blocks: a high χ means the blocks interact very weakly and therefore favor phase separation, and a low χ means the bock interact strongly and favor mixing. This is shown by the phase diagram as described by mean-field calculations as is shown in Figure 1.3.[27-31] The phase is primarily determined by the block volume fraction (commonly referred to as f_A or φ_A), while the order-disorder transition (ODT) is determined by a combination of the block volume fraction and the product χN. The ODT is found to be at $\chi N \sim 10.5$ for $f_A = 0.5$, though as will be seen later, this is true only for very ideal cases.[32-34] For the purposes of IC fabrication, the lamellar morphology is of primary interest because they resemble the line and space patterns formed by traditional optical lithography. Cylinder forming BCPs are also of interest for the specific purpose of forming or rectifying vias (connections between layers in the IC)[35,36] and for bit patterned media fabrication[37].

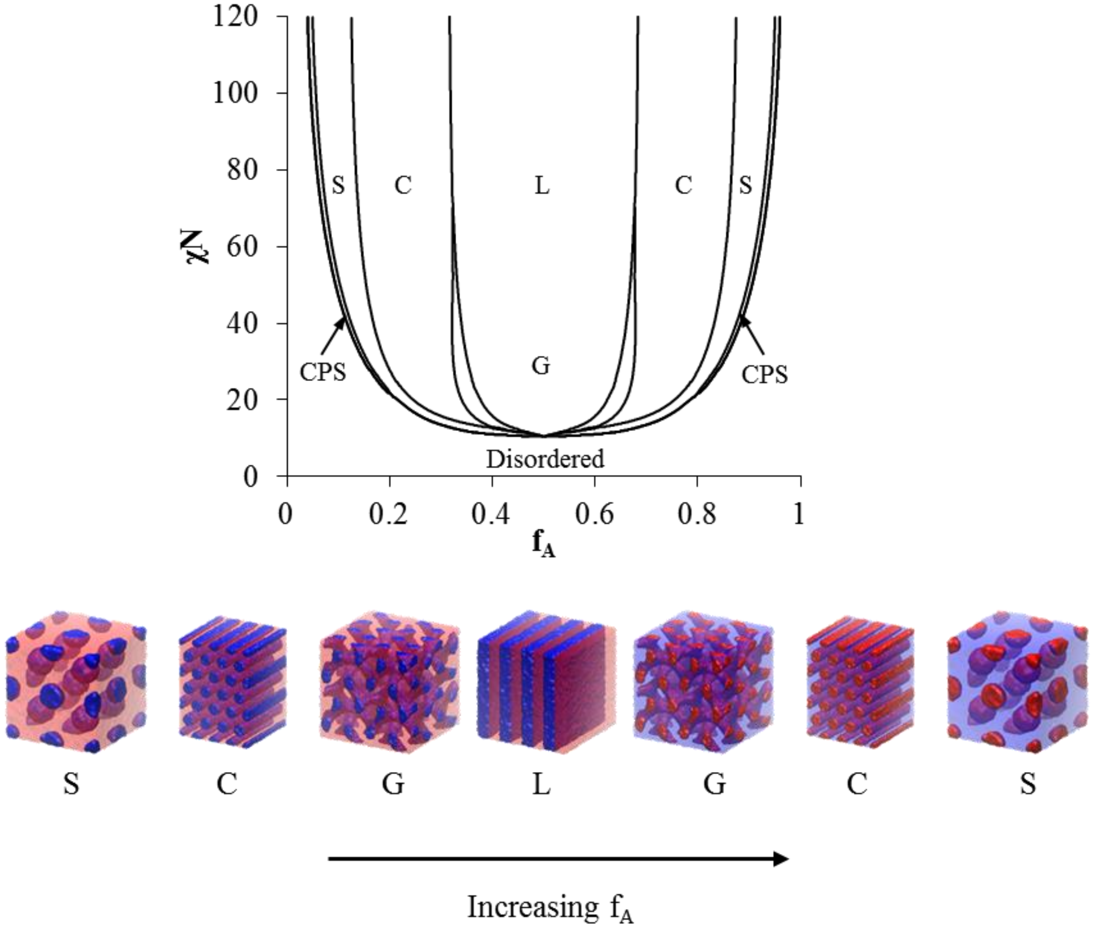

Figure 1.3. Mean-field block copolymer phase diagram and images of various possible morphologies: Close Packed Spheres (CPS), Body Centered Cubic Spheres (S), Hexagonally Close Packed Cylinders (C), Gyroid (G), and Lamellae (L). Adapted from Bates and Fredrickson.[27]

It is important to note that the smallest feature size a BCP is capable of forming is limited by the ODT. The size of a BCP domain is determined primarily by N (though χ and the stiffness of a polymer play a small role). This means that the feature size in a BCP is shrunk by reducing N. As N is decreased, χN decreases, so decreasing N will eventually lead to too small a χN value which will cause the BCP to mix. This means that the smallest pitch that a BCP can form is limited by χ; a higher χ allows N to be reduced further before the system mixes. PS-b-PMMA forms a minimum pitch of about 17 nm at the ODT. A plot showing the minimum pitch as a function of χ assuming the homopolymers have similar stiffness is shown in Figure 1.4 on a semi-log scale. In order to achieve significant reductions in minimum pitch, χ must be significantly increased; an order of magnitude increase in χ from 0.04 (PS-b-PMMA) to 0.4 yields a decrease in minimum pitch from ~17 nm to ~5.5 nm, and this assumes that BCP-DSA processes will work at the ODT. In order to reach 10 nm pitch, a χ of ~ 0.12 is required. However, it is much more likely that a χN well above the ODT will be required for effective BCP-DSA processes, so the true useable minimum pitch will be well above this value. If the required value of χN is 20 (a fairly low estimate) then a χ of ~ 0.36 is required (about an order of magnitude higher than the oft studied PS-b-PMMA). If a χN of 40 is required (a rather high estimate) then a χ of ~ 0.71 is required to reach a pitch of 10 nm. Because of this, development of high χ materials is a focus of many in the BCP-DSA community.

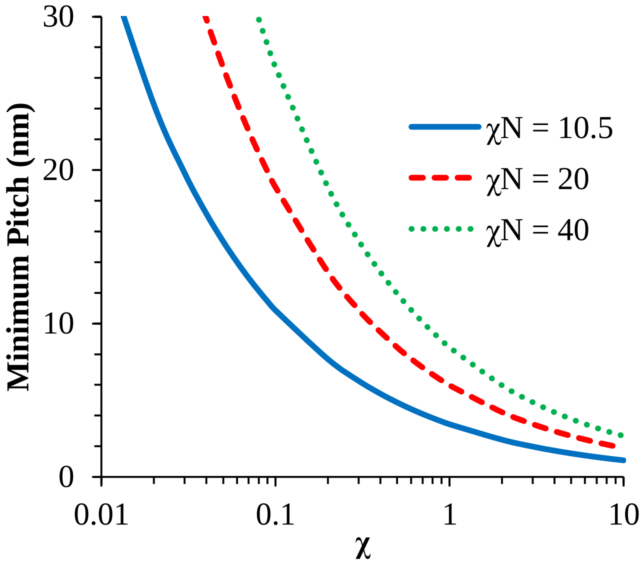

Figure 1.4. Minimum pitch as a function of χ assuming polystyrene like stiffness. Different curves refer to assuming a different minimum χN value for effective DSA processes.

1.2.2. Directing BCP Self-Assembly

As stated before, BCPs phase separate on the length scale of interest for IC fabrication, but without any direction or alignment cues, a thin film of lamellae forming BCP will form what is called a fingerprint pattern as seen in Figure 1.5, which is not useful. In order to overcome this limitation, BCPs are externally directed, generally by some pre-patterned underlayer, though BCPs have also been aligned using electric fields[38] and shear[39]. BCP alignment generally falls into two categories: chemoepitaxy, shown in Figure 1.6, and graphoepitaxy, shown in Figure 1.7, though some hybrid methods have been recently introduced.[40,41]

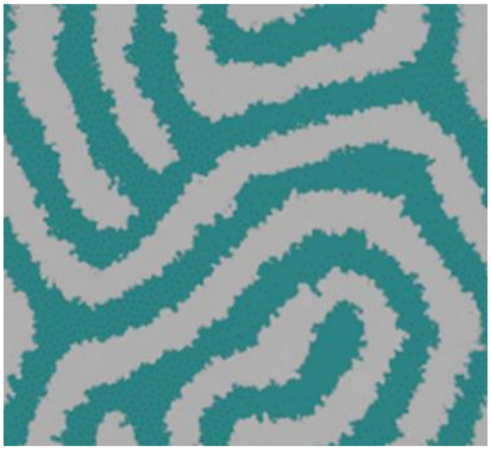

Figure 1.5. Image of fingerprint in a simulated BCP.

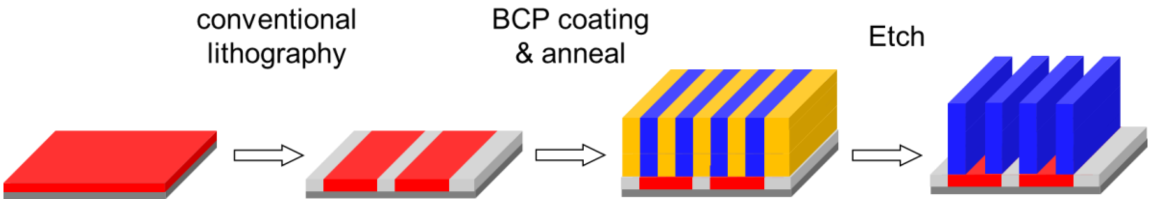
conventional lithography
BCP coating & anneal
Etch

Figure 1.6. Example schematic of a chemoepitaxial process.

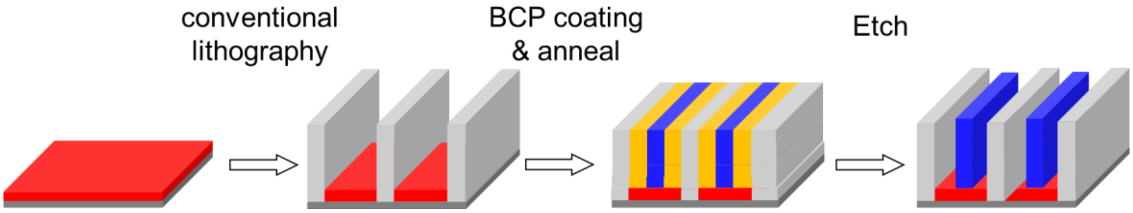
conventional lithography
BCP coating & anneal
Etch

Figure 1.7. Example schematic of a graphoepitaxial process.

In chemoepitaxy, conventional optical lithography is used to define a chemical pattern in the underlayer. The BCP is then coated and annealed, either by heating the BCP above the glass transition temperature (T_g) of the polymer, or by incorporating solvent vapor into the BCP film and thereby depress the T_g of the polymer system,[42] or some combination of the two[43]; this allows the BCP to self-assemble and align to the guiding layer. One common method is to have a so-called pinning stripe that is preferential to one of the block of the BCP, and a wider so-called background stripe that is relatively neutral to both blocks of the BCP. The pinning stripe pins one block (say the "A" block) in place and then the remaining B and A domains lay over the background stripe. The alignment propagates from the A block pinned to the pinning stripe to the adjacent blocks. Figure 1.6 shows a 1:3 pattern, that is, the pinning stripe defined by conventional lithography has width equal to the width of a block in the BCP, and the neutral stripe has a width equal to three times the width of a block in the BCP, leading to BCP pattern that is twice the density of the pattern made by optical lithography (a 2x density multiplying process), as shown in Figure 1.6. Higher density multiplying processes can also be used, such as a 3x density multiplying process that has a 1:5 pattern with a neutral stripe five times the width of one of the BCP blocks. One example of a process using this method of guidance is the Liu-Nealey (LiNe) process.[44] After the pattern has been formed by the BCP, one of the blocks is removed via a selective etch or some other selective removal process, resulting in a line and space pattern which can then be used in subsequent IC fab steps.

Similar to chemoepitaxy, graphoepitaxy uses conventional lithography to define a guiding layer, but instead of defining a chemical contrast it defines a topographical contrast. The BCP aligns to the walls and alignment propagates into the middle of the space between the aligning walls. After removing one of the blocks via an etch or some other selective removal, the pitch is again reduced from the original pitch of the optical lithographic pattern, but only in the area between the guiding walls. The guiding walls themselves (which can be many times wider than the BCP blocks) are not modified and so the pitch is not changed in that region. Figure 1.7 uses a wall that is the same size as one of the block of the BCP, but this is not typical as such walls are usually much wider than the blocks. These wide walls amount to wasted space in an IC pattern and so chemoepitaxy is generally the preferred method.

1.3. Challenges in BCP-DSA

According to the keynote paper at the 2015 SPIE Advanced Lithography: Alternative Lithographic Technologies conference: "For consideration as a manufacturing method, BCP-DSA must generate a pattern with equivalent or improved (A) pattern quality in terms of line CD and roughness and (B) defect density."[45] Studying the causes and methods for controlling these properties is a major focus of this thesis.

1.3.1. Line Roughness

Line roughness comes in two varieties: line edge roughness (LER) and line width roughness (LWR). LER refers to variations in a line edge away from a straight line while LWR refers to variations in width along the length of the line as seen in Figure 1.8. It has been shown that LWR is more important than LER when considering device performance at current length scales,[46-48] but because the two are so closely related (in traditional lithographic systems LWR is generally equal to $\sqrt{2}LER$)[49] and the same types of phenomena cause each, they are both commonly studied. LER and LWR are both commonly reported as 3σ values, that is they are reported as 3 times the standard deviation of either the deviation from a straight line edge (LER) or 3 times the standard deviation from a uniform line width (LWR).

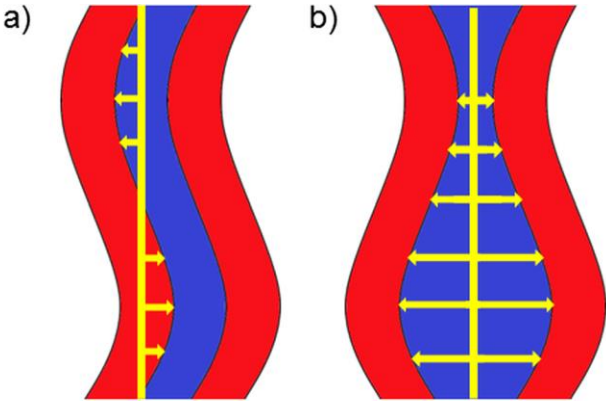

Figure 1.8. Top–down schematic of (a) LER and (b) LWR. LER is the deviation from a straight line edge, and LWR is the deviation from a uniform line width.

According to the International Technology Roadmap for Semiconductors,[50] for the 11 nm CD node, 3σLWR must be below 0.9 nm, well below the 2.5 nm to 3 nm that current best practices reach in PS-b-PMMA.[51] In the 90's, Semenov studied the roughness of BCPs in the strong segregation limit (that is, when χN is high).[52,53] However, until recently, not much study has been done on line roughness in the context of BCP-DSA. Portions of this work will consider the effect of material properties and processing conditions on LER and LWR in BCP-DSA.

1.3.2. Defectivity

Defectivity is probably the primary limitation of BCP-DSA. Though much work has been done to reduce defectivity in BCP-DSA, defectivity is still on the order of tens of defects per cm^2 in the best processes.[54] This is still orders of magnitude above the desired defect density of 0.01 defects per cm^2.[50] Defects are still rampant in many demonstrated process flows, and though understanding is increasing as to the fundamental causes of these defects, there is still a long way to go towards a complete understanding.[55,56] As can be seen in Figure 1.9 which shows the defect density of an IMEC process[54] over the 2013 year of study, defectivity still struggles to improve. Previous studies have calculated the free energy of defects in laterally confined systems (that is graphoepitaxy guiding), and in chemically aligned systems as a function of guiding linewidth but there are still a great many factors involved in defect formation that are not yet well understood.[55-57] There are two possible causes for such high defectivity: the free energy difference between the defective and the defect free state is small enough that the equilibrium concentration of defects is simply above the desired density, or defects are being kinetically trapped during the annealing step. The defect density can be related to the defect free energy via Equation 1.2.[55]

$$n_d = a^{-2} \exp\left(\frac{-E_{defect}}{kT}\right) \tag{1.2}$$

The parameter a is the size of the defect. Because the defect density depends exponentially on the defect free energy, an accurate calculation of this value is critical to understanding anticipated defect levels in DSA processes. Both defect free energy and kinetics of defect healing will be investigated in this work.

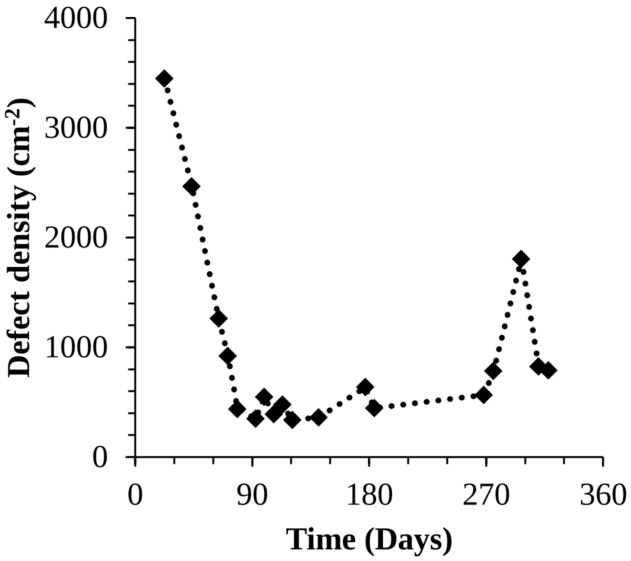

Figure 1.9. Plot of defect density over time for an IMEC process from March 2013 to February 2014.[54] Defect density is slow to improve.

1.4. Modeling of BCPs and BCP-DSA

The standard model and theory for the simulation and study of block copolymers has for decades been the Gaussian model and self-consistent field theory, also called mean-field theory.[58] It was first extended to BCPs in 1975 by Helfand.[59,60] In this theory, diblock copolymers are treated as elastic threads that must fill space uniformly and which interact with an unfavorable contact energy. Instead of modeling all chains at once, the interactions are replaced by fields which represent the total time averaged interactions experienced by individual A and B segments, as seen in Figure 1.10. This makes the calculations extremely efficient with only a minimal cost in accuracy. Because time averaged fields are used, fluctuations at the interface are ignored. When χN is large and structures are very well ordered then the fields are large compared to the interfacial fluctuations and the model is accurate. Near the ODT the fluctuations are strong enough to affect the chain configurations, and accuracy is significantly diminished.

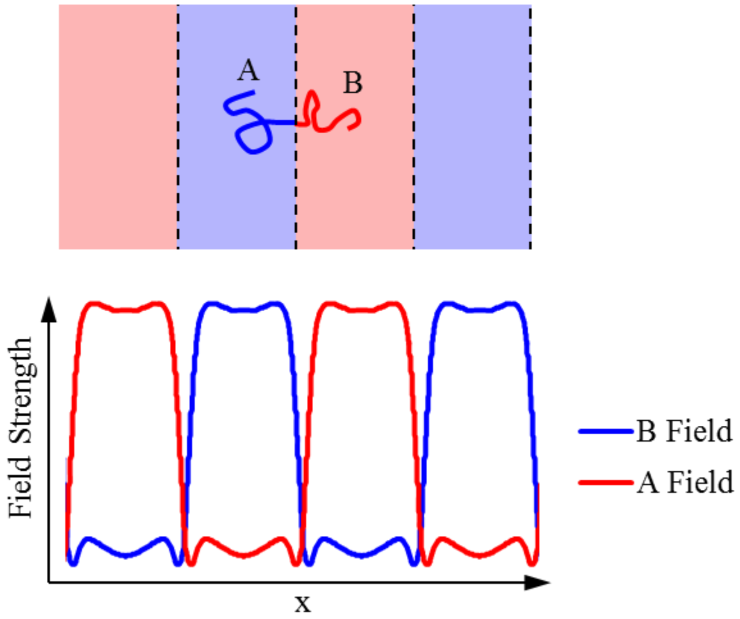

Figure 1.10. Mean-field theory models focus on a single molecule and models the interactions by two static fields, one for the A blocks, and one for the B blocks.

These models and their derivatives are responsible for almost all of the modeling of BCP systems since the 1970's until recently. It was mean field models that developed the phase diagram shown in Figure 1.3 and yielded valuable insight into BCP phase separation. In 1980 Leibler developed an analytical approximation to the full mean theory for use in weakly-segregated melts commonly referred to as weak-segregation theory.[61] This model provided a nice explanation of the structure of the mean-field phase diagram near the ODT, and yielded mixed state scattering functions which are still used today to measure χ.[62,63] However, the weak-segregation theory becomes inaccurate in the demixed state above $\chi N \sim 12$,[64] and even in this region the mean field model is inaccurate. Eventually, fluctuation corrections were made to this model improving its accuracy,[65] but evidence now suggests even with the corrections the weak-segregation theory is inaccurate in the demixed state.[58,66]

In 1985 Semenov developed a theory for an analytical analysis in the strong segregation regime.[52,53,67] When χN is very large, the A and B blocks are so stretched that they can be modeled as essentially straight chains perpendicular to the interface. This theory, generally called strong segregation theory (SST), gives similar phase boundaries as the full mean field calculations and indicates that the more complex phases such as the gyroidal phase are unstable, consistent with experiment.[68-70] So far, researchers have considered corrections for the junction entropy,[52,71] chain end entropy[72], chain fluctuations,[73] and interface overcrowding[74]. However, direct comparisons with SCFT at $\chi N \sim 1000$ suggest that the strong-segregation limit is still not fully understood.[75] Perhaps more importantly, most BCPs are studied when $\chi N < 100$ and SST is very inaccurate at these segregation.

Mean-field and self-consistent field theory methods have been used for decades and provided valuable insight into BCP fundamentals. Today mean-field models are still commonly used to study BCPs in a variety of arenas, even with its fundamental inaccuracies near the ODT. However, in recent years, new models have been developed to compensate for the shortcomings of mean-field and self-consistent field theories.

One method that has recently become more popular is the coarse-graining of BCP polymer systems. Instead of reducing calculations by modeling the interactions as a time averaged field, the calculations of the many-body problem are reduced by lumping together multiple atoms as a single entity. This results in a significant reduction in calculations over a full atomistic or sub-atomistic representation of these chains, but a significant increase in calculations over the older mean-field models. This has been possible because of great increases in computing power available to researchers in recent years. Once coarse-grained, both Monte Carlo methods[76] and molecular dynamics (MD) methods[77-79] are used. Whether Monte Carlo methods or MD methods are used, these coarse-grained models are fundamentally more accurate than mean-field models because they include all relevant fluctuations. The only error that will exist is due to the errors associated with coarse-graining, which includes both the inherent spatial averaging and the development of accurate interaction potentials. In general, these errors are small, especially compared to the previously discussed mean-field models. This work uses a coarse-grained model and MD calculations to study BCP-DSA.

Molecular dynamics is essentially a very large initial value problem where Newton's equations of motions are solved through time. In the microcanonical or NVE ensemble, the number of molecules (N), volume (V), and energy (E) are kept constant. This corresponds to an adiabatic system. In this ensemble the governing differential equation is:

$$F(x) = m\dot{v}(t) = -\nabla U(x) \tag{1.3}$$

where F is the force on the particles with position x, m is mass, t is time, v is the velocity, and U is the potential energy. Given some initial set of positions and velocities, the positions are integrated through time using a method such as the Velocity-Verlet method.[80] However, simulating systems that are not adiabatic would be greatly advantageous. Other common ensembles include the canonical ensemble (NVT) and the isothermal-isobaric ensemble (NPT).

In the NVT ensemble the number of particles (N), volume (V), and temperature (T) are kept constant. In this case the energy of endothermic and exothermic processes are exchanged with a heat sink. Common thermostats for NVT simulations include the Nosé-Hoover thermostat[81], the Berendsen thermostat[82,83], and the Andersen thermostat[84].

In the NPT ensemble the number of particles (N), pressure (P), and temperature (T) are kept constant. This ensemble uses both a thermostat and a barostat. The barostat must change the volume of the box as the pressure changes. Barostats include the Berendsen barostat, the Nosé-Hoover barostat, the Parrinello-Rahman barostat[85], and the Martyna-Tobias-Klein barostat[86].

One other model for simulating BCPs worth noting is the so called single-chain in mean field (SCMF) model.[87,88] This model is a combination of mean field and coarse grained MC or MD methods. Polymer chains are explicitly modeled as in the MD and MC techniques described above, but these chains act in response to a field that is periodically updated based on the modeled chains. The chains are explicitly modeled but do not directly interact. This method tries to reduce the impact of the inaccuracies of mean-field models, but does not go as far as complete MC or MD methods. Because of this, and its slightly more complicated implementation, it is less commonly used than either the mean-field models or the coarse-grained MC and MD models.

BCPs have been studied using various models since the 1970s, most notably via mean-field methods. These methods are computationally efficient, but suffer a loss of fluctuations and so exhibit inaccuracies, especially near the ODT. In order to overcome these shortcomings, and because of the advent of increased availability of computing power, coarse grained MC and MD models have become more common. A coarse grained MD model is used in this work.

1.5. References

1 Gorton, W. S. “The Genesis of the Transistor“ Proceedings of the IEEE 1998 (originally 1949), 86.

2 http://www.intel.com/pressroom/kits/events/moores_law_40th/index.htm

3 Borodovsky, Y. Proc. SPIE 2006, 6153, 615301.

4 Moore, G. Electronics Magazine 1965.

5 Moore, G. Proc. SPIE. 1995, 2437, 2.

6 Thompson, S. E.; Parthasarathy, S. Mater. Today. 2006, 9, 20.

7 May, G. S.; Sze, S. M. “Fundamentals of Semiconductor Fabrication” John Wiley & Sons, Inc 2004, p. 64.

8 Finders, J.; Eurlings, M.; Schenau, K. V. I.; Dusa, M. V.; Jenkins, P. “Low-k1 imaging: how low can we go?” Proc. SPIE. 2000, 4226.

9 Harriott, L. R. “Limits of Lithography” Proceedings of the IEEE 2001, 89, 366.

10 Bakshi, V. “EUV Lithography” SPIE Press 2009.

11 Rothschild, M “A Roadmap for Optical Lithography” Optics and Photonics News, Jun 2010.

12 Ph.D. Proposal by Wei-Ming Yeh, “A Study on the Improvement of Pattern Collapse by Surface Modification and Adhesion Promoter”

13 Pitcher, G. "Semiconductor industry pushes ahead to 7nm, even if EUV lithography isn’t ready" newelectronics, Findlay Media Ltd. December 9, 2014, March 27th, 2015. <http://www.newelectronics.co.uk/electronics-technology/semiconductor-industry-pushes-ahead-to-7nm-even-if-euv-lithography-isnt-ready/66415/>

14 McGrath, D. " Issues of EUV lithography" EETAsia, Global Sources. November, 22, 2011. March 27, 2015. < http://www.eetasia.com/ART_8800656186_480200_NT_a81058ff.HTM>

15 Stamm, U.; Kleinschmidt, J.; Gaebel, K.; Birner, H.; Ahmad, I.; Bolshukhin, D.; Brudermann, J.; Chinh, T. D.; Flohrer, F.; Goetze, S.; Hergenhan, G.; Kloepfel, D.; Korobotchko, V.; Mader, B.; Mueller, R.; Ringling, J.; Schriever, G.; Ziener, C. " EUV source power and lifetime: the most critical issues for EUV lithography" Proc. SPIE 2004, 5374, 133.

16 Levinson, H. J.; Principles of Lithography, Second Edition, SPIE Press, Bellingham, WA (2005).

17 Krasnoperova, A. A.; Rippstein, R.; Flamholz, A.; Kratchmer, E.; Wind, S.; Brooks, C.; Lercel, M. “Imaging capabilities of proximity x-ray lithography at 70-nm ground rules,” Proc. SPIE 1999, 3676, 24–39.

18 Folta, J. A.; Bajt, S.; Barbee, T. W.; Grabner, R. F.; Mirkarimi, P. B.; Nguyen, T.; Schmidt, M. A.; Spiller, R.; Walton, C. C.; Wedowski, M.; Montcalm, C. “Advances in multilayer reflective coatings for extreme-ultraviolet lithography,” Proc. SPIE 199, 3676, 702–709.

19 Bajt, S. “Molybdenum-ruthenium/beryllium multilayer coatings,” J. Vac. Sci. Technol. A 2000, 18, 557–559.

20 Brandt, P.; Sardana, C.; Ibbotson, D.; Wieland, M.; Fay, A. " Comparison between e-beam direct write and immersion lithography for 20nm node" Proc. SPIE 2015, 9423, 942311.

21 Takeishi, H.; Sreenivasan, S. V. " Nanoimprint system development and status for high volume semiconductor manufacturing" Proc. SPIE 2015, 9423 94230C.

22 Hawker, C. J.; Russell, T. P. "Block Copolymer Lithography: Merging "Bottom-Up" with "Top-Down“ Processes" MRS Bulletin 2005, 30, 952.

23 Hashimoto, T.; Shibayma, M.; Fujimura, M.; Kawai, H. "Block Copolymers, Science and Technology", edited by D.J. Meier (Harwood Academic, London, 1983) p. 63.

24 Bates, F. S.; Fredrickson, G. H. Annu. Rev. Phys. Chem. 1990, 41, 525.

25 Fredrickson G. H.; Bates, F. S. Annu. Rev. Mater. Sci. 1995, 1.

26 Hamley, I. W. "The Physics of Block Copolymers" (Oxford University Press, New York, 1998) p. 125.

27 Bates, F. S.; Fredrickson, G. H. "Block Copolymers – Designer Soft Materials" Physics Today 1999, 52, 32.

28 Matsen, M. W.; Schick, M. Phys. Rev. Lett. 1994,72, 2660.

29 Matsen, M. W.; Schick, M. Macromolecules 1994,27, 6761.

30 Matsen, M. W.; Schick, M. Macromolecules 1994,27, 7157.

31 Bates, F. S. Macromolecules 1996, 29, 1091.

32 Fredrickson, G. H.; Helfand, E. "Fluctuation effects in the theory of microphase separation in block copolymers“ J. Chem. Phys. 1987, 87, 697.

33 Lin, C. C.; Jonnalagadda, S. V.; Kesani, P. K.; Dai, H. J.; Balsara, N. P. “ Effect of Molecular Structure on the Thermodynamics of Block Copolymer Melts“ Macromolecules 1994, 27, 7769-7780.

34 Abuzaina, F. M.; Patel, A. J.; Mochrie, S.; Narayanan, S.; Sandy, A.; Garetz, B. A.; Balsara, N. P. “Structure and Phase Behavior of Block Copolymer Melts near the Sphere-Cylinder Boundary“ Macromolecules 2005, 38, 7090-7097.

35 Laachi, N.; Iwama, T.; Delaney, K. T.; Kim, B.; Bristol, R.; Shykind, D.; Weinheimer, C. J.; Fredrickson, G. H. "Field-theoretic simulations of directed self-assembly in cylindrical confinement: placement and rectification aspects" Proc. SPIE. 2014, 9049, 90491M.

36 Iwama, T.; Laachi, N.; Delaney, K. T.; Fredrickson, G. H. "Computational study of directed self-assembly for contact-hole shrink and multiplication" J. Micro/Nanolith. MEMS MOEMS. 2015, 14(1), 013501.

37 Griffiths, R. A.; Williams, A.; Oakland, C.; Roberts, J.; Vijayaraghavan, A.; Thomson, T. " Directed self-assembly of block copolymers for use in bit patterned media fabrication" Journal of Physics D: Applied Physics 2013, 46, 503001.

38 Manksy, P.; DeRouchey, J.; Russell, T. P.; Mays, J.; Pitsikalis, M.; Morkved, T.; Jaeger, H. "Large-Area Domain Alignment in Block Copolymer Thin Films Using Electric Fields" Macromolecules 1998, 31, 4399-4401.

39 Qiang, Z.; Zhang, Y.; Groff, J. A.; Cavicchi, K. A.; Vogt, B. D. "A generalized method for alignment of block copolymer films: solvent vapor annealing with soft shear" Soft Matter 2014, 10, 6068-6076.

40 Kim, J.; Yin, J.; Cao, Y.; Her, Y.; Peterman, C.; Wu, H.; Shan, J.; Tsutsumi, T.; Lin, G. " Toward high-performance quality meeting IC device manufacturing requirements with AZ SMART^{TM} DSA process" Proc. SPIE 2015, 9423, 94230R.

41 Kasahara, Y.; Seino, Y.; Kobayashi, K.; Kanai, H.; Sato, H.; Kubota, H.; Tobana, T.; Minegishi, S.; Miyagi, K.; Kihara, N.; Kodera, K.; Shiraishi, M.; Kawamonzen, Y.; Nomura, S.; Azuma, T. " RIE challenges for sub-15 nm line-and-space patterning using directed self-assembly lithography with coordinated line epitaxy (COOL) process" Proc. SPIE 2015, 9428, 94280S.

42 Jarnagin, N. D.; Yeh, W.; Cheng, J.; Peters, A.; Lawson, R. A.; Tolbert, L. M.; Henderson, C. L. "PS-b-PHOST as a high χ block copolymers for directed self assembly: optimization of underlayer and solvent anneal processes" Proc. SPIE 2013, 8680, 86801X.

43 Gotrik, K. W.; Ross, C. A. "Solvothermal Annealing of Block Copolymer Thin Films" Nano Letters 2013, 13, 5117-5122.

44 Liu, C. C.; Nealey, P. F.; Raub, A. K.; Hakeem, P. J.; Brueck, S. R. J.; Han, E.; Gopalan, P. " Integration of block copolymer directed assembly with 193 immersion lithography" Journal of Vacuum Science and Technology B 2010, 28, C6B30.

45 Millward, D. B.; Lugani, G. S.; Light, S. L.; Niroomand, A.; Hustad, P. D.; Trefonas, P.; Quach, D.; Ginzburg, V. V. " Graphoepitaxial and chemoepitaxial methods for creating line-space patterns at 33nm pitch: comparison to a HVM process" Proc. SPIE 2015, 9423, 942304.

46 Chuang, Y.; Jack, K.; Cheng, H.; Whittaker, A.; Blakey, I. Adv. Func. Mater. 2013, 23, 173 .

47 Hyun-Woo, K.; Ji-Young, L.; Shin, J.; Sang-Gyun, W.; Han-Ku, D.; Joo-Tae, M. IEEE T. Electron. Dev. 2004, 51, 1984.

48 Asenov, A.; Kaya, S.; Brown, A. R.; IEEE T. Electron. Dev 2003, 50, 1254.

49 Nikitin, A.; Sicignano, A.; Yeremin, D.; Sandy, M.; Goldburt, T. Critical Issues in Quantifying Line Edge Roughness. Proc. SPIE 2005, 5752, 1098

50 International Technology Roadmap for Semiconductors http://www.itrs.net/ March 21, 2015.

51 Kim, J.; Yin, J.; Her, Y.; Peterman, C.; Wu, H.; Shan, J.; Tsutsumi, T.; Lin, G. "Toward High Performance Quality Meeting IC Device Manufacturing Requirements with AZ SMARTTM DSA Process" Proc. SPIE 2015, 9423 94230R.

52 Semenov, A. N. Macromolecules 1993, 26, 6617.

53 Semenov, A. N. Macromolecules 1994, 27, 2732.

54 Gronheid, R.; Delgadillo, P. R.; Pathangi, H.; Van den Heuvel, D.; Parnell, D.; Chan, B. T.; Lee, Y.; Van Look, L.; Her, Y.; Lin, G.; Harukawa, R.; Nagaswami, V.; D'Urzo, L.; Somervell, M.; Nealey, P. "Defect reduction and defect stability in IMEC's 14nm half-pitch chemo-epitaxy DSA flow" Proc. SPIE 2014, 9049,904905.

55 Takahashi, H.; Laachi, N.; Delaney, K. T.; Hur, S. M.; Weinheimer, C. J.; Shykind D.; Fredrickson, G. J. "Defectivity in Laterally Confined Lamella-Forming Diblock Copolymers: Thermodynamic and Kinetic Aspects," Macromolecules 2012, 45, 6253.

56 Kim, B.; Laachi, N.; Fredrickson, G. H. "Defectivity study of directed elf-assembly of cylindrical diblock copolymers in laterally confined thin channels," Proceedings of SPIE 2013, 8680, 868016.

57 Laachi, N.; Takahashi, H.; Delaney, K. T.; Hur, S. M.; Shykind, D.; Weinheimer C.; Fredrickson, G. H. "Self Consistent Field Theory of Directed Self-Assembly in Laterally Confinded Lamellae-Forming Diblock Copolymers," Proceedings of SPIE 2012, 8323, 83230K.

58 Matsen, M. W. "The standard Gaussian model for block copolymer melts" Journal of Physics: Condensed Matter 2002, 14, R21-R47.

59 Helfand, E. "Theory of inhomogeneous polymers: Fundamentals of the Gaussian random-walk model" J. Chem. Phys. 1975, 62, 999.

60 Helfand, E. Macromolecules 1975, 8, 552.

61 Leibler, L. "Theory of Microphase Separation in Block Copolymers" Macromolecules 1980, 13, 1602.

62 Durand, W. J.; Blachut, G.; Maher, M. J.; Sirard, S.; Tein, S.; Carlson, M. C.; Asano, Y.; Zhou, S. X.; Lane, A. P.; Bates, C. M.; Ellison, C. J.; Willson, C. G.; "Design of high-χ block copolymers for lithography," J. Polym. Sci. A1 2015,53, 344-352.

63 Bates, F. S.; Rosedale, J. H.; Fredrickson, G. H. “Fluctuation effects in a symmetric diblock copolymer near the order–disorder transition” J. Chem. Phys. 1990, 92, 6255.

64 Matsen, M. W.; Bates, F. S. Macromolecules 1996, 29, 1091.

65 Fredrickson, G. H.; Helfand, E. J. Chem. Phys. 1987, 87, 697.

66 Maurer, W. W.; Bates, F. S.; Lodge, T. P.; Almdal, K.; Mortensen, K.; Fredrickson, G. H. J. Chem. Phys. 1998, 108, 2989.

67 Semenov, A. N.; Sov. Phys.-JETP 1985, 61, 733.

68 Likhtman, A. E.; Semenov, A. N. Macromolecules 1997, 30, 7273.

69 Olmsted, P. D.; Milner, S. T.; Macromolecules, 31, 4011.

70 Hajduk, D. A.; Gruner, S. M.; Rangarajan, P.; Register, R. A.; Fetters, L. J.; Honeker, C.; Albalak, R. J.; Thomas, E. L. Macromolecules 1994, 27, 490.

71 Matsen, M. W.; Gardiner, J. M. J. Chem. Phys. 2000, 113, 1673.

72 Matsen, M. W.; Bates, F. S. Macromolecules 1995, 28, 8884.

73 Goveas, J. L.; Milner, S. T.; Russel, W. B. Macromolecules 1995, 28, 8884.

74 Likhtman, A. E.; Semenov, A. N. Europhys. Lett. 2000, 51, 307.

75 Matsen, M. W. J Chem Phys 2001, 114, 10528.

76 Detcheverry, F. A.; Pike, D. Q.; Nagpal, U.; Nealey, P. F.; de Pablo, J. J. "Theoretically informed coarse grain simulations of block copolymer melts: method and applications" Soft Matter 2009, 5, 4858.

77 Lawson, R. A.; Ludovice, P. J.; Henderson, C. L. " Development of realistic potentials for the simulation of directed self-assembly of PS-PMMA di-block copolymers" Proc. SPIE 2011, 7970, 79700N.

78 Medapuram, P.; Glaser, J.; Morse, D. C. "Universal Phenomenology of Symmetric Diblock Copolymers near the Order−Disorder Transition" Macromolecules 2015, 48, 819-839.

79 "Publications using HOOMD-blue" http://codeblue.umich.edu/hoomd-blue/publications.html March 23, 2015.

80 Verlet, L. "Computer "Experiments" on Classical Fluids. I. Thermodynamical Properties of Lennard-Jones Molecules" Physical Review 1967, 159, 98.

81 Nosé, S. "A unified formulation of the constant temperature molecular dynamics methods" J. Chem. Phys. 1984, 81, 511.

82 Berendsen, H. J. C.; Postma, J. P. M.; van Gunsteren, W. F.; DiNola, A.; Haak, J. R. "Molecular dynamics with coupling to an external bath" J. Chem. Phys. 1984, 81, 3684.

83 Harvey, S. C.; Tan, R. K. Z.; Cheatham III, T. E. "The flying ice cube: Velocity rescaling in molecular dynamics leads to violation of energy equipartition" 1998, 19,726-740.

84 Tanaka, H.; Nakanishi, K.; Watanabe, N. "Constant temperature molecular dynamics calculation on Lennard‐Jones fluid and its application to water" J. Chem. Phys. 1983, 78, 2626.

85 Parrinello, M.; Rahman, A. "Polymorphic transitions in single crystals: A new molecular dynamics method" Journal of Applied Physics 1981, 52, 7182.

86 Martyna, G. J.; Tobias, D. J.; Klein, M. L. "Constant pressure molecular dynamics algorithms" J. Chem. Phys. 1994, 101, 4177.

87 Daoulas, K. C.; Müller, M. J. Chem. Phys. 2006, 125, 184904.

88 Daoulas, K. C.; Müller, M.; de Pablo, J. J.; Nealey, P. F.; Smith, G. D. Soft Matter 2006, 2, 573.

CHAPTER 2

COARSE-GRAINED MODEL

Directed self-assembly (DSA) of block copolymers (BCPs) is a promising technique for producing sub-30 nm pitch regular patterns and the development of these DSA techniques could benefit greatly from computer simulation of such methods.[1-5] Many theories and simulations have been used to study block copolymers already, with a great deal of work focusing on the order disorder transition (ODT), the order-order transitions between various morphologies such as hexagonally packed cylinders, or lamellae, and the spacing between the various structural units that make up a morphology. Leibler used mean-field theory to predict the phase diagram for a di-block copolymer system, which Helfand, and later Fredrickson, improved to include fluctuations.[6-8] This change brought the product of χ (the Flory-Huggins interactions parameter) and N (the degree of polymerization) at the ODT and the periodic spacing prediction into agreement with experiment in the weak segregation regime, where the drive to phase separate is small. Others developed various mean-field and self-consistent field theory (SCFT) to study the strong segregation regime where the drive to phase separate is large.[9,10] Simulation methods such as mean field and self-consistent field theory suffer from a number of limitations, especially the exclusion of fluctuations, that affect their accuracy and their level of detail. Simulation methods that include fluctuations, such as molecular dynamics (MD) methods often use unrealistic potentials such as purely repulsive or non-interacting potentials for unlike monomers, and/or are very slow. [11,12] By combining molecular dynamics and realistic potentials, a model can potentially provide more accurate simulations of the inherent polymer behavior, dynamics, and equilibrium states without a need to guess modes of molecular movement (as is necessary for Monte Carlo methods). This is especially true for polymer systems that have very different densities or interaction strengths, as is the case for almost all real polymer systems. The effects of mismatched density or interaction strength on the behavior of the BCP is not well understood, therefore a model that can handle these differences is valuable. We have developed a novel model for simulation of BCP behavior and DSA processes based on molecular dynamics of coarse-grained polymer chains simulated using graphics processing units (GPUs) to perform the calculations.

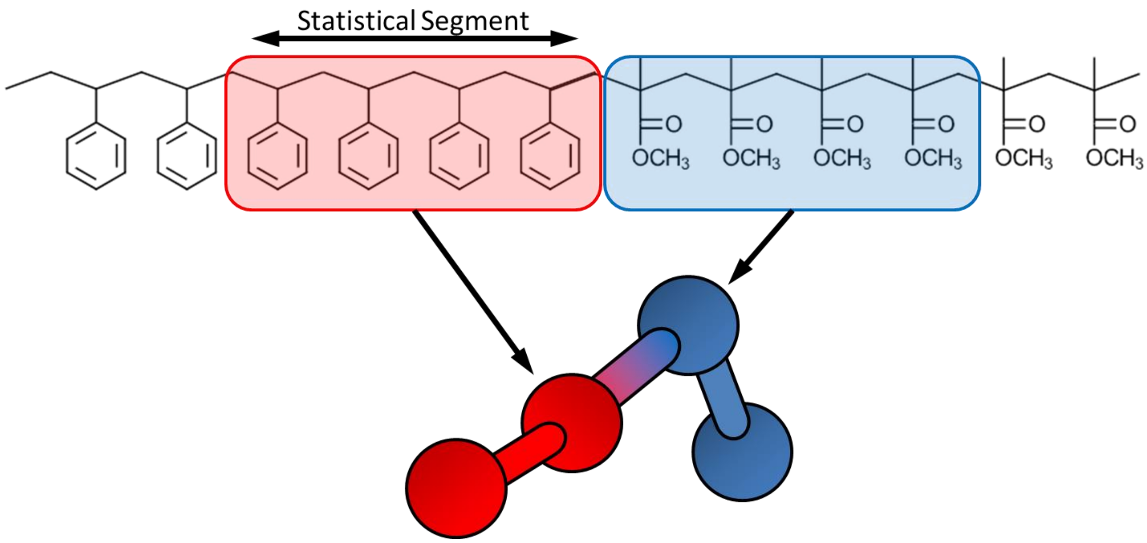

Figure 2.1. Description of coarse graining of polymer. Some number of monomers, corresponding to the statistical segment length, are modeled as a single bead and linked tougher.

The polymers consist of a bead-spring type system where a single bead corresponds to multiple monomers as shown in Figure 2.1. This coarse graining can result in simulations ~100-200 times faster than atomistic simulations, depending on the scale of coarse graining used in the polymer model. In addition, this work uses graphics processing units (GPUs) to perform the calculations. This is very effective because of the natural parallelizability of MD simulations. Using HOOMD-Blue simulations can run up to 200 times faster on a GPU enabled computer as compared to a standard desktop computer.[13,14] By combining the two speed gains from coarse graining the simulation and using GPUs for the calculations, the simulation executes at speeds 40,000 times faster than conventional atomistic simulations and approaches the speed of other more commonly used simulation techniques for BCPs. The purpose of this chapter is to more fully describe the model, describe commonly used techniques, and compare the model with other existing models. In this chapter, I describe a method to measure the pitch of an off-lattice BCP model, a method to determine the ODT of the off-lattice MD system, and a method to calculate χ for that same system.

2.1. Coarse Grained Model

We modeled polymers by grouping a number of monomers into a single bead, as shown in Figure 2.1. Each bead, when modeling a real polymer, corresponded to approximately a statistical segment length of that polymer. To verify this, fully periodic atomistic simulations of various polymers were run using the software Molecular Operating Environment (MOE) and Equation 2.1 was fit to the resulting state.[15]

$$\langle cos(\theta)\rangle = e^{-k/k_p} \qquad 2.1$$

θ is the angle between the vector defining the direction of the polymer chain at any given monomer and the vector defining the direction of the polymer chain k monomers away.

k_p is the statistical segment length in number of monomers. The vector defining the direction of the polymer chain at some monomer *i* is the vector from the center of mass of monomer *i-1*, to the center of mass of monomer *i+1*. The resulting data is shown in Figure 2.2 for various polymers of interest and the resulting fit parameters are shown in Table 2.1. For most of this work, a statistical segment length corresponding to 4 monomers was chosen as it best matched the polymers of interest.

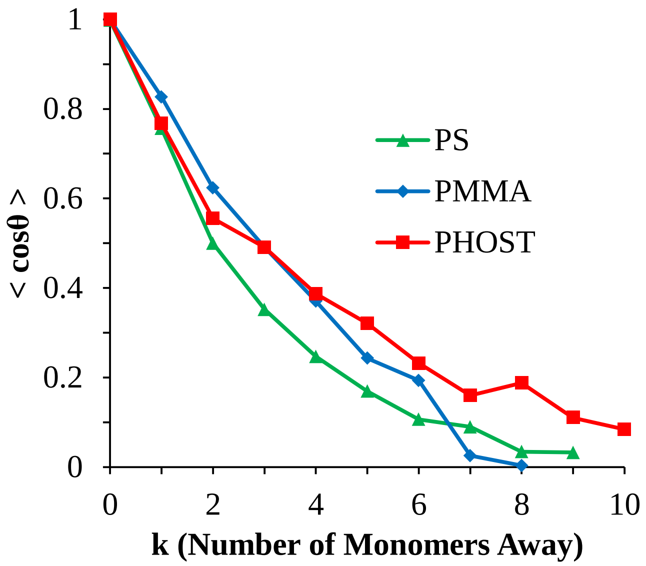

Figure 2.2. Plot of $\langle cos\theta \rangle$ as a function of monomeric separation. θ is the angle between the vector defining the direction of the polymer chain at any given monomer and the vector defining the direction of the polymer chain *k* monomers away.

Table 2.1.Table of fit parameters of Equation 2.1 to the data in Figure 2.2.

	PS	**PMMA**	**PHOST**
K_p (monomers)	2.85	4.02	4.14

Each coarse grained bead interacts via three potentials, a stretching potential that acts between two bonded beads, an optional angle potential that acts between every set of three consecutively bonded beads, and a non-bonded potential that affects all beads that are not bonded and are not two bonds apart. This is illustrated in Figure 2.3 and the equations used are shown in Equations 2.2 - 2.4.

$$E_{str}(r) = k_{str}(r - L)^2 \qquad 2.2$$

$$E_{ang}(r) = k_{ang}(a - A)^2 \qquad 2.3$$

$$E_{Non\text{-}bonded} = \varepsilon_{ij}\left[\left(\frac{\sigma_{ij}}{r}\right)^8 - 2\left(\frac{\sigma_{ij}}{r}\right)^4\right] \qquad 2.4$$

The stretching potential (Equation 2.2) has a harmonic form and tethers the beads together. k_{str} is the strength of the harmonic oscillator, r is the distance between bonded beads, and L the equilibrium distance of the given bond. The angle potential (Equation 2.3) also has a harmonic form and is used primarily to prevent collapse of the polymer chain, where k_{ang} is the strength of the harmonic oscillator, a is the angle of three collinear beads, and A the equilibrium angle. In some cases when beads that are separated by 2 bonds (bead i and bead $i+2$) interact via the non-bonded potential, crystallization of polymers theoretically amorphous polymers occurred. For this reason, instead of the 1-3 beads interacting via the non-bonded potential an angle potential was introduced which has been shown to give realistic chain statistics. If there was no direct interaction between beads separated by two bonds then there beads would often overlap to increase density and increase non-bonded interaction; however, this is unrealistic so the angle potential was used. Equation 2.4 gives the non-bonded potential where ε_{ij} is the strength of interaction between type *i* and type *j* beads, σ_{ij} is the equilibrium distance between bead type *i* and bead type *j*, and *r* is the actual distance between the two beads. This is similar to a Lennard-Jones potential, but softer and broader because the exponents are 8 and 4 instead of 12 and 6, which works well for such a coarsely grained system.

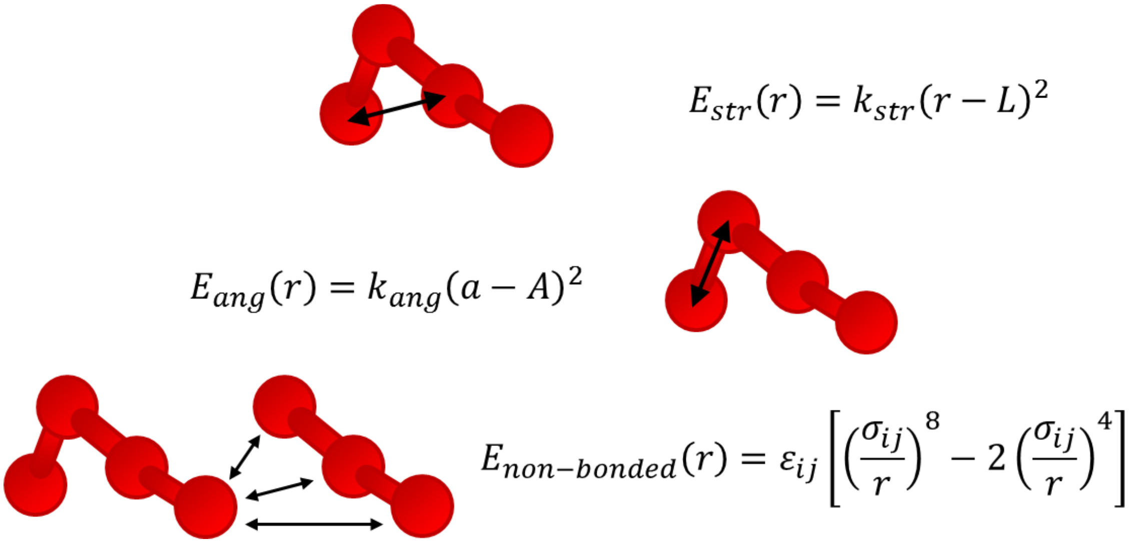
$E_{str}(r) = k_{str}(r - L)^2$
$E_{ang}(r) = k_{ang}(a - A)^2$
$E_{non-bonded}(r) = \varepsilon_{ij}\left[\left(\frac{\sigma_{ij}}{r}\right)^8 - 2\left(\frac{\sigma_{ij}}{r}\right)^4\right]$

Figure 2.3. The three potentials used in this model. E_{str} corresponds to the energy of bond stretching, E_{ang} corresponds to the energy of angle bending, and $E_{non\text{-}bonded}$ refers to the energy of the non-bonded interactions.

This potential set was then used in HOOMD-Blue, using GPUs and the Nosé-Hoover thermostat for constant volume and temperature, or the Nosé-Hoover thermostat and the Anderson barostat for constant pressure and temperature simulations. Generally, only diblock copolymers were considered, but it is quite simple to extend the model to higher order block copolymers (e.g. triblock copolymers), as well as star polymers or other non-linear polymers. Generally, one of two simulation builds was used: either a bulk simulation where the system is periodic in all three dimensions or a thin film simulation where the system is periodic in the x and y dimension, but not the in z dimension. The bulk simulations were built by placing the first bead on a chain randomly in space. Subsequent beads on that chain were built at the equilibrium angle and bond length in a random direction, simulating a random walk. The thin film simulations contained two parts: the underlayer and the BCP film. The underlayer was built using the same beads that constitute the film. The underlayer was built to model a brush with the bottom-most bead of the chain, i.e. the one in contact with the hypothetical substrate, fixed in space. This condition corresponds to the brush polymer chains being tethered to a substrate such as silicon. The tethered bead chains were placed on a square lattice 15 Å apart in the x and y directions. Brushes tethered closer than this distance formed an unrealistic density wave (large oscillations in density) in the BCP film near the film-underlayer interface. In addition, the BCP film had no apparent interpenetration of the BCP into the underlayer. Brushes tethered further than 15 Å distance led to BCP chains quickly penetrating completely through the underlayer no matter how long the brush chains were made which is unrealistic since in a real system a brush is tethered to a hard surface which prevents this. A plot demonstrating these issues is shown in Figure 2.4 and related pictures from instances of the simulations are shown in Figure 2.5. The length of the underlayer chains used was six beads. Fewer than six beads per chain again resulted in density waves in the BCP film near the film interface because the fixed underlayer beads at the substrate surface were not sufficiently shielded from the film, which leads to changes the packing structure of the film beads. Another layer of fixed beads was placed below the brush to act as a hard surface and prevent inversion of the brush. The patterning of these underlayers was done by setting the beads in the underlayer chains as either A or B as a function of position.

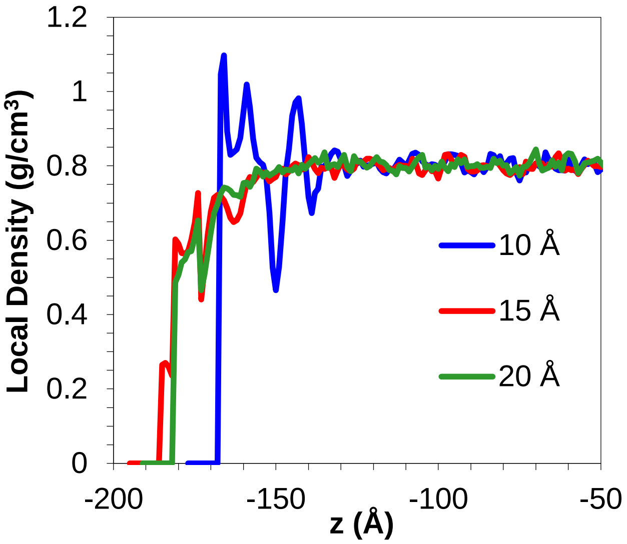

Figure 2.4. Density as a function of depth through the simulation. Different spacing of the tethered points in the underlayer give different density profiles. When the spacing is too low, density waves propagate from the interface before leveling off to bulk density.

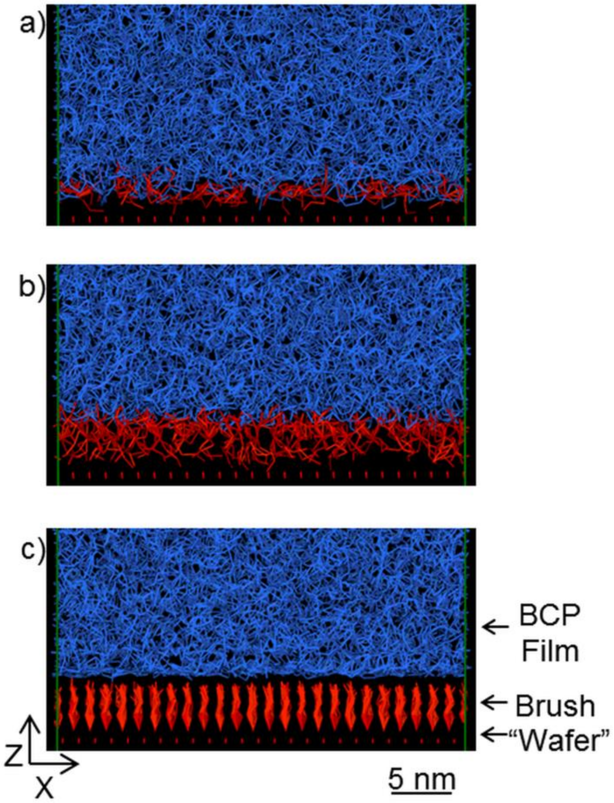

Figure 2.5. Images of simulation with various underlayer chain spacings. The film is colored blue and the underlayer brush (with artifical wafer) is colored red. The film is a homopolymer film. a) 25 Å spacings result in a very low density underlayer and penetration of the film beyond the bottom of the underlayer. b) 15 Å spacings result in some penetration, but it does not penetrate through the entire brush. c) 10 Å spacings result in a poor interface and no interpenetration. For this work, and intermediate spacing of 15 Å was used.

2.1.1. Parameterization of Coarse Grained Model

The six parameters that can be manipulated in the three potential sets must be parameterized in order to reproduce real polymer properties. The segment stretching and angle terms can be fit to match rigorous atomistic simulation results or to match experimental R_g values. The atomistic and coarse grained models were compared by calculating an equivalent coarse grain location for the atomistic simulation. The center of mass of each group of monomers that constituted a bead in the coarse grained model was taken as the equivalent coarse grained bead location. As seen in Figure 2.6, which plots histograms of atomistic and mesoscale bonds and angle distributions for PS and the coarse grained equivalent, good agreement between the two simulations was obtained regarding bead to bead distance and the angles between each bead. The non-bonded interaction can be fit to experimental density, which is primarily controlled by σ, and cohesive energy density, which is primarily controlled by ε. The effects of each non-bonded parameter are largely separable, but some fine tuning over the entire set is required for very good accuracy.

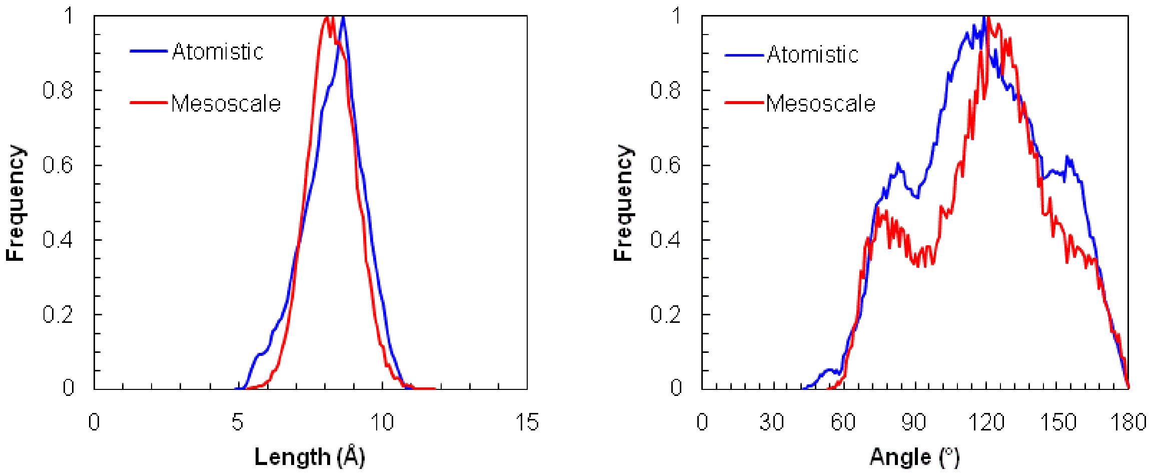

Figure 2.6. Bond and angle distributions for atomistic and mesoscale simulations of PS.

For many studies, it is more desirable to study an idealized system than a realistic system. For this purpose we choose a set of parameters that resulted in realistic densities, cohesive energy densities, and angle and bond length distribution similar to that of polystyrene. To investigate a BCP system, the same potentials are used for both the A and B polymers. The A-B interaction potentials are identical to the homopolymer potentials, except for the non-bonded scalar ε_{AB}. A difference in this value from the homopolymer values (ε_{AA} and ε_{BB}) accounts for the existence of χ in a system. Further discussion of this interaction is included in section 2.3. This model can then be perturbed by varying the parameters in Table 2.2 in order to study the effects density, cohesive energy density, stiffness, or other polymer properties have on different BCP systems. The exact parameters used in the symmetric potential, that is, a system where polymer A has the same parameters as polymer B, is found in Table 2.2.

Table 2.2. Potentials used for generic, symmetric, BCP.

	L (Å)	**k_{str} (kcal/(mol*nm^2))**	**A (rad)**	**k_{ang} (kcal/(mol*rad^2))**	**σ_{ij} (Å)**	**ε_{ij} (kcal/mol)**
A Hompolymer	8.2	100	$2\pi/3$	5	12.6	0.5
B Homopolymer	8.2	100	$2\pi/3$	5	12.6	0.5
A-B	8.2	100	$2\pi/3$	5	12.6	Determined by χ

2.2. Measuring Pitch

It is necessary to be able to measure the size of the structures formed when studying BCP structures and alignment. In order match a guiding layer's repeat distance with the BCPs natural repeat distance, or to look at the effects of deviations in the underlayer away from that distance, the natural pitch of the BCP must be measured.

In simulations of block copolymers, the structure factor *S(q)* can be evaluated from the Fourier transform of the radial pair distribution function. The structure factor provides equivalent information to the pattern observed in a small-angle scattering experiment such as small-angle x-ray scattering (SAXS) and small-angle neutron scattering (SANS).[6] Small-angle scattering is commonly used to evaluate a number of properties of the system such as the BCP domain size based on the position of the peak maximum, *q**.[16-20] *S(q)* is calculated using Faber-Ziman methods in Equation 2.5 where the pair distribution function is denoted by *g(r)*.[21-23] representative plot of *S(q)* is shown in Figure 2.7.

$$S(q) - 1 = 4\pi\rho_0 \int_0^\infty r^2 \frac{\sin qr}{qr} [g(r) - 1] dr \qquad 2.5$$

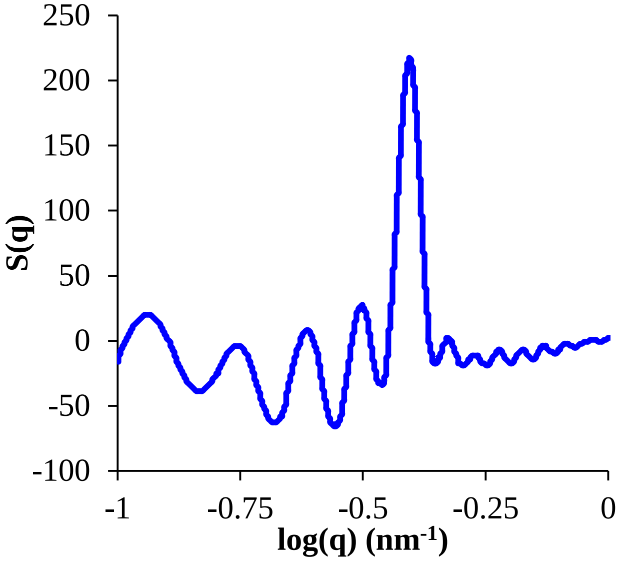

Figure 2.7. Representative plot of *S(q)*. The location of the largest peak corresponds to the pitch of the BCP system.

The q location of the largest peak corresponds to the repeat distance of the polymer as given in Equation 2.6.

$$L_0 = \frac{2\pi}{q^*} \qquad 2.6$$

It is common to use modification functions to improve the evaluation of the integral in scattering since one cannot evaluate the integral to infinity. The smaller peaks in Figure 2.7 correspond to such errors. One of the most commonly applied modification functions is the Lorch window function: sin(πr/R)/(πr/R)[24] used as outlined in Du et. al.[25] This produces Equation 2.7.

$$S(q) - 1 = 4\pi\rho_0 \int_0^R \frac{\sin qr}{qr}[g(r) - 1]\frac{\sin(\pi r/R)}{\pi r/R}dr \qquad 2.7$$

Applying this produces a positive spectra with only one obvious dominant peak as seen in Figure 2.8. Although use of the Lorch window function improves the look of the spectra and likely its quantitative accuracy, it is not needed to simply obtain the position of the strongest peak.

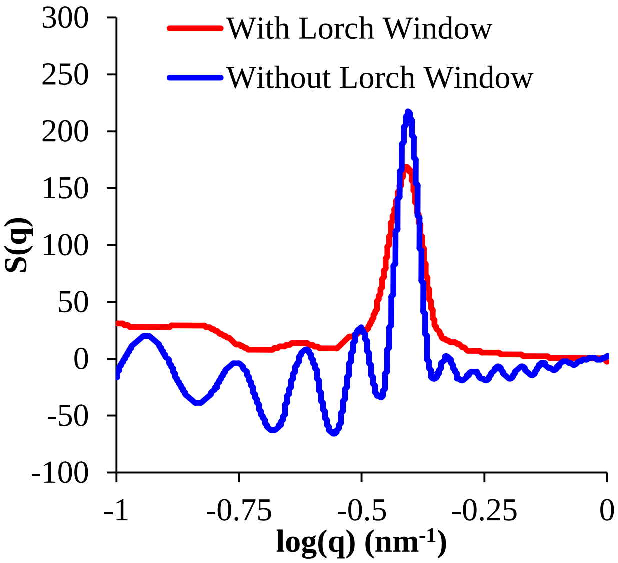

Figure 2.8. Representative plot comparing the raw S(q) calculation to that including the Lorch window function.

Whether using the Lorch window function or not this method is effective, but the limited integration lengths we could achieve relative to the domain size of the systems, especially for large domain systems results in some error. In order to account for the error associated with these limited integration lengths, systems were built at various known repeat distances and *S(q)* was calculated for various integration lengths. Plotting the error (defined in Equation 2.8) as a function of $D_{measured}/R_{max}$ (R_{max} is the limit of the *S(q)* integration in Equations 2.5 and 2.7) yields a single curve as shown in Figure 2.9. The fit to this data is used as a correction factor in subsequent measurements of unknown repeat distances. In general, values of R_{max} that are much greater than $D_{measured}$ are used so that the error is relatively small.

$$\%Error = \frac{D_{measured} - D}{D} \times 100 \qquad 2.8$$

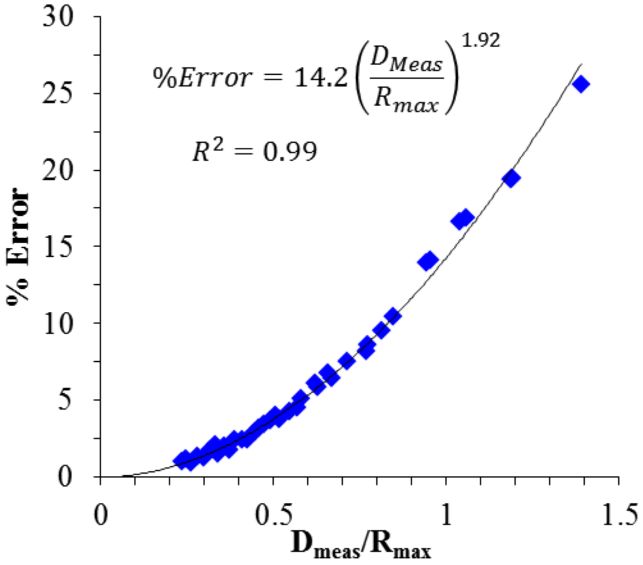

Figure 2.9. Plot of the measurement error vs. measured dimension / integration length. This calculated error is used to correct measurements of unknown natural pitches in BCP systems.

2.3. Measuring χ

A very common way to experimentally measure χ is by fitting scattering results to Liebler's theory for BCP scattering.[26,27] Because Leibler's random phase approximation

(RPA) theory is only valid in the mixed phase, measurements are either made at high temperatures and extrapolated into the demixed phase or measurements are taken at small chain lengths and then the χ value measured is applied to larger chains. A similar method is used in our simulations. The structure factor from Liebler's theory in the mixed state is fit and extrapolated to the demixed state. Instead of extrapolating via temperature or via chain length, both of which have their own set of assumptions, the extrapolation is performed in ε_{AB}. A similar approach is taken by Medapuram et al.[28] A full explanation is given below.

χ is defined by Equation 2.9 by Flory.[29]

$$\chi = z\Delta w/kT \qquad 2.9$$

where z is the coordination number, Δw is the exchange energy, k is the Boltzmann constant, and T is the temperature of the system. The exchange energy, Δw, is defined by Equation 2.10 as the energy penalty for replacing an A-A or a B-B interaction with an A-B interaction.

$$\Delta w = w_{AB} - \frac{1}{2}(w_{AA} + w_{BB}) \qquad 2.10$$

w_{ij} is the interaction energy between an i bead and a j bead. Since the interaction energy in this model is defined by the non-bonded potential parameter ε, Δw can be defined for our system by Equation 2.11

$$\mathit{\Delta w} = \varepsilon_{AB} - \frac{1}{2}(\varepsilon_{AA} + \varepsilon_{BB}) \qquad 2.11$$

This shows that Δw scales linearly with changes in ε_{AB}. As long as the density of the A-B interface does not significantly perturb the system, z, coordination number (the number of beads a single bead interacts with), will remain a constant. Since kT is a constant, χ is will scale linearly with ε_{AB} until z is perturbed by density variations at the A-B interface.

Liebler's theory is defined by Equation 2.12 (explanations and definition of F can be found in Liebler's work).[6]

$$S_{Tot}(q) = \frac{N}{F(q, \varphi_A) - 2\chi N} \qquad 2.12$$

N is the degree of polymerization and is known. φ_A is the volume fraction of the A block and is also known. a and χ are the parameters fit to the BCP structure factor. $S_{Tot}(q)$ used in Equation 2.12 combines the $S(q)$ values calculated from all pair distribution functions. There are three methods of calculating of $S_{Tot}(q)$ found in literature: the Faber – Ziman method[21,22,23], the Ashcroft – Langreth method,[21,23-32] and the Bhatia – Thornton method[23,33]. Which should be used to match Leibler's random phase approximation theory? The Faber – Ziman method is calculated via Equation 2.13 where ρ_0 is the monomer density and g_{ij} is the pair distribution function calculated between i and j components.

$$S_{ij}(q) = 1 + 4\pi\rho_0 \int_0^{\infty} r^2 \frac{\sin qr}{qr} \left[g_{ij}(r) - 1\right] dr \qquad 2.13$$

This results in three different structure factors: S_{AA}, S_{BB}, and S_{AB}. Faber – Ziman uses Equation 2.14 to calculate the total structure factor.

$$S_{Tot}(q) = \sum_{i,j}^{n} c_i c_j b_i b_j \left[S_{ij}(q) - 1\right] \qquad 2.14$$

where c_i is the normalized concentration of atoms i ($c_i = n_i/n_{total}$, which is equivalent to f_A or φ_A in Flory nomenclature) and b_i is the neutron or X-ray scattering length of species i. However, b_i is not well defined for our system, which is problematic. Ashcroft and Langreth define $S_{Tot}(q)$ using equations 2.15 and 2.16 where δ is the Kronecker delta.

$$S_{ij}^{AL}(q) = \delta_{ij} + \left(c_i c_j\right)^{1/2} \int_0^{\infty} \frac{\sin qr}{qr} r^2 \left(g_{ij}(r) - 1\right) dr \qquad 2.15$$

$$S_{Tot}(q) = \frac{\sum_{i,j} b_i b_j \left(c_i c_j\right)^{1/2} \left[S_{ij}^{AL}(q) + 1\right]}{\sum_i c_i b_i^2} \qquad 2.16$$

Again, b_i is not well defined for our system. Additionally, the Ashcroft – Langreth method is much less commonly used in literature. Bhatia and Thornton define $S_{ij}(q)$ using Faber – Ziman formalism (Equation 2.13), but define three different ways of calculating the overall $S(q)$ as defined in Equations 2.17 - 2.19.

$$S_{NN}(q) = c_i^2 S_{ii}(q) + c_j^2 S_{jj}(q) + 2c_i c_j S_{ij}(q) \qquad 2.17$$

$$S_{CC}(q) = c_i c_j \left[1 + c_i c_j \left(S_{ii}(q) + S_{jj}(q) + 2S_{ij}(q)\right)\right] \qquad 2.18$$

$$S_{NC}(q) = c_i c_j \left[c_i \left(S_{ii}(q) - S_{ij}(q)\right) - c_j \left(S_{jj}(q) - S_{ij}(q)\right)\right] \qquad 2.19$$

$S_{NN}(q)$ is the number-number partial structure factor. It allows a global description of the structure of a solid, that is, the repartition of the experimental scattering centers, but the nature of the chemical species spread in the scattering centers is not considered. $S_{CC}(q)$ is the concentration-concentration partial structure factor. It describes the chemical order in the material. $S_{NC}(q)$ is the number-concentration partial structure factor. This gives a correlation between the scattering centers and the chemical species that occupy them. In the case of an ideal mixture, $S_{NC}(q) = 0$ and all the structural information is given in $S_{NN}(q)$. Because we care about the chemical repartitioning of the A and B beads, $S_{CC}(q)$ is the appropriate structure factor to use. McCarty et al. agrees and uses $S_{CC}(q)$ to find χ.[34]

$S_{CC}(q)$ (Equation 2.18) is fit to Leibler's theory (Equation 2.12)[6] in the mixed state for multiple values of ε_{AB}. A representative plot of the fit is shown in Figure 2.10. The results of this fitting are shown in Figure 2.11, which plots χ versus $\varepsilon_0 - \varepsilon_{AB}$, where $\varepsilon_0 = \varepsilon_{AA} = \varepsilon_{BB}$ for the symmetric system as shown here, for $N = 128$ monomers, $\varphi_A = 0.25$ and $\varepsilon_{AA} = \varepsilon_{BB} = 0.5$ kcal/mol. When $\varepsilon_0 - \varepsilon_{AB} = 0$, then χ is by definition 0 because the A and B beads are energetically interchangeable; there is no difference between them except by label. Because of this, when fitting χ vs. $\varepsilon_0 - \varepsilon_{AB}$ the intercept is fixed at 0 because it must be so by definition. The slope of this fit is equal to z (the number of nearest neighbors) in Equation 2.9, because $\varepsilon_0 - \varepsilon_{AB}$ is equal to Δw in the case where the A block and B block are identical (Equation 2.10), as is the case here.

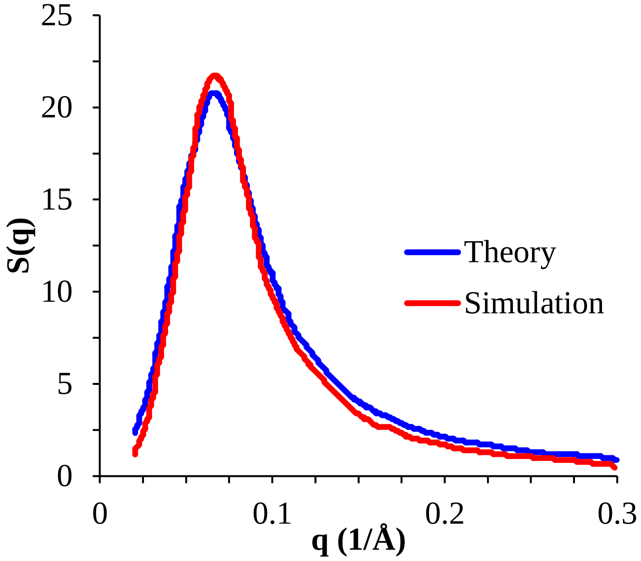

Figure 2.10. Representative fit of Liebler's theory to our simulation results.

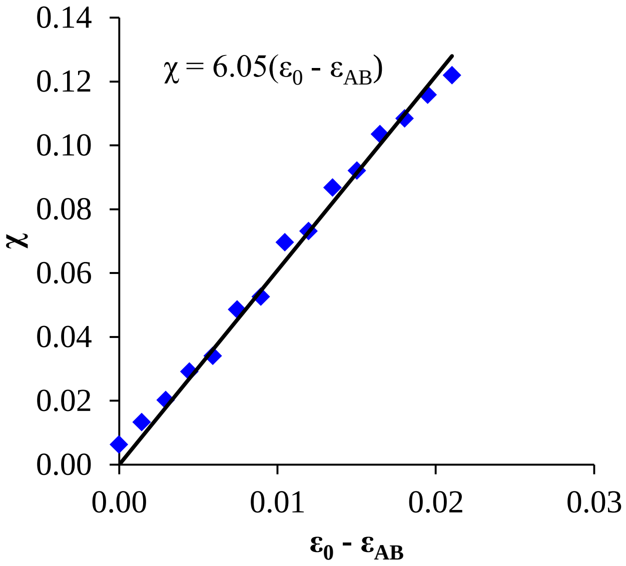

Figure 2.11. Representative plot of χ vs. $\varepsilon_0 - \varepsilon_{AB}$ for $N = 128$ and $\varphi_A = 0.25$.

The slope of the fits, (z), for $\varphi_A = 0.5$ as a function of N are shown in Figure 2.12. When $N \geq 128$, z is constant at 6. For lower N values, the shown fit is taken. An N dependence on χ at short chain lengths is expected from mean field calculations[35] and verified experimentally[36]. The slope of the fits, (z), for $\varphi_A < 0.25$ and $N \geq 128$ are found in Figure 2.13. It was found that the volume fraction had no noticeable effect until $\varphi_A < 0.25$. Figure 2.13 is only valid for $N \geq 128$ because it does not account for the change in z as a function of N at low N. Similar plots could be generated for lower N, but such simulations would result in BCPs where one block is very small (< 6 beads per block) which would likely have significant deviations from the random coil approximation and so were not of great interest. For $N > 256$ very long simulations times are required and no such chains were used in this work, except in very high PDI cases where a small fraction of the chains exceed 256 monomers in length. An N dependence on χ at short chain lengths is expected from mean field calculations[37] and verified experimentally[38]. χ is also expected to vary with volume fraction from mean field calculations.[39] Figure 2.13 and Figure 2.12 give the z values required to calculate χ for any N, φ_A, or ε_{AB} given the parameters in Table 2.2. These z values, combined with Equation 2.9, allow us to calculate the χ value for any $\varepsilon_0 - \varepsilon_{AB}$.

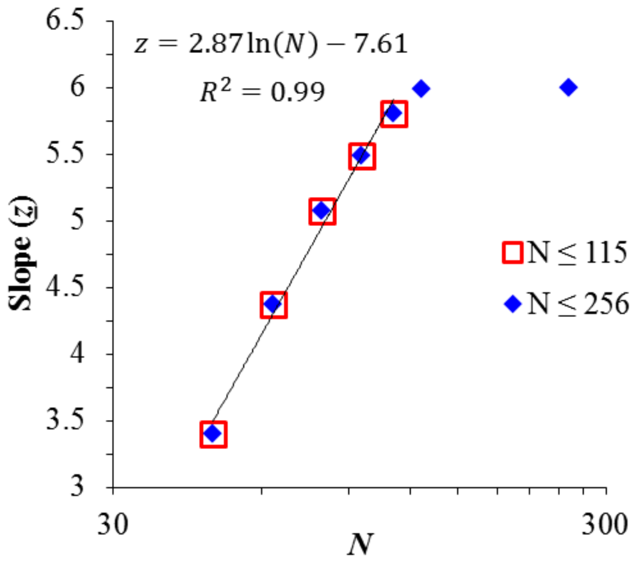

Figure 2.12. Plot of z values found for $f_A = 0.5$ as a function of N. For $N <$ 115, the shown fit is used. Above this value, z is constant at 6.

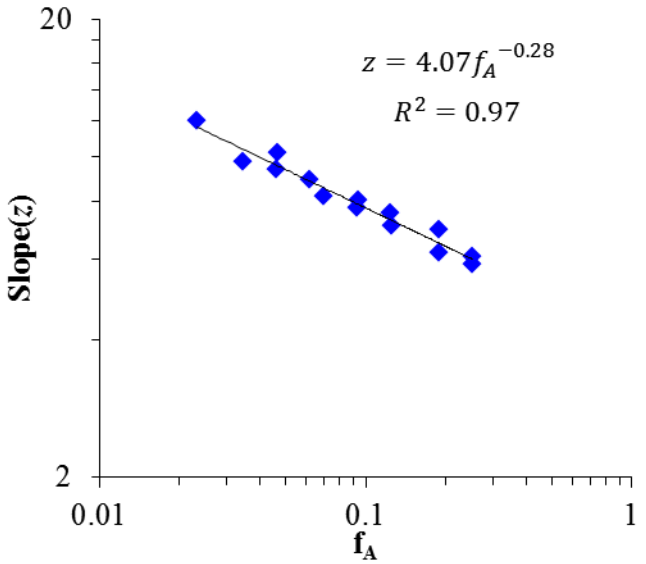

Figure 2.13. Plot of z values found as a function of volume fraction for N ≥ 128.

It would be possible to fit χ to $\varepsilon_0 - \varepsilon_{AB}$ to *S(q)* using the corrections made by Fredrickson and Helfand,[37] but their corrections fail at low *N* where all our simulations operate and which is of interest in BCP lithography. In addition, even when N is large enough, the corrections made by Fredrickson and Helfand will only affect values very close to the ODT and so would not significantly affect the values shown in Figure 2.11 through Figure 2.13. It would extend figures like Figure 2.11 close to the ODT (for large N), the linear fit would not change significantly.

2.4. Measuring ODT

If any quantitative parameter is used to identify the ODT, it must at least be consistent with the qualitative visual observation of the ODT. While two different methods of observing the ODT will be discussed for a range of simulation conditions and degrees of polymerization, it is informative to visually compare a single common set of simulation results to each of the methodologies. Figure 2.14 shows images of a simulation using the symmetric forcefield for $N = 32$ as AB interaction strength ε_{AB} changes from weak (Figure 2.14a, $\varepsilon_{AB} = 0.2$) to strong (Figure 2.14f, $\varepsilon_{AB} = 0.5$). Since the AB interaction strength is inversely proportional to the driving force to phase separate (Equations 2.9 - 2.11), this series goes from large χ to smaller χ. The system appears to undergo a visible transition from ordered to disordered between $\varepsilon_{AB} = 0.36$ (Figure 2.14c) and $\varepsilon_{AB} = 0.37$ (Figure 2.14d). It also qualitatively matches the expected trends with interaction strength above and below the ODT. At weaker interactions, it is enthalpically more favorable for each phase to associate with itself rather than each other so the system phase separates with relatively sharp interfaces. When the AB interaction is stronger

(Figure 2.14c), the system still phase separates, but the enthalpic penalty for unlike interactions is less so the system has less sharp interfaces. At some point as the AB interaction strengthens, the enthalpic penalty for unlike interactions is not strong enough to overcome the entropic benefit of mixing, and the system mixes (Figure 2.14d and Figure 2.14e). Since the two homopolymers used in this forcefield are identical (ε_{AA} = ε_{BB} = 0.5), the system is fully mixed when $\varepsilon_{AB} = 0.5$ (Figure 2.14f), which is where $\chi = 0$ as discussed in the previous chapter.

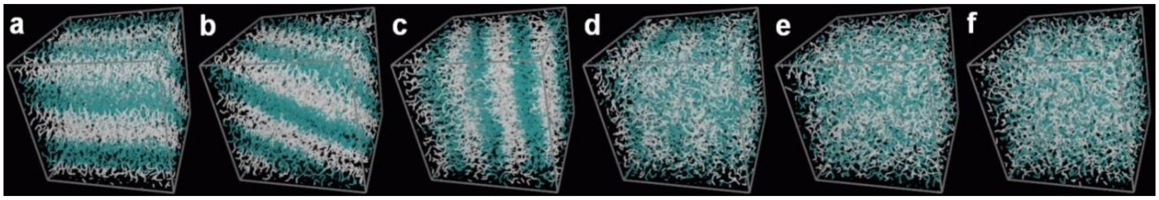

Figure 2.14. Bulk BCP structure after 100 ns simulation time for increasing ε_{AB} (decreasing χ), (a) $\varepsilon_{AB} = 0.2$, (b) $\varepsilon_{AB} = 0.3$, (c) $\varepsilon_{AB} = 0.36$, (d) $\varepsilon_{AB} = 0.37$, (e) $\varepsilon_{AB} = 0.4$, (f) $\varepsilon_{AB} = 0.5$, $\chi = 0$.

In simulations of block copolymers, the structure factor $S(q)$ can be evaluated from the Fourier transform of the radial pair distribution function via Equations 2.5 or 2.7. The structure factor provides equivalent information to the pattern observed in a small-angle scattering experiment such as small-angle x-ray scattering (SAXS) and small-angle neutron scattering (SANS). Small-angle scattering is commonly used to evaluate a number of properties of the system such as the BCP domain size based on the position of the peak maximum, q^*.[16-20] The width of the peak can be used to provide a qualitative observation of the ODT.[6,16,40] However, this does not provide a sufficiently quantitative descriptor for observation of the ODT, especially for simulations. This is because the simulation size will have a strong effect on the width of the peak and errors associated with a relatively small upper limit of the integral in Equation 2.7 can have a strong effect on the peak width. It is also complicated by the requirement to choose a peak shape (e.g. Gaussian, Lorentzian, etc.) with which to fit the width in a system where the shape of the peak can potentially change whether the system is ordered or mixed.[41] The intensity of the peak, $I(q^*)$ for scattering experiments and $S(q^*)$ from the structure factor, is a better descriptor in that it does not have to be fit by an arbitrary function and should be more sensitive to changes in structure.[16-19] Thus, the first descriptor that is discussed as a method for determination of ODT will be the intensity of peak of the structure factor $S(q^*)$.

The SAXS peak intensity has been previously used experimentally to determine ODT temperature for different molecular weights of poly(oxyethylene)-poly(oxybutylene) diblock copolymers.[41] Data from this study is shown in Figure 2.15. In the experimental study, the peak intensity was studied as a function of temperature. At high temperatures the system is mixed, but as the sample is cooled χ increases. The peak intensity is a nearly constant at temperatures where the system is mixed, but rapidly jumps to a much larger value at the ODT as the sample is cooled. Further cooling the sample in the ordered state shows a slowly increasing peak intensity as χ further increases. Identification of the ODT temperature by the rapid jump in scattering intensity was shown to give equivalent results to identification of the ODT temperature by conventional rheological measurements. The maximum intensity of the structure factor

S(q)* should therefore give equivalent accuracy for identification of the ODT with changing interaction strength in simulation.

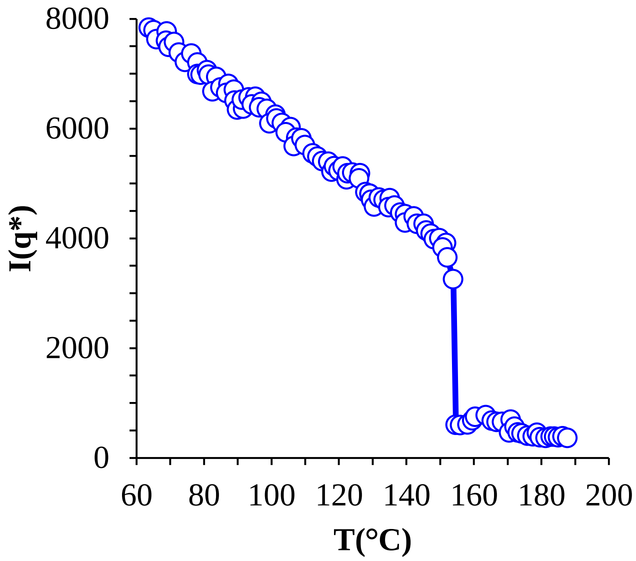

Figure 2.15. Changes in the scattering peak height for poly(oxyethylene)-poly(oxybutylene) diblock copolymers. A sharp increase in peak height is seen at the ODT. Data from Mai et al.[41]

The structure factor for a BCP simulation with $N = 32$ at different values of ε_{AB} is shown in Figure 2.16; these results are directly extracted from the series of simulations shown in Figure 2.14. Figure 2.16a shows the full structure factor while Figure 2.16b shows just the peak height *S(q*)*. The full structure factor shows the expected behavior. The well separated structures at small ε_{AB} show strong sharp peaks corresponding to the domains of the BCP. As the interaction strength between A and B segments increases, the peaks become weaker and broader as the interface between domains becomes more diffuse. Peaks are still observed below the visual ODT of $\varepsilon_{AB} = 0.37$ (Figure 2.14) because of the correlation hole effect[6] and become very weak nearing the homogeneously mixed state. Considering the change in peak height in Figure 2.16b, there is an obvious jump in $S(q^*)$ as the system crosses the ODT and a slowly increasing peak intensity in the ordered phase as the AB interaction decreases; both results are fully consistent with the experimental results shown in Figure 2.15. What appears different from the experimental result is that there is a reasonable increase in the peak intensity even in the disordered phase at $\varepsilon_{AB} > 0.37$.

The increase in intensity in the disordered phase is fully consistent with Leibler theory[6] , and so should not be unexpected. The major difference between the experiment and our simulation results is likely due to the small system size in our simulation. The experimental scattering is the result of measurements over a volume that is likely microns to millimeters in length, while our experiments are only run on simulations that are nanometers in length. The radial pair distribution function can only be evaluated up to a distance r that is the smallest simulation box dimension divided by the square root of two. As a result, the upper limit on the integral in Equation 2.7 used to calculate the structure factor is limited to this same r value. Since the integration is only over a few periods (with one period being roughly 10-20 nm), the intensity of the scattering peak is relatively small, while in the experiment the periodicity may persist for microns and is included in the scattering spectra.

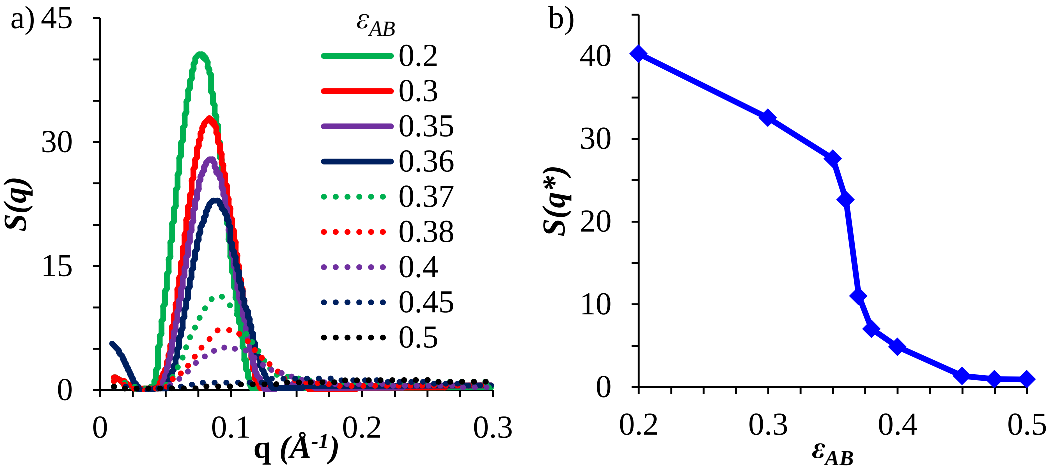

Figure 2.16. Changes in the structure factor for a BCP with N = 32 for different values of the AB interaction strength ε_{AB} (a) the full structure factor; (b) the peak intensity of the structure factor $S(q^*)$.

To demonstrate the effect of system size on intensity of the measured scattering spectra, the equivalent simulation as was run in two different simulation box sizes. The previous results were obtained from a simulation with an initially built simulation box of 20 nm per side; additional simulations were run using boxes of 45 nm per side. Increasing the simulation box size allows integration to higher values of R_{max} in Equation 2.7 which should allow for a slightly better match to the experimental results. Figure 2.17 shows a comparison for the peak intensity of the structure factor for the 20 nm and 45 nm boxes. As expected, the intensity of the peak in the ordered regime is much higher for the bigger box size, and the ODT appears much more like a step change as seen in the experimental results. Even bigger box sizes could potentially be run; however, there is always the tradeoff between simulation run time and the required level of accuracy.

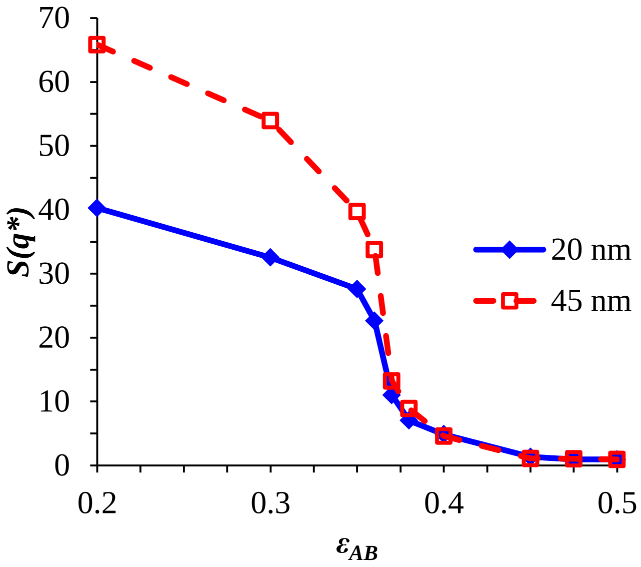

Figure 2.17. Effect of system size on structure factor peak intensity, closed symbols are for cubic simulation with 20 nm per dimension, open symbols are for simulation with 45 nm per dimension.

While box size does create a difference in the magnitude of *S(q*)* as a function of box size, the location of the ODT (the point of highest magnitude derivative), is identical in each simulation. In Figure 2.17, this is found to be at ε_{AB} = 0.36 in both simulations using a three point central difference method to calculate derivatives. More accurate calculations can be found by using a finer ε_{AB} spacing.

2.5. Comparison with Mean-Field Theory

In order to verify our model, we compared results from our model with some well accepted results from mean-field calculations. The phase diagram described by mean field is a well-known result that has been used and accepted for decades.[42] We compare our results using the symmetric potential (Table 2.2) with that of mean field in Figure 2.18. Because our model yields an elevated ODT because of the inclusion of fluctuation effects, the ODT at $f_A = 0.5$ is scaled to match mean field results. Excellent agreement is found between the coarse-grained model result and the mean field result.

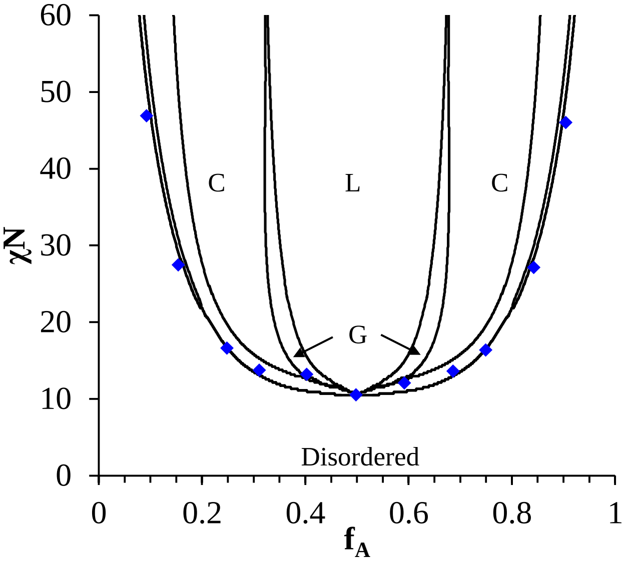

Figure 2.18. Comparison of our simulation results with the mean field phase diagram from Bates and Fredrickson[42]

Our model was also compared with mean-field data for concentration profiles as done by Matsen and Bates in Figure 2.19.[43] Boxes were created that were 1*L_0 by 4*L_0 by 4*L_0 for a degree of polymerization of 64 using the symmetric potential at various χN values. The beads were then binned using 0.1 nm wide bins in the dimension perpendicular to the lamellae and number fraction (equivalent to volume fraction) was calculated. As can be seen in Figure 2.25, there is very good agreement in the composition profiles. The interfacial width (w) was also compared and is shown in Figure 2.20. The SCFT results were calculated using a full SCFT treatment while the SST (strong segregation theory) results are calculated by Equations 2.20 and 2.21.[43]

$$\frac{D}{aN^{1/2}} = 2\left(\frac{8}{3\pi^4}\right)^{1/6} \qquad 2.20$$

$$\frac{w}{aN^{1/2}} = \frac{2}{(6\chi N)^{1/2}}\left[1+\frac{4}{\pi}\left(\frac{3}{\pi^2\chi N}\right)^{\frac{1}{3}}\right] \qquad 2.21$$

Our results match the SCFT results well. At lower χN, the deviation between SST and the full SCFT calculation increases, and our model follows the SCFT calculation as expected.

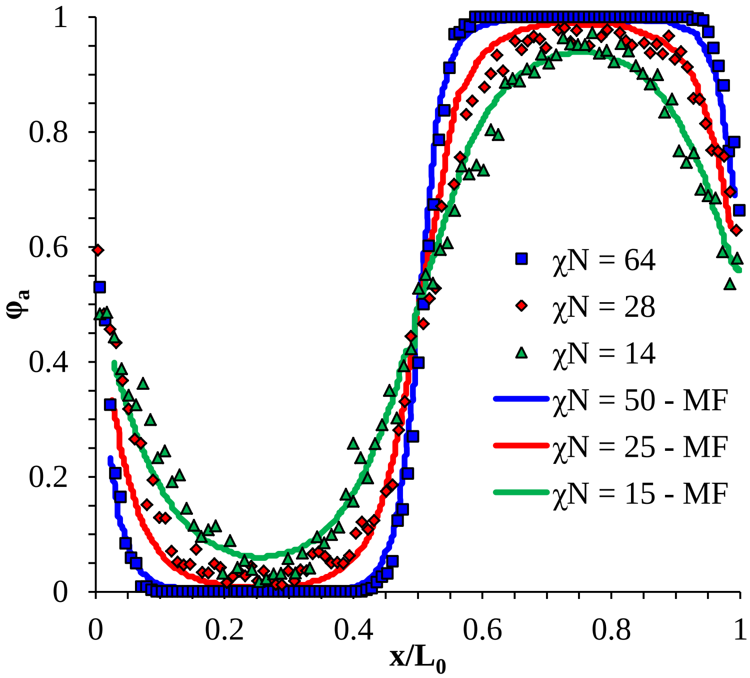

Figure 2.19. Comparison of average volume fraction through a single domain for SCFT and our model. The results match well.

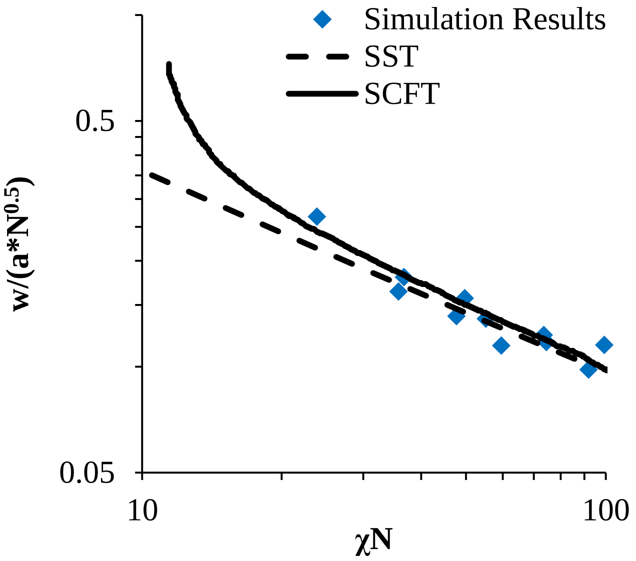

Figure 2.20. Comparison of the interfacial width (*w*) as a function of χN with SCFT and strong segregation theory (SST) calculations.[43] There is good agreement throughout with SCFT, while SST agrees until χN is low, at which the assumptions in SST fail.

The domain scaling from this simulation is also compared with that of Shull's mean-field analysis[44] and with experimental PS-PMMA domains as extracted from literature[45-60]. As seen in Figure 2.21, the domain scaling with χN matches that of the mean-field analysis over a large range of χN from ~12 to ~ 100 and probably beyond. Experimental PS-b-PMMA results also match our results. Our results match these well tested results in all three regimes; the weak, intermediate, and the strong regimes. Our model matches well known and tested theories in three different ways; ODT location, concentration profile/interfacial width, and domain size scaling.

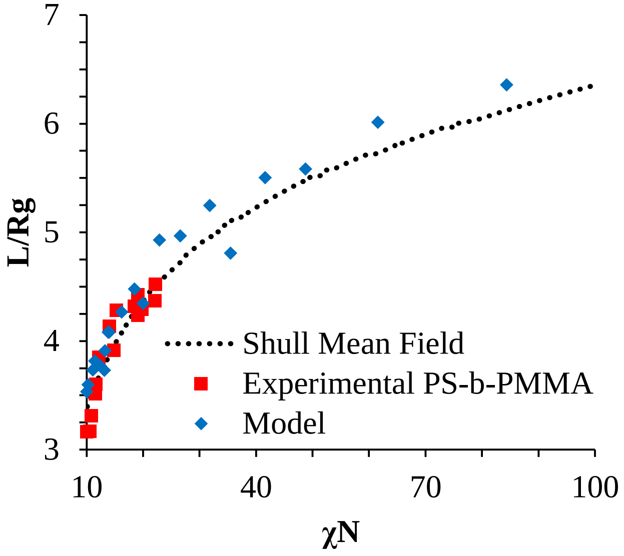

Figure 2.21. Comparison of pitches from our symmetric BCP model, Shull's mean-field calculation of pitch,[44] and experimental measurements of PS-b-PMMA[45-60]. Good agreement is found at low, medium, and high χN.

2.6. References

1 Bencher, C.; Yi, H.; Zhou, J.; Cai, M.; Smith, J.; Miao, L.; Montal, O.; Blitshtein, S.; Lavi, A.; Dotan, K.; Dai, H.; Cheng, J. Y.; Sanders, D. P.; Tjio , M.; Holmes, S. "Directed self-assembly defectivity assessment. Part II," 2012 Proc. SPIE 8323, 83230N.

2 Bencher, C.; Smith, J.; Miao, L.; Cai, C.; Chen, Y.; Cheng, J. Y.; Sanders, D. P.; Tjio, M.; Truong, H. D.; Holmes , S.; Hinsberg, W. D. "Self-Assembly Patterning for sub-15nm Half-Pitch: A Transition from Lab to Fab," 2011, Proc. SPIE, 7970.

3 Tiron, R.; Chevalier, X.; Gaugiran, S.; Pradelles, J.; Fontaine, H.; Couderc, C.; Pain, L.; Navarro, C.; Chevolleau, T.; Cunge, G.; Delalande, M.; Fleury , G.; Hadziioannou, G. "Pattern density multiplication by direct self assembly of block copolymers: toward 300mm CMOS requirements," Proc. SPIE 8323, 2012 83230O.

4 Rathsack, B.; Somervell, M.; Hooge, J.; Muramatsu, M.; Tanouchi, K.; Kitano, T.; Nishimura, E.; Yatsuda, K.; Nagahara, S.; Hiroyuki, I.; Akai , K.; Hayakawa, T.

“Pattern scaling with directed self assembly through lithography and etch process integration," Proc. SPIE 8323, 2012, 83230B.

5 Delgadillo, P. A.; Gronheid, R.; Thode, C. J.; Wu, H.; Cao, Y.; Somvervell, M.; Nafus , K.; Nealey, P. K. "All track directed self-assembly of block copolymers: process flow and origin of defects," Proc. SPIE 8323, 2012, 83230D.

6 Leibler, L Macromolecules, 1980, 13, 1602-1617.

7 Fredrickson, G. H.; Helfand, E. Journal of Chemical Physics, 1987, 87, 697.

8 Barrat, J.; Fredrickson, G.H. Journal of Chemical Physics, 1991, 95, 1281.

9 Semenov, A.N. Soviet Physics, JETP, 1985, 61, 733.

10 Banaszak, M.; Whitmore, M. D. Macromolecules, 1992, 25, 3406.

11 Anderson, J. A.; Sknepnek, R.; Travesset, A. " Design of polymer nanocomposites in solution by polymer functionalization" Physical Review E 2010, 82, 021803.

12 Zhang, J.; Lu, Z.; Sun, Z.; "A possible route to fabricate patchy nanoparticles via self-assembly of a multiblock copolymer chain in one step" Soft Matter 2011, 7,9944.

13 "(HOOMD), Highly Optimized Object-oriented Many-particle Dynamics -- Blue Edition http://codeblue.umich.edu/hoomd-blue," [Online].

14 Anderson, J. A.; Lorenz , C. D.; Travesset, A. "General purpose molecular dynamics simulations fully implemented on graphics processing units," Journal of Computational Physics, 2008, 227, 10, 5342-5359.

15 Molecular Operating Environment (MOE), 2009.10; Chemical Computing Group Inc., 1010 Sherbooke St. West, Suite #910, Montreal, QC, Canada, H3A 2R7, 2009.

16 Takahashi, Y.; Kitade, S.; Noda, M.; Ochiai, N; Noda, I; Imai, M; Matsushita, Y. “Order-Disorder Transition of Symmetric Poly(styrene-b-2-vinylpyridine) in Bulk and Solution” Polymer Journal 1998, 30,388.

17 Bates, F. S.; Rosedale, J. H.; Fredrickson, G. H. “Fluctuation effects in a symmetric diblock copolymer near the order–disorder transition” J. Chem. Phys. 1990, 92, 6255.

18 Hasegawa, H.; Sakamoto, N.; Takeno, H.; Jinnai, H.; Hashimoto, T.; Schwahn, D.; Frielinghaus, H; Janβen, S.; Imai, M.; Mortensen, K. “Small-angle neutron

scattering studies on phase behavior of block copolymers" J. Phys. Chem. Solids 1999, 60, 1307.

19 Maurer, W. W.; Bates, F. S.; Lodge, T. P.; Kristoffer, A.; Mortensen, K.; Fredrickson, G. H. "Can a single function for χ account for block copolymer and homopolymer blend phase behavior?" J. Chem. Phys. 1998, 108, 2989.

20 Gu, X.; Gunkel, I.; Hexemer, A.; Gu, W.; Russell, T. P.; "An In Situ Grazing Incidence X-Ray Scattering Study of Block Copolymer Thin Films During Solvent Vapor Annealing" Adv. Mat. 2013, 26, 273-281.

21 Fischer, H, E.; Barnes, A. C.; Salmon, P. S. "Neutron and x-ray diffraction studies of liquids and glasses" Reports on Progress in Physics 2006, 69, 233.

22 Faber, T. E.; Ziman, J. M. "A theory of the electrical properties of liquid metals" Philosophical Magazine 1965, 11, 153-173.

23 "X-ray and neutron scattering: definitions" ISAACS, March 19, 2015, <http://isaacs.sourceforge.net/phys/scatt.html>

24 Lorch, E. A. J. Phys. C: Solid State Phys. 1969 , 2, 229.

25 Duy, J.; Benmore, C. J.; Corrales, R.; Hart, R. T.; Weber, J. K. R. "A molecular dynamics simulation interpretation of neutron and x-ray diffraction measurements on single phase Y2O3–Al2O3 glasses" J. Phys. Cond. Matt.2009, 21, 205102.

26 Bates, F. S.; Rosedale, J. H.; Fredrickson, G. H. "Fluctuation effects in a symmetric diblock copolymer near the order–disorder transition" J. Chem. Phys. 1990, 92, 6255.

27 Durand, W. J.; Blachut, G.; Maher, M. J.; Sirard, S.; Tein, S.; Carlson, M. C.; Asano, Y.; Zhou, S. X.; Lane, A. P.; Bates, C. M.; Ellison, C. J.; Willson, C. G.; "Design of high-χ block copolymers for lithography," J. Polym. Sci. A1 2015,53, 344-352.

28 Medapuram, P.; Glaser, J.; Morse, D. C. "Universal Phenomenology of Symmetric Diblock Copolymers near the Order−Disorder Transition" Macromolecules 2015, 48, 819-839.

29 Flory, P; "Principles of Polymer Chemistry" Cornell University Press 1953.

30 Ashcroft, N. W.; Langreth, D. C. Phys. Rev. 1967, 156(3), 685-692.

31 Ashcroft, N. W.; Langreth, D. C. Phys. Rev. 1967, 159(3), 500-510.

32 Ashcroft, N. W.; Langreth, D. C. Phys. Rev. 1968, 166(3), 934.

33 Bhatia, A. B.; Thornton, D. E. Phys. Rev. B 1970, 2(8),3004-3012.

34 McCarty, J.; Lyubimov, I. Y.; Guenza, M. G. “Effective Soft-Core Potentials and Mesoscopic Simulations of Binary Polymer Mixtures” Macromolecules 2010, 43, 3964-3979.

35 Fredrickson, G. H.; Helfand, E. "Fluctuation effects in the theory of microphase separation in block copolymers“ J. Chem. Phys. 1987, 87, 697.

36 Lin, C. C.; Jonnalagadda, S. V.; Kesani, P. K.; Dai, H. J.; Balsara, N. P. “ Effect of Molecular Structure on the Thermodynamics of Block Copolymer Melts“ Macromolecules 1994, 27, 7769-7780.

37 Fredrickson, G. H.; Helfand, E. "Fluctuation effects in the theory of microphase separation in block copolymers“ J. Chem. Phys. 1987, 87, 697.

38 Lin, C. C.; Jonnalagadda, S. V.; Kesani, P. K.; Dai, H. J.; Balsara, N. P. “ Effect of Molecular Structure on the Thermodynamics of Block Copolymer Melts“ Macromolecules 1994, 27, 7769-7780.

39 Abuzaina, F. M.; Patel, A. J.; Mochrie, S.; Narayanan, S.; Sandy, A.; Garetz, B. A.; Balsara, N. P. “Structure and Phase Behavior of Block Copolymer Melts near the Sphere-Cylinder Boundary“ *Macromolecules* 2005, 38, 7090-7097.

40 Lee, S.; Gillard, T. M.; Bates, F. S. “Fluctuations, Order, and Disorder in Short Diblock Copolymers” AICHE J. 2013, 59, 3502-3513.

41 Mai, S.; Fairclough, J. P. A.; Hamley, I. W.; Matsen, M. W.; Denny, R. C.; Liao, B.; Booth, C.; Ryna, A. J. „Order−Disorder Transition in Poly(oxyethylene)−Poly(oxybutylene) Diblock Copolymers“ Macromolecules 1996, 29, 6212-6221.

42 Bates, F. S.; Fredrickson, G. H. "Block copolymers - Designer soft materials," Phys. Today 1999, 52, 2.

43 Matsen, M. W.; Bates, F. S. "Unifying Weak- and Strong-Segregation Block Copolymer Theories," Macromolecules 1996, 29, 1091-1098.

44 Shull, K. R."Mean-Field Theory of Block Copolymers: Bulk Melts, Surfaces, and Thin Films," Macromolecules 1992, 25, 2122-2133.

45 Han, E., Stuen, K. O.; La, Y.; Nealey, P. F.; Gopalan, P. "Effect of Composition of Substrate-Modifying Random Copolymers on the Orientation of Symmetric and Asymmetric Diblock Copolymer Domains." Macromolecules 2008,41(23), 9090-9097.

46 Ham, S.; Shin, C.; Kim, E.; Ryu, D. Y.; Jeong, U.; Russell, T. P.; Hawker, C. J "Microdomain Orientation of PS-b-PMMA by Controlled Interfacial Interactions." Macromolecules 2008,41(17), 6431-6437.

47 Anastasiadis, S. H.; Russell, T. P.; Satija, S. K.; Majkrzak, C. F.. "The morphology of symmetric diblock copolymers as revealed by neutron reflectivity." The Journal of Chemical Physics 1990, 92(9), 5677-5691.

48 Vu, T.; Mahadevapuram, N.; Perera, G. M.; Stein, G. E. Macromolecules 2011, 44, 6121-6127.

49 Liu, C.-C.; Han, E.; Onses, M. S.; Thode, C. J.; Ji, S.; Gopalan, P.; Nealey, P. F. Macromolecules 2011, 44, 1876-1885.

50 Ji, S.; Liao, W.; Nealey, P. F. "Block Cooligomers: A Generalized Approach to Controlling the Wetting Behavior of Block Copolymer Thin Films." Macromolecules 2010, 43(16), 6919-6922.

51 Mansky, P.; Russell, T. P.; Hawker, C. J.; Pitsikalis, M.; Mays, J. "Ordered Diblock Copolymer Films on Random Copolymer Brushes." Macromolecules 1997, 30(22), 6810-6813.

52 Coulon, G., Russell, T. P.l; Green, P. F. "Surface-induced orientation of symmetric, diblock copolymers: a secondary ion mass-spectrometry study." Macromolecules 1989, 22(6), 2581-2589.

53 Russell, T. P.; Coulon, G.; Deline, V. R.; Miller, D. C. "Characteristics of the surface-induced orientation for symmetric diblock PS/PMMA copolymers." Macromolecules 1989, 22(12), 4600-4606.

54 Park, S. M.; Stoykovich, M. P.; Ruiz, R.; Zhang, Y.; Black, C. T.; Nealey, P. F.. "Directed Assembly of Lamellae- Forming Block Copolymers by Using Chemically and Topographically Patterned Substrates." Advanced Materials 2007, 19(4), 607-611.

55 Edwards, E. W., Müller, M; Stoykovich, M. P.; Solak, H. H.; de Pablo, J. J.; Nealey, P. F. "Dimensions and Shapes of Block Copolymer Domains Assembled on

Lithographically Defined Chemically Patterned Substrates." Macromolecules 2006, 40(1), 90-96.

56 Holoubek, J.; Baldrian, J.; Lednicky, F.; Lal, J. "Self-assembled structures in blends of disordered and lamellar block copolymers: SAXS, SANS and TEM study." Polymer International 2009, 58(1), 81-87.

57 Stein, G. E.; Liddle, J. A.; Aquila, A. L.; Gullikson, E. M. "Measuring the Structure of Epitaxially Assembled Block Copolymer Domains with Soft X-ray Diffraction." Macromolecules 2010, 43(1), 433-441.

58 Drockenmuller, E.; Li, L. Y. T.; Ryu, D. Y.; Harth, E.; Russell, T. P.; Kim, H. C.; Hawker, C. J. "Covalent stabilization of nanostructures: Robust block copolymer templates from novel thermoreactive systems." Journal of Polymer Science Part A: Polymer Chemistry, 2005 43(5), 1028-1037.

59 Russell, T. P.; Menelle, A.; Hamilton, W. A.; Smith, G. S.; Satija, S. K.; Majkrzak, C. F. "Width of homopolymer interfaces in the presence of symmetric diblock copolymers." Macromolecules 1991, 24(20), 5721-5726.

60 Points at $\chi N = 14.3$ and $\chi N = 62.7$ are taken from unpublished data in Henderson Group.

CHAPTER 3

IMPACT OF PERIODIC CELL DIMENSIONS ON ALLOWABLE LAMELLAR DOMAIN SIZES: APPLICATION TO BLOCK COPOLYMER MICRO-PHASE SEPARATION

It is common in computer simulations to use periodic boundaries conditions to approximate bulk material behavior. A simple formula is derived that allows direct calculation of all defect free lamellae pitches that are possible in given rectangular cell dimensions. It is found that in some cases the allowed lamellae repeat distances are restricted even when the cell edge dimensions are large relative to the lamellar repeat distance. Using elongated periodic cells that have edge lengths with the least number of common factors increases the density of allowable pitches. Using a coarse-grained BCP model, the impact of such boundary condition matching is verified in lamellae forming block copolymer simulations. By taking into account the periodic cell edge dimension restrictions using the methodology developed in this work, researchers can intelligently choose simulation dimensions that minimize the impact of periodic boundary conditions on the most energetically favorable equilibrium states for lamellae forming systems.

3.1. Introduction

Computer simulations using a variety of modeling techniques, ranging from exquisitely detailed density functional theory (DFT) and atomistically detailed molecular dynamics (MD) to continuum methods such as mean field techniques, have become extremely useful tools for understanding and predicting the behavior and properties of a wide variety of material systems. The recent Materials Genome Initiative (MGI) is predicated on the fact that substantially faster cycle times in moving from basic materials research to material applications can be achieved by tightly coupling material simulation and modeling with more traditional experimental materials science and engineering methods. However, even with modern computational tools and computer capabilities, memory limitations and the large calculation times required for detailed simulations still limits our ability to perform large volume macroscopic simulations of materials using atomistically detailed methods such as molecular dynamics. Therefore, it is extremely common to perform many such "bulk" material simulations using periodic boundary conditions in which a finite size simulation volume, commonly referred to as a periodic cell, is effectively translated into an infinite volume such that the presence of interfaces can be avoided and bulk material behavior can be approximated. It is well known that simulation volume size effects can occur, and it is common in amorphous material simulations to test for such effects by performing simulations at different simulation volume sizes and checking for consistent results.[1,2] However, amorphous materials represent only a fraction of the spectrum of useful engineering material systems. In general, non-amorphous systems pose more challenges in terms of their proper representation in periodic cell simulation volumes. Unfortunately, less attention has been given to the special challenges encountered in such non-amorphous systems due to the variety of different material system configurations that are important. Furthermore, as a result of initiatives like MGI, amazing advances in computing power (e.g. the advent of graphics processor unit or GPU-based computing), and improvements in and commercialization of user-friendly molecular modeling software, molecular simulations are becoming ubiquitous in science and engineering. Such easy access to these modeling tools, their increased utility and more wide-spread use, and their adoption by scientists and engineers who may not have extensive experience in molecular simulations provides strong motivation for additional work on understanding the conditions under which molecular simulations achieve the desired goal of accurate representation of material thermophysical properties. This paper addresses this issue of understanding the conditions under which molecular simulations using repeating boundary conditions can properly represent material systems that exhibit formation of layered lamellae such as in the case of lamellae-forming block copolymers.

As mentioned earlier, special care must be taken in understanding the impact of periodic boundary condition simulations when the material system to be simulated exhibits ordered or crystalline behavior, since boundary condition matching at the repeating boundaries places limits on the number of possible configurations in a particular set of simulation volume dimensions.[3] One such application for molecular simulations in which periodic material structures are important is in the study of the micro-phase separation of block copolymers. Even relatively simple diblock copolymers can exhibit rich phase behaviors and produce nanostructured materials that are impacting a variety of fields in applications ranging from nanopatterning of integrated circuits to active nanostructured materials for solar energy harvesting. While the individual polymer chains in these block copolymers maintain a high level of disorder and have characteristic dimensions only on the order of 10 nanometers or less typically, the overall micro-phase separated system can exhibit long range order in a variety of phase morphologies including lamellar, cylindrical, and gyroidal forms with much larger characteristic dimensions.[4] These systems have been studied via mean field simulations since the 1980's,[5] but in recent years various Monte Carlo and molecular dynamics models using periodic boundaries are becoming more prevalent[6,7]. When the simulation dimensions are not significantly larger than the periodicity of the micro-phase separated morphology, it is known that the pitch of repeating structures and morphology of such system can be affected.[3,8-14] Because the effect is geometric in nature, other systems which form periodic order, such as some crystalline polymers,[15] will also have similar such limitations. In the case of block copolymer simulations, some researchers have ignored these finite simulation volume size effects, assuming that the restriction and effect on material behavior is not large since multiple possible orientations of the periodic structure in the simulation volume are perceived to allow a sufficient density of possible micro-phase periodicities.[3] Without actually knowing the degree to which possible lamellae dimensions or other periodic spacings are constrained in small simulation volume sizes, it is impossible to tell if a given simulation volume size will perturb the thermodynamics of the system significantly and thereby introduce unnecessary errors of unknown magnitude into the equilibrium states calculated from such simulations. Therefore, researchers have also in some instances used advanced simulation dimension search algorithms based on optimization techniques that allow a simulation volume size to change in order to mitigate these finite size effects.[16,17] However, these methods do not handle all situations effectively, particularly in the case where multiple minima or maxima are present in the objective function being optimized in such simulation dimension search algorithms.[16] Advanced simulation dimension search methods also come at the expense of increased simulation time, with the time penalty being directly affected by the type of optimization method chosen and its convergence behavior. Finally, these search methods also are inherently more complex than standard simulation methods and are not generally available in commercial simulation tools. A third approach that could be employed is to simply use a simulation volume with dimensions that are much larger than the repeat distances expected in the simulation and assume that such volumes allow for essentially all possible periodic configurations. However, larger systems have the major drawback of significantly increased computation time and memory usage, especially when the periodic repeat distance is large compared to conventional molecular dynamics simulation volume sizes. This problem of blind use of large simulation volumes is particularly troublesome in block copolymer simulations where the periodicities of interest in various micro-phases are multiples of the characteristic macromolecular length scale and can easily be on the order of 10 nm to 100 nm. There has, to our knowledge, been no published method that allows easy determination of the impact of periodic cell dimensions on the number of allowed lamellae states and their characteristic dimensions.

In order to better understand this problem and provide a simple set of rules to guide selection of optimal periodic cell dimensions for a given simulation, a method is developed in this paper that allows for calculation of the possible non-defective repeat distances for lamellar structures in periodic rectangular solid simulation volumes. This method is demonstrated in the context of selecting simulation volume dimensions for a lamellae-forming block copolymer simulation and it is shown that such finite size effects can be important depending on the specifics of the simulation size and lamellar repeat distance. Using the ability to calculate the allowable lamellae dimensions in a given simulation volume, it is shown that finite volume effects can be mitigated not only by an increase in total volume, but by intelligent choice of simulation volume dimensions. It is shown that elongated simulation volumes are particularly useful in increasing the density of allowable lamellae repeat dimensions. The methods presented here allow one to quickly and intelligently choose dimensions that do not significantly affect lamella formation, do not have the large computation costs of very large simulations, and do not have the complexity of advanced simulation dimension search algorithms.

3.2. Calculation of Allowed Lamellar Domain Size

The challenge with simulating any material system that exhibits periodic ordering when using periodic boundary conditions on the simulation volume, as is commonly done in MD and Monte Carlo methods, is that not all repeat distances and dimensions for a particular morphology can fit into a single periodic cell size without requiring formation of a defect. This is due to the fact that use of repeating or periodic boundary conditions on the simulation volume requires that the locations of material domains formed in the volume match in location at opposing boundaries of the simulation volume since they are effectively in physical contact. This symmetry constraint places energetic limitations on the particular states that a material can take on in a given simulation volume size and shape. In order to better understand these constraints, consideration is first given to perhaps the simplest case, formation of a layered lamellae structure in a rectangular solid simulation volume for cases where the lamellae align parallel to one of the simulation volume edge planes.

It is trivial to define the largest repeat distance that can fit into a 3D rectangular solid simulation volume since it is simply equal to the length of the longest edge of the volume. By dividing this single coordinate into an integer number of evenly spaced lengths, smaller repeat distances can be accommodated, as seen in Figure 3.1. Let us refer to the number of divisions that a simulation volume edge is broken into as n. A lamellar phase, if single crystal in nature, can only repeat in one dimension, so this division could take place along any of the three simulation dimensions. If we do not consider any possible tilting of lamellae with respect to edge planes of the simulation volume (which will be considered later), then this results in Equation 3.1:

$$P = D_l/n \qquad 3.1$$

where P is the pitch for n repeated lamellae in a simulation with a side length of D_l, where n is a positive integer. A simulation may be divided along any side, not just its longest side, so D_l can have up to three different values for given set of dimensions. Considering this fact alone, a simulation volume whose edge dimensions share fewer factors is preferable to a volume whose edge dimensions are all identical (i.e. as in a cubic simulation volume) or whose edge dimensions share common factors. This is because each factor that is not shared between the edge dimension results in a new possible pitch for a lamellae forming system in the volume. For example, a simulation that has all three dimensions equal to 12 has possible pitches of 12, 6, 4, 3 …, but a simulation that has dimensions of 13, 12, and 11 has possible pitches of 13, 12, 11, 6.5, 6, 5.5, 4.3, 4, 3.7, 3.25, 3 …. The second set of simulation volume dimensions obviously has many more possible pitches than the first simulation above any chosen cutoff value for the possible pitch, even though the simulation volume in the second case is actually smaller than the first case. However, not all possible pitches have yet been considered since we have only considered the possibility of lamellae forming parallel to one of the simulation volume edge planes.

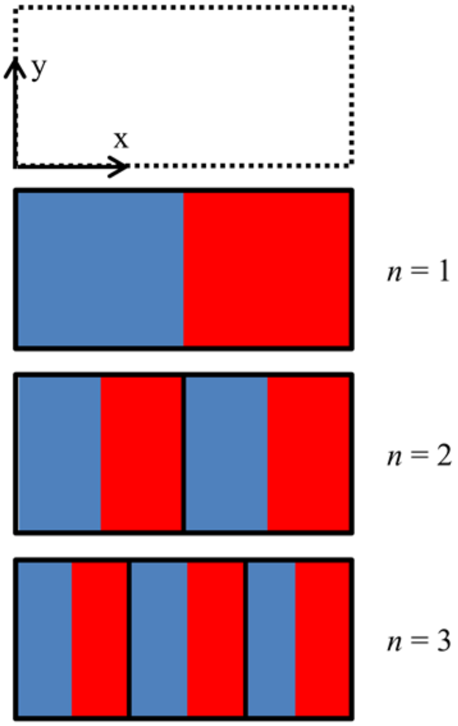

Figure 3.1 Schematic of the division of a simulation volume along the x dimension into multiple lamellae, though a similar image could be made for the division of a simulation along the y or z dimension. n corresponds to the number of divisions. The blue and red areas correspond to the subdomains of the lamellae.

Periodic structures in a material system such as the lamellar phase of a block copolymer do not necessarily need to orient parallel to the simulation volume edge planes. In reality, the system will equilibrate to the lowest free energy configuration available to it (see Figure 3.2). Thus, it is possible that in a lamellar system that the lowest free energy configuration may require the lamellae to tilt with respect to simulation volume edge axes (i.e. with respect to one or more of the simulation volume edge planes) to create the most favorable pitch configuration. In general, the lowest free energy states will also still be ones that form continuous domains across the repeating boundaries with the phantom neighboring simulation volumes when using periodic repeating boundary conditions. Therefore, only pitches and tilts that create lamellar configurations where the domain edges still line up at opposite edge planes of the simulation volume will be effectively sampled in such simulations. Failure of the lamellae domain edge locations to match position at opposite sides of the simulation volume will result in a defect at the boundary at that particular lamellae pitch in the chosen simulation volume dimensions, as seen in diagrams in Figure 3.2. In general this will be a high energy state for the system and will be represented at the incorrect free energy for that pitch. The “true free energy”, i.e. the free energy in a truly infinite size simulation without periodic boundaries, as a function of pitch for a periodically ordered material is also shown schematically in Figure 3.2.[17] The tilt angles that do not produce a continuous domain across the interface will be higher in free energy than those that do, resulting in a series of local minima in the system free energy as a function of pitch (i.e. corresponding to some specific tilt angle). Since molecular dynamics and other similar simulations converge to a local free energy minimum, and these local free energy minima occur when there are continuous domains across the periodic boundary, only those tilts that produce continuous domains will be sampled from such periodic simulations and are thus considered “allowed” states for the purposes of the discussions and calculations presented in this paper.

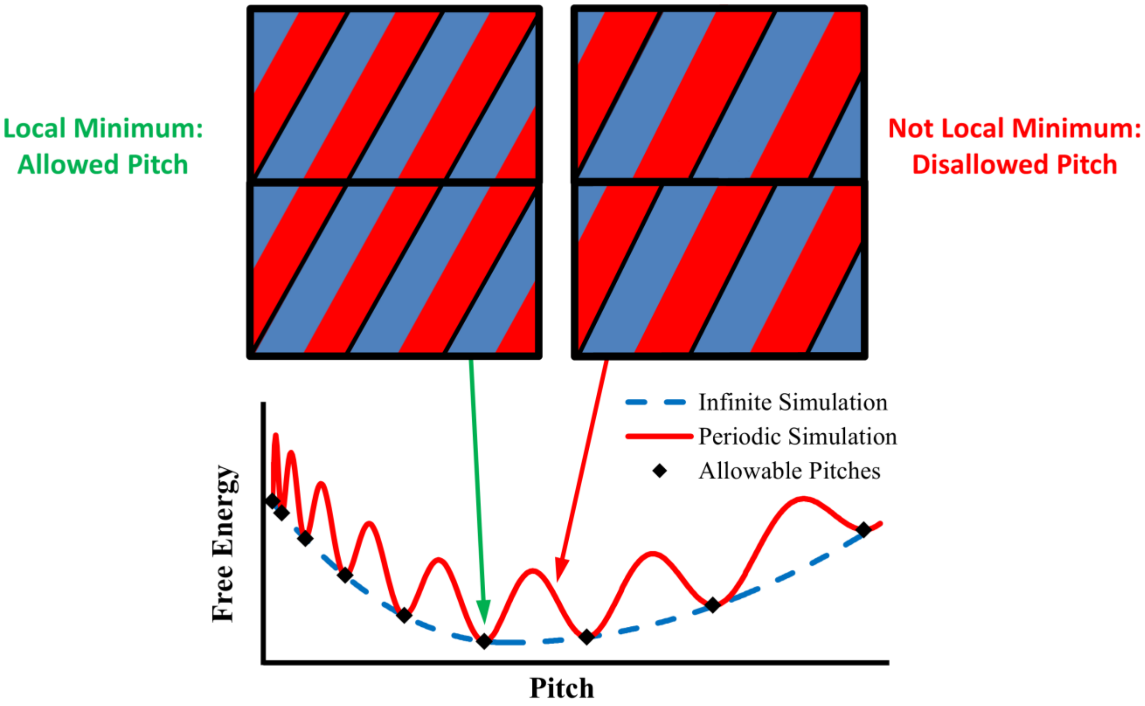
Local Minimum:
Allowed Pitch
Not Local Minimum:
Disallowed Pitch
Infinite Simulation
Periodic Simulation
Allowable Pitches
Free Energy
Pitch

Figure 3.2. Diagram demonstrating allowed (local minima in free energy) and disallowed tilts (not local maxima in free energy). Some tilt angles result in continuous domain at the boundaries (local minima) while others produce discontinuous domains. The tilt angles that produce a defect will be significantly higher in energy than those without a defect. A simulation will converge to a local minima, and these local minima occur when there are continuous domains across the periodic boundary, and so only those tilts that produce continuous domains will be considered allowed.

The interfaces between repeating lamellae (highlighted in yellow in Figure 3.3) will be referred to as lamellar interfaces, and their intersections with the simulation volume edge boundaries as lamellar vertices (highlighted as yellow circles in Figure 3.3). In order for a tilt to produce a continuous domain across the boundary and therefore be allowed several boundary matching conditions must be met: (1) the lamellar vertices must be in the same position on opposite side of the simulation volume, (2) each lamellar interface must connect two lamellar vertices on opposite boundaries, and (3) the lamellar interfaces must all be parallel. This is demonstrated in Figure 3.3 in two dimensions for $n = 3$, and in Figure 3.4 in 3 dimensions for $n = 3$. In Figure 3.3, the bottom and top lamellar vertices have the same x position, fulfilling condition 1. These vertices are labeled 0 through 3 on both the bottom and the top. Each vertex on the bottom is connected to a vertex on the top via one of a set of lamellar interfaces which are parallel to one another, fulfilling conditions 2 and 3.

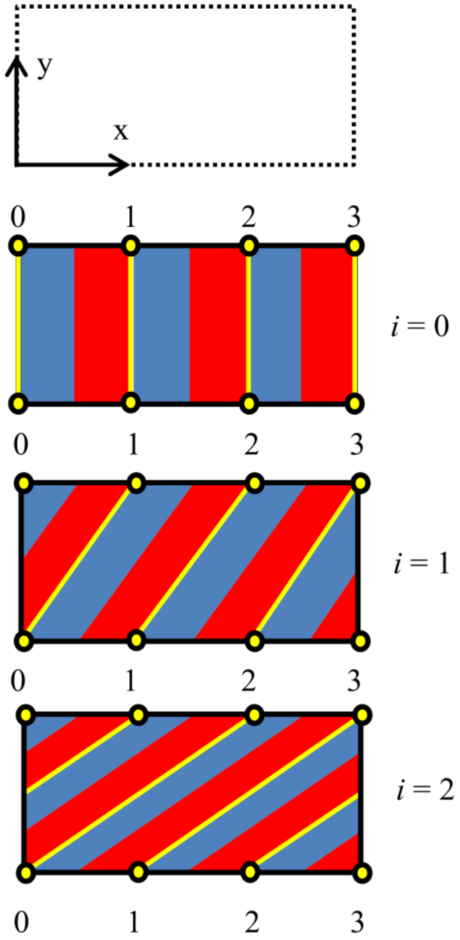

Figure 3.3. Diagram demonstrating allowed tilts in one dimension. In order to produce an allowed pitch: 1) The lamellar vertices (yellow dots) must be at the same positions along both the top and bottom boundaries. 2) The lamellar interfaces (yellow lines) must connect two vertices on opposites boundaries. 3) The interfaces must all be parallel. i corresponds

to the difference between the indices of the vertexes connected by an interface and can range from 0 to ∞. A larger i results in a smaller pitch.

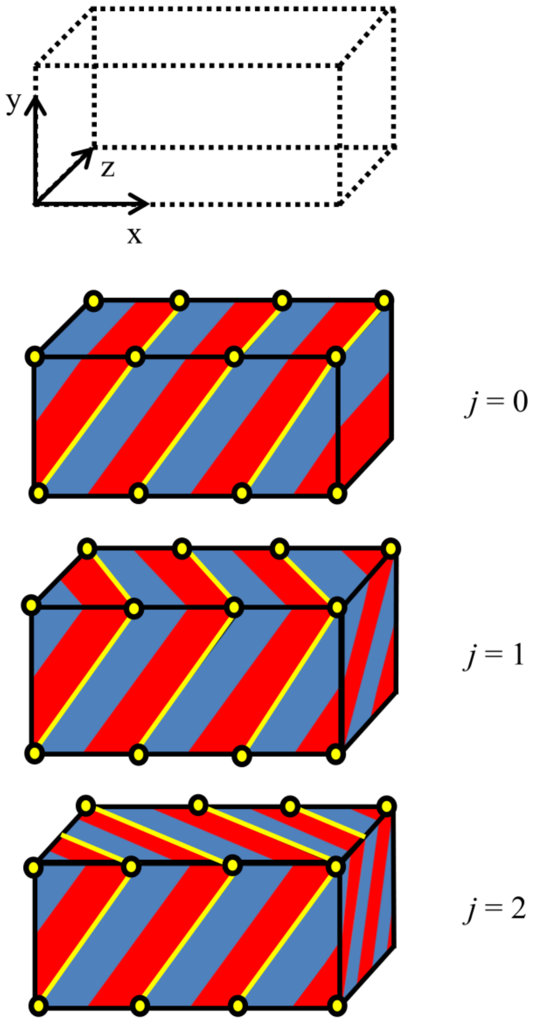

Figure 3.4. Diagram demonstrating allowed tilts in two dimensions for $n = 3$ and $i = 1$. Tilts in the second dimension are independent of tilts in the first dimension. The same requirements exist for this tilt as the first dimensional tilt in order to assume defect free and continuous lamellae. j corresponds to the differences between the indices of the vertexes connected by an interface between the front and back ($z = 0$ to $z = D_z$) of the simulation volume and can range from 0 to ∞. A larger j results in a smaller pitch.

Figure 3.3 shows an example of some possible lamellae configurations for a case where the lamellae are rotated with respect to a single axis, i.e. the *z*-axis in this case. Every possible tilt for rotations around a single axis can be described using an integer *i*, where *i* corresponds to the difference between the indices of the vertices connected by a lamellar interface along an opposite set of simulation volume edges defining a plane normal to the axis of rotation, i.e. the x-y plane in Figure 3.3. The choice of which edge of the plane normal to the axis of rotation is thought of as being divided by the lamellar interfaces is an arbitrary choice. In the case of Figure 3.3, the edges parallel to the x-axis are chosen. Later, it will be shown that this choice is of no consequence. In Figure 3.3, when *i* is 0, then the 0th vertex on the bottom front edge of the periodic cell is connected to the 0th vertex on the top front edge, and when *i* is 1, then the 0th vertex on the bottom front edge is connected to the 1st vertex on the top front edge, and the 1st vertex on the bottom front edge is connected to the 2nd vertex on the top front edge and so on. A larger *i* corresponds to greater degree of tilt. There is no limit to *i* since there is no prohibition to a vertex being connected to a vertex many periods away since all boundary matching conditions are still met. However, a larger *i* results in a smaller pitch, so there is some practical limit to *i* above which the pitch is much smaller than the lamellar repeat distance of interest. If the tilt was in the opposite direction and vertices on the bottom were connected to vertices with lower indexes, then *i* would be a negative number. However, these tilts only produce mirror images of their positive counterparts and so do not add any new allowable pitches.

Thus far, only a rotation around one axis has been considered. In a three dimensional system, it is obvious that rotation around all three axes is possible, but only rotation around two axes (i.e. the ones along which the simulation volume was not originally divided) will create unique states with different lamellar pitches, as shown in Figure 3.4. The system in Figure 3.4 is rotated around both the z-axis (similar to the system in Figure 3.3) and the y-axis. The tilt with respect to the second axis of rotation must follow the same boundary matching conditions as the tilt with respect to a single axis of rotation as discussed earlier. The degree of tilt along a second axis can be described by an integer *j*, where *j* corresponds to the difference between the indices of the vertices connected by a lamellar interface along an opposite set of simulation volume edges defining a plane normal to the second axis of rotation, i.e. a plane parallel to the x-z plane in Figure 3.4. Because the interfaces must line up across the periodic boundary, all the possible tilts are accounted for by allowing *i* and *j* to be equal to any two integers that are zero or greater. Because every tilt has been considered, as well as every division along every axis, all the possible orientations and therefore all the possible pitches in a rectangular periodic simulation for defect free lamellae can be described by the parameters *n, i, j,* and the three simulation volume edge dimensions.

The pitch for every combination of *n, i,* and *j* can be calculated by defining two adjacent lamellae interfaces as planes and then calculating the distance between those planes. Three points are required to define a plane, so given *n*, *i*, *j*, and the three simulation volume edge dimensions it is possible to calculate three points on any interface. First, the intersection of an arbitrary lamellae interface with the bottom front edge of the simulation volume is defined as the origin (see Figure 3.4), yielding one point (P_1) on a first lamellae interface plane equal

$$P_1 = [0\,,0\,,0] \qquad 3.2$$

The intersection of this lamellar interface with the top front edge of the simulation volume (i.e. $y=D_y$, $z=0$) can be described by the point

$$P_2 = \left[i \cdot \frac{D_x}{n}, D_y, 0\right] \qquad 3.3$$

Finally, the intersection of this lamellar interface with the rear top edge of the simulation volume (i.e. at $y=D_y$, $z= D_z$) is:

$$P_3 = \left[(i-j) \cdot \frac{D_x}{n}, D_y, D_z\right] \qquad 3.4$$

P_1, P_2, and P_3 define a lamellar interface plane. Since a vector between any two points in a plane gives a vector in that plane, we can easily define two vectors in that lamellar interface plane by taking the vector from P_1 to P_2 $\left(\overrightarrow{V_1}\right)$ and the vector from P_1 to P_3 $\left(\overrightarrow{V_2}\right)$.

$$\overrightarrow{V_1} = \left(i \cdot \frac{D_x}{n}\right)\hat{x} + \left(D_y\right)\hat{y} + (0)\hat{z} \qquad 3.5$$

$$\overrightarrow{V_2} = \left((i-j)\cdot\frac{D_x}{n}\right)\hat{x} + \left(D_y\right)\hat{y} + (D_z)\hat{z} \qquad 3.6$$

The cross product of these two vectors yields a vector normal to the lamellae interface plane.

$$\vec{N} = \left(D_y D_z\right)\hat{x} + \left(D_x D_z\frac{i}{n}\right)\hat{y} + \left(D_x D_y\frac{j}{n}\right)\hat{z} \qquad 3.7$$

The equation for a plane is:

$$ax + by + cz + d_i = 0 \qquad 3.8$$

where a, b, c and d are numerical coefficients. It is also the case that a, b, and c in Equation 3.8 define the vector normal to the plane, so by combining Equations 3.7 and 3.8 values for a, b, and c can be found in terms of parameters describing the simulation volume.

$$[a\,, b\,, c] = \left[D_y D_z\,,\, D_x D_z\frac{i}{n}\,,\, D_x D_y\frac{j}{n}\right] \qquad 3.9$$

In Equation 3.8, d accounts for the offset distance between parallel planes. Since all the lamellar interfacial planes are parallel, a, b, and c are identical for every plane. Since the first interfacial lamellar plane goes through [0,0,0], d_1 (d for the first interfacial lamellar plane) is solved for as 0. The adjacent lamellar interface must go through the point $[D_x/n, 0{,}0]$ and so:

$$d_2 = -D_x D_y D_z / n \tag{3.10}$$

The distance between two parallel planes (P) where the first plane passes through the origin is:

$$P = \frac{d_2}{\sqrt{a^2 + b^2 + c^2}} \tag{3.11}$$

Substituting from Equation 3.9 and 3.10 yields:

$$P = \frac{D_x D_y D_z / n}{\sqrt{\left(D_y D_z\right)^2 + (D_x D_z \cdot i/n)^2 + \left(D_x D_y \cdot j/n\right)^2}} \tag{3.12}$$

Multiplying Equation 3.12 by *n*/*n* yields:

$$P = \frac{D_x D_y D_z}{\sqrt{\left(n \cdot D_y D_z\right)^2 + (i \cdot D_x D_z)^2 + \left(j \cdot D_x D_y\right)^2}} \tag{3.13}$$

In the derivation of Equation 3.13, the *x* dimension was handled differently than the *y* and *z* dimensions. In the *x* dimension, *n* referred to number of lamellae into which the simulation was divided along that axis (that is, the number of lamellae that cross the *x*-axis), while in the *y* and *z* dimensions *i* and *j* referred to the degree of tilt. This difference caused *n* to be restricted to positive integers while *i* and *j* were equal to positive integers or zero. Because the *x* dimension is treated differently, we must rederive Equation 3.13 for the case when the lamellae first divide along the *y*-axis and then rotate in the *x* and *z* dimension, and for the case when the lamellae first divide the *z*-axis and then rotate in the *x* and *y* dimensions. This amounts to simply switching D_y and D_z with D_x in Equation 3.13, resulting in Equation 3.14 and 3.15.

$$P = \frac{D_x D_y D_z}{\sqrt{(n \cdot D_x D_z)^2 + \left(i \cdot D_y D_z\right)^2 + \left(j \cdot D_x D_y\right)^2}} \tag{3.14}$$

$$P = \frac{D_x D_y D_z}{\sqrt{\left(n \cdot D_x D_y\right)^2 + (i \cdot D_x D_z)^2 + \left(j \cdot D_y D_z\right)^2}} \tag{3.15}$$

Equations 3.13 – 3.15 can be used to calculate all the possible pitches in a box. However, when the math is examined more closely, it becomes clear that a single equation is all that is necessary.

Equation 3.14 is the same as Equation 3.13, except that *i* and *n* are switched. For every value of *n*, *i*, and *j* when *i* is not zero, they will yield the exact same possible pitches. When *i* is zero, then *i* and *n* cannot be switched because this results in *n* being equal to zero. The same is true when we consider Equations 3.13 and 3.15. The only difference is that *n* and *j* are switched. So, just like Equation 3.13 and 3.14, all pitches are calculated in both equations except when *j* is zero because switching *n* and *j* results in *n* being equal to zero, which is impossible. The only pitches that Equations 3.14 and 3.15 calculate that are not included in Equation 3.13 are those that are excluded because *n* cannot be zero. If we allow *n* to be zero in Equation 3.13, then Equation 3.14 and 3.15

become redundant, thus simplifying the calculation. This can be understood when it is recognized that while i and j were defined as the difference between the indices of the vertexes connected by an interface, the value of i and j also correspond to the number of lamellae that cross the y and z axes respectively, though this may not at first be obvious. This is however apparent in both Figure 3.3 and Figure 3.4. A value of zero for i or j means that the lamellae are parallel to that dimension. As i and j increase, the number of lamellae that cross the y and z axes respectively must increase as well. When i is one, then one lamellae (and one lamellar interface) will cross the y axis in the simulation volume. In the case of Figure 3.3c, the interface that connects vertex 1 at the top ($y = D_y$) of the simulation to vertex 0 at the bottom of the simulation ($y = 0$) is the only interface that crosses the y-axis. In Figure 3.3d, both the interfaces that start from vertices 1 and 2 on the top ($y = D_y$) cross the y axis since. Since they must go two vertices over, two interfaces must cross the y-axis. The same follows for the z-axis as j increases and for higher values of i and j.

This means that $n = 0$ in Equation 3.13 gives a valid pitch, because all this means is that the lamellae align parallel to the x-axis and never cross it. In fact, it would perhaps be more proper to define three parameters n_x, n_y, and n_z instead of n, i, and j where n_x, n_y, and n_z are all integers greater than or equal to zero and are defined as the number of divisions the lamellae make along the corresponding axis. This leads to a new equation, Equation 3.16:

$$P = \frac{D_x D_y D_z}{\sqrt{\left(n_x \cdot D_y D_z\right)^2 + \left(n_y \cdot D_x D_z\right)^2 + \left(n_z \cdot D_x D_y\right)^2}} \qquad 3.16$$

where n_x, n_y, and n_z are all integers greater than or equal to zero. This will yield the same pitches that Equation 3.13, 3.14, and 3.15 did, except that it is not required to switch D_y and D_z with D_x. All the extra pitches that would be calculated by switching D_y and D_z with D_x are accounted for because any of n_x, n_y, and n_z may be zero. Of course, they cannot all be zero as that yields an infinite pitch and also assumes that the lamellae are parallel to all three axes at once, which is impossible.

Though n_x, n_y, and n_z are not bounded and can in principle go to infinity, they are practically limited since the resulting pitch calculated for a set of n_x, n_y, and n_z values becomes very small (relative to the simulation dimensions) quickly as n_x, n_y, and n_z increase. In practice, it is of no value to calculate possible pitches that are smaller than the smallest characteristic dimension of the material being simulated. It is also important to remember however that Equation 3.16 calculates the allowed pitches that are possible for defect free lamellae. Any lamellae forming material system in which the energy to form a defect (e.g. dislocation, etc.) is on the order of the thermal energy in the system may form a defect, which would also then allow for additional allowed pitches in a particular set of simulation volume dimensions beyond what Equation 3.16 would indicate. This is not a concern however, since if defects are possible in a system they only increase the number of allowed states for a given simulation volume.

3.3. Block Copolymer Simulations

As mentioned earlier, molecular dynamics simulations of block copolymers is one application where use of a periodic cell and periodic boundary conditions could impact the simulated equilibrium material structure. In the case of lamellae forming block copolymer simulations as presented here, the concern is that choice of periodic cell dimensions could affect the equilibrium lamellae pitch. To probe this effect and demonstrate its importance in such systems, molecular dynamics simulations were performed in which micro-phase separation of an initially mixed diblock copolymer was studied using a coarse-grained diblock copolymer model. These simulations were performed for polymers of constant degree of polymerization (N) but for varying polymer χ values (i.e. the Flory-Huggins interaction parameter). The choice to study micro-phase separation as a function of polymer χ value was made since it is expected from theory that the equilibrium lamellae pitch for a diblock copolymer is a function of the copolymer χ and N values. According to previous theoretical treatments by Shull[18] and Bates and coworkers,[19] the lamellar pitch of lamellae-forming diblock copolymers will vary as $\chi^{1/6}$ in the strong segregation limit (i.e. $\chi N > 40$). As the block copolymer χN value is decreased, the dependence on both the polymer χ and N values increases, with the pitch scaling with $\sim\chi^{0.5}$ at χN values approaching the order-disorder transition (ODT). Therefore, by simulating diblock copolymers with varying χ values, that change in small steps, it should be possible to produce polymer systems with that exhibit small and predictable changes in natural lamellae pitch. The pitches of these polymers should form a smooth curve as a function of χN,[18] unless artifacts are introduced by factors such as the periodic cell dimensions and their impact on allowed pitches. Simulations of these lamellae forming polymers in specific periodic cell sizes that restrict the allowable pitches should verify the above calculations and highlight the limitations of certain box size. These calculations, while applied to lamellae forming BCPs here, should apply to any lamellae forming system simulated in a periodic unit cell because the assumptions made are geometric in nature and not based on anything specific to BCPs.

The coarse grained model used has been described elsewhere,[6,20,21] but will be briefly described here. Polymers are coarse-grained by modeling groups of 4 monomers (corresponding to a statistical segment length) as individual beads connected by harmonic bond potentials. Every group of three sequential bonded beads has a harmonic angle potential applied to prevent collapse due to non-bonded interactions. Every bead pair that does not participate in a bond potential or angle potential experiences a non-bonded potential similar to a Lennard-Jones (LJ) potential as given in Equation 3.17:

$$E_{Non-Bonded} = \varepsilon_{ij}\left[\left(\frac{\sigma_{ij}}{r}\right)^{8} - 2\left(\frac{\sigma_{ij}}{r}\right)^{4}\right] \qquad 3.17$$

The parameter σ_{ij} controls the average spacing between non-covalently attached beads and therefore has a major effect on controlling density. The parameter ε_{ij} controls the strength of the non-covalent interactions and therefore has a major effect on controlling cohesive energy density (*CED*). Since molecular dynamics simulations are off-lattice and each parameter can be modified somewhat independently, the density and *CED* for a homopolymer can be set to almost any desired value to represent a real polymer.[21] The segment and angle terms can be fit by running rigorous atomistic simulations to determine the equivalent coarse-grained equivalent distributions of segment lengths and angles. In this case, the parameters for both A and B blocks are set to roughly reproduce the density and segment distribution of polystyrene. ε_{AA} and ε_{BB} are set to 0.5 kcal/mol, while σ_{AA} and σ_{BB} are set to 1.26 nanometers. The equilibrium bond length used for both A and B polymers was 0.82 nm, with a harmonic strength of 100 kcal/mol×nm^2. The equilibrium angle used for both A and B polymers was 2.094 radians (120 degrees) with a harmonic strength of 5 kcal/mol×radian^2. Simulations were run at 500 K, a realistic thermal anneal temperature for DSA-BCP systems. A further discussion of these parameters can be found elsewhere.[6,22] The Flory-Huggins χ parameter is set using the ε_{AB} parameter, which determines the strength of non-bonded interactions between unlike polymer beads. When the A-B interaction strength is low relative to the A-A and B-B interactions (i.e. ε_{AB} is much smaller than ε_{AA} and ε_{BB}), χ is higher because the more favorable A-A and B-B interactions tend to minimize mixing. When A-B interaction strength is comparable to the A-A and B-B interactions, χ is low because there is little energy penalty for forming A-B interactions at the cost of A-A and B-B interactions. Thus for our system, the strength of the Flory-Huggins interaction parameter χ is related to the magnitude of the difference between ε_{AB} and the values of ε_{AA} and ε_{BB}. Details of how this relation is calculated can be found elsewhere and in Chapter 2 of this work.[23]

All simulations were run using the HOOMD-Blue software package[24,25] and visualized in VMD[26]. Because of the natural parallelizability of molecular dynamics (MD) simulations as well as the parallel architecture inherent in graphics processing units (GPUs), this software package allows a GPU enabled computer to run MD simulations up to 200 times faster than a standard desktop computer. Simulations were run in fully periodic, 3D, rectangular unit cells under NVT conditions at the average density of the homopolymers. The simulations were initialized by placing chains randomly at the equilibrium angle and bond length uniformly in the simulation volume. Two minimization steps were used. The first minimization step slowly moves apart beads that were randomly placed too close together, and thus have a very strong repulsive interaction. The σ_{AA}, σ_{BB}, and σ_{AB} values were initialized at a very small value and then a brief minimization was run using the Fast Inertial Relaxation Engine (FIRE) minimization algorithm in HOOMD. The σ values were then increased in small steps and a short minimization run, until the desired value of σ_{AB} (1.26 nm in this case) was reached. Any beads that were too close together are thus gently moved apart as the interaction distance between them increases. Once this step is complete, a second, longer minimization is run. All simulations then were run for 100 ns at 500 K.

3.4. Results and Discussion

Previous simulations in large box sizes revealed that the polymer model described above yielded pitches between approximately 10 nm and 14 nm for χN values from 25 to 65. To demonstrate the accuracy and utility of Equation 3.16, and to investigate the effect that different periodic cell dimensions can have on the equilibrium pitch calculated for lamellae forming diblock copolymers, two simulation sizes were chosen: a cubic simulation with 18 nm sides, and a more elongated simulation with dimension of 36.6 nm, 13.3 nm, and 12 nm. These dimensions result in simulations of essentially the same volume, but with very different allowable pitches. Using Equation 3.16 above, it is found that in the range of 10 to 14 nm, the allowable pitches of the 18 nm cube are 10.4 nm and

12.7 nm, while the elongated simulation has allowable pitches of 10.0 nm, 10.7 nm, 11.4 nm, 12 nm, 12.2 nm, 12.5 nm, and 13.3 nm as shown in Table 3.1. Allowable pitches for three different simulation sizes between 10 and 14 nm.. The elongated simulation volumes will allow more polymers to get closer to their natural pitch because of the better sampling of states in the relevant region. Table 3.1. Allowable pitches for three different simulation sizes between 10 and 14 nm.also includes allowable pitches for a 36 nm cube which is eight times larger by volume than the other two simulations. Even though the volume of the 36 nm cube is 8 times larger than the other two simulations, and it has approximately three times the number of possible pitches in the relevant region (10-14 nm) than the smaller cubic periodic cell, it still has fewer allowable pitches than the much smaller volume elongated periodic cell simulation.

Table 3.1. Allowable pitches for three different simulation sizes between 10 and 14 nm.

18 nm Cube[a]	10.4	12.7					
36 nm Cube[a]	10.4	10.9	11.4	12.0	12.7		
Elongated Simulation[a,b]	10.0	10.7	11.4	12.0	12.2	12.5	13.3

[a]Units shown in nm. [b]36.6 nm by 13.3 nm by 12 nm.

Domain sizes of the simulation results were calculated from these simulations by calculating the structure factor from the radial pair distribution function. The results for the 18 nm cube are shown in Figure 3.5, and the results for the elongated simulation (36.6 nm x 13.3 nm x 12 nm) are shown in Figure 3.6. Simulations that contain defects are neglected as the math above assumes a defect free configuration. The dotted red lines are the allowable pitches as calculated above. The green line is the pitch of a lamellae forming BCP with *a* (the statistical length of a polymer repeat unit) equal to 0.761 nm.

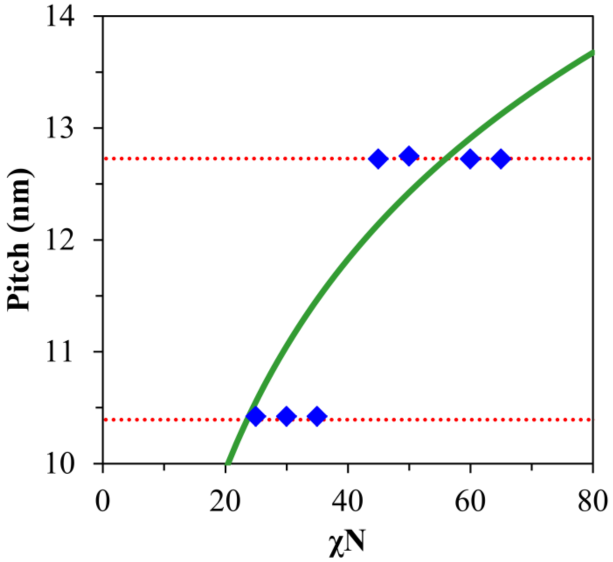

Figure 3.5. Resulting pitches for the 18 nm cube (volume = 5832 nm3) simulation. The only two pitches measured (blue diamonds) are the two pitches calculated in Table 3.1 (red dotted lines). The green line corresponds to the calculation of natural pitches for a BCP with a = 0.761 nm using Shull's theory.[18] This simulation size causes the resulting pitches to deviate from this theory and adopt only the discrete allowed pitches.

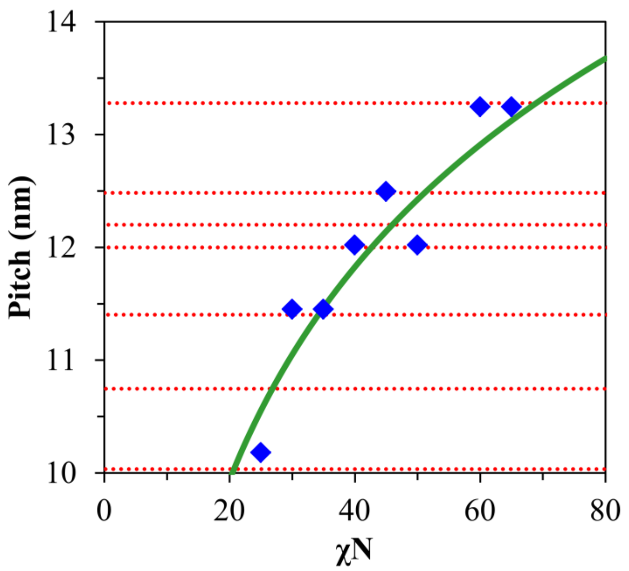

Figure 3.6. Resulting pitches from the 36.6 nm by 13.3 nm by 12 nm simulation volume (volume = 5841 nm^3) which has a very similar volume as the used in generating Figure 3.5. Again the measured pitches (blue diamonds) align well with the allowed pitches from Table 3.1. Allowable pitches for three different simulation sizes between 10 and 14 nm.(shown as red dotted lines). However, the existence of many more allowable pitches from this rectangular simulation volume produces a curve that better matches, as compared to the result shown in Figure 3.5, Shull's theory (green line) which describes the relationship between block copolymer lamellae pitch and polymer χN value.

As can be seen in Figure 3.5 and Figure 3.6, the polymers only form defect-free lamellae at pitches that are allowed by the given simulation size. Because the elongated simulation has more allowable pitches than the 18 nm cube, the measured pitches form a more continuous line, which is more consistent with real BCP behavior. There is some noise in the measured pitch primarily due to a finite integration length in the structure factor calculation, but the measured pitches still clearly line up with expected pitches in every case. In Figure 3.6, the simulation at χN of 50 unexpectedly formed a smaller pitch than the simulation at χN of 45. It is likely that the simulation result at a χN of 50 is actually a metastable state that may anneal out given a longer run time. Because the allowable pitches are not continuous, and changing pitch requires a rotation of the entire simulation, or requires large amounts of beads to move through regions of opposite type beads, the energy penalty to transition from one pitch to another is likely very high. This may stabilize metastable states.

Though intelligently picking a non-cubic simulation will often yield a higher density of allowable pitches in the relevant region, care needs to be taken to avoid unrealistic simulation dimensions. A simulation of dimensions 200 nm by 12 nm by 2.43 nm has 17 allowable pitches in the range of 10 nm to 14 nm, but a dimension as small as 2.43 nm is likely to cause problems with chains interacting with other images of themselves or approaching the non-bonded potential cut-off distance.

3.5. Conclusions

A simple formula was derived to allow calculation of the defect free pitches allowed in a rectangular solid simulation volume implemented in repeating boundary conditions for a lamellae forming system simply based on the three edge dimensions of the solid. It was found that elongated simulation volumes generally allow a higher density of possible pitches than much larger cubic periodic simulations, and that edge dimensions that share the least number of common factors are more advantageous. Large cubic simulations still showed significant restrictions on the number of allowed lamellae pitches, even at pitches that were on the order of 1/3 of a simulation volume edge length or less. To demonstrate the utility of the formula, block copolymer micro-phase separation simulations for a lamellae forming block copolymer system were conducted using a coarse-grained molecular dynamics block copolymer model in conjunction with simulation volumes of roughly equivalent volume but different edge dimensions. It was clearly shown in these simulations that intelligently chosen simulation volume edge dimensions can greatly increase the number of allowed pitches observed. This higher density of allowed pitches can be very important in determining behavior in which the pitch of a lamellae forming system is expected to vary as a function of some independent variable, such as the case of block copolymer lamellae pitch variation with χN value. Choice of simulation volume dimensions using the methodology described in this work can also be very advantageous in setting up simulations to determine the “natural” pitch for a lamellae forming system for which the pitch is unknown since dimensions can be chosen that provide a high density of possible allowed pitches.

3.6. References

1 Weber , H.; Paul, W., Phys. Rev. E, 1996, 54, 3999.

2 de Souza , O. N.; Ornstein, R.L., Biophys. J., 1997, 72, 2395.

3 Muller, M.; Daoulas , K. C.; Norizoe, Y., PCCP, 2009, 11, 2087.

4 Bates , F. S.; Fredrickson, G. H., Phys. Today, 1999, 52, 32.

5 Leibler, L. Macromolecules, 1980, 13, 1602.

6 Lawson, R. A.; Peters, A.; Ludovice , P.; Henderson, C. L., Proc. SPIE 8680, 2013, 8680, 86801Y.

7 Detcheverry, F. A.; Pike, D. Q.; Nagpal, U.; Nealey , P. F.; de Pablo, J. J. , Soft Matter, 2009, 5, 4858.

8 Micka , U.; Binder, K., Macromol. Theory Simul., 1995, 4, 419.

9 Parrinello , M.; Rahman, A., Phys. Rev. Lett. 1980, 45, 1196.

10 Parrinello , M.; Rahman, A., J. Appl. Phys., 1981, 52, 7182.

11 Najafabadi , R.; Yip, S., Scr. Metall., 1983, 17, 1199.

12 Cleveland, C. L. J. Chem. Phys., 1988, 89, 4984.

13 Cleveland, C. L.; Landman, U.; Schaaff, T. G.; Shafigullin, M. N.; Stephens , P. W.; Whetten, R. L., Phys. Rev. Lett., 1997, 79, 1873.

14 Larson, R. G. Macromolecules, 1994, 27, 4198.

15 Shimizu , T.; Yamamoto, T., J. Chem. Phys, 2000, 113, 3351.

16 Schultz, A. J.; Hall , C. K.; Genzer, J. J. Chem. Phys, 2004, 120, 2049.

17 Barrat, J.L.; Fredrickson , G. H.; Sides, S. W. J. Chem. Phys, 2005, 109, 6694.

18 Shull,K. R. Macromolecules, 1992, 25, 2122.

19 Matsen , M. W.; Bates, F. S. Macromolecules, 1996, 29, 1091.

20 Peters, A. J.; Lawson, R. A.; Ludovice , P. J.; Henderson, C. L., J. Vac. Sci. Technol. B, 2013, 31, 06F302.

21 Lawson, R. A.; Peters, A. J.; Nation, B. D.; Ludovice , P. J.; Hender, C. L. son, J. Micro-Nanolith. Mem., 2014, 13, 031308.

22 Lawson, R. A.; Ludovice , P. J.; Henderson, C. L., Proc. SPIE, 2011, 7970, 79700N.

23 Lawson, R. A.; Peters, A. J.; Nation, B. D.; Ludovice , P. J.; Henderson, C. L. (in preparation).

24 (HOOMD), Highly Optimized Object-oriented Many-particle Dynamics -- Blue Edition http://codeblue.umich.edu/hoomd-blue, (accessed December 2014).

25 Anderson, J. A.; Lorenz , C. D.; Travesset, A. J. Chem. Phys, 2008, 227, 5342.

26 Humphrey, W.; Dalke , A.; Schulten, K. J. Mole. Graphics, 1996, 14, 33.

CHAPTER 4

EFFECT OF GUIDING LAYER PROPERTIES ON LINE ROUGHNESS

Detailed molecular dynamics simulations have been performed to explore the effect of guiding layer properties and errors on resulting directed self-assembly (DSA) pattern properties produced in block copolymer (BCP) thin films. Guiding patterns that are non-commensurate to the natural BCP pitch are considered, as are guiding lines that have correlated or anti-correlated line edge deviations. The process window is detailed for non-commensurate line widths. Guiding lines with various correlated and anti-correlated roughnesses show that under the high χ conditions used here, very significant guiding roughness is required to have any effect on the BCP film, and most of the guiding roughness is damped out within 5 nm of the bottom surface of the BCP film. Also, pitch sub-division patterns (where the BCP natural periodicity is some integer multiple smaller than the guiding pattern periodicity) damp out guiding line roughness more easily than pitch replicating patterns where a guiding pattern exists for each line formed in the BCP film.

4.1. Introduction

In the field of semiconductor manufacturing, directed self-assembly (DSA) using block copolymers (BCP) is a promising technique for extending lithographic patterning capabilities beyond the limits of current optical lithography tools. BCP-DSA utilizes the natural micro-phase separation properties of BCPs combined with a guiding pattern to create the long-range order required for electronic devices fabrication and the pattern registration required to assemble multiple levels on top of one another. It is enthalpically favorable for each polymer block in the BCP to interact with like blocks, but because each polymer block is bonded to an unlike block, the domains and patterns formed due to the micro-phase separation of the polymer blocks are of limited size.[1] Depending on the relative volume fraction of the two polymer blocks in the copolymer, a variety of interesting morphologies including cylindrical, gyroidal, and lamellar phases can be formed. Without outside guidance, BCPs that contain approximately 50% of each of the two polymer block types will form lamellae. When the substrate surface is sufficiently neutral in its interaction with both of the polymer block types and the BCP film is coated at a thickness that is not commensurate with its natural periodicity, a somewhat disordered "fingerprint" pattern will form in the film where the lamellae are oriented normal to the substrate surface. In contrast, when a topographically or chemically patterned substrate surface is used specific long or short range order can be induced.[1-3] Using 193 nm (or future EUV) lithographic patterning technology, a guiding pattern can be made which then can be sub-divided in terms of its dimensions using a subsequent BCP-DSA process. Such a process effectively shrinks the smallest dimension and smallest repeat distance in the pattern. There are two main ways in which BCP are guided: topographically (referred to as graphoepitaxy) where confinement between two walls or in some other shape guides the BCP structure, and chemically (referred to as chemoepitaxy) where ideally flat underlayers that are chemically patterned guide the BCP assembly. In chemoepitaxy, a common strategy is to form a line that is the width of a single polymer block domain that interacts preferentially with one of the two polymer block types which is interlaced with a much wider neutral line.[3-5] The strongly interacting line in the chemoepitaxial guiding layer, or “pinning line”, is the pattern to which the BCP aligns. That alignment is then propagated over the width of the neutral stripe by the natural lamellae structure in the BCP. However, such guiding patterns will not in general be perfect, and it is critical to know how the BCP reacts to non-ideal guiding lines. Line edge roughness (LER) and Line Width Roughness (LWR) are two important factors to be considered in semiconductor patterns because both negatively affect transistor performance, causing variations in transistor speed, current leakage and threshold voltage.[6-8] Subsequently, LER and LWR in the BCP and the guiding pattern are important because the roughnesses in the BCP lines will be transferred to some degree via etch into the final components of the transistors. Logically, both the intrinsic roughness of the BCP,[9-14] and the underlayer LER/LWR in the original guiding pattern[15-20] would be expected to affect the final BCP LER/LWR roughness. While underlayer roughness is important, pitch commensuration is also important. When the guiding pattern pitch and BCP natural pitch does not match, then strange morphologies can occur, and it may be possible that even if the correct morphology occurs, that it may roughen undesirably.[21] As seen in Figure 4.1, LER is the deviation from a straight line edge, and LWR is the deviation from a uniform line width. In Figure 4.1(a), though the image demonstrates a high LER, it actually has an LWR of 0 nm. Figure 4.1(b) shows a high LER and LWR. This paper considers both correlated roughness (i.e. a sinusoidal guiding stripe) and anti-correlated roughness (i.e. a peristaltic guiding stripe) in pitch replication and pitch sub-division patterns and the effects of these guiding patterns on the resulting BCP pattern properties. Details of the particular model used here can be found in the modeling section, but in short, a coarse grained molecular dynamics model is used to study these effects.[22]

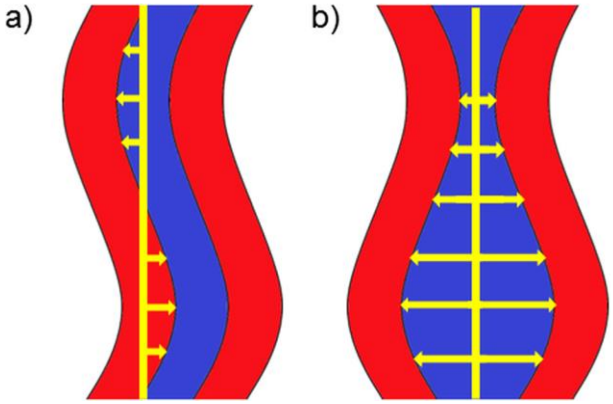

Figure 4.1. Top–down schematic of (a) LER and (b) LWR. LER is the deviation from a straight line edge, and LWR is the deviation from a uniform line width.

4.2. Modeling

4.2.1. Coarse Grained Model

This work has used a coarse grained molecular dynamics model as described elsewhere.[22-24] In brief, the polymers are modeled by representing four monomers (corresponding to a statistical segment length) as a single bead. Four monomers were chosen because that corresponds approximately to a statistical segment length for polystyrene and poly(methyl methacrylate), two types of polymers commonly used in BCP-DSA. Grouping a different number of monomers into one bead would approximate a different statistical segment length, and change the flexibility of the chain. These beads experience three different potentials, a non-bonded potential (similar to a Lennard-Jones potential, but made softer and broader by using an 8-4 potential function), a harmonic bond potential (corresponding to stretching or compressing the BCP), and a harmonic angle potential (corresponding to bending the BCP). The non-bonded potential uses the form:

$$E(r) = \varepsilon\left[\left(\frac{\sigma_{ij}}{r}\right)^{8} - 2\left(\frac{\sigma_{ij}}{r}\right)^{4}\right] \qquad 4.1$$

where ε_{ij} refers to the strength of the interaction between beads of type i and j, σ_{ij} refers to the end of the repulsive shell (that is, the point at which the potential intersects 0), and r refers to the distance between the two interacting particles. This potential is attractive when beads are close enough together, and repulsive when they are too close. All beads undergo this potential as long as they do not also participate in a bond or angle potential. Two bead types were used, referred to here as type A and type B, representing two different arbitrary monomer types. The potential function parameters for these two bead types were set to reproduce polymer properties similar to typical BCP polymers such as polystyrene and poly(methyl methacrylate), with a χ value (i.e. the common Flory-Huggins parameter used as a measure of driving force for micro-phase separation[1]) that can easily be changed by modifying the potential function parameters. The details of the block copolymer model and the method used to relate the potential function parameters to a χ value are found in Chapter 2. The same potential values that were used elsewhere[25] were used here. For the bond potential, the spring constant (k_{str}) used was 100 kcal/(mol*nm^2) and the equilibrium length used was 0.82 nm. For angle potential, the spring constant (k_{ang}) used was 5 kcal/(mol*nm^2) and the equilibrium angle used was 120°. For the non-bonded potential, ε_{AA} and ε_{BB} were both set at 0.5 kcal/mol and ε_{AB} was set at 0.3 kcal/mol. All σ values (σ_{AA}, σ_{BB} and σ_{AB}) were set at 1.26 nm. A degree of polymerization of 120 was used, resulting in a χN of 91 and a natural pitch of 20 nm.

All simulations were performed in a thin film state. The x and y dimensions were set as periodic while the z direction was set to be effectively non-periodic by setting the periodic distance very large compared to the thickness of the polymer film. That is, the z direction is periodic every ~80 nm, but the simulation only takes place within a ~20 nm region in the z dimension. So, there is no interaction across the z boundary. The patterned thin film simulations contained two parts: the underlayer and the BCP film. The underlayer was built using the same beads that constitute the film. The underlayer was built to model a brush with the bottom-most bead of the chain, i.e. the one in contact with the hypothetical substrate, fixed in space. This boundary condition corresponds to the brush polymer chains being tethered to a substrate such as silicon. The tethered bead chains were placed on a square lattice 15 Å apart in the x and y directions. If the beads were placed much closer than this distance, then the interface between the underlayer and the BCP film was judged as unrealistic since a large density discontinuity existed at the interface with large density oscillations occurring in the BCP film near the interface and no apparent interpenetration of the BCP into the underlayer. If the lattice spacing was set much larger than this 15 Å distance, then the BCP chains quickly penetrated completely through the underlayer no matter how long the chains composing the underlayer were made. In a real system, a brush is tethered to a hard surface (like a Si substrate) which prevents this. A plot demonstrating these issues is shown in Figure 4.2 and related pictures from instances of the simulations are shown in Figure 4.3. The length of the underlayer chains used for the simulation results reported here was six beads. Fewer than six beads per chain again resulted in density waves in the BCP film near the film interface because the fixed underlayer beads at the substrate surface were not sufficiently shielded from the film. The fixed nature of these beads changes the packing structure of the film beads if not sufficiently shielded by a length of brush. Another layer of fixed beads was placed below the brush to act as a hard surface and prevent inversion of the brush. The patterning of these underlayers was done by setting the beads in the underlayer chains as either A or B as a function of position. These simulations were 4 BCP pattern pitches wide and at least 120 nm long, because it was found that at least 100 nm was required to get accurate roughness measurements.[25] Stripes of A or B beads (the same beads that make up the BCP film) are used in the underlayer to guide the BCP and are set to the desired type and degree of roughness using sine wave boundary functions when setting the compositional patterns in the underlayer. The BCP film was built initially mixed; chains were placed at the correct bond length and angle randomly through the simulation box through the desired thickness. The underlayer was then placed underneath this film. All initial chain building was done in Molecular Operating Environment[26] (MOE) followed by an energy minimization step in MOE. Subsequently, molecular dynamics was performed on these simulation volumes using HOOMD-Blue.[27,28]

4.2.2. Measurement of line edge roughness (LER) and line width roughness (LWR)

Line edge roughness and line width roughness were measured through the thickness of the film. The beads of one type, e.g. A beads, were binned based on their positions. A 1 nm square lattice was used for x and y (i.e. a surface lying in the same plane as the thin film), to make a map of the number density of beads. A 1 nm lattice spacing was chosen to be comparable to a high resolution SEM image and to get good sampling. In the z direction (through the thickness of the film) a 3.5 nm binning depth was used. This allowed the LER to be measured as a function of depth. The bead density histograms were then used to define line edges by choosing a particular bead density as a cutoff. This threshold cutoff in bead density was selected as to minimize the roughness and match the line edge as inspected visually. A threshold cutoff of approximately 35% of the highest bead number density was deemed optimal in most cases. LER and LWR were then measured from the determined line edges and averaged over ~10 points in time after equilibration for ~4 lines per point in time, ultimately yielding roughness values that were averaged over ~40 lines.

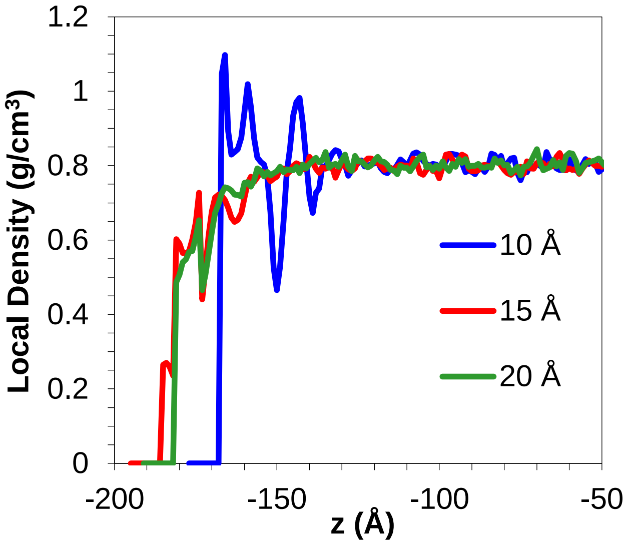

Figure 4.2. Density as a function of depth through the simulation. Different spacing of the tethered points in the underlayer give different density profiles. When the spacing is too low, density waves propagate from the interface before leveling off to bulk density.

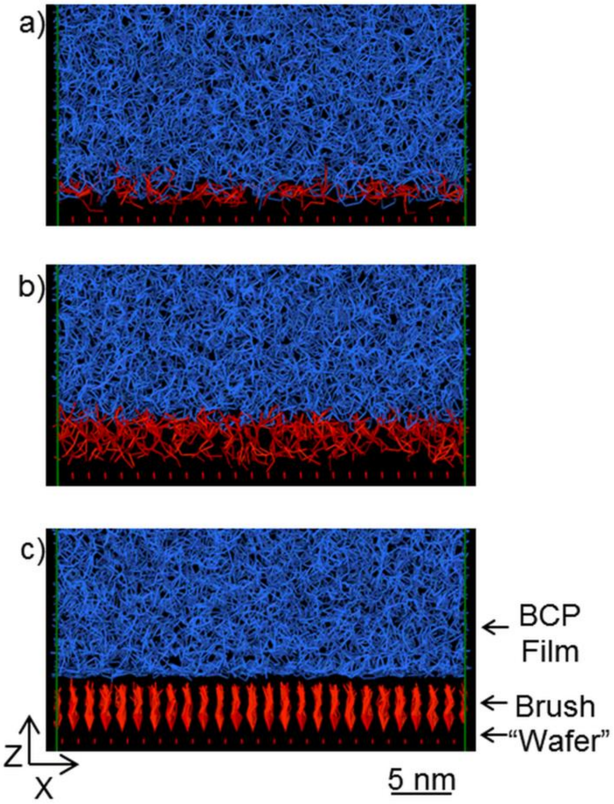

Figure 4.3. Images of simulation with various underlayer chain spacings. The film is colored blue and the underlayer brush (with artificial wafer) is colored red. The film is a homopolymer film. a) 25 Å spacings result in a very low density underlayer and penetration of the film beyond the bottom of the underlayer. b) 15 Å spacings result in some penetration, but it does not penetrate through the entire brush. c) 10 Å spacings result in a poor interface and no interpenetration. For this work, and intermediate spacing of 15 Å was used.

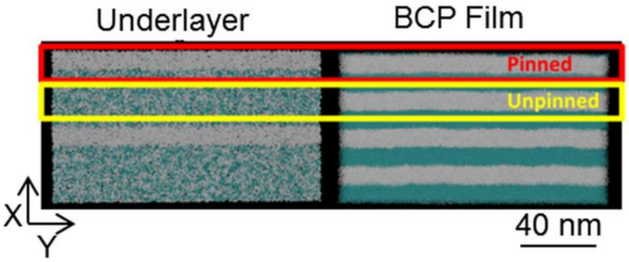

Figure 4.4. Depiction of pinned and unpinned lines. Lines appearing above guiding stripes are considered pinned, while lines over neutral stripes are considered unpinned.

4.3. Results and Discussion

4.3.1. Effect of Guiding Pattern Pitch Mismatch

The effect of a mismatch between the guiding pattern pitch and natural pitch of the BCP was considered for both pitch replicating and pitch halving simulations. Line roughness was measured as the underlayer guiding pattern pitch was changed. Both pinned and unpinned lines (as defined in Figure 4.4) were also compared in terms of line edge roughness. All simulations were four pitches wide and 8 pitches long. These dimensions gave sufficient lengths for measured roughness values to be independent of length.[25] As seen in Figure 4.5, there is a ~2 nm window for the guiding pattern pitch on either side of the natural pitch of the BCP where roughness in the BCP pattern is unaffected. For guiding pattern pitches that deviate by a magnitude larger than this, the lines do not follow the guiding pitch and instead buckle as seen in Figure 4.6, which is consistent with predictions from mean field models such as the Leibler-Ohta-Kawaski model.[29] When the guiding pitch was set below 18nm, there appeared to be a drop in roughness, but this is likely a simulation artifact. Because the BCP lamellae were built aligned to the guiding stripes, they become trapped and are not able to realign to their desired pitch easily. It would likely take some time for larger scale rearrangement to occur. Figure 4.5 also shows that there is little difference between pinned and unpinned line roughness, though this may increase with larger degree of pitch sub-division. Propagation of roughness is limited to only one line here, and this will only increase with larger pitches and levels of pitch sub-division in the guiding patterns. However, there is a measurable difference between pitch replicating and pitch halving roughness, though the 2nm limit on either side remains the same.

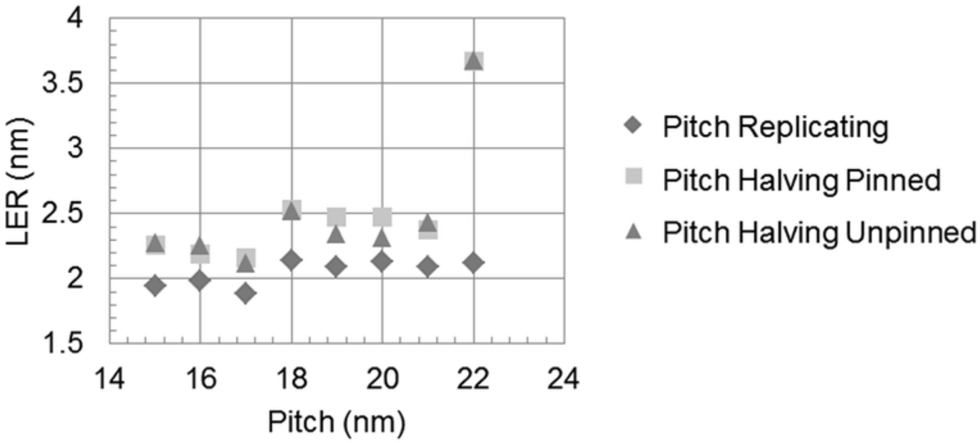

Figure 4.5. Line edge roughness as a function of pitch for both pitch replicating guiding layers and pitch halving guiding layers. Between 18 nm and 21 nm, there is little change in roughness, and above 22nm the BCP does not align to the pitch of the guiding pattern. Below 18nm, there seems to be a confinement effect due to simulation specifics.

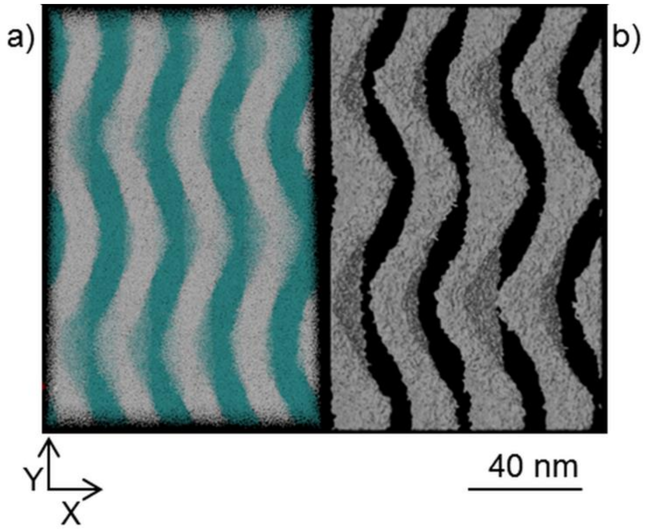

Figure 4.6. Both images show 24 nm guiding pitch pattern with 20 nm natural pitch BCP. When the guiding layer pitch is too large, the BCP force themselves into their natural pitch in the bulk of the film while being pinned at the underlayer. a) All beads shown. b) Only A beads shown.

4.3.2. Effect of Sinusoidal and Peristaltic Guiding Lines

Both sinusoidal and peristaltic (see modeling section) guiding lines were considered. These represent systematic roughness and errors in the guiding line, both correlated and anti-correlated, that could occur in the patterning process. Figure 4.7 shows the line edge roughness and line width roughness through the depth of the film for sinusoidal guiding lines for a BCP with a natural pitch of 20 nm and a χN of ~85. In most cases, the underlayer roughness does not significantly affect the LER of the BCP, damping out within 5 nm vertical distance away from the brush layer interface. However, when both the amplitude and wavelength are large, and the simulation is a pitch replicating simulation (that is, the guiding pattern has the same pitch as the BCP pattern) the roughness persists throughout the entire film. It may be that as the film thickness increases, this too will damp out further, but this has not yet been studied. Pitch halving simulations (which are more like those that would be used in semiconductor manufacturing) are more resistant to such underlayer deviations, where even very significant underlayer line roughness has little to no effect on the BCP roughness. Figure 4.8 shows LER and LWR through thickness for peristaltic guiding lines. In all cases, the guiding pattern makes little difference in the measured roughness after ~5 nm of film thickness away from the guiding layer interface. Based on a comparison of the sinusoidal versus the peristaltic guiding pattern results, it appears that BCP patterns are more tolerant of fluctuations in guiding line width than fluctuations in line edge position. This is consistent with the most common defects where the lines remain roughly the correct width throughout, though they branch and twist. Though the underlayer line roughness does not affect the BCP roughness significantly, the effect of these underlayers on defectivity was not studied here, so it should not be assumed that any roughness in the underlayer can be tolerated without penalty, only that such guiding pattern roughness will not likely affect BCP pattern roughness significantly.

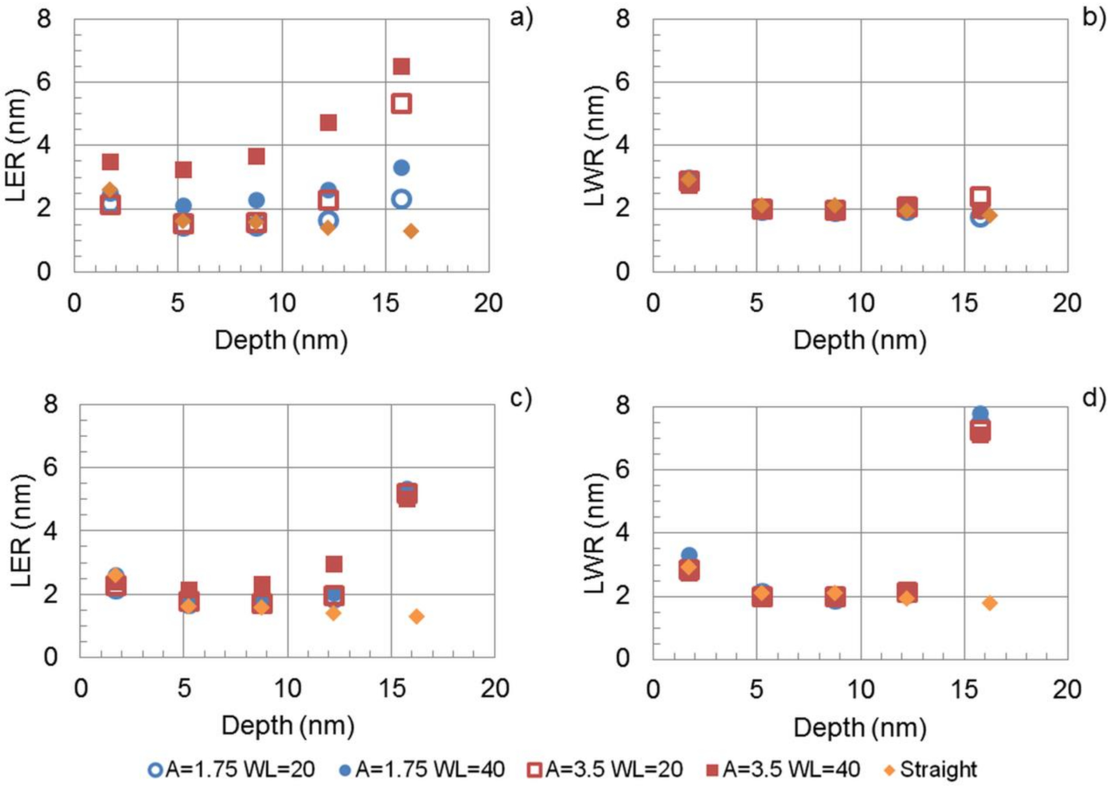

Figure 4.7. LER and LWR through depth for sinusoidal guiding lines. The film surface is located at a depth of 0 nm, and the film-underlayer interface is located at 15 nm. A refers to the amplitude and WL the wavelength of the underlayer sine wave. LER and LWR as shown are 3 σ. In most cases, roughness in the underlayer is mitigated in the first ~5nm. a) LER of pitch replicating simulation. When the amplitude and wavelength of the guiding stripe are very high relative to the line width (in this case the amplitude=35% of line width while the wavelength is 4 times the line width) then there is some roughness that persists through thickness. b) LWR of pitch replicating simulation. LWR is unaffected except perhaps right at the underlayer. c) LER of pitch halving simulation. Effects of underlayer are more damped. d) LWR of pitch halving simulation.

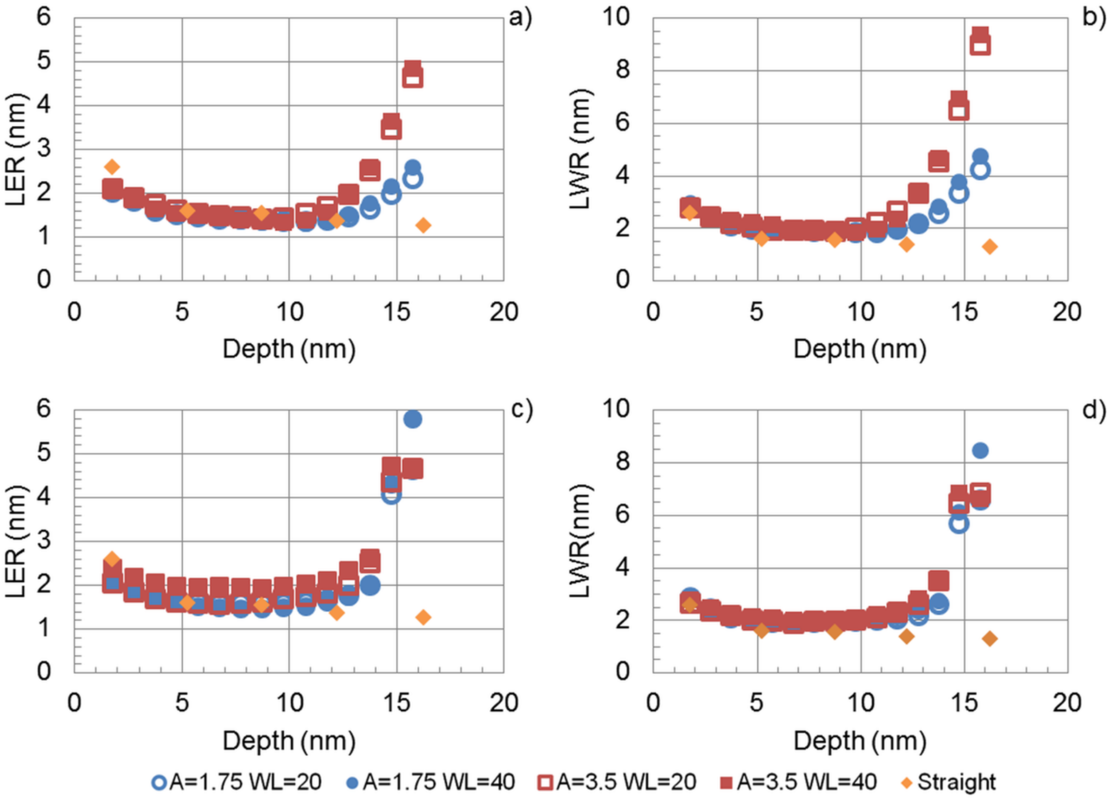

Figure 4.8 LER and LWR through depth for peristaltic guiding lines. The film surface is located at a depth of 0 nm, and the film-underlayer interface is located at 15 nm. In all cases the roughness is damped out within 5 nm of the underlayer. LER and LWR as shown are 3 σ. a) LER of pitch replicating simulation. b) LWR of pitch replicating simulation. c) LER of pitch halving simulation. d) LWR of pitch halving simulation.

4.4. Conclusions

By using our coarse grained BCP model we have studied the process window for pitch mismatch for a high χ system. There is about a 10% window on either side of the natural pitch of the BCP, as measured by line roughness, outside of which lines buckle or deform. The effect of roughness in the guiding layer pattern on resulting BCP pattern roughness was also studied. Only in cases of extreme roughness (i.e. long range roughness with total deviations more than one quarter of the BCP pitch, or more than one half the guiding pattern line width) was any roughness perpetuated throughout the thickness of the BCP film. Anti-correlated roughness (high LWR patterns) had less effect on the BCP line patterns, showing no roughness perpetuation throughout the BCP film thickness for any guiding stripe. Finally, BCP DSA processes using pitch subdivision patterns were more tolerant of guiding layer pattern roughness as compared to processes using pitch replication patterns.

4.5. References

1 Bates , F. S.; Fredrickson, G. H. Phys. Today 52, 2 (1999).

2 Cheng, J. Y.; Rettner, C. T.; Sanders, D. P.; Kim , H.-C.; Hinsberg, W. D. Adv. Mater. 20, 3155 (2008).

3 Bencher, C.; Smith, J.; Miao, L.; Cai, C.; Chen, Y.; Cheng, J. Y.; Sanders, D. P.; Tjio, M.; Truong, H. D.; Holmes , S.; Hinsberg, W. D. Proc. SPIE 7970, 79700F (2011).

4 Park, S.M.; Stoykovich, M.; Ruiz, R.; Zhang, Y.; Black , C.; Nealey, P.F. Adv. Mater. 19, 4 (2007).

5 Nealey, P. F.; Raub, A. K.; Hakeem, P. J.; Brueck, S. R. J.; Han , E.; Gopalan, P. J. Vac. Sci. Technol. B 28, 6 (2010).

6 Chuang, Y.; Jack, K.; Cheng, H.; Whittaker , A.; Blakey, I. Adv. Func. Mater. 23, 173 (2013).

7 Hyun-Woo, K.; Ji-Young, L.; Shin, J.; Sang-Gyun, W.; Han-Ku , D.; Joo-Tae, M. IEEE T. Electron. Dev. 51, 1984 (2004).

8 Asenov, A.; Kaya , S.; Brown, A. R. IEEE T. Electron. Dev 50, 1254 (2003).

9 Bosse, A. W. Macromol. Theory Simul. 19, 399406 (2010).

10 Bosse, A. W. J. Vac. Sci. Technol. B 29, 06F202 (2011).

11 Bosse, A. W. J. Vac. Sci. Technol. B 29, 031803 (2011).

12 Bosse, A. W.; Lin, E. K.; Jones , R. L.; Karim, A. Soft Matter 5, 4266 (2009).

13 Hiraiwa , A.; Nishida, A., J. Appl. Phys. 108, 034908 (2010).

14 Hiraiwa , A.; Nishida, A., J. Appl. Phys. 106, 074905 (2009).

15 Farrell, R.; Fitzgerald, T.; Borah, D.; Holmes , J.; Morris, M. Int. J. Mol. Sci. 10, 3671 (2009).

16 Stein, G.; Liddle, J.; Aquila , A.; Gullikson, E. Macromolecules 43, 433 (2010).

17 Stoykovich, M.; Daoulas, K.; Muller, M.; Kang, H.; de Pablo , J.; Nealey, P.F. Macromolecules 43, 2334 (2010).

18 Daoulas , K. C.; Muller, M. Langmuir 24, 1284 (2008).

19 Patrone , P. N.; Gallatin, G. M. Macromolecules 45, 9507 (2012).

20 Patrone , P. N.; Gallatin, G. M. Proc. SPIE 8680, 86801I (2013).

21 Detcheverry, F. A.; Pike, D. Q.; Nealey, P. F.; Müller , M.; de Pablo, J. J. Faraday Discuss. 144, 111 (2010).

22 Lawson, R. A.; Peters, A. J.; Ludovice , P. J.; Henderson, C. L. Proc. SPIE 8680, 86801Y (2013).

23 Lawson, R. A.; Ludovice , P. J.; Henderson, C. L. Proc. SPIE 7970, 79700N (2011).

24 Peters, A. J.; Lawson, R. A.; Ludovice , P. J.; Henderson, C. L. Proc. SPIE 8323, 83231T (2012).

25 Peters, A. J.; Lawson, R. A.; Ludovice , P. J.; Henderson, C. L. Proc. SPIE 8680, 868020 (2013).

26 Molecular Operating Environment (MOE), 2009.10. (Chemical Computing Group Inc., Montreal, QC, Canada, 2009).

27 Anderson, J. A.; Lorenz , C. D.; Travesset, A. J. Comput. Phys. 227, 5342 (2008).

28 HOOMD-blue web page: http://codeblue.umich.edu/hoomd-blue

29 Laachi, N.; Takahashi, H.; Delaney, K.T.; Hur, S.; Shykind, D.; Weinheimer , C.; Fredickson, G.H. Proc. SPIE 8323, 83230K (2012).

CHAPTER 5

EFFECT OF POLYDISPERSITY ON LINE ROUGHNESS

A coarse-grained molecular dynamics model was used to study the thin film self-assembly and resulting pattern properties of block copolymer (BCP) systems with various molecular weight polydispersities. Diblock copolymers (i.e. A-b-B type) were simulated in an aligned lamellar state, which is one of the most common patterns of potential use for integrated circuit fabrication via directed self-assembly of block copolymers. Effects of the polydispersity index (PDI) on feature pitch and interfacial roughness, which are critical lithographic parameters that have a direct impact on integrated circuit performance, were simulated. It was found that for a realistic distribution of polymer molecular weights, modeled by a Wesslau distribution, both line edge roughness (LER) and line width roughness (LWR) increase approximately linearly with increasing PDI, up to ~ 45% of the monodisperse value at PDI = 1.5. Mechanisms of compensation for increase A-A and B-B roughness were considered. It was found that long and short chain positions were not correlated, and that long chains were significantly deformed in shape. The increase in LWR was due to the increase in LER and a constant correlation between the line edges. Unaligned systems show a correlation between domain width and local molecular weight, while systems aligned on an alternating pattern of A and B lines did not so any correlation. When the volume fraction of individual chains was allowed to vary, similar results were found when considering the PDI of the block as opposed to the PDI of the entire system.

5.1. Introduction

Block copolymer (BCP) patterning via directed self-assembly (DSA) has been studied for roughly the past decade for potential use in the semiconductor manufacturing industry.[1-4] By using surface features to guide the phase separation of block copolymers into structures with long range order, BCP-DSA is a prime candidate for use in sub-20nm patterning. These patterning techniques could be used in conjunction with conventional 193 nm lithography tools, or with newer EUV lithography tools, to transform an initially large pitch pattern produced via optical lithography into a much smaller feature pitch structure through directed self-assembly of a block copolymer pattern. In such methods, the traditional optical lithography tools would be used to form the initial guiding pattern to which the BCP would then align, thus allowing pitch subdivision of the primary lithographic pattern and creation of ever smaller features.[1-4] Some effects of polydispersity on block copolymer phase separation in the context of semiconductor manufacturing have been considered including the effect of PDI on the order-disorder transition,[5-7] and on defectivity in laterally confined lamellae,[8] but many more effects of polydispersity in this context are still unstudied. By using our coarse grained molecular dynamics (MD) model,[9] we have studied the effects of PDI on pitch (feature repeat distance) and interfacial roughness in lamellae forming BCPs. Interfacial roughness is studied by specifically considering line edge roughness (LER), and line width roughness (LWR), relevant parameters in to semiconductor manufacturing industry.

The pitch of the self-assembled polymer domains must be controlled precisely to produce reliable and useful patterns for semiconductor fabrication. When the guiding pattern deviates sufficiently from the natural pitch of the BCP, then the block copolymer no longer produces the desired line patterns. Therefore the lithographic guiding pattern must precisely adapt a pitch that is a multiple of the block copolymer pitch so the BCP will reliably reproduce the targeted feature pitch via alignment with the guiding pattern.[10] Roughness, in the form of line edge roughness (LER, which is the standard deviation of the actual line edge compared to a linear fit of the edge) and line width roughness (LWR, which is the standard deviation of the line width) must also be controlled to ensure device success. Roughness in these forms has been shown to result in current leakage, threshold voltage deviations, and variations in transistor speed, all of which translate into poor device performance.[11] Some work on BCP directed self-assembly roughness has been done,[12-16] showing that BCP DSA can, under some conditions, repair some of the effects of roughness in the guiding pattern, and therefore could be used to control roughness[14]. However, the effect of PDI on these values has not been extensively studied and is presented here.

5.2. Models and Methods

5.2.1. Coarse-Grained Model

A coarse-grained polymer model has been used and is described in detail elsewhere,[9,17] but a brief description will be given here. Polymers are coarse-grained by modeling groups of 4 monomers (corresponding to a statistical segment length) as individual beads connected by harmonic bond potentials. Every group of three sequential bonded beads has a harmonic angle potential applied to prevent collapse of the polymer chain due to non-bonded interactions. Every bead pair that does not participate in a bond potential or angle potential experiences a non-bonded potential similar to a Lennard-Jones (LJ) potential as given in Equation 5.1:

$$E_{Non-Bonded} = \varepsilon_{ij}\left[\left(\frac{\sigma_{ij}}{r}\right)^8 - 2\left(\frac{\sigma_{ij}}{r}\right)^4\right] \qquad 5.1$$

The parameter σ_{ij} controls the average spacing between non-covalently attached beads and therefore has a major effect on controlling polymer density. The parameter ε_{ij} controls the strength of the non-covalent interactions and therefore has a major effect on controlling the polymer cohesive energy density (*CED*). Since molecular dynamics simulations are off-lattice and each parameter can be modified somewhat independently, the density and *CED* for a homopolymer can be set to almost any desired value to represent the polymer of interest.[18] The bond and angle terms can be fit by running rigorous atomistic simulations to determine the coarse-grained equivalent distributions of segment lengths and angles. In this case, the parameters for both A and B blocks are set to approximately reproduce the density, bond and angle distribution of polystyrene. ε_{AA} and ε_{BB} are set to 0.5 kcal/mol, while σ_{AA} and σ_{BB} are set to 1.26 nanometers. The equilibrium bond length used for both A and B polymers was 0.82 nm, with a harmonic strength of 100 kcal/mol×nm^2. The equilibrium angle used for both A and B polymers was 2π/3 radians with a harmonic strength of 5 kcal/mol×radian^2. Simulations were run at 500 K, a realistic thermal anneal temperature for DSA-BCP systems. Simulations used a timestep of 0.05 ps. A further discussion of these parameters can be found elsewhere.[9,19]

As explained in Chapter 2, we follow experimental methods[20] and fit the structure factor (similar to an x-ray scattering profile) to Leibler's theory for BCP scattering. This gives a relation for χ as a function of ε_{AB}, N, and volume fraction of the A block. In this paper, ε_{AB} is 0.3 kcal/mol, χ is 1.2, the averaged degree of polymerization is 120 monomers, χN is approximately 144, and except when otherwise noted every chain has a volume fraction of A of 0.5.

All simulations were run using the HOOMD-Blue software package[21,22] and visualized in VMD[23]. Because of the natural parallelizability of molecular dynamics (MD) simulations as well as the parallel architecture inherent in graphics processing units (GPUs), this software package allows a GPU enabled computer to run MD simulations up to 200 times faster than a standard desktop computer. Three types of simulations were carried out in this work: cubic bulk simulations, high aspect ratio bulk simulations, and patterned thin film simulations as shown in Figure 5.1. Bulk simulations were carried out in a fully periodic 3D rectangular unit cell. The cubic bulk simulations measured 45 nm on each side and were used to measure the pitch of the BCP. The simulations were initialized by placing chains built at the equilibrium angle and bond length randomly throughout the simulation volume. Two minimization steps were used. The first minimization step slowly moves apart beads that were randomly placed too close together, and thus have a very strong repulsive interaction. To do this, the σ_{AA}, σ_{BB}, and σ_{AB} values were initialized at a very small value and then a brief minimization was run using the Fire minimizer in HOOMD. The σ values were increased in small steps and with a short minimization run at each step, until the desired value of σ_{AB} (1.26 nm in this case) was reached. Any beads that initially placed too close are gently moved apart as the interaction distance between them increases. Once this step is complete, a second, longer minimization is run. All bulk periodic simulations were run for 100 ns at 500 K.

Domain sizes are calculated from these simulations by calculating the structure factor from the radial pair distribution function. The high aspect ratio bulk simulations are run in a periodic box with dimensions 100 nm by 100 nm by 15 nm. These simulations are used to view a large area of BCP phase separation.

The patterned thin film simulations, which are used for LER and LWR measurements, contain two parts, the underlayer and the BCP film. The underlayer is built using the same beads that constitute the film. It is built to model a brush underlayer, an underlayer where short polymer chains are grafted to a hard substrate. In our model, the bottommost bead of the chain that composes the underlayer is fixed in space, as it would be if tethered to a silicon substrate as described previously. The tethered beads are placed on a square lattice 15 Å apart. If the beads are placed much closer than this distance, then the interface between the underlayer and the film becomes unrealistic and shows density waves (i.e. alternating regions of very high and very low density) and no interpenetration between the film and the underlayer. If the lattice spacing is too far apart, then the underlayer is simply penetrated all the way through no matter how long the chains composing the underlayer are. The length of the underlayer chains are composed of six beads. Fewer than six beads per chain again results in density waves at the interface because the fixed underlayer beads are not sufficiently shielded from the film.. Another layer of fixed beads is placed below the brush to act as a hard surface and prevent inversion of the brush. The patterning of these underlayers was done by setting the beads in the brush chains as either A or B as a function of their position. For the purposes of this work, the underlayer is composed of straight, alternating lines of A and B at half the natural pitch of the polymer. This is done to ensure that all measured roughness in the film is due to the BCP itself and not the guiding pattern. These simulations were some multiple of the pitch wide (1, 4, 8, and 12 pitches wide), 100 nm long (except when otherwise noted), 15 nm thick, and periodic along their width and length, though not in height in order to allow a thin film state. The film was built in the same manner as the bulk BCP simulations and placed on top of the patterned underlayer. The minimization steps are the same as in the bulk simulations. The BCPs are pre-aligned by applying an external force field described by:

$$U_{ext} = A \cdot tanh\left(\frac{\cos\left(\frac{2\pi x}{L}\right)}{2\pi w}\right) \tag{5.2}$$

where U_{ext} is the potential energy, A is a constant that scales the strength of the potential, x is the position in the x-dimension of the simulation box, L is the repeat distance of the potential, and w is the width of the interface relative to the pitch. The potential applied to B beads is negative of that applied to the A beads. This potential drives the system to be pre-aligned to the underlying pattern, which reduces simulation time.

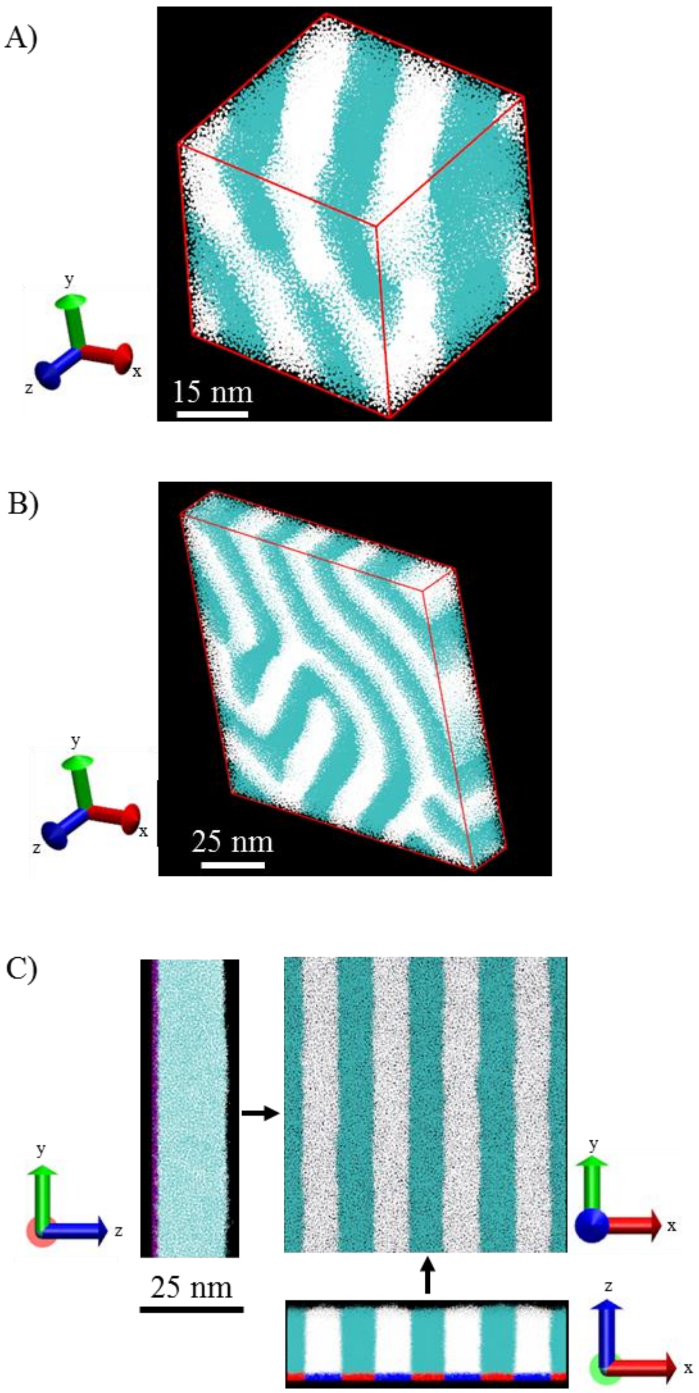

Figure 5.1. Images of various simulation types used in this work. A beads are shown in white while B beads are shown in cyan. A) Cubic bulk simulation. These simulations are 45 nm cubes, periodic in all three dimensions, and are used to find the natural pitch of polymer systems. B) High aspect ratio bulk simulation. These simulations are 100 nm by 100 nm by 15 nm, fully periodic simulation box, and are used to view large cross sections of polymer systems at a low computational cost compared

to a cubic simulation. C) Short length of a patterned underlayer film simulation. These simulations are at least 100 nm long and 15 nm thick on average. A 4 pitch wide simulation is shown, but various multiples of the natural pitch were used. This simulation is periodic in the x and y dimensions, but not in the z dimension, modeling a thin film. The underlayer (shown in red and blue instead of white and cyan for clarity) is patterned to produce alignment in the overlying polymer system.

Polydispersity was modeled using a Wesslau distribution. The Wesslau distribution is an empirical distribution model that has been shown to faithfully reproduce the weight average molecular weight and polydispersity index (PDI) of linear polymers for a large range of molecular weights and distributions.[24] The Wesslau distribution is described by:

$$P(N) = \frac{1}{N\beta\pi^{1/2}} exp\left(-\frac{1}{\beta^2} ln^2\left(\frac{N}{N_0}\right)\right) \tag{5.3}$$

$$\beta = ln\left(\frac{X_w}{X_n}\right) \tag{5.4}$$

$$N_0 = X_n exp\left(\frac{\beta^2}{4}\right) \tag{5.5}$$

where $P(N)$ is the probability of a chain having a degree of polymerization N, X_w is the weight-average degree of polymerization, and X_n is the number-average degree of polymerization. The number of expected chains of length N in a given simulation is equal to $P(N)$ multiplied by the total number of chains, which is determined by the volume of the box, the density of the polymer (~1.4 beads per nm^3), and the desired X_n.

When a simulation is initially built, the expected number of molecules of each possible chain length is calculated and rounded to the nearest integer. The first part of this work fixes the A bead fraction of each chain to 0.5. The later part relaxes this restriction and applies a Wesslau distribution to each block. These block are then linked together randomly resulting in chains that vary in fraction of A.

5.2.2. Measurement of line edge roughness (LER) and line width roughness (LWR)

Roughness of the BCP lamellae was measured in the patterned underlayer thin film simulations. The BCP simulation is transformed into a top-down projection in order to measure roughness. Because a coarse grained model is used, the visual representation of the chains has significantly more empty space than a real polymer would have. A Gaussian blur was used to intelligently fill in this space and prevent unrealistic holes from appearing in the image. To create a Gaussian blur, each bead is blurred using a Gaussian distribution in the plane parallel to the underlayer. The bead location is used as the center of the distribution, and 3 pixels (0.3 nm) is used as the standard deviation of the distribution. The values of the distributions for all the A beads were summed for each point on a 0.1 nm array. This array was converted to a grayscale image where each point on the array corresponds to a pixel, and the value at each array point corresponds to the brightness of that pixel. The image was normalized so that the highest value corresponded to white, and the lowest value to black. The line edges are then identified in the grayscale image by the use of a threshold value similar to the way thresholding is done in SEM image analysis of line-space patterns. The threshold was picked to qualitatively match the line edge and chose to be 0.275 out of a max of 1. This cutoff was used for all LER and LWR measurements. Figure 5.2 shows the transformation from the original simulated lamellae to the grayscale image used for roughness measurements. Figure 5.2A is a top down view of the simulation visualized in VMD. Figure 5.2B is the line after transformation into a Gaussian blurred, grayscale image. Figure 5.2C is the grayscale image with the threshold applied as a yellow line. Patterned underlayer simulations are run for 100 ns to allow for good statistics of the roughness measurements. As seen in Figure 5.3, LWR converges well before the end of the simulation time, though larger PDI did take longer to reach this equilibrium. Roughness measurements are made every 1 ns, and roughness measurements over the last 40 ns were averaged. Simulations used for the measurement in Figure 5.3 were 1 pitch of the guiding underlayer wide, 300 nm long, and the block copolymer film is 15 nm thick. Other experiments have shown that the LER is a constant when the inspection length, the length over which roughness is calculated, is above ~100nm for this particular potential set (see Chapter 6).

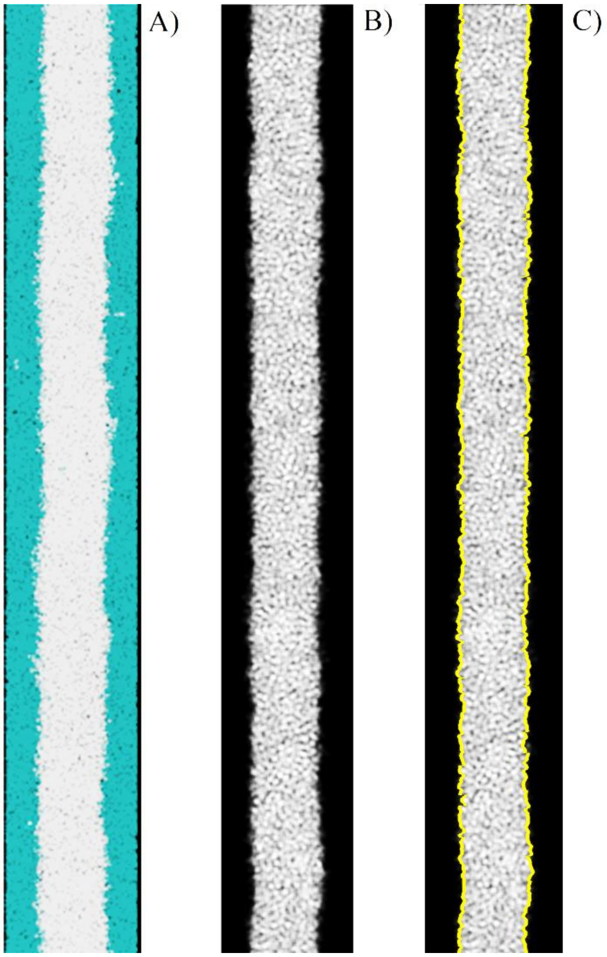

Figure 5.2 Images of BCP aligned to a patterned underlayer for a PDI of 1.54 with X_N=120 monomers. The entire line was 300 nm long, but only 150 nm is shown here for clarity. A) A top-down view of the simulation in VMD. B) The line transformed using a 0.3 nm Gaussian blur with a pixel size of 0.1 nm for only A beads. C) The same Gaussian blurred image with a threshold highlighted in yellow denoting the line edge used in the calculation of LER and LWR.

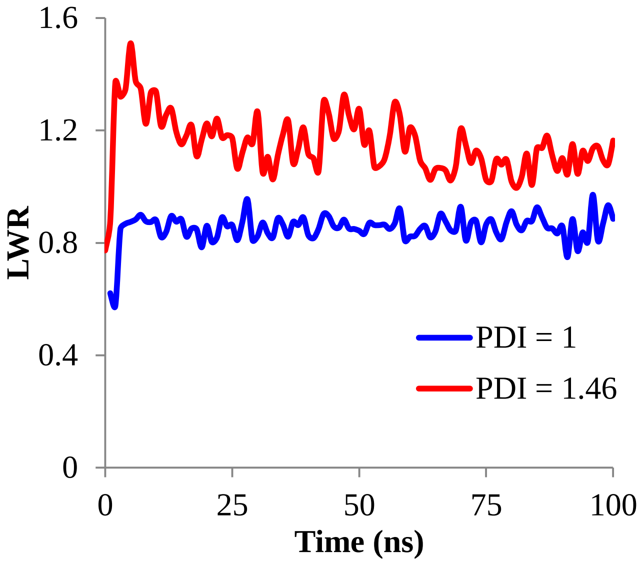

Figure 5.3. LWR measured at individual timesteps as the simulation runs in a patterned underlayer simulation. Roughness levels off after a short time. High PDI take longer to equilibrate, but still equilibrate well within the simulation time. The jump at very short time occurs because the external ordering potential has just been turned off.

5.2.3. Measurement of chain pair distribution function

In order to find any correlation between the location of various chain lengths, a two dimensional pair distribution function (PDF) was calculated. The distance in the y-z plane (the plane parallel to the lamellar interfaces) between every chain centered on adjacent lines was calculated. The pairs of chains were then binned based on the distance between the chains and the difference in N between the two chains, including only pairs that had one chain on either side of X_N. The values of the bins at each distance were normalized by the total number of pairs that exist at that distance. This results in a set of data for each ΔN as a function of distance that elucidates any correlation in position of small and large chains.

5.2.4. Measurement of line width as a function of local number averaged degree of polymerization

Line width and the local degree of polymerization were measured. The simulation is divided into 1 nm long sections along the length of the line. In each section, both the average line width is calculated as well as the local number averaged degree of polymerization (X_n'), as defined in Equation 5.6.

$$X_n' = \frac{n}{\sum_i^n 1/N_i} \tag{5.6}$$

n is the number of monomers in the given section, and N_i is the number of beads in the chain that bead i is on. The denominator of Equation 5.6 is the number of chains in the section in question, allowing for partial chains. For example, if there were two chains, one with 100 monomers, and one with 200 monomers, and each had half of the chain in the given section, then there would be one entire chain in the section, and the denominator would be one. The numerator would be 100*0.5+200*0.5 = 150. So X_n' would be 150/1 = 150. When this is calculated over the entire simulation, it yields the overall number averaged degree of polymerization X_n. The local line width is the average line width over that 1 nm section. In unaligned simulations, the same analysis was performed except that the line width was calculated along a vector perpendicular to the line edge. In the aligned system, this direction is already defined by the nature of the alignment, but in the unaligned case, the direction perpendicular to the line edge must be calculated at every point.

5.3. Results and Discussion

Fully periodic, bulk simulations (45 nm cube) with a χN of 144 and X_N of 120 were run at various PDI values. The pitch was measured by calculating the structure factor from the radial pair distribution function. The calculated polymer pitch as a function of PDI is shown in Figure 5.4 alongside experimental results using poly(ethylene-al-propylene)-b-poly(D,L-lactide) (PEP–PLA) varying the polydispersity in the PLA block by Lynd and Hillmyer[25]. Figure 5.4, in agreement with experimental results published by Lynd and Hillmyer[25,26] as well as Matsushita et al.[27], shows that an increase in PDI increases the pitch of a polymer. While this effect is apparent even at low PDI, the effect is still relatively small. One possible technique to account for this increase in pitch is to blend different batches of polymers that have different number averaged molecular weight. Because pitch scales with molecular weight ($L \sim N^{2/3}$ in the strong segregation limit[28]), changing the average molecular weight of a system by blending allows one to control the pitch of a polymer system. By adding smaller polymers to these distributions, one might be able to lower the average molecular weight of the system enough to counteract the increase in pitch associated with the increased PDI. This has been conceptually demonstrated and thoroughly discussed elsewhere.[29] However, blending BCP's of different molecular weights in order to tune the domain size will yield a blend with a higher PDI than a monodisperse system at an equivalent pitch, and the results of such an increase in PDI (such as increased roughness and defectivity) would need to be considered.

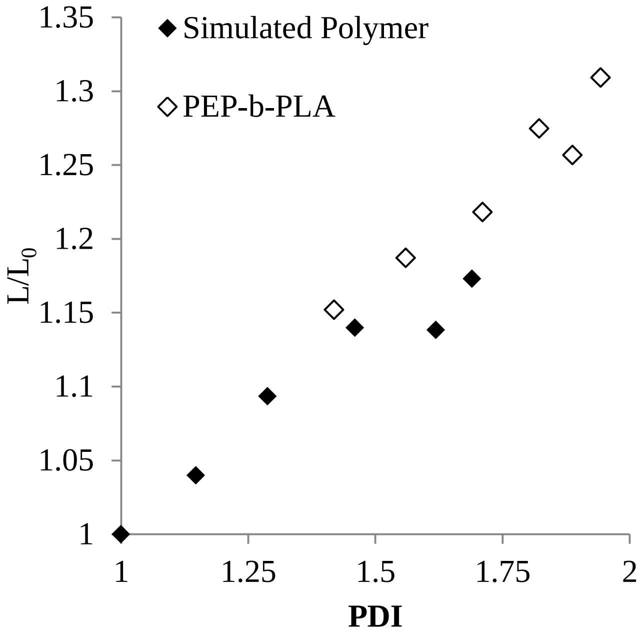

Figure 5.4. Pitch normalized to the monodisperse pitch. The PEP-b-PLA experimental results were obtained by Lynd and Hillmyer[25] by varying the polydispersity in the PLA block at a χN value of ~80. Simulation results shown here use a Wesslau distribution and are at a χN of 144. Both data sets show that the scaled pitch increases with PDI at similar rates.

Patterned thin film simulations were run at various PDI with a χ of 1.2 and X_n of polymerization of 120 monomers (resulting in a χN of 144). The width of the simulation was set at a multiple of the natural pitch of the polymer at the simulated PDI. For any PDI at which the natural pitch was not measured directly, the natural pitch used was taken from a linear fit to the data in Figure 5.4. As seen in Figure 5.5A, LER increases approximately linearly with PDI. The width of the simulation (in multiples of the natural pitch L_0) has a significant effect at low PDI, but no clear effect at high PDI (above PDI ~ 1.3), and increasing simulation size to 4 L_0 wide removes any effect above a PDI of 1.1.

The effect is due to the correlation forced between line edges and will be discussed in further detail later. In the widest simulations ($8L_0$ and 12 L_0), LER increased an average of 43.5% above its monodisperse value at a PDI of ~1.5 and an average of 13.5% above its monodisperse value at a PDI of ~ 1.1 (a PDI value which is generally achievable in these types of systems). Line roughness must be controlled in integrated circuit fabrication to prevent current leakage, threshold voltage deviations, and variations in transistor speed, all of which result in poor device performance[11]. Using Figure 5.5, the roughness benefit for a decrease in PDI can be estimated and compared to the financial and temporal cost of reducing PDI, giving guidance to those designing BCP-DSA systems as well as those synthesizing the polymers for these systems. However, other important properties of BCPs (including defectivity) may still be affected by PDI and are still in need of further study.

Although both LER and LWR are detrimental to semiconductor device performance, LWR is generally considered to have the strongest negative effect on device performance.[30] Here, LWR is higher than LER in all cases and generally increases at a similar rate to LER as shown in Figure 5.5B. In this case, the 1 L_0 wide simulation yielded a lower LWR than the wider simulations, but 4, 8, and 12 L_0 wide simulations all yielded similar results. In general, high PDI systems show more noise (as in Figure 5.3), and this likely accounts for the spread of data at higher PDI in the 4, 8 and 12 L_0 wide simulations. LWR in the 4, 8, and 12 wide simulations increased average of 45.1% at a PDI ~ 1.5, and 11.6% at PDI ~ 1.1, comparable to the increase in LER.

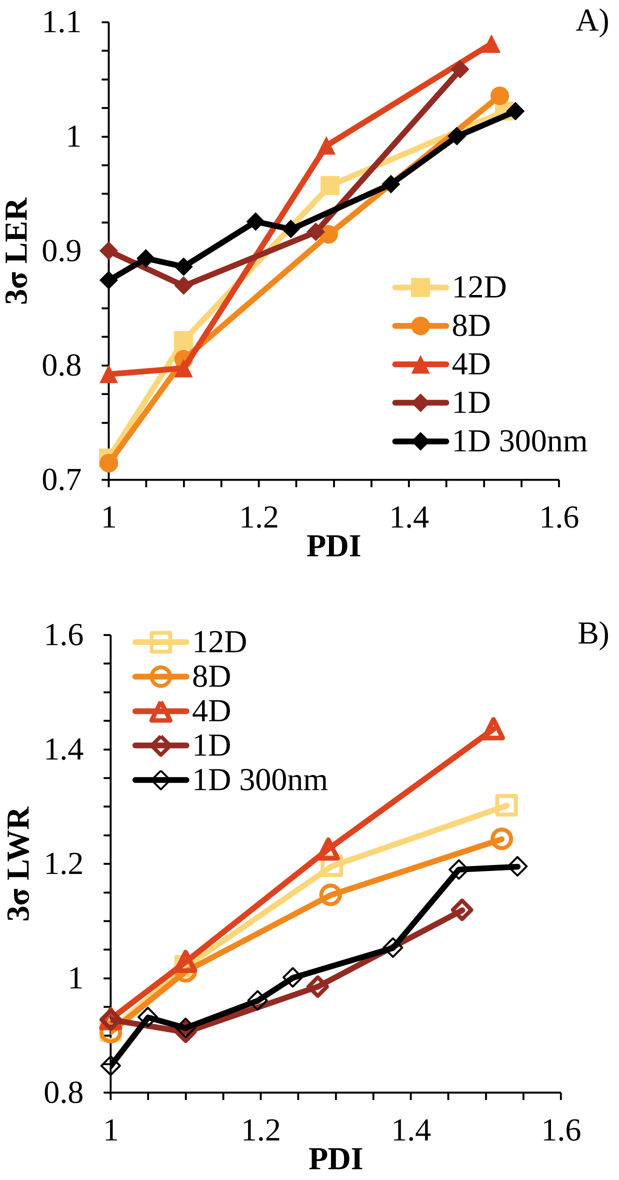

Figure 5.5. LER (A) and LWR (B) as a function of PDI and simulation size with a X_n of 120 and a χN of 144. Both LER and LWR increase at a similar rate as PDI increases.

Polydispersity will affect LER and LWR by increasing the roughness at the A-A and B-B interfaces (in this middle of the A or B domains). Because chains of different length will necessarily extended different distances into the A or B domain, the roughness at this interface will increase. Figure 5.6 shows the increase in LER of the A-A domains as a function of PDI. This effect is independent of simulation size, and always higher than the A-B LER because there is no enthalpic restoring force at the A-A interface. Because the simulated polymers here are energetically symmetric (that is, the A-A interactions are identical to the B-B interactions), the B-B roughness is affected similarly. The polymers must accommodate this increased A-A and B-B roughness in one of three ways as shown in Figure 5.7: 1) increased line roughness, 2) correlation of chain lengths in adjacent lines (small chains favoring interaction with long chains at the adjacent interface and vice versa), and 3) deformation of chain shapes. Figure 5.5 shows that the first effect occurs to at least some degree. However, the A-A roughness increases 2.6 times faster than the A-B roughness (on a normalized basis), so one of the other two modes must be important as well.

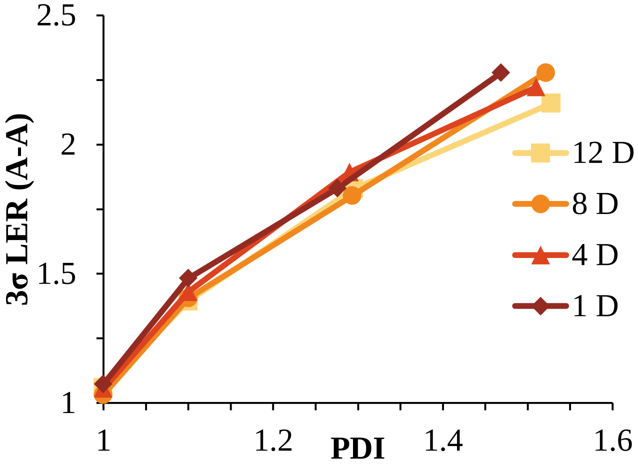

Figure 5.6. A-A LER as a function of PDI and simulation size.

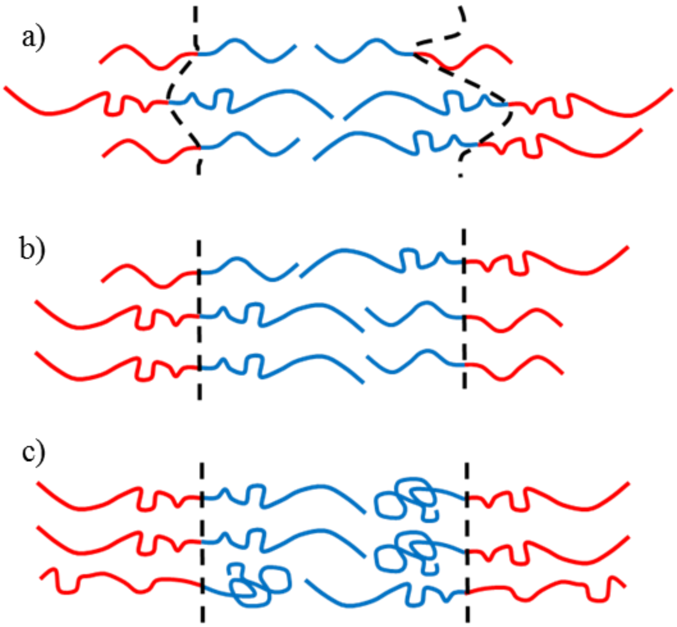

Figure 5.7. Different mechanisms to compensate an for increase in A-A and B-B roughness. A) Increasing A-B roughness. B) Correlating short and long chains. C) Deforming chains.

Figure 5.8A shows the probability that the center to center distance (where the center is the average position of the center two beads in the chain) of a pair of chains on adjacent lines and with a particular difference in chain length (*ΔN*) will be found at a particular distance in the yz plane (the plane parallel to the lamellae). This probability is shown in the form of a pair distribution function (PDF). Only pairs of chains where one pair is shorter than the average and one chain is longer than the average are considered so that the expected long-short chain correlation, if it exists, is amplified. If long chains and short chains are coordinating to limit the effect on the A-B roughness, this plot should be higher at low values of *r*, but this is not the case: there is no change in the pair distribution as a function of distance for any value of *ΔN*. Therefore, there is no evidence that the mechanism as depicted by Figure 5.7B occurs here. Figure 5.8B shows the

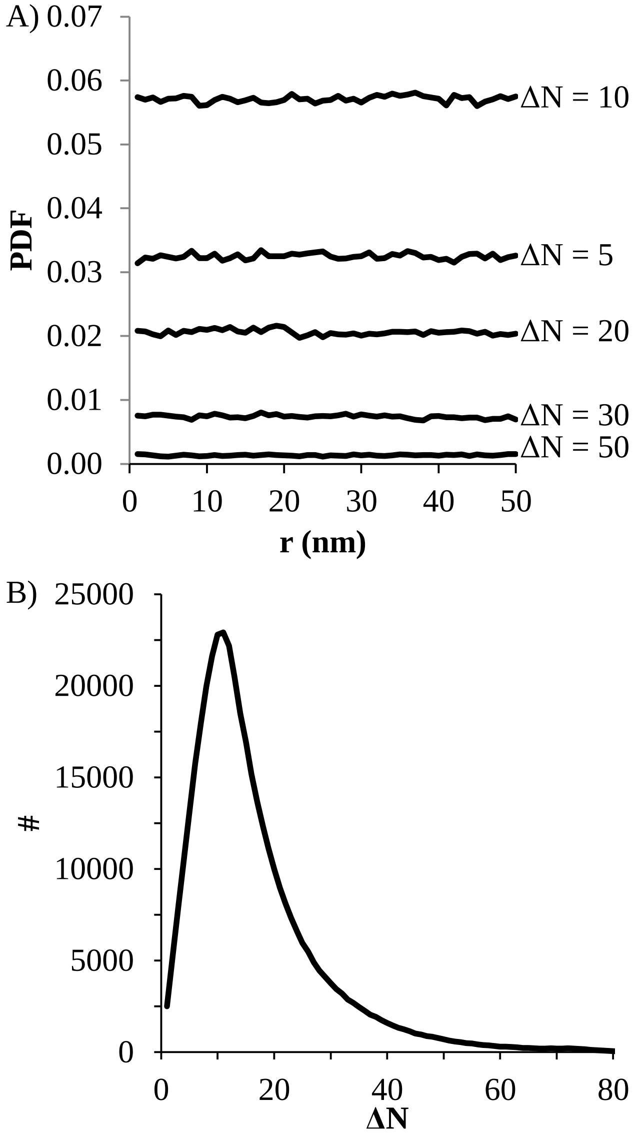

Figure 5.8. Pair distribution function for PDI = 1.53 $4L_0$ wide simulation. A) Pair distribution function for a variety of ΔN. The PDF is the # of pairs of the given ΔN over the total number of pairs of that distance. There is no clear dependence of the PDF on distance for any ΔN. B) shows the total number of pairs as a function of ΔN. This variations explains the offset for each ΔN shown in A) (i.e. there are a greater number of interactions with a ΔN of 10 than of 5 and therefore the line for ΔN = 10 is higher in A)).

number of interactions that occur for each value of ΔN. It is this relation that causes the ΔN in Figure 5.8A to be at different normalized values.

The only other way in which increased A-A and B-B roughness caused by increased PDI can be accommodated is the deformation of chain shapes at higher PDI. This preserves the A-B interface, but is energetically unfavorable for the chains themselves. Figure 5.9 shows the average end to end distance of the polymer chain in the x dimension as a function of chain length for various polydispersities. The average end to end distance in the x dimension for monodisperse systems (at varying X_n) is shown as the unperturbed case. Long chains in the polydisperse systems are significantly shortened, while short chains are relatively unperturbed. Interestingly, chains are similarly affected at both PDI values. The small difference between the two PDI values in Figure 5.9 for large N is likely due to the small increase in pitch in case of the large PDI. Overall there is less perturbation of chains at smaller PDI values, because there are fewer long chains in those cases, but the degree to which a certain chain length is shortened is independent of PDI. Two of the three ways increased A-A and B-B roughness can be accommodated in these systems described in Figure 5.7, specifically increased A-B roughness and perturbation of chain lengths, are present in the systems studied here. Quantitative analysis of the contributions and energetics of these two mechanisms may be addressed in future work.

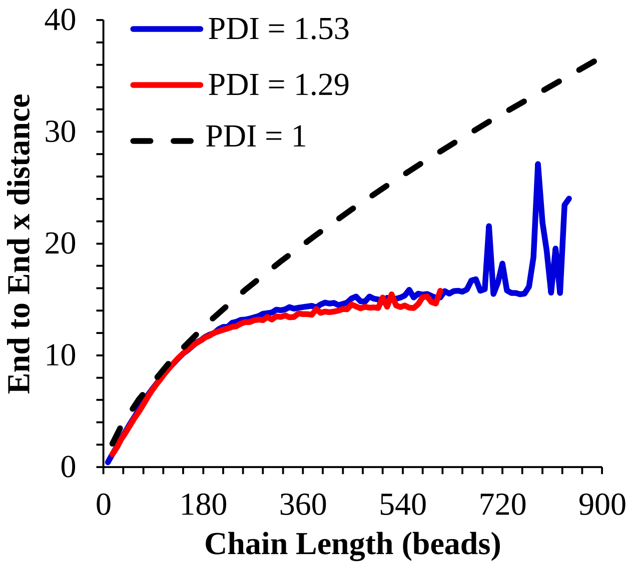

Figure 5.9. Chain size in the x dimension as a function of chain length and PDI. The PDI = 1 line is half the natural pitch of a monodisperse system at the given N determined for the χ value used here. The longer chains are clearly perturbed from their natural state.

It is interesting that the 1 L_0 wide simulations exhibited decreased LWR across all PDI (though the effect is smaller when PDI is near 1), while LER was only affected at low PDI. It is to be expected that narrow simulations would cause increased correlation between lines[31,32], but the change in effect with dispersity may not be so obvious. The relationship between LER and LWR can be mathematically shown to be[31]:

$$LWR^2 = LER_A^2 + LER_B^2 - 2 * LER_A * LER_B * CC_{LE} \qquad 5.7$$

where A and B denote to adjacent line edges. CC is Pearson's correlation coefficient as defined by:

$$CC = \frac{n\sum x_i y_i - \sum x_i \sum y_i}{\sqrt{n\sum x_i^2 - (\sum x_i)^2}\sqrt{n\sum y_i^2 - (\sum y_i)^2}} \qquad 5.8$$

n is the number of points in a data set, and x and y define the two components of that data set. In this case, n is the number of points that define a line, x is the set of positions defining one line edge and y is the set of positions defining the corresponding line edge. When CC_{LE} = 1 the two line edges are perfectly correlated, while when CC_{LE} = 0 the two line edges are completely independent, and when CC_{LE} = -1 two line edge are perfectly anti-correlated, as shown in Figure 5.10.

A CC_{LE} of one results in $LWR = |LER_A - LER_B|$ where LER_A and LER_B are the line edge roughnesses of the two edges that constitute a line. In the case where LER_A is the same as LER_B , which would be generally true for the systems considered here, then LWR = 0. A CC_{LE} of 0 results in $LWR = \sqrt{LER_A^2 + LER_B^2}$. When LER_A is the same as LER_B then LWR simplifies to $\sqrt{2}LER$. This is the case often assumed in traditional photolithography.[31] A CC_{LE} of -1 results in $LWR = LER_A + LER_B$ which simplifies to $LWR = 2LER$.

The correlation coefficient between adjacent line edges for each PDI was calculated and is shown in Figure 5.11A. In all cases the CC_{LE} for adjacent interfaces is above 0 as opposed to traditional photolithography where it is often assumed to be 0. If a fluctuation occurs in one line edge then either there is a change in line width, or the opposing line edge must move to match this fluctuation, or some combination of the two. Because the lowest free energy state of a BCP system is at a specific pitch, the system will adjust the line edge to prevent the increase in line width. The polymers at each interface will interact and adjust to fluctuations to avoid deviations in line width, resulting in a correlation between the two interfaces that determine a line. There is no apparent dependency of the correlation coefficient of adjacent interfaces on polydispersity for simulations that are 4 L_0 or more wide. Figure 5.11B shows the correlation between lines as a function of the distance between lines for the 12 L_0 wide simulations and for one representative 4 L_0 wide simulation . Lines that are adjacent (ΔLine = 1) have a relatively high correlation. By the time the interfaces are 2 or 3 interfaces apart, the correlation has dropped significantly and is nearly 0. The use of a one to one guiding pattern in these simulations likely increases fluctuation dampening beyond the BCPs inherent ability by adding an additional restoring force to every domain.

The general decrease in correlation with simulation width explains the general increase in LWR with wider simulations (Figure 5.5B); given a constant LER (as seen in the high PDI case of Figure 5.5A) decreased correlation mathematically leads to increased LWR. The 1 L_0 wide correlation is clearly an artifact of simulation size, but it is interesting that an increased PDI shows the ability to decouple the two line edges to some degree. The propensity for PDI to do this may be important when studying other systems involving PDI. Additionally, this artifact explain the decreased LWR for the 1 L_0 wide simulations. The increased correlation compared to wide simulations mathematically depresses the LWR of the 1 L_0 wide simulations.

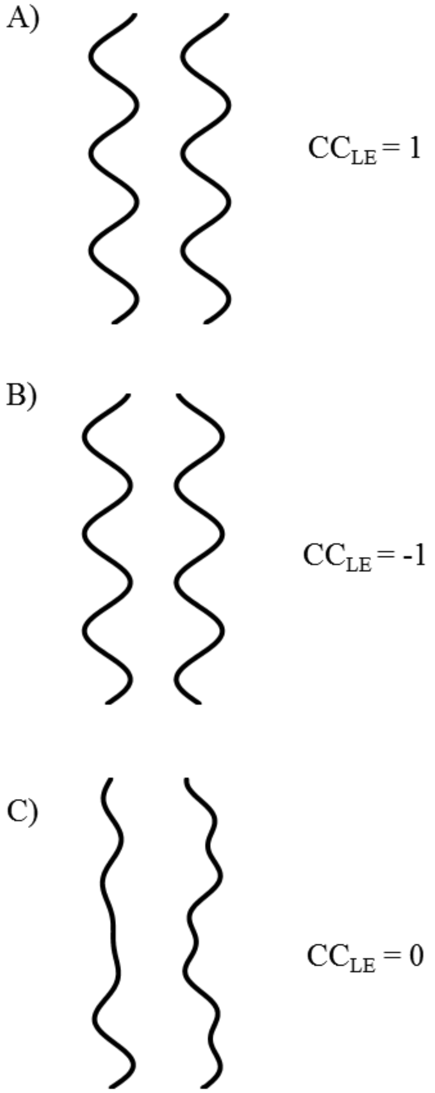
A)
$CC_{LE} = 1$
B)
$CC_{LE} = -1$
C)
$CC_{LE} = 0$

Figure 5.10. Line edge correlation coefficient (CC_{LE}) examples.

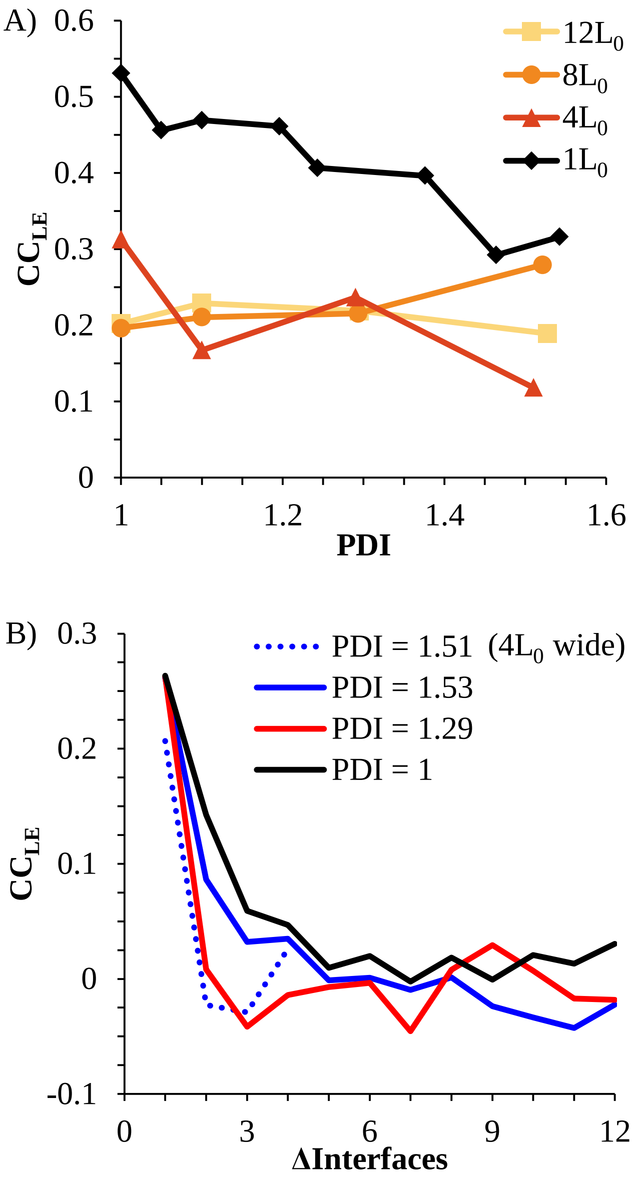

Figure 5.11. A) Correlation coefficient (CC_{LE}) as a function of PDI for patterned thin film simulations. B) CC_{LE} as a function of the number of interfaces separating the two lines being compared.

Figure 5.12 shows top down images of high aspect ratio bulk simulations at various PDI. While for lower PDI values, such as in Figure 5.12A and Figure 5.12B the lines are roughly uniform in line width and appear to contain fewer terminations. At a high PDI of 1.56, seen in Figure 5.12C, variations of line width become clearly evident, with the lines bulging and bending much more, especially at the ends of lines. These lines also seem to have shorter run lengths than monodisperse systems, but this has not been quantitatively studied. It seems that the disparity in chain lengths stabilizes the non-ideal formations in the system, such as ends of lamellae or bulges in the system. This could translate to higher defectivity in systems with high PDI.

There appears to be an increase in anti-correlation at increased PDI when there is not a guiding underlayer, as can be seen in Figure 5.12C. Figure 5.12D and Figure 5.12E break down Figure 5.12C into images showing only chains longer than X_n (Figure 5.12D) and chains shorter than X_n (Figure 5.12E). In these images it can be seen that small chains localize themselves to the interfaces while larger chains span the whole domain. These large chains seem to concentrate the bulk of their mass in the middle of the A or B domains, causing their the shape of these chains to be look like a dumbbell, being narrower in the center and larger at the ends.. When the small chains and large chains are not evenly dispersed (i.e. there is local aggregation of small or large chains), local fluctuations in the line width can be observed. The red circle made with a solid line in Figure 5.12D and Figure 5.12E shows a region where small chains have aggregated leading to a narrower line, while the red circle made with a dashed line shows a region where large chains have aggregated, leading to a wider line. Other similar regions are also apparent in Figure 5.12D and Figure 5.12E. The increase in domain size or decrease in domain size does not have to be identical in the A and B domains. Locally, the A phase (white) may have few large chains, while the B phase (cyan) has an abundance of large chains as seen near the circle made with a solid red line in Figure 5.12D and Figure 5.12E. Of course, the A portion of the large chains has to go somewhere in the A domain, thus swelling the A domain somewhere else. This leads to the A phase having different variations in width than the B phase which helps produce the bulging, pinching, and bending seen in the high PDI systems.

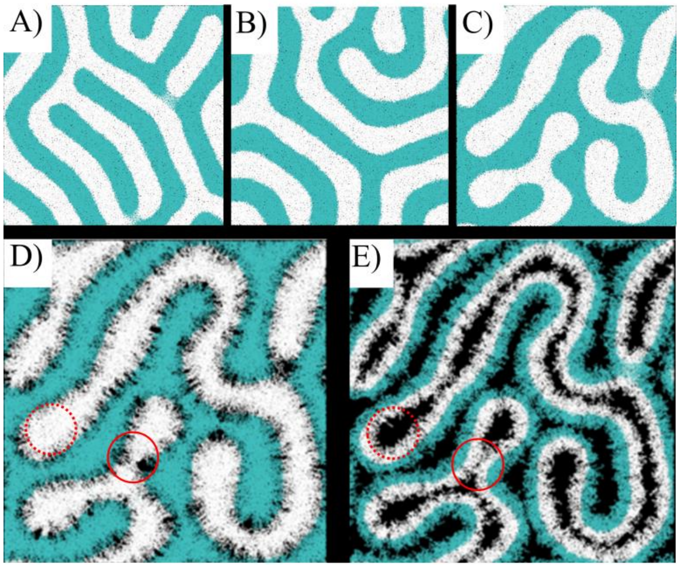

Figure 5.12. Top down views of high aspect ratio bulk simulations. A)-C) show images at PDIs of 1, 1.3, and 1.5 respectively. As PDI increases, local swelling and pinching of lines due to local variations in chain length is apparent. Run length is also decreased as PDI increases. D) and E) show the PDI = 1.5 simulation (C) showing only large chains ($X > X_n$) and small chains ($X < X_n$) respectively.

Figure 5.12 suggests that the local line width should increase with a change in local X_N. The line width as a function of local number averaged degree of polymerization was calculated for the high aspect ratio bulk simulation with a PDI of 1.56 (Figure 5.12C) and an aligned simulations that was 12 L_0 wide and had a PDI of 1.29. Sections of lines in the unaligned system very close to branches were excluded as line width becomes hard to define. Normalized line width (W/W_{ave}) for both the aligned and unaligned simulations are plotted versus local number averaged degree of polymerization in Figure 5.13. There is a clear increase in line width of the unaligned system as X_n' increases. The smallest X_n' values give line widths ~20% (~4.5 nm) smaller than the average line width while the largest chains give line widths 10-15% (~2-3.5 nm) higher than the average. The aligned system shows little to no correlation between line width and X_n'. The guiding stripes add a large penalty to line width variations and defects that is not present in unaligned system. While the unaligned system can swell the domain in one region while reducing the domain in another region, the aligned system suffers a significant penalty for doing so because of the underlayer. It would be expected that underlayers with more infrequent pinning stripes would reduce this penalty, eventually retuning this behavior to the bulk simulation.

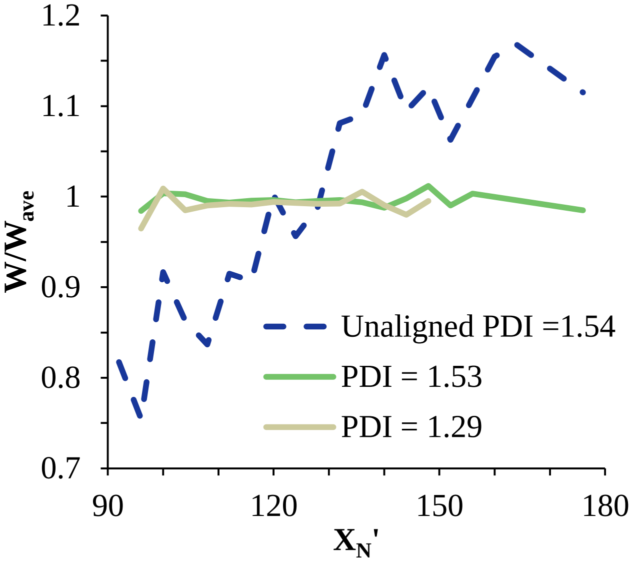

Figure 5.13. Analysis of line width and weight averaged degree of polymerization (X_n'). Data for simulations that are 12 pitches wide on a patterned underlayer are shown along with the high aspect ratio bulk simulation (no patterned underlayer).

The results above only consider chains which contain equivalent numbers of A and B monomers, but in real systems, the composition of each chain will vary. PDI was modeled by creating A blocks using a Wesslau distribution, and B blocks using a Wesslau distribution. The chains lengths that result from these distributions are then linked together (A blocks with B blocks) randomly. Producing PDI in this way is similar to “click chemistry” methods.[33] One interesting result of producing PDI in this way is that when linking together groups of A blocks and B blocks that both have a PDI of 1 + *D*, the resulting polymers will have a PDI of approximately 1+ *D/2*. In the case where all chains are 50% A, small A blocks must be matched with small B blocks and large A blocks must be matched with large B blocks, but in the case where the blocks are randomly linked, small A blocks get matched with the whole array of B blocks, so the length of many chains is shifted towards the average. 4 simulations that were 4 domains wide and 100 nm long were simulated using this method of incorporating polydispersity. The PDI of the A and B blocks (Block PDI) used were 1.10 , 1.20 , 1.51 , and 2.26. Each simulation linked together A and B blocks with identical PDI, so 4 simulations were produced with PDIs (System PDI) of 1.05 , 1.10 , 1.24 , and 1.53. The highest two values produced unrealistic results, as seen in Figure 5.14. Small blocks of A connected to larger blocks of B resulted in a large number of beads in the incorrect domain, especially at the free interface. Some chains with very large volume fractions of one of the blocks may be filtered out with unreacted homopolymer if produced in a real system, but have not been removed here. Regardless, the mechanism of LER and LWR increase is clearly different in these cases than in the lower PDI cases and in the constant volume fraction cases. Such materials would likely present many difficulties before LER and LWR became an issue. The measured LER and LWR was significantly higher than all other simulations, mostly due to significant blurring of the image by the beads in the wrong domain.

The new results for PDI = 1.05 and 1.10 are plotted in Figure 5.15 alongside the data obtained from the distributions that maintained a 50-50 proportion of A and B. The data is plotted twice: once using the actually PDI of the system (labeled System PDI), and once using the PDI of the blocks before the two blocks were connected to for BCPs (labeled Block PDI),. When plotted using the system PDI, there is a clear shift away from the data obtained using the fixed volume fraction polymers, in both LER and LWR, and in A-A LER. However, when plotted by block PDI, the data aligns very well with the previously found results using a fixed volume fraction, for which the system PDI and the block PDI are identical. This suggests that the important dispersity when considering line roughness is not the overall system PDI, but the block PDI. This implies that the volume fraction of an individual chain does not matter, so long as the volume fraction of that chain is not so large or small that effects as seen in Figure 5.14 occur, and that the volume fraction of the whole system is constant.

In these simulations, the A and B blocks were always identical, both in energetics and in PDI. Real systems of course are not so symmetric. When one block has a different PDI than the other block, then the effect on LER on either side of the line would be different. How this translates into overall LER is a question deserving of further study, but presumably the appropriate PDI to use would be somewhere in between the block and system PDI. These asymmetries may have an effect on correlation and therefore on LWR.

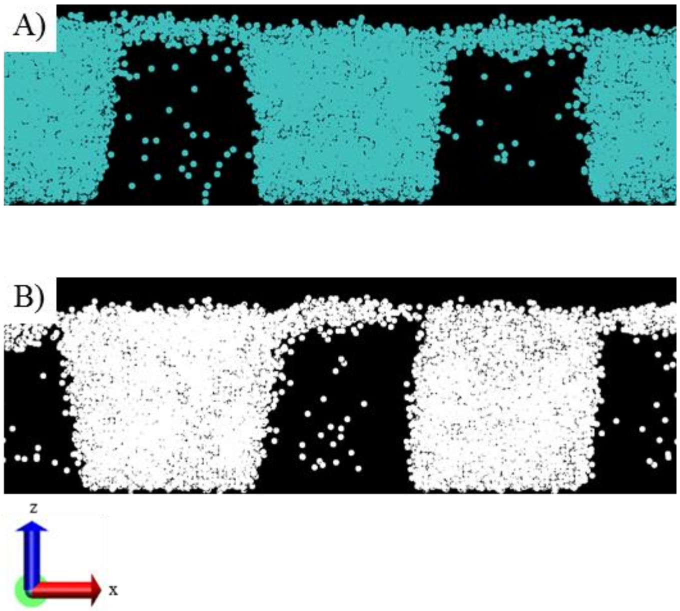

Figure 5.14. Images of a BCP with block PDI = 2.26 and a system PDI = 1.53, showing A) A beads and B) B beads. The large numbers of very

small chains and chains who volume fractions are extremely small or large results in a large number of beads in the wrong domain and in a wetting layer of short chains.

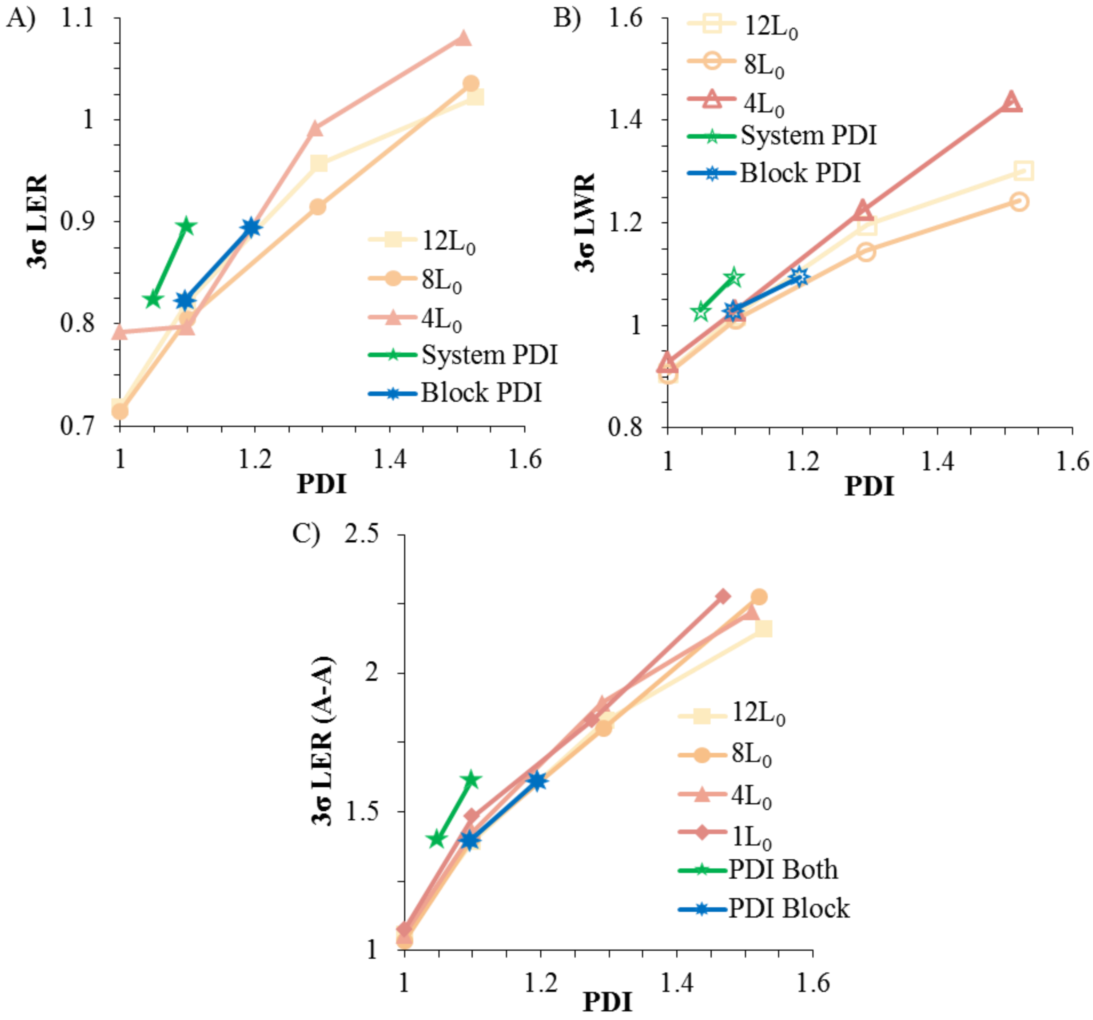

Figure 5.15. LER (A) , LWR (B) , and A-A LER (C) including results from simulations that have variations in volume fraction for each chain. The green 5 point stars plot the data using the PDI of the entire chain. The blue 8 point stars plot that data using the PDI of the blocks only. PDI calculated either way for the simulations whose chains are all at a volume fraction of 0.5 is equal. Using the PDI of the blocks only, the roughness of the simulations that allow volume fractions to vary on each chain matches the roughness of the simulations where chains are all 50% A.

5.4. Conclusions

A coarse grained molecular dynamics model was used to study the effect of block copolymer polydispersity on lamellae pitch, lamellae edge roughness, and local chain effects. LER and LWR in block copolymer DSA patterns both increase approximately linearly with PDI, increasing about 45% of the monodisperse LER or LWR at a PDI of 1.5. it was found that the A-A and B-B interfacial roughness increased significantly with increased PDI. Three mechanisms of compensation for the increase in A-A roughness were considered: an increase in A-B interfacial roughness, correlation in position of long and short chains, and deformation of chain lengths. It was found that long and short chains showed no correlation, and that long chains were significantly deformed. The increase in LWR was explained by the increase in LER modified by the correlation between adjacent line edges. On the guiding layers used here, the correlation between line edges decreased rapidly after adjacent line edges. Unaligned systems showed local swelling an pinching as a function of local chain length, but the aligned systems showed no such correlation between line width and local chain length. Systems were run where volume fraction was allowed to vary on each chain. At low PDI (system PDI< 1.25), it was the PDI of the individual blocks, not the overall system PDI, that determined LER and LWR.

5.5. References

1 Bencher, C.; Smith, J.; Miao, L.; Cai, C.; Chen, Y.; Cheng, J. Y.; Sanders, D. P.; Tjio, M.; Truong, H. D.; Hinsberg, S. H. a. W. D. Self-Assembly Patterning for sub-15nm Half-Pitch: A Transition from Lab to Fab. Proc. SPIE 2011, 7970.

2 Cheng, J. Y.; Rettner, C. T.; Sanders, D. P.; Kim, H.-C.; Hinsberg, W. D. Dense Self-Assembly on Sparse Chemical Patterns: Rectifying and Multiplying Lithographic Patterns Using Block Copolymers. Adv. Mater. 2008, 20, 3155-3158.

3 Kim, H.-C.; Hinsberg, W. Surface patterns from block copolymer self-assembly. J. Vac. Sci. Technol. A 2008, 26 (6), 1369-1382.

4 Detcheverry, F. A.; Nealey, P. F.; de Pablo, J. J.; Pike, D. Q.; Nagpal, U. Theoretically informed coarse grain simulations of block copolymer melts: method and applications.

5 Lynd, N. A.; Hillmyer, M. A. Effects of Polydispersity on the Order-Disorder Transition in Block Copolymer Melts. Macromolecules 2007, 40, 8050-8055.

6 Sides, S. W.; Fredrickson, G. H. Continuous polydispersity in a self-consistent field theory for diblock copolymers. J. Chem. Phys. 2004, 121 (10), 4974.

7 Pandav, G.; Ganesan, V. Fluctuation effects on the order-disorder transition in polydisperse copolymer melts. J. Chem. Phys 2013, 139 (21).

8 Weinheimer, C. J.; Shykind, D.; Fredrickson, G. H. Directed Self-assembly of Laterally Confined Lamellae-forming Diblock Copolymers: Polydispersity and Substrate Interaction Effects. Proc. SPIE 2012, Alternative Lithographic Technologies IV (83231N).

9 Lawson, R. A.; Peters, A.; Ludovice, P.; Henderson, C. L. Coarse grained molecular dynamics model of block copolymer directed self-assembly. Proc. SPIE 2013, Alternative Lithographic Technologies V.

10 Dethcheverry, F. A.; Liu, G.; Nealy, P. F.; Pablo, J. J. d. Interpolation in the Directed Assembly of Block Copolymers on Nanopatterned Substrates: Simulation and Experiments. Macromolecules 2010, 43, 3446-3454.

11 Chuang, Y.-M.; Jack, K. S.; Cheng, H.-H.; Whittaker, A. K.; Blakely, I. Using Directed Self Assembly of Block Copolymer Nanostructures to Modulate Nanoscale Surface Roughness: Towards a Novel Lithographic Process. Advanced Functional Materials 2013, 23, 173-183.

12 Peters, A.; Lawson, R.; Ludovice, P.; Henderson, C. Effects of block copolymer polydispersity and χN on pattern line edge roughness and line width roughness from directe self-assembly of diblock copolymers. Proceedings of SPIE 2013, Alternative Lithographic Technologies V.

13 Daoulas, K. C.; Muller, M. Directed Copolymer Assembly on Chemical Substrate Patterns: A Phenomenolofical and Single-Chain-inMean-Field Simulations Study of the Influence of Roughless in the Substrate Pattern. Langmuir 2008, 24, 1284-1295.

14 Stoykovich, M. P.; Daolos, K. C.; Muller, M.; Kang, H.; Pablo, J. J. d.; Nealey, P. F. Remediation of Line Edge Roughness Chemical Nanopatterns by the Directed Assembly of Overyling Block Copolymer Films. Macromolecules 2010, 43, 2334-2342.

15 Patrone, P. N.; Gallatin, G. M. Macromolecules 2012, 45, 9507-9516.

16 Patrone, P. N.; Gallatin, G. M. Modeling line-edge roughness in lamellar block copolymer systems. Proc. SPIE 8323 2012, Alternative Lithographic Technologies IV, 83232Q.

17 Peters, A. J.; Lawson, R. A.; Ludovice, P. J.; Henderson, C. L. Detailed Molecular Dynamics Studies of Block Copolymer Directed Self-Assembly: Effect of Guiding Layer Properties. J. Vac. Sci.Technol. B 2013, 31, 06F302.

18 Lawson, R. A.; Peters, A. J.; Nation, B. D.; Ludovice, P. J.; Henderson, C. L. Simulation study of the effect of differences in block energy and density on the self-assembly of block copolymers. J. Micro-Nanolith. Mem. 2014, 13 (3), 031308.

19 Lawson, R.; Ludovice, P.; Henderson, C. Development of realistic potentials for the simulation of directed self-assembly of PS-PMMA di-block copolymers. Proc. SPIE 2011, 7970.

20 Bates, F.; Rosedale, J. H.; Fredrickson, G. H. Fluctuation effects in a symmetric diblock copolymer near the order-disorder transition. Journal of Chemical Physics 1990, 92, 6255.

21 (HOOMD), Highly Optimized Object-oriented Many-particle Dynamics -- Blue Edition http://codeblue.umich.edu/hoomd-blue.

22 Anderson, J. A.; Lorenz, C. D.; Travesset, A. General purpose molecular dynamics simulations fully implemented on graphics processing units. Journal of Computational Physics 2008, 227 (10), 5342-5359.

23 Humphrey, W.; Dalke, A.; Schulten, K. VMD - Visual Molecular Dynamics. J. Mole. Graphics 1996, 14, 33.

24 Rodriguez, F.; Cohen, C.; Ober, C. K.; Archer, L. A. Principles of Polymer Systems 5th Edition; Taylor and Francis: New York, NY, 2003.

25 Lynd, N. A.; Hillmyer, M. A. Influence of polydispersity on the self-assembly of diblock copolymers. Macromolecules 2005, 38, 8803.

26 Lynd, N. A.; Meuler, A. J.; Hillmyer, M. A. Polydispersity and block copolymer self-assembly. Progress in Polymer Science 2008, 33, 875-893.

27 Matsushita, Y.; Noro, A.; Linuma, M.; Suzuki, J.; Ohtani, H.; Takano, A. Macromolecules 2003, 36, 8074-8077.

28 Shull, K.; Kramer, E. Mean-Field Theory of Polymer Interfaces in the Presence of Block Copolymers. Macromolecules 1990, 23, 4769-4779.

29 Lawson, R. A.; Peters, A. J.; Ludovice, P. J.; Henderson, C. L. Tuning domain size of block copolymers for directed self assembly using polymer blending: molecular dynamics simulation studies. Proc. SPIE 8680 2013, Alternative Lithographic Technologies V, 86801Z.

30 Kim, H.-W.; Lee, J.-Y.; Shin, J.; Woo, S.-G.; Cho, H.-K.; Moon, J.-T. Experimental Investigation of the Impact of LWR on Sub-100-nm Device Performance. IEEE TRANSACTIONS ON ELECTRON DEVICES 2004, 51 (12), 1984.

31 Nikitin, A.; Sicignano, A.; Yeremin, D.; Sandy, M.; Goldburt, T. Critical Issues in Quantifying Line Edge Roughness. Proc. SPIE 2005, 5752, 1098.

32 Stoykavich, M. P.; Muller, M.; Kim, S. O.; Solak, H. H.; Edwards, E. W.; de Pablo, J. J.; Nealey, P. F. Directed Assmebly of Block Copolymer Blends into Nanregular Device-Oriented Structures. Science 2005, 308, 1442.

33 Pressly, E.; Amir, R. J.; Hawker, C. J., Rapid synthesis of Block and Cyclic Copolymers via Click Chemistry in the Presence of Copper Nanoparticles. Journal o Polymer Science Part A 2011, 49, 814-819.

CHAPTER 6

EFFECT OF χ AND N ON LINE ROUGHNESS

The effect of χN on the block domain interfacial roughness and block domain width variation for lamellae forming BCP systems in thin film form was studied using molecular dynamics simulations. This roughness was quantified in particular for the case of lamellae oriented perpendicular to a substrate surface in which directed self-assembly methods are used to provide long-range order in the system. The domain interfacial roughness was characterized in terms of line edge roughness (LER) at the A-B lamellar domain interface as defined by bead density mapping. The block domain width variation was characterized in terms of a line width roughness (LWR) of the A and B domains again as defined by bead density mapping of the aligned BCP films. These two parameters were chosen and quantified since they are particularly important for the potential application of block copolymer directed self-assembly in semiconductor manufacturing as an enhancement to current optical lithography techniques. LER and LWR behavior at low χN values received particular attention in this work because of the lack of prior studies in this area. Previously, the behavior of LER and LWR at high χN values has been probed using analytical techniques based on mean-field Leibler, Ohta, and Kawasaki (LOK) models, but these models use assumptions that limit their accuracy in the low χN regime. Using a coarse grained molecular dynamics model, this low χN region was explored. A sharp increase in LER and LWR in aligned BCP patterns is found for low χN values. A model proposed by Semenov gives similar behavior, but other models under estimate at low χN though good agreement is found at high χN values.

Using guiding stripes with programmed roughness instead of idealized straight guiding stripes does not change the dependence of BCP LER and LWR on χN.

6.1. Introduction

Self-assembly of block copolymers (BCPs) has received significant attention in recent years in the field of semiconductor manufacturing with the hope that such block copolymers could augment existing lithographic technology to help decrease feature size.[1] Directed self-assembly (DSA) uses the natural micro-phase separation properties of BCPs, with the help of a guiding layer, to produce the long range order required for electronic device fabrication.[1,2,3] It is enthalpically favorable for each block in the BCP to maximize its interaction with like blocks. This would cause homopolymers to bulk phase separate, but because each block is bonded to an unlike block, the size of micro-phases are limited to the nanometer length scale. Two particular microphases of BCPs are of interest in such semiconductor patterning applications, namely lamellar morphologies and cylindrical morphologies. This work focuses in particular on lamellar forming BCP systems which enable the production of line-space type patterns that are pervasive in semiconductor manufacturing. Neglecting outside factors, diblock copolymers that contain roughly equal volumes of each block will form lamellae.[2] When coated on a sufficiently neutral underlayer, the BCP will form a short range ordered “fingerprint” pattern that is still disordered over length scales much larger than the block copolymer domain size. However, when a topographical or chemical pattern is created in the underlayer, intermediate and long range order can be induced.[3] Such ordered BCP films can be used to shrink the smallest feature dimension that can be achieved using direct optical lithography methods via pitch division.[1] The two common ways in which BCPs are guided are graphoepitaxy, where the polymers are guided via topographic patterns, and chemoepitaxy, where the polymers are guided via chemical patterns on ideal flat surfaces.[3,4,5] One common scheme by which BCP are chemically guided is the use of a small line that interacts preferentially with one of the blocks, that is adjacent to a much wider neutral line.[1] The strongly interacting line (here called the pinning line) is the pattern to which the BCP aligns. The BCP lamellae will naturally align to each other, propagating the original pattern over the neutral stripe.

Regardless of the processes, the BCP lamellae will have some inherent deviations from ideally straight lines. In the semiconductor manufacturing field, variations from a straight line edge, known as line edge roughness (LER), and variations away from a uniform line width, known as line width roughness (LWR), are important to device performance.[6,7,8] They will negatively affect transistor performance by creating variations in transistor speed, as well as current leakage and threshold voltage.[6,7,8] The degree to which the copolymer blocks will phase separate is typically described by the product of the total polymer degree of polymerization (N) and the enthalpic interaction parameter (χ) from Flory-Huggins polymer lattice theory for the particular block copolymer of interest. According to mean field theory,[2] the order-disorder transition for BCPs occurs at $\chi N = 10.5$ (or slightly above this when fluctuations corrections are considered), so the drive to phase separate is considered high when $\chi N >> 10.5$. To date, most models have focused on the strong segregation regime (SSR), where the drive to phase separate (as described by the product of χ and N) is high.[9-16] When this condition is met, models have had success describing LER, but when χN approaches 10.5, less is known about how BCPs will respond. This is an important issue since it advantageous to use lower N values for a given block copolymer since a shorter polymer chain leads directly to smaller domain sizes and ultimately smaller feature sizes. Thus for any block copolymer, there will always be an interest in extending the use of such a polymer to as small a value of χN as is possible. This paper presents results for the first time using detailed molecular dynamics simulations that show the LER and LWR behavior that is expected in block copolymer DSA when χN is not in the SSR.

6.2. Modeling

6.2.1. Coarse-Grained Model

This work has used a coarse grained molecular dynamics model described elsewhere.[17-19] In brief, the polymers are modeled by representing four monomers as a single bead. Four monomers were chosen because it corresponds approximately to the statistical segment length for polystyrene and poly(methyl methacrylate), two types of polymers commonly used in BCP-DSA. Grouping a different number of monomers into one bead would approximate a different statistical segment length, and change the flexibility of the chain. These beads experience three different potentials, a non-bonded potential (similar to a Lennard-Jones potential, but made softer and broader by using an 8-4 potential function), a harmonic segment potential (corresponding to stretching or compressing the BCP), and a harmonic angle potential (corresponding to bending the BCP). The non-bonded potential uses the form

$$E(r) = \varepsilon_{ij}\left[\left(\frac{\sigma_{ij}}{r}\right)^{8} - 2\left(\frac{\sigma_{ij}}{r}\right)^{4}\right] \qquad 6.1$$

where ε_{ij} refers to the strength of the interaction between beads of type *i* and *j*, σ_{ij} refers to the equilibrium distance (that is, the minimum of the potential), and r refers to the distance between the two interacting particles. All beads experience this potential as long as they do not also participate in a bond or angle potential together (i.e. 1-2, and 1-3 bonded interactions are not subject to this non-bonded potential). Two bead types were used, referred to here as type A and type B, representing two different arbitrary monomer types. The potential function parameters for these two bead types were set to reproduce polymer properties similar to typical BCP polymers such as polystyrene and poly(methyl methacrylate), with a χ value (i.e. the common Flory-Huggins parameter) used as a measure of driving force for micro-phase separation that can easily be changed by modifying the potential function parameters. The details of the block copolymer model and the method used to relate the potential function parameters to a χ value are found elsewhere.[17] The same potential values that were used elsewhere were used here.[20] For the harmonic segment potential, the spring constant (k_{str}) used was 100 kcal/(mol nm^2) and the equilibrium length used was 0.82 nm. For angle potential, the spring constant (k_{ang}) used was 5 kcal/(mol nm^2) and the equilibrium angle used was 120°. For the non-bonded potential, ε_{AA} and ε_{BB} were both set at 0.5 kcal/mol and ε_{AB} was varied to change χN, as described in Chapter 2. All σ values (σ_{AA}, σ_{BB} and σ_{AB}) were set at 1.26 nm. Polymers composed of 144, 120, 96 and 64 monomers were used. Each polymer was composed of two blocks of equal length, one composed of A beads and one composed of B beads.

All simulations were performed in a thin film state in the same manner as described elsewhere.[20] A polymer film 15 nm thick is placed on top of a patterned polymer brush underlayer. The simulation is periodic in the *x* and *y* dimensions, but not in the *z* dimension so as to allow a thin film configuration. These simulations are four BCP domains wide and at least 200 nm long, far longer than the 100 nm necessary to get accurate roughness measurements, as shown in Figure 6.1, and wide enough that with this underlayer, the periodic boundary has a small effect on roughness measurements[21]. The dense guiding layer used here is likely a lower estimate of the true LER and LWR in a BCP system, since real processes require a wider, more neutral stripe provides little guidance. The BCP film was built initially aligned; beads were built at the correct bond lengths and angles and with A beads above the A guiding stripe, and B beads above the B guiding stripe. The underlayer was then placed beneath this film. All initial chain building was done in Molecular Operating Environment (MOE) followed by an energy minimization step in MOE[22] and in HOOMD-Blue[23,24]. Subsequently, molecular dynamics was performed on these simulation volumes using HOOMD-Blue.

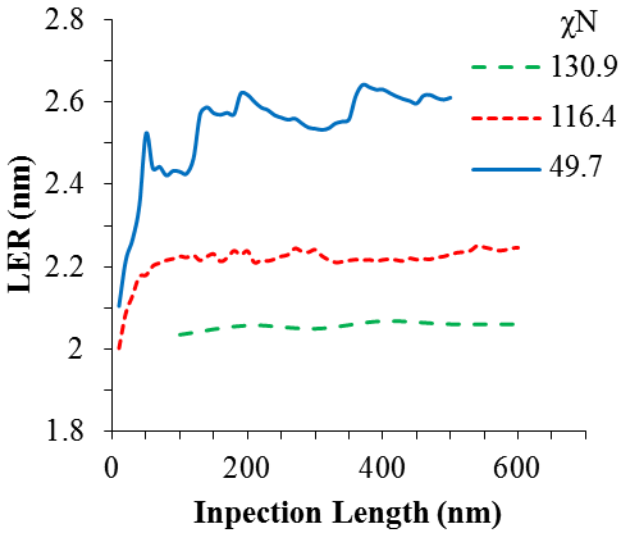

Figure 6.1 LER as a function of inspection length. Above ~ 100 nm, LER becomes inspection length independent.

The underlayer pattern is composed of alternating lines of A and B beads each half the width of the natural periodicity of the polymer. Each line is built straight so that the measured roughness is due to the natural polymer roughness and not the underlayer. However, as it has been demonstrated elsewhere, the BCPs are not strongly affected by underlayer pattern roughness.[5,20]

6.2.2. Measurement of line edge roughness (LER) and line width roughness (LWR)

To measure the roughness through the thickness of the film, the beads of one type (e.g. A beads) were binned based on their positions. A square lattice was used for *x* and *y* (i.e. a surface lying in the same plane as the thin film), to make a map of the number density of beads. In the z direction, a 3.5 nm binning depth was used. Details can be found in the supporting information section. The bead density histograms were then used to define line edges by choosing a particular bead density as a cutoff. This threshold cutoff in bead density was selected as to minimize the roughness and match the line edge as inspected visually. A threshold cutoff of approximately 35% of the highest bead number density was deemed optimal in most cases.

To measure the roughness through the thickness of the film, the beads of one type (e.g. A beads) were binned based on their positions. A square lattice was used for x and y (i.e. a surface lying in the same plane as the thin film), to make a map of the number density of beads. In the z direction, a 3.5 nm binning depth was used. Using different binning depths has an effect on measured LER and LWR because averaging over a greater number of beads smooths out roughness. Figure 6.2 shows the same state using different binning depths, and Figure 6.3A shows LER measurements at various binning depths. LER measurements were not taken for a binning depth of 1 nm because some of the lines are not continuous at some points, which makes it impossible to define a line edge or width at that point. Even though all the images are of the same state, and each is centered in the BCP film, merely by averaging over more beads, the roughness clearly decreases. To isolate this effect, all simulations used a binning depth of 3.5 nm. This was done to be consistent with our previous work which also used a 3.5 nm binning depth to look at roughness through the depth of the film. It is important to point out that even though the roughness values will change based upon the binning depth, when these values are normalized, they collapse onto the same curve, so the overall curvature is the same regardless of binning depth. This is shown in Figure 6.3B.

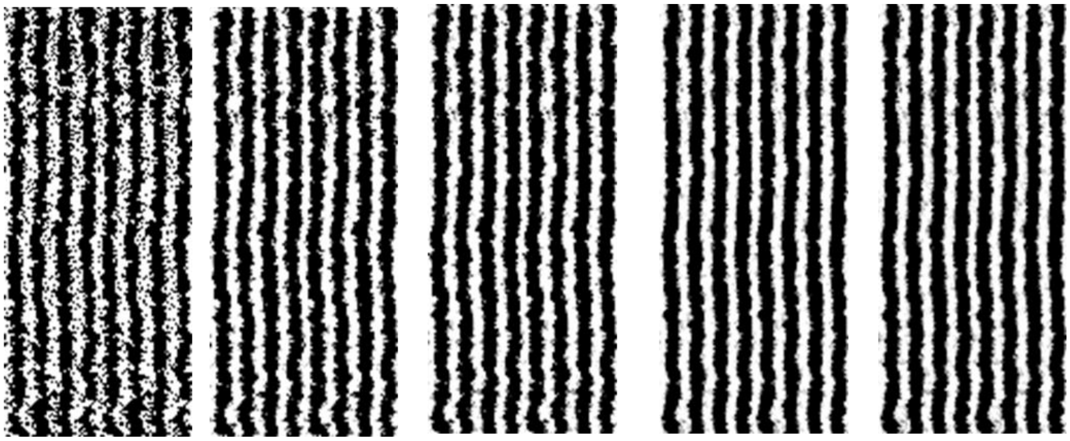

1 nm 3.5 nm 5 nm 10 nm 15 nm

Figure 6.2 Images of bead density histograms at various binning depths. All images show the same simulation at the same time step. $N = 96$ $\chi N = 20$. All bins are centered in the z dimension of the film.

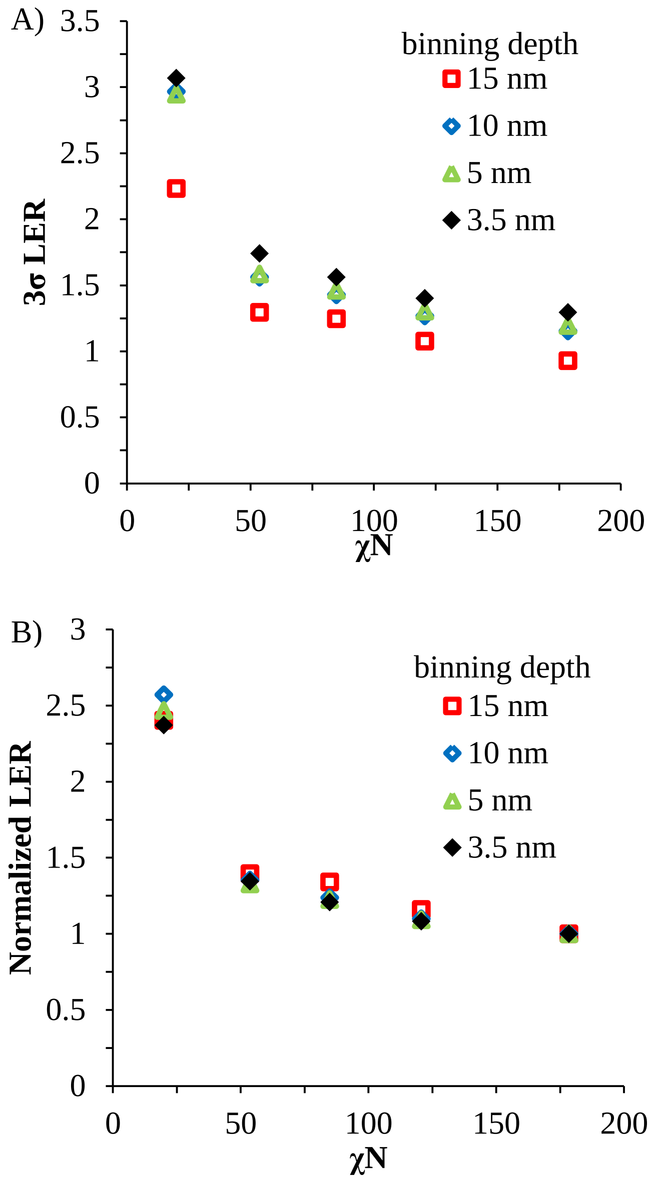

Figure 6.3 LER and normalized LER as a function of χN at various binning depths for *N* = 96. (a) 3σ LER. Increasing the binning depth decreases the measured roughness because of the smoothing due to the averaging through depth that occurs. (b) LER is normalized by LER at χN ~180. Though a different binning depth shifts the measured roughness, it does not change the sharp increase at low χN.

6.3. Results and Discussion

6.3.1. Effect of χN on LER and LWR

A polymer system was simulated at various χ values by changing the ε_{AB} value. The system was simulated on a 1:1 patterned brush with lines of A and B where the underlayer line widths were equivalent to half the BCP domain. Polymers containing 120 monomers were used. For χN of 22, the domain size is 12.5 nanometers, for a χN of 70, the domain is 16.7 nanometers, and for a χN of 286, the domain is 20.8 nanometers. This scenario limits the source of roughness to the BCP itself, and not the pattern, a very difficult task to do experimentally at small pitches. By varying χ via the parameter ε_{AB} and measuring the LER and LWR of the line, we find that LER and LWR are weakly dependent on χN above a χN of ~100, but strongly dependent below χN~100 as seen in Figure 6.4. At the lowest χN value of 20, the roughness is actually greater than half the width of a line. The image of this simulation along with a higher χN simulation for comparison is shown in Figure 6.5. This sharp increase as χN drops may prohibit use of BCPs at low χN values to achieve small patterned feature sizes using this technology. The International Technology Roadmap for Semiconductors[25] (ITRS) specifies a 3σ LWR limit of 0.8 nm for a half pitch of 10 nm. Even with great improvements in etching or other methods of line smoothing,[26] such methods likely cannot heal such roughness sufficiently. The model polymer studied here is not inherently able to achieve that specification even in the SSR ($\chi N > 100$). However, the lowest LER measurments appear to be approaching the noise limit of our techniques so that the measurments at very high χ may be artifically high, though the effect does not look to be very great. Etch and post-processing smoothing techniques have not been considered and may help achieve the ITRS specification, and. Other changes, such as smaller segmental lengths (more flexible polymers) may also help achieve smaller domain sizes and smaller roughness values. It is also possible that using a much larger χ (the maximum χ used here is 2.38) and a smaller N would produce lower roughnesses because of the larger interfacial penalty due to the high χ, without dramatically increasing χN. Patrone and Gallatin[13] suggest that a χ value perhaps as high as five is necessary to meet specifications.

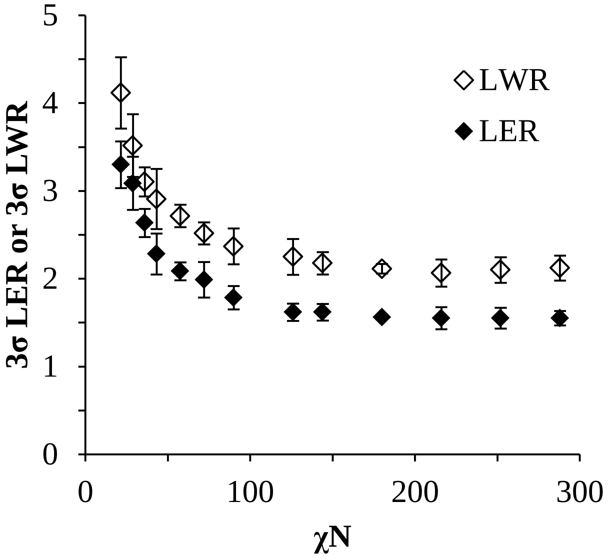

Figure 6.4 LER and LWR as a function of χN. There is a sharp increase in roughness as χN approaches the ODT.

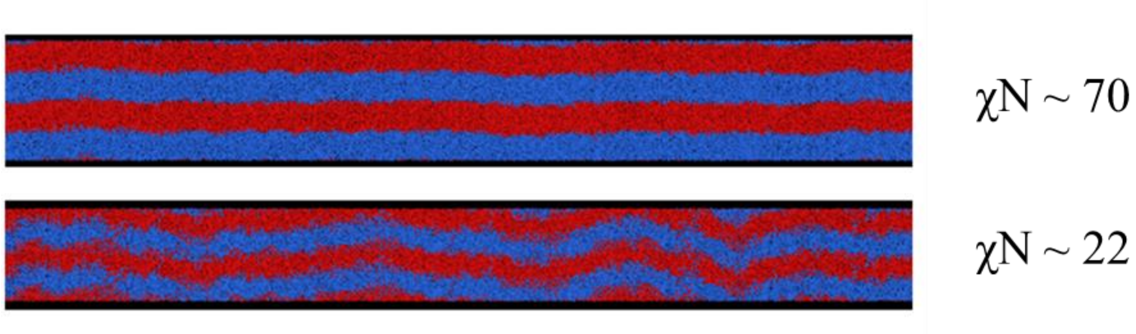

Figure 6.5 Top down images of lines at a fairly high χN and at a low χN. The low χN system shows large deviations in the location of the line edges.

The same simulation was run with chains composed of 144, 96 and 64 monomers. As seen in Figure 6.6A, polymer systems with smaller N have a slightly lower roughness than polymers with large N, though all chains lengths show a similar overall dependence on χN. When this data is plotted as a function of χ (Figure 6.6B) instead of χN, the data approximately collapses to a single curve. This may indicate that the roughness is probably primarily due to interfacial width, as interfacial width is determined more by χ than by N or χN.

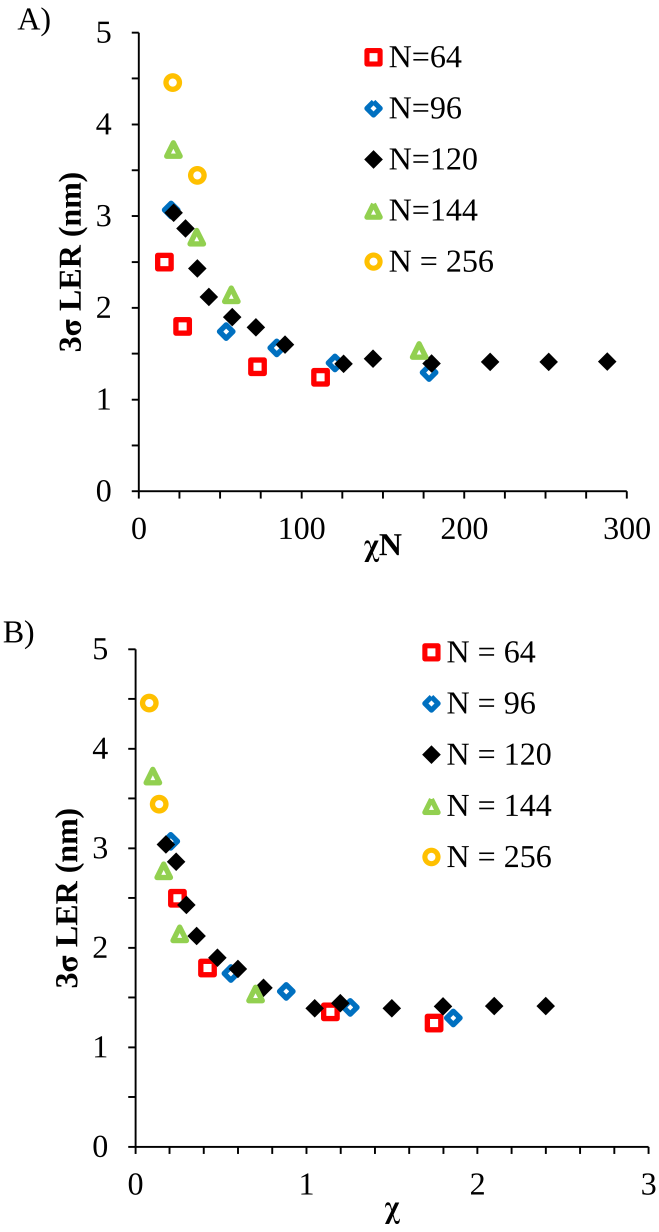

Figure 6.6 A) LER as a function of χN for various N. All N show a sharp decrease as χN approaches the ODT. Smaller N yield slightly smaller roughnesses. B) LER is plotted as a function of χ. This collapses the data to a single curve.

6.3.2. Effect of χN on LER with sinusoidal guiding patterns

The effect of sinusoidal guiding layers was studied elsewhere, however, the effect of changing χ was not tested.[20] It is conceivable that low χN systems would be less strongly tied to the guiding pattern, and so the waves produced by the underlayer could damp out more quickly. Conversely, it is also conceivable that high χ systems may cause the waves introduced in the system to damp out more quickly because the of energy penalty for increased interfacial area between dissimilar blocks. As shown previously, sine wave guiding stripes only caused roughness increases for guiding patterns with relatively high amplitudes (~35% of the line width) and large wavelengths (~double the pitch). For smaller amplitudes or wavelengths, no persistent roughness increase was observed. In this work, two different sinusoidal guiding patterns were studied at various χN for comparison: a larger the amplitude (3.5 nm) and wavelength (40 nm) worst case from the earlier study[20] and a weaker sinusoidal guiding pattern at half the amplitude (1.75 nm) and wavelength (20 nm). The simulations were four domains wide and 160 nm long and were built in the same manner as the straight lines in this work. If the amplitude of the sine wave is high enough, then it will increase roughness at all χN values, but small amplitudes do not increase roughness, as seen in Figure 6.7A. However the sine wave strength does not change the relative effect of χN on LER. Normalizing the data to high χN gives the results seen in Figure 6.7B.

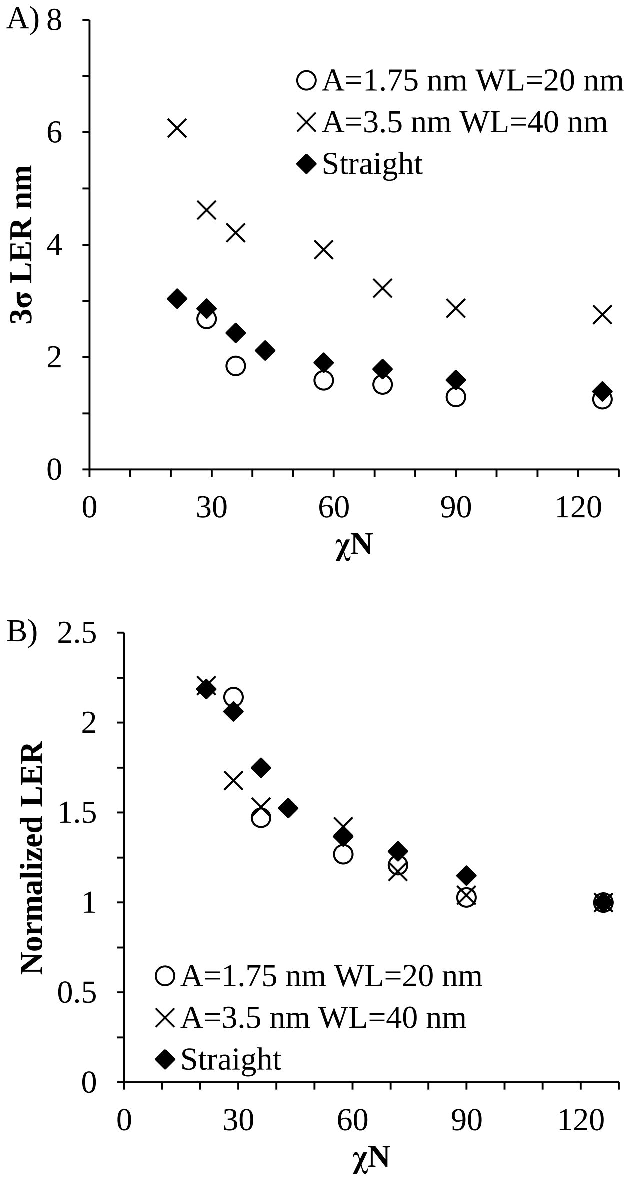

Figure 6.7 A) 3σ LER for sine wave guiding stripes and straight guiding stripes. A corresponds to the amplitude of the sine wave guiding function, and WL corresponds to the wavelength of that same function. B) LER normalized to value at χN = 125 for sine wave guiding stripes and straight guiding stripes. When A=3.5nm and WL=40 nm, there is a persistent increase in the roughness through the film. However, this effect is proportionally the same for all χN, as can be seen when the data is normalized.

6.3.3. Comparison to other models

Semenov developed a theory that can be used to calculate the roughness of BCP interfaces.[15,16] The roughness is broken down into two frequency regimes: the high frequency regime which corresponds to the interfacial width and individual chain variations, and the low frequency regime which corresponds to thermal fluctuations in the polymer. The defined boundary between the two regimes is designated Δ_0. The following equations describe the theory.

$$\Delta_0 = \frac{2a}{\sqrt{6\chi}} \qquad 6.2$$

$$\gamma_0 = \frac{a}{v}\sqrt{\frac{\chi}{6}} \qquad 6.3$$

$$\Delta = \Delta_0\left[1 + \frac{1.34}{(\chi N)^{1/3}}\right] \ (high\ frequency\ roughness) \qquad 6.4$$

$$\langle \delta^2 \rangle = \frac{1}{2\pi\gamma_0} ln\left(\frac{d}{\Delta_0}\right) \ (low\ frequency\ roughness) \qquad 6.5$$

$$\Delta_{Total} = \sqrt{\Delta^2 + 2\pi\langle \delta^2 \rangle} \qquad 6.6$$

a is the statistical segment length, v is the monomer volume, γ_0 is the interfacial tension, Δ is the high frequency roughness (measured from 0 to Δ_0) and δ is the low frequency roughness (measured above Δ_0). It is instructive to compare the simulation results generated here to this theory. In order to analyze the simulation data in this fashion, it was necessary to calculate *a* and *v* for the polymer potential used in this work. In a lattice model, *a* is simply the lattice spacing, but the simulations discussed here do not have a lattice, so an effective *a* must be determined. Shull predicted the pitch of BCPs as a function of χ, *N*, and *a* for all ranges of χ.[27] By assuming this model, and that *a* is constant, we can fit an effective *a* for our model. In this work it was found that an *a* of 7.61 Å fits best, so this *a* was used to compare our data. *v* must also be defined for the simulation results. Since *v* is not easily ascertained, the *v* found for polystyrene of 0.17 nm^3 is used. Though this is not completely accurate for this simulation model, only an estimate is necessary for comparison here.

Because the simulation model used in this work combines 4 monomers into a single bead, the very highest frequency LER and LWR is not captured using such a model. This makes it difficult to account for only a portion of the high frequency LER. So, only the low frequency regime of Semenov's theory was considered when comparing the model and simulations. Fortunately, the long wavelength, low frequency roughness is much more important for device performance. In order to fairly compare with Semanov's low frequency regime, we needed to eliminate the high frequency contribution to total LER in our simulation. This was done by resizing the minimum pixel size in the image to match Semanov's cutoff for high frequency. This removes all roughness at wavelengths smaller than the pixel size, i.e. the high frequency roughness. The high/low frequency cutoff changes as a function of χN, so this must be taken into account when analyzing the simulation images. The cutoff as a function of χN from Semenov's work is found in Figure 6.8.

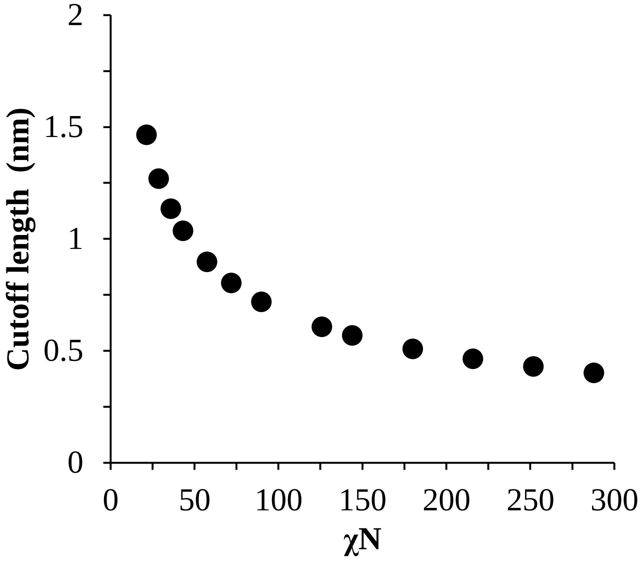

Figure 6.8 Cutoff between high and low frequency regime from Semenov's theory.

When compared with Semenov theory in Figure 6.9 the agreement between the theory and simulation results are good when χN is high, but they deviate sharply from one another when χN approaches 10.5. Semenov's model was not intended for use in the low χN region, and as one can see, does not capture the increase in roughness at low χN. The cause for the difference is likely an underestimation of the cutoff length, which is the interfacial thickness. SCFT calculations of interfacial roughness match Semenov's theory (SST) at high χN, but deviate significantly at low χN. This means that the degree to which high frequency roughness plays a role is under estimated in Semenov's theory, as is the necessary cutoff length. Assuming that no high frequency roughness is measured is almost certainly untrue as can be seen in Figure 6.2. This is probably because Semenov severely underestimates the length scale of interfacial roughness at low χN (Figure 2.20). Incorporating this interfacial increase may result in a significantly better match between models.

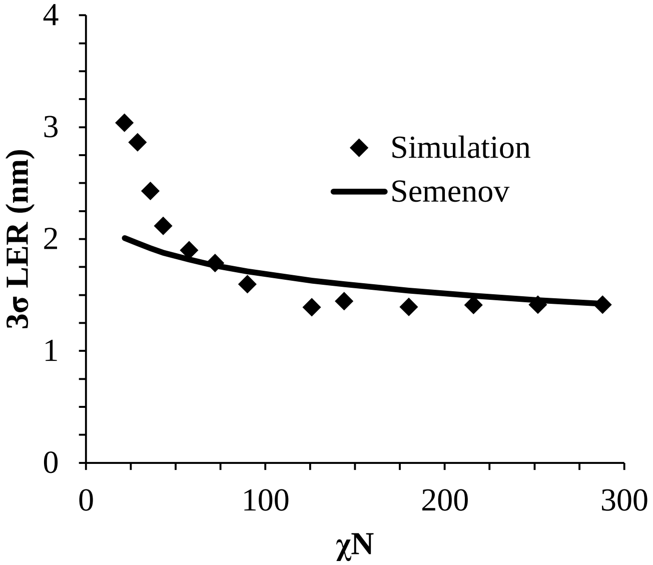

Figure 6.9 Simulation LER data plotted Semenov low frequency roughness theory results at a depth of 7.5 nm, the middle of the film. For relatively high χN (>60) there is good agreement between our results and Semenov with a gentle increase in LER. However, when χN is small, our simulation predicts a much higher LER.

Patrone and Gallatin also more recently developed a method of calculating LER using the Leibler, Ohta, and Kawasaki (LOK) model.[13] It is an analytical model that models roughness in the SSR and uses a perturbative approach to give explicit expressions for interface tension, as well as a stretching energy associated with the deformation of a polymer at an interface. Using the equations and values given in Patrone and Gallatin, their method can be compared to the method used in this work. Using an h = 15 nm, N = 120 monomers, a = 0.761 nm, n = 1 interface from guiding line, we calculate the results of equation (27) from Patrone and Gallatin and plot them in Figure 6.10. Because this model is not designed to handle the low χN regime, it also does not capture the sharp increase in roughness below *χN*= ~ 100. This model results in better agreement with our model, but it still under estimates at low *χN*.

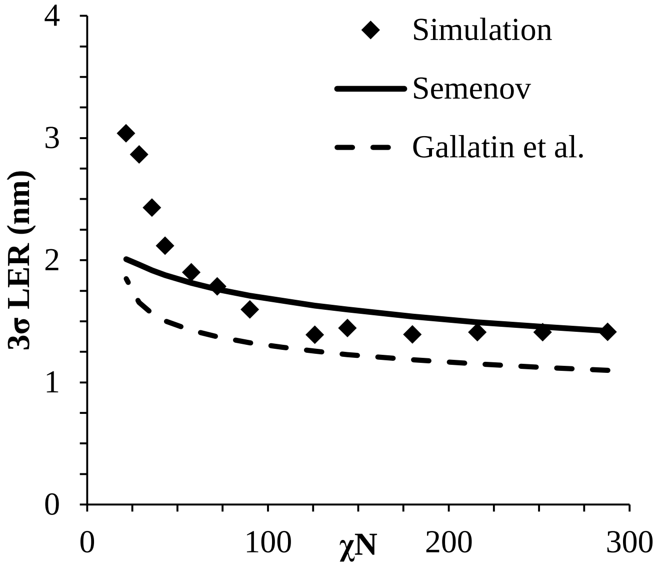

Figure 6.10 Comparison of calculation from Gallatin et al. model and the model used in this work. The Gallatin et al. model does not capture the dependence on *χN* for low *χN*, showing only a very slight increase at low *χN* values.

6.4. Conclusions

The dependence of polymer block domain interfacial roughness and domain size variation, as measured using the LER and LWR from aligned BCP lamellar thin film samples, on the block copolymer *χN* value was studied using a coarse grained molecular dynamics model. It was found that LER and LWR are almost independent of *χN* at large *χN* values greater than approximately 100. Below this value, both LER and LWR increase sharply with decreasing *χN* values. A similar dependence is found even when using non-idealized guiding patterns that contain pre-programmed roughness (e.g.

guiding stripes with sinusoidal width variation). Consequently, when using BCP directed self-assembly to make integrated circuits, copolymer χN values will likely have to be kept well above the ODT if aligned pattern roughness is an important limiting factor. This will limit the minimum feature size achievable using a given block copolymer to values much larger than what might considered possible based on order-disorder transition considerations only. When compared with previously published models, good agreement is found for the dependence of BCP pattern LER at higher χN values, but these other previous models do not capture the increase in roughness at low χN values.

6.5. References

1 Cheng, J. Y.; Rettner, C. T.; Sanders, D. P.; Kim, H. C.; Hinsberg, W. D. Macromolecules 2008, 20, 3155.

2 Bates, F. S.; Fredrickson, G. H.; Phys. Today 1999, 52, 2.

3 Bencher, C.; Smith, J.; Miao, L.; Cai, C.; Chen, Y.; Cheng, J. Y.; Sanders, D. P.; Tjio, M.; Truong, H. D.; Holmes, S.; Hinsberg, W. D. Proc. SPIE 2011, 7970, 79700F.

4 Park, S. M.; Stoykovich, M.; Ruiz, R.; Zhang, Y.; Black, C.; Nealey, P. F. Adv. Mater. 2007, 19, 4.

5 Nealey, P. F.; Raub, A. K.; Hakeem, P. J.; Brueck, S. R. J.; Han, E.; Gopalan P. J. Vac. Sci. Technol. B 2010, 28, 6.

6 Chuang, Y.; Jack, K.; Cheng, H.; Whittaker, A.; Blakey, I. Adv. Func. Mater. 2013, 23, 173.

7 Hyun-Woo, K.; Ji-Young, L.; Shin, J.; Sang-Gyun, W.; Han-Ku, D.; Joo-Tae, M. IEEE T. Electron. Dev. 2004, 51, 1984.

8 Asenov, A.; Kaya, S.; Brown, A. R.; IEEE T. Electron. Dev. 2003, 50, 1254.

9 Bosse, A. W. Macromol. Theory Simul. 2010, 19, 399406.

10 Bosse, A. W. J. Vac. Sci. Technol. B 2011, 29, 06F202.

11 Bosse, A. W. J. Vac Sci. Technol. B 2011, 29, 031803.

12 Bosse, A. W.; Lin, E. K.; Jones, R. L.; Karim, A. Soft Matter 2009, 5, 4266.

13 Patrone, P. N.; Gallatin, G. M. Macromolecules 2012, 45, 9507.

14 Patrone, P. N.; Gallatin, G. M Proc. SPIE 2013, 8680, 86801I.

15 Semenov, A. N. Macromolecules 1993, 26, 6617.

16 Semenov, A. N. Macromolecules 1994, 27, 2732.

17 Lawson, R. A.; Peters, A. J.; Ludovice, P. J.; Henderson, C. L. Proc. SPIE 2013, 8680, 86801Y.

18 Lawson, R. A.; Ludovice, P. J.; Henderson, C. L. Proc SPIE 2011, 7970, 79700N.

19 Peters A. J.; Lawson, R. A.; Ludovice, P. J.; Henderson, C. L. Proc. SPIE 2012, 8323, 83231T.

20 Peters, A. J.; Lawson, R. A.; Ludovice, P. J. Henderson, C. L. J. Vac. Sci. Technol. B 2013, 31, 06F302

21 Chapter 5

22 Molecular Operating Environment (MOE), 2009.10. (Chemical Computing Group Inc., Montreal, QC, Canada, 2009).

23 Anderson, J. A.; Lorenz, C. D.; Travesset, A. J Comput. Phys. 2008, 227, 5342.

24 HOOMD-blue web page: http://codeblue.umich.edu/hoomd-blue

25 The International Technology Roadmap for Semiconductors (ITRS), Lithography, 2012, http://www.itrs.net

26 Chandhok, M.; Frasure, K.; Putna, E. S.; Younkin, T. R.; Rachmady, W.; Shah, U.; Yueh, W. J. Vac. Sci. Technol. B 2008, 26, 2265.

27 Shull, K. R.; Mayes, A. M.; Russell, T. P. Macromolecules 1993, 26, 3929.

CHAPTER 7

FREE ENERGY DIFFERENCE OF PITCH VARIATION AND CALCULATION OF THE ODT USING THERMODYNAMIC INTEGRATION

Thermodynamic integration and the calculations involved in using thermodynamic integration in a coarse-grained molecular dynamics model are explained was used to measure the energy penalty of altering the pitch of polymers with various χN. The minimum free energy occurred at a pitch that corresponded to the calculated natural pitch from scattering calculations. The penalty for pitches lower than the natural pitch was found to scale with χ and the proportional decrease in pitch, indicating a purely enthalpic driving force and resulting in a universal energy penalty curve. The penalty for pitches larger than the natural pitch is entropically driven and requires more complex calculations. The entropic and enthalpic terms must be separated to investigate such behavior. The ODT was also measured in a manner similar to Müller et al.[6] by calculating the free energy in the mixed state and of the demixed state. The intersection of these curves is the ODT. The measured ODT depends on the pitch used in the demixed calculation. If the pitch is too large, then the χN at the ODT will be over estimated. The measurement was taken as a function of pitch and found to approach the expected ODT of 10.5 when smaller pitches were used, thus correcting the work by Müller et al.[6]

7.1. Introduction

Self-consistent field theory (SCFT) has proven useful in calculating the free energy of many different states, but it has its limitations. Specifically, SCFT neglects thermal fluctuations, which are known to be important near phase transition.[1] While SCFT is well suited for equilibrium properties, capturing the dynamic properties of system is more difficult.[2] These factors, along with a drastic increase in available computational power, have led to an increased use of particle based models including both Monte Carlo based models and molecular dynamics (MD) based models.[2-4] In order to study polymers, these models must generally be coarse-grained to mitigate the significant computational requirements due to the required time and lengths present in polymer systems. While particle based methods naturally include fluctuations and are often well suited to studying kinetics pathways, accurate calculations of free energy are more difficult.[2] While SCFT inherently calculates the free energy of the system, particle based models do not automatically calculate the free energy therefore, if such a calculation is desired, the system must be systematically perturbed.. One method to do so in MD models is to use thermodynamic integration.[2-10] In short, the free energy difference between two arbitrary states is calculated by defining a reversible thermodynamic path between those states and integrating over ensemble-averaged enthalpy changes along that defined path. These paths need not be realistic paths and can be defined by imagined potentials or coupling parameters. Two useful examples include the measurement of the order-disorder transition (ODT) in diblock copolymer melts, and the measurement of natural repeat distances in lamellae forming diblock copolymers and these measurements will be demonstrated here. While the ODT can be measured in other ways, a clear picture of the associated free energies of the mixed and demixed state can be useful when considering parameters that may modify the ODT such as PDI, confinement or asymmetry in block interactions. Insight into the exact causes for ODT perturbation caused by the aforementioned parameters could be obtained using thermodynamic integration that could not be achieved with a simple identification of the ODT.

7.2. Thermodynamic Integration

The free energy between two states can be calculated by[5-7]

$$\Delta F_{A\rightarrow B} = \int_{u_A}^{u_B} \left\langle \frac{\delta H}{\delta u} \right\rangle du \qquad 7.1$$

where *u* is any parameter that defines a path that is reversible and continuous between state *A* and state *B*, *H* is the Hamiltonian, and the brackets < > denote a thermodynamic average. The Hamiltonian is composed of the potential energy as described by the interactions between beads (see Chapter 2), the potential energy of external forcefields, and a kinetic term *K*.

$$H = E_{Bond} + E_{Ang} + E_{Non-Bonded} + E_{Ext} + K \qquad 7.2$$

$$K = \sum_{i=1}^{N} \frac{{p_i}^2}{2m_i} \qquad 7.3$$

Here, *p* is the momentum of a bead and *m* is the mass. Equation 7.1 can be used to find the free energy between any two states provided that some reversible and continuous path can be envisioned between the two states. An external potential can be used to take a system from one state to another, or a parameter internal to the model (such as ε_{AB} or σ_{AA} (See chapter 2)) can be varied, but abrupt changes in state must be avoided so that reversibility is maintained. Multiple steps can be taken in succession, with different parameters being varied in each step. Because free energy is a state function, the sum of the free energy differences of each step is equal to the free energy difference between the initial state and the final state, as described by Equation 7.4.

$$\Delta F_{Total} = \sum_{i} \Delta F_i \tag{7.4}$$

This allows multiple parameters to be varied, and more complicated paths between states to be taken. This work strives to demonstrate some uses of thermodynamic integration by finding the free energy difference between various pitches for a given BCP, as well as the effect of pitch on the calculation of the order disorder transition.

7.2.1. Thermodynamic Integration: Pitch Variations

In order to calculate the free energy difference between various pitches, a path between those pitches, or a path from a one common state to the various pitches is required. While it may be possible to envision a continuous, reversible, and direct path from one pitch to another via a change in a set of external potentials, it is much simpler to execute a path from a disordered state to any arbitrary pitch. Then, knowing the difference between every state and a disordered state, the ordered states can be compared to each other. To do this, a three branch path is used.

The overall scheme of this integration is shown in Figure 1. It consists of 3 branches; one where an external potential, which orders the system into lamellae, is slowly turned on, one where χ is slowly increased, and one where the external potential is slowly turned off. The overall free energy is the sum of the free energies of each branch (Equation 7.4). The external potential is described by Equation 7.5 and yields a potential similar in shape to the composition profile of a lamellar BCP, as shown in Figure 7.2.

$$U_{ext} = A * tanh\left(\frac{cos\left(\frac{2\pi x}{L}\right)}{2\pi w}\right) \qquad 7.5$$

A is the strength of the potential, *x* is the position in the x dimension, *L* is the pitch, and *w* is the width of the interface relative to the pitch. *w* was chosen by fitting the potential to a compositional profile of spontaneously formed lamellae.

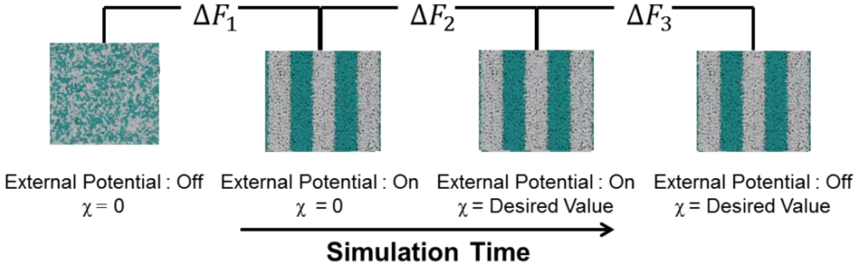
ΔF_1
ΔF_2
ΔF_3
External Potential : Off
χ = 0
External Potential : On
χ = 0
External Potential : On
χ = Desired Value
External Potential : Off
χ = Desired Value
Simulation Time

Figure 7.1. Schematic of the 3 branch method for calculating the free energy between the mixed state and demixed state. The first branch increases the external potential and phase separates the system. The second branch increases χ. Little morphological change occurs during this branch. The third branch removes the external potential and achieves the final state. Each branch is reversible and so the free energy can be calculated over each of them. The total free energy difference is the sum of the free energy differences of each branch.

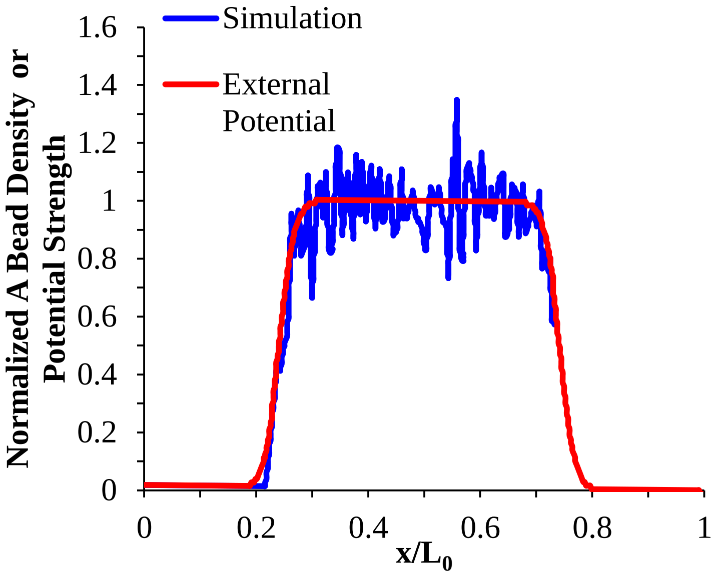

Figure 7.2. Compositional profile of simulation results and the external potential.

In branch 1, the parameter *A* in Equation 7.5 is the parameter over which the system is integrated in equation 1. Since the Hamiltonian consists of the potential and kinetic energy, $<\delta H/\delta A>$ is equal to $<\delta U_{ext}/\delta A>$ which is Equation 7.6.

$$\left\langle \frac{\delta U_{ext}}{\delta A} \right\rangle = \left\langle tanh\left(\frac{cos\left(\frac{2\pi x}{L}\right)}{2\pi w} \right) \right\rangle \qquad 7.6$$

This value is integrated over *A* from 0 (the potential is off) to some larger value intended to be strong enough to produce a desired state in the system. *x* refers to the positions of all the beads in the system and changes in response to the external potential as *A* is changed. In this case, a maximum value of 2.63 for *A* was chosen. Other values would work as long as the lamellae were clearly formed. A was changed in small increments (100 steps in all) and the system was allowed to equilibrate at each step in A for 320,000 timesteps. Due to the noise in the total energy of the system, at each step in A, after the system energy was no longer changing the final values of the total energy were averaged. The resulting data was then numerically integrated yielding the free energy difference. Figure 7.3 plots the integrand ($\delta U_{ext}/\delta A$) and the free energy along branch 1 for the case of a 16 nm pitch with an N of 120 monomers. Figure 7.3 shows that there were two slopes in the integrand for branch 1. The large initial slope is due to many beads moving from an initially mixed state to their correct locations (A beads to the A domain, and B beads to the B domain). In other words, this large initial slope is due bulk phase separation in the system, which is confirmed with visual observation of the system. Once the initial phase separation is completed, there is a smaller slope which corresponds to fewer beads moving to their correct domains. During this second section, the morphology is essentially formed and the external potential is primarily sharpening the interface. It is likely that as long as the maximum potential strength is $\geq \sim 0.5$ the results should be accurate because this is the point at which the integrand begins to flatten. The total energy of the system at each step in A must be taken at equilibrium, so each step must be run slowly enough to allow for equilibrium to be reached. If the equilibration time is too small, the path will no longer be reversible, introducing error in the calculation. However, long equilibration times cause the simulations to take far too long to be feasibly run. At each step in the integration, 320,000 timesteps were used as this was determined to be sufficient to eliminate non-equilibrium errors, even during the first regime in Figure 7.3 where the integrand is changing sharply with small changes in A. A fuller examination of the effect of equilibration time is found in Chapter 8. In cases where the entire simulation was performed in a mixed state (used to determine the ODT later), no external potential was used and the free energy calculation consisted only of the calculation shown in branch 2.

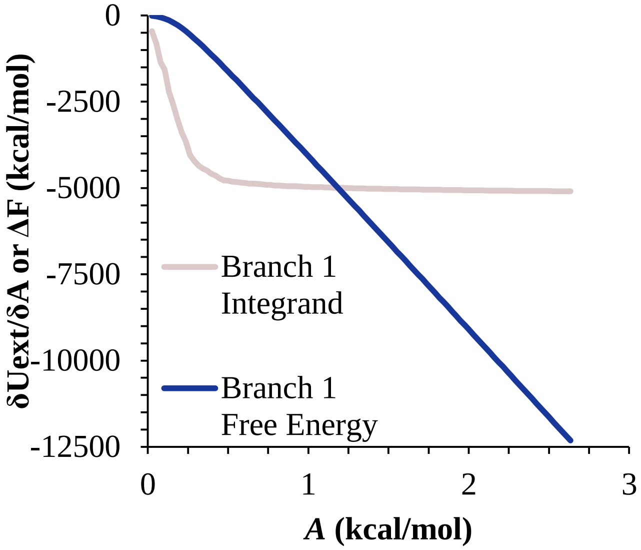

Figure 7.3. Plot of the integrand and free energy of the first branch for N = 120 and a pitch of 16 nm as a function of the external potential strength, *A*.

After this first branch of the integration, the BCP has been ordered by the external potential, but χ is still 0. In the second branch of the integration χ will be increased to its final value.. In our model, χ is not a parameter, but rather χ is derived from other parameters. The primary parameter used to manipulate χ in our system is ε_{AB}, the strength of the non-bonded potential between unlike beads at their equilibrium distance. The relationship between χ and ε_{AB} can be calculated as described in Chapter 2 so ε_{AB} can be varied from its starting condition (a χ of 0) to the value that gives the desired final χ. So, in Equation 7.1 for this branch, u is $\varepsilon_{AB.}$ The relevant portion of the Hamiltonian (the only part containing ε_{AB}) is the nonbonded A-B interaction, Equation 7.7.

$$E_{AB} = \varepsilon_{AB}\left[\left(\frac{\sigma_{AB}}{r}\right)^{8} - 2\left(\frac{\sigma_{AB}}{r}\right)^{4}\right] \qquad 7.7$$

$<\delta H/\delta u>$ is $<\delta E_{AB}/\delta\varepsilon_{AB}>$ which is Equation 7.8.

$$\left\langle\frac{\delta E_{AB}}{\delta\varepsilon_{AB}}\right\rangle = \left\langle\left[\left(\frac{\sigma_{AB}}{r}\right)^{8} - 2\left(\frac{\sigma_{AB}}{r}\right)^{4}\right]\right\rangle \qquad 7.8$$

The resulting integrand and free energy is shown in Figure 7.4 for the case of a 16 nm pitch with an N of 120 monomers and an external potential strength of $A = 2.63$. The integral is performed from $\varepsilon_{AB} = 0.5$ ($\chi N = 0$) to $\varepsilon_{AB} = 0.3$ ($\chi N = 84.5$). There is little morphological change along this branch because order was already induced by the external potential. This allowed a shorter simulation to be run at each step in ε_{AB} since each step resulted in a smaller change in state. In this case, 50 steps were taken to vary ε_{AB}. The integrand is fairly linear since morphological change is primarily limited to interfacial straightening, as in Figure 7.3 after phase separation had already occurred.

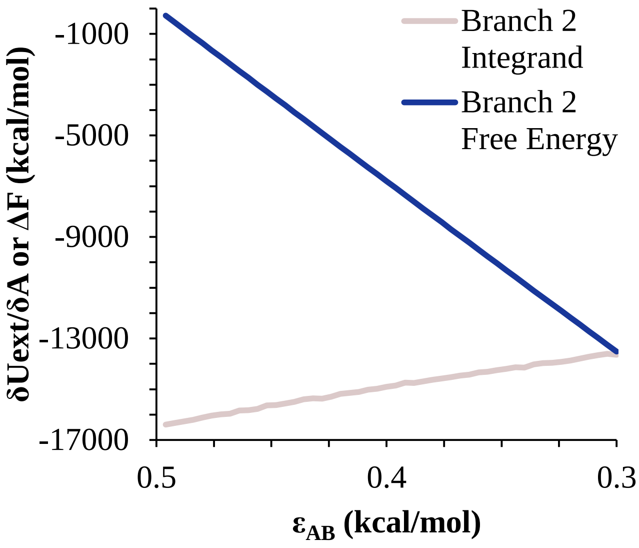

Figure 7.4. Plot of the integrand and free energy of the second branch for N = 120, an external potential strength *A* = 2.63 kcal/mol, and a pitch of 16 nm as a function of the unlike bead interaction strength, $\varepsilon_{AB.}$ The integral is performed from $\varepsilon_{AB} = 0.5$ ($\chi N = 0$) to $\varepsilon_{AB} = 0.3$ ($\chi N = 84.5$).

The final branch in the integration involves turning the external potential off, which will essentially repeat branch 1 of this scheme in reverse. The resulting integrand and free energy is shown in Figure 7.5 for the case of a 16 nm pitch with an N of 120 monomers and a χN of 84.5, integrating from and external potential strength of 2.63 to a value of 0. As with branch 2, there is little morphological change so less steps in the external potential were required to maintain a reversible path, so 50 steps were used. Because the external potential was parameterized as to match the natural interfacial width of the BCP (see Figure 7.2), there is very little change in the integrand as the external potential is turned off. There is a slight increase in line roughness associated with larger wavelength roughness that was damped by the external potential, but the effect is small.

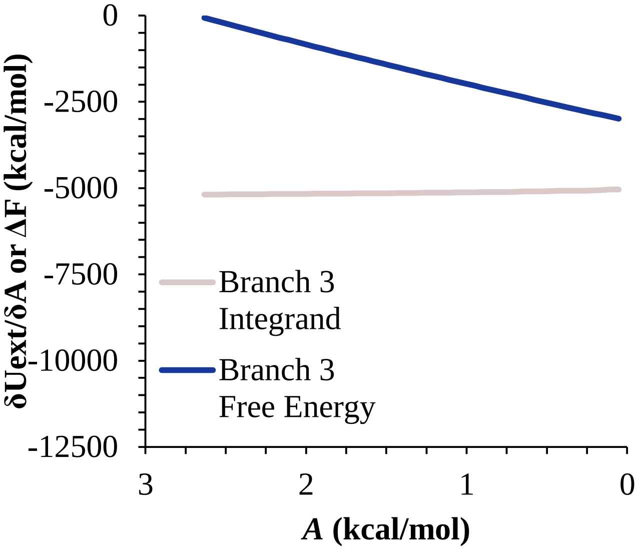

Figure 7.5. Plot of the integrand and free energy of the third branch for N = 120, χN = 84.5, and a pitch of 16 nm as a function of the external potential strength. The integral is performed from a value of *A* = 2.63 to *A* = 0.

7.2.2. Thermodynamic Integration: Order-Disorder Transition

The order-disorder transition (ODT) can be calculated using thermodynamic integration by finding the point where the free energy of the mixed state and the phase separated state intersect. When these two free energy curves intersect, the lowest free energy states switches from the ordered state to the disordered state or vice versa. The free energy of the disordered state is easily calculated by performing an integration such as the one in Branch 2 of the previous section (except with no external potential), beginning with an ε_{AB} = 0.5 (χN = 0) and ending with some low value of ε_{AB} (higher χN) In this case, the simulation will start mixed at a χN of 0 and integrate through an increase in χN towards the ODT. The resulting free energy is shown by the red line in Figure 7.6. This simulation was run using an *N* of 120 monomers. The dashed line is an extrapolation in free energy because near the ODT the ordering begins to occur and the disordered phase is unstable. The free energy of the ordered state requires more work. The calculation cannot begin to be calculated at a χN of 0 because the ordered state is not stable there. It must begin at a χN value above the ODT and at a specified pitch. This initial value is the difference in free energy between the mixed state and a specified pitch and is found using the calculations in the previous section. Next, the free energy can be calculated for various values of χN by integrating to lower χN, approaching the ODT. This calculation was done at a pitch of 20 nm and is shown in Figure 7.6 by the blue line. The dashed line is the extrapolation of this calculation because as the simulation nears the ODT, the lamellae become unstable. The intersection of the two curves results in a calculation of the ODT at $\chi N = 14.07$. This work scales χ to match mean field calculation in order to better compare results with previous work using other modes such as SCFT, as is used in Müller et al.[6] This means that the ODT of this model should occur at $\chi N = 10.5$ even though our model includes fluctuations that SCFT does not. The cause for the free energy's over estimation of the ODT was the restriction of the domain size in the ordered state when performing the integration. It is only the free energy of that specified domain size and the mixed state that is being compared. Therefore, this result means that when χN is less than 14.07 for this system, the mixed state is preferable over an ordered state with a pitch of 20 nm. If the pitch at which the ODT was calculated was reduced to the pitch near the ODT, then this χN at the ODT should converge to ~10.5. Müller and Daoulas performed a similar calculation using a Single-Chain-in-Mean-Field (SCMF) calculation and also found that finite size effects in the ordered state produced a higher than expected χN_{ODT}, just as we do.[6] They did not perform calculation at pitches near the natural pitch at the ODT, and so they could not account for this finite size effect. This work will account for that effect and calculate χN_{ODT} at various pitches so that the dependence of pitch on the calculated χN_{ODT} is found and the true χN_{ODT} can be found. This is a correction of the work done by Müller et al.[6] and can be extended to other systems or models .

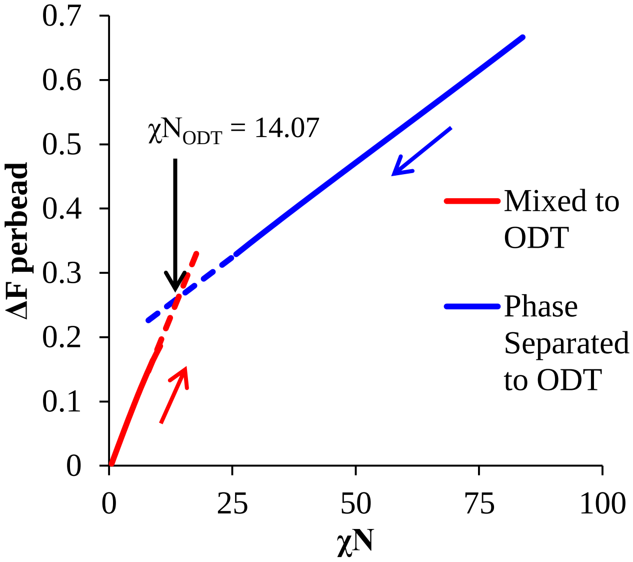

Figure 7.6. Plot of free energy compared to the $\chi = 0$ mixed state. The red line corresponds to the free energy as calculated from the $\chi = 0$ mixed state to large χN in the mixed state. The blue line corresponds to the free energy calculated from the phase separated state (determined the three branch calculation described before) to low χN in the phase separated state. The extrapolation of the two lines is shown in dashed lines. The intersection of these lines corresponds to the calculated ODT.

7.3. Results and Discussion

7.3.1. Free Energy of Extension or Compression

The free energy difference between the ordered and disordered states of various pitches at various χ values was calculated. Figure 7.7 shows a range of χN values, with a constant degree of polymerization of 120 monomers and various χ values. The lowest free energy pitch at a given χN value is the natural pitch (L_0) of that polymer. It is observed that as χN increases the natural pitch increases[11] and so the minimum in our calculation shifts to higher pitches. As a comparison, and to verify our calculations, the natural pitch was also measured directly by calculating the structure factor from the radial pair distribution function using a simulation that spontaneously phase separated due to χ as described in Chapter 2. These simulations were run in 45 nm periodic cubes at 500K for 100 ns. Figure 7.8 compares the directly measured natural pitch and the minimum free energy pitch as calculated by thermodynamic integration and great agreement across a wide range of χN is found.

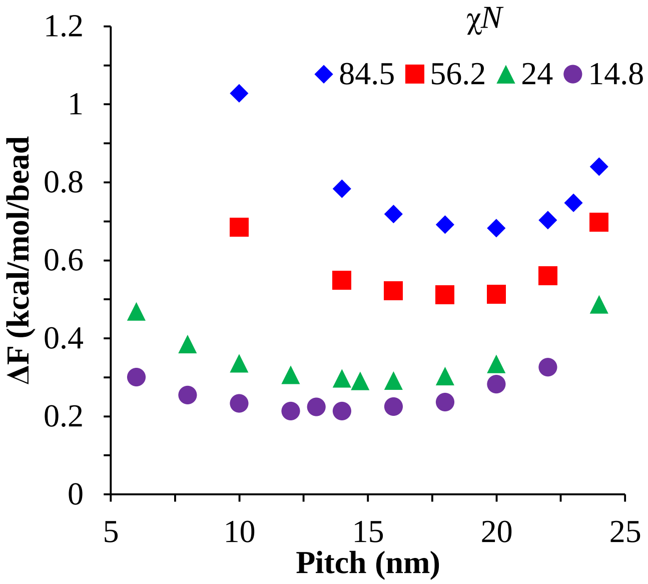

Figure 7.7. Difference in free energy between the final state and a mixed state with $\chi = 0$ as a function of pitch and χN for $N = 120$.

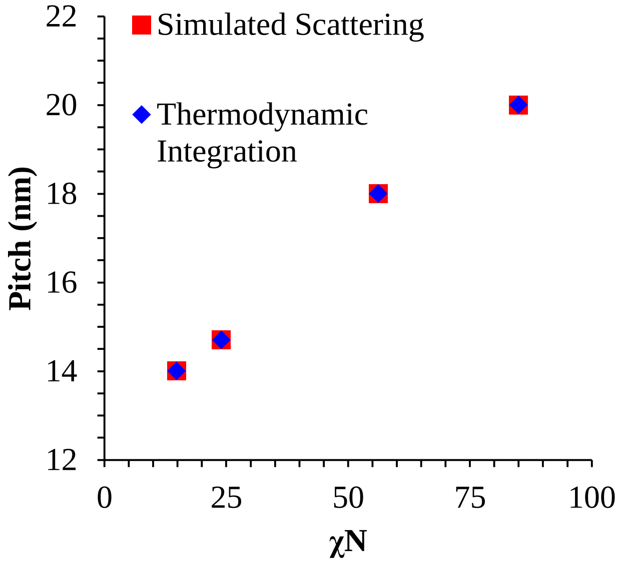

Figure 7.8. Comparison of measured natural pitch using the scattering method described in Chapter 2 and the thermodynamic integration method used here. Excellent agreement is found.

It is also found that the free energy difference between the mixed state and the phase separated state increases as χN increases (the higher χN curves are higher up in Figure 7.7). This makes sense because the free energy difference between the mixed state and the phase separated state is calculated between two different χ values and there is a loss of potential energy as χN is increased. To increase χ, ε_{AB} is decreased so that the interaction between unlike beads is less favorable. This change results in less cohesive energy and a smaller enthalpy, yielding a smaller free energy in the phase separated state. The value of most importance is perhaps not the shift in the curves away from zero, but in the difference between free energies at different pitches. Lower χ values result in a flattening of the free energy curve representing a smaller penalty for forming a pitch other than L_0. For pitches smaller than $L_{0,}$ χ determines the penalty for the extra A-B interactions that occur because of the smaller pitch so a smaller χ corresponds to a smaller penalty for increased interface, accounting for the flattening of the curve. This can be seen more demonstrated more clearly by performing two normalizations on the data in Figure 7.7.. The first normalization shifts the difference in free energy such that the difference in free energy at the natural pitch of each polymer is 0 (ΔF penalty) and normalizes by χ for each polymer. The second normalization divides the abscissa of the data by the natural pitch of the polymer (L_0) resulting in an x-axis proportional to the percent change in the pitch. This change in the pitch is inversely proportional to the A-B interfacial area. If the pitch (L) is half of L_0 ($L/L_0 = 0.5$) then there is twice as much interfacial area in that system than in a system where L is equal to L_0. The enthalpic penalty for this increased interfacial area, neglecting any stresses due to compressed chains, is proportional to χ just as the energy difference between the mixed and demixed state is proportional to χ because χ is the penalty for the extra A-B interactions at the interface. These two normalizations result in a universal curve for pitches lower than L_0 as seen in Figure 7.9. For pitches above L_0, it is entropy that increases the free energy because the reduction in interfacial area would only result in a larger enthalpic term. The form for this is more complicated and so does not result in a universal curve in Figure 7.9. Further work may yield the exact nature of the entropic increase at pitches larger than L_0.

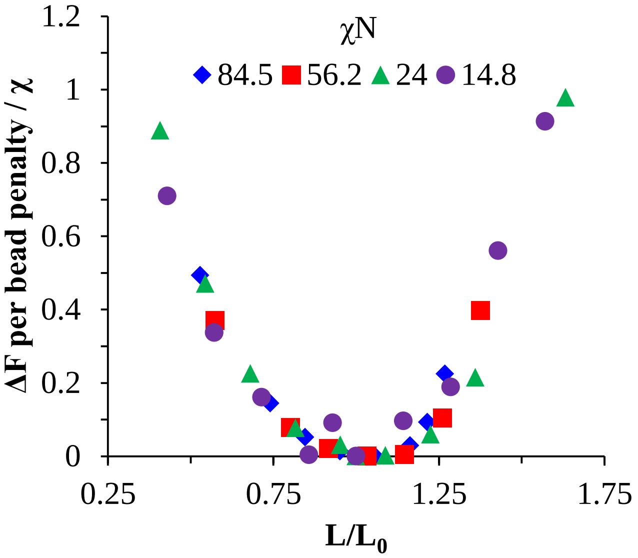

Figure 7.9. Free energy penalty normalized by χ plotted as a function of L/L_0.

7.3.2. ODT Calculation and the Effect of Pitch

The ODT can be calculated by calculating the free energy of the system through χN for a mixed state and for a phase separated state. The intersection of these two curves (see Figure 7.6) is the estimated ODT since below this χN the mixed state has a lower free energy while above this χN the phase separated state has a lower free energy. The phase separated state using in this estimation must be at a set repeat distance, and so the comparison is being made between a mixed state and a phase separated state at that particular repeat distance. When this set repeat distance is very different from the natural repeat distance close to the ODT, then the intersection between the mixed state free energy curve and the phase separated state free energy curve may over-estimate the ODT as shown in Figure 7.10. Figure 7.10 plots the free energy as a function of χN for 20 nm pitch, 26 nm pitch and for the mixed state (which is independent of pitch). The intersection of the 26 nm pitch with the mixed state curve occurs at a much higher χN than the 20 nm pitch. The curve also cut off right before the intersection with the mixed state curve because they will spontaneously start to mix during the free energy calculation, thus the need for the short extrapolation. Because the 26 nm pitch is far away from the natural pitch near the true ODT ($\chi N = 10.5$) the ODT is found at a larger N since it is preferable for the system to mix at this high χN than to stay in the highly perturbed pitch. For an accurate measure of the ODT, the pitch used for the phase separated case needs to be as close to the equilibrium pitch right above the ODT as possible.

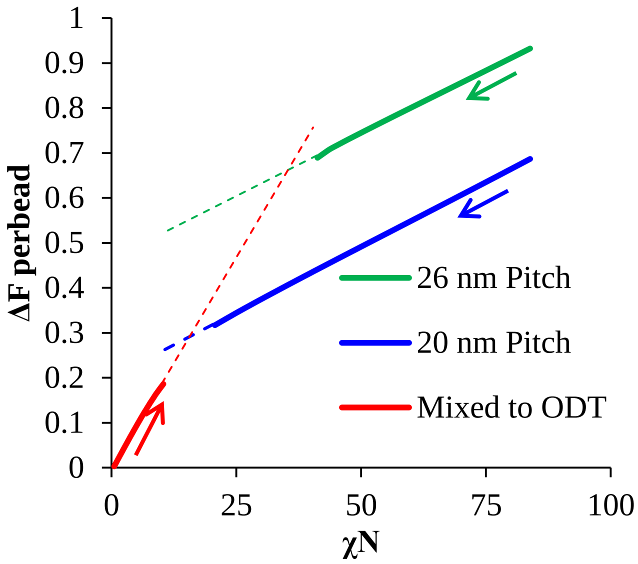

Figure 7.10. Free energy compared to the mixed $\chi = 0$ case. The Mixed to ODT curve is identical to that shown in Figure 7.6. The other curves correspond to free energy calculation in the phase separated state at 26 and 20 nm pitches .

In order to account for the change effect of the pitch, the phase separated state was simulated at various pitches and the estimate of the ODT at each pitch was found. These results are shown in Figure 7.11 for a polymer with a degree of polymerization of $N = 120$ and a volume fraction of 50% A beads. When simulated at large pitches, the ODT is found at relatively high χN. Low pitches asymptote to approximately the expected value of 10.5. This corrects the previous work by Müller et al.[6] which only calculated the ODT at a single pitch and therefore overestimated the ODT.

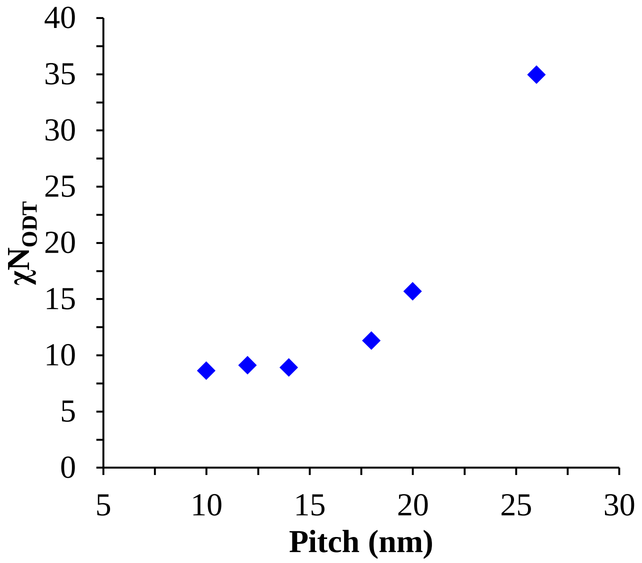

Figure 7.11. χN_{ODT} as a function of pitch for N = 120.

7.4. Conclusions

Thermodynamic integration was used to measure the energy penalty of altering the pitch of polymers with various χN. The minimum free energy occurred at a pitch that corresponded to the calculated natural pitch from scattering calculations. The penalty for pitches lower than the natural pitch was found to scale with χ and the proportional decrease in pitch, indicating a purely enthalpic driving force and resulting in a universal energy penalty curve. The penalty for pitches larger than the natural pitch is entropically driven and requires more complex calculations. The entropic and enthalpic terms must be separated to investigate such behavior. The ODT was also measured in a manner similar to Müller et al.[6] by calculating the free energy in the mixed state and of the demixed state. The intersection of these curves is the ODT. The measured ODT depends on the pitch used in the demixed calculation. If the pitch is too large, then the χN at the ODT will be over estimated. The measurement was taken as a function of pitch and found to approach the expected ODT of 10.5 when smaller pitches were used, thus correcting the work by Müller et al.[6]

7.5. References

1 Fredrickson, G. H.; Helfand, E. Journal of Chemical Physics, 1987, 87, 697.

2 Detcheverry, F. A.; Nealey, P. F.; de Pablo, J. J.; Pike D. Q.; Nagpal, U. "Theoretically informed coarse grain simulations of block copolymer melts: method and applications" Soft Matter 2009, 24, 4858-4865.

3 Lawson, R. A.; Peters, A.; Ludovice, P.; Henderson, C. L. "Coarse grained molecular dynamics model of block copolymer directed self-assembly," Proc. SPIE 2013, 8680, 86801Y.

4 Peters, A. J.; Lawson, R. A.; Ludovice, P. J.; Henderson, C. L. "Detailed Molecular Dynamics Studies of Block Copolymer Directed Self-Assembly: Effect of Guiding Layer Properties," J. Vac. Sci.Technol. B 2013, vol. 31, 2013, 31, 06F302.

5 Dethcheverry, F. A.;Liu, G.; Nealy, P. F.; de Pablo, J. J. "Interpolation in the Directed Assembly of Block Copolymers on Nanopatterned Substrates: Simulation and Experiments," Macromolecules 2010, 43, 3446-3454.

6 Müller, M.; Daoulas,K. C. "Calculating the free energy of self-assembled structures by thermodynamic integration," J. Chem. Phys. 2008, 128, 024903.

7 Müller, M.; Daoulas, K. C.; Norizoe, Y. "Computing free energies of interfaces in self-assembling systems," Physical Chemistry Chemical Physics 2009, 11, 2087.

8 Peters, A. J.; Lawson, R. A.; Nation, B. D.; Ludovice, P. J.; Henderson, C. L. " Understanding defects in DSA: calculation of free energies of block copolymer DSA systems via thermodynamic integration of a mesoscale block-copolymer model" Proc. SPIE 2014, 9049, 90492E.

9 Nagpal, U.; Müller, M.; Nealey, P. F.; de Pablo, J. J. "Free Energy of Defects in Ordered Assemblies of Block Copolymer Domains" ACS Macro Letters 2012, 1, 418.

10 Pohorille, A.; Jarzynski, C.; Chipot, C. "Good Practices in Free-Energy Calculations" J. Phys. Chem. B 2010, 114, 10235.

11 Shull, K. R."Mean-Field Theory of Block Copolymers: Bulk Melts, Surfaces, and Thin Films," Macromolecules 1992, 25, 2122-2133.

CHAPTER 8

FREE ENERGY OF DEFECTS USING THERMODYNAMIC INTEGRATION

Directed self-assembly of block copolymers (BCPs) is a process that has received great interest in the field of nano-manufacturing in the past decade, and great strides towards forming high quality aligned patterns have been made. But state of the art methods still yield defect densities orders of magnitude higher than is necessary in semi-conductor fabrication. Equilibrium defect density can be measured if the free energy difference between a defective and a defect free state is known. The defect free energy of a dislocation pair or jog defect, one of the most common defect found in BCP-DSA, is calculated via thermodynamic integration using a coarse grained molecular dynamics model as a function of χ and N. It is found that χN is not the best predictor of defect free energy and that a single χN value can yield vastly different free energies when χ and N are different (though their product is identical). This means that higher χ systems that are being produced to allow for smaller feature size DSA will likely have a lower equilibrium intrinsic defect density. Measurements of defect densities are reasonable for the oft-studied PS-PMMA. Defect free energies were measured as a function of defect placement relative to the underlayer and as a function of background composition. The effect of background composition was unclear but the defect free energy was highly dependent on defect location relative to the underlayer. Free energy differences ~ 100 kT were found between the three possible defect locations on a 1-3 guiding pattern. The effect of PDI on defect free energy was also studied. It was found that PDI significantly reduced defect free energy. Extrapolating form PDI up to 1.5 suggests that the defect will occur in equal proportions with a PDI of around 1.6 for this system. It was found that long chains tended to concentrate near the defect and stabilize the defect.

8.1. Introduction

Directed self-assembly (DSA) of block copolymers (BCPs) is a promising technique for producing sub-20 nm pitch regular patterns because of both the propensity for BCPs to phase separate at relevant length scales and the ability to guide such patterns into long range order using lithographically derived templating layers.[1,2] Both topological and chemical patterns in underlayers can be used to organize the phase separated BCPs into specific patterns.[3-5] Processing techniques for DSA of BCPs are becoming more and more effective at producing useful patterns for nanofabrication, but many hurdles must still be overcome to achieve low defect aligned patterns for semi-conductor fabrication. Defects are still rampant in many demonstrated process flows, and though understanding is increasing as to the fundamental causes of these defects, there is still a long way to go towards a complete understanding.[6-8] Previous studies have calculated the free energy of defects in laterally confined systems[6], and in chemically aligned systems as a function of guiding linewidth[7], but there are still a great many factors involved in defect formation that are not yet well understood.

The development of these DSA techniques could benefit greatly from computer simulation of such methods, especially in the area of defect modeling because of the difficulty of differentiating intrinsic BCP defects from faulty guiding patterns, particle or contamination influences, or other defect modes beyond thermodynamically or kinetically trapped microphase separation defects. Simulations can more easily identify the causes of defects and calculate the free energy of defects to yield defect density estimates. Unlike other models, molecular dynamics (MD) combined with realistic potentials for polymer behavior can potentially provide more accurate simulations of the inherent polymer behavior, dynamics, and equilibrium states in microphase separated block copolymers without a need to guess modes of molecular movement, as in Monte Carlo (MC) methods, and without oversimplifying interatomic interactions, as in self consistent field theory (SCFT).

Through the use of thermodynamic integration, MD simulations allows for calculation of free energy differences between various states, provided a reversible path can be envisioned between them. Using this technique, various equilibrium and metastable states can be compared. Defect free energies (which relate exponentially to defect densities[6]) can be calculated as functions of polymer and underlayer properties. Defectivity is one of the primary hurdles for implementation of BCP-DSA into semiconductor fabrication and defect free energies are critical to guide defectivity reduction via processing and patterning techniques. Free energy as a function of system properties like pitch, and polymer parameters can also be calculated. These calculations can provide insight into ideal and practical best case scenarios for both polymer properties and system guiding properties, whereas vast number of experiments would have to be run to achieve the same conclusions.

The defect chosen for study in this work is one of the most common intrinsic BCP defects (a defect not caused by poor processing conditions, such as particle defects).

These defects are frequently seen both in experimental data and in our own simulations[6-10]. This defect, called a dislocation pair or a jog defect, is represented in Figure 8.1. They will often come with various spacings between the defect pair, but for the purpose of this paper, a dislocation pair separated by a single tilted lamellae will be studied.

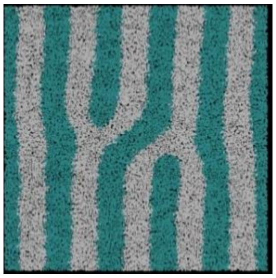

Figure 8.1. Top down image of the defect type studied in this paper. This is a common defect found in literature.[6-10]

While such defects occur for various pattern types and various polymers, a good understanding of how these patterns and polymer properties actually affect defect density is lacking. The defect density has been found to be described by:

$$n_d = a_c{}^{-2} exp(-\frac{\Delta F}{kt}) \qquad 8.1$$

where ΔF is the free energy between the defective state and the defect free state, k is boltzmann's constant, and T is the temperature.[7,8,11,12] Because of the exponential dependence of defect levels on the defect free energy ΔF, accurate estimations of this parameter are critical to understanding anticipated defect levels in DSA processes.

8.2. Model and Methods

8.2.1. Thermodynamic Integration

A method similar to DePablo and coworkers[7] and Mueller and coworkers[13] was used here. The free energy difference between two states can be calculated by the equation:

$$\Delta F_{a \to b} = \int_{u_A}^{u_B} \left\langle \frac{\delta H}{\delta u} \right\rangle du \qquad 8.2$$

H is the Hamiltonian of our model, u is any parameter that can define a continuous, thermodynamically reversible path between state A and state B, and the brackets $\langle\ \rangle$ denote a thermodynamic average, that is the average value at equilibrium. The states that were compared were a dislocation pair or jog defect (Figure 8.1) and a defect free ordered lamellae state. In order to compare these states, two simulations were run: one from a mixed state to a defect free lamellae state, which yields the free energy between the mixed state and the defect free state ($\Delta F_{\text{Defect Free - Mixed}}$), and another simulation from a mixed state to a defective state, which yields the free energy between a mixed state and a defective state ($\Delta F_{\text{Defect - Mixed}}$). Then:

$$\Delta F_{\text{Defect - Defect Free}} = \Delta F_{\text{Defect - Mixed}} - \Delta F_{\text{Defect Free - Mixed}} \qquad 8.3$$

Instead of trying to define a reversible, continuous path between a well aligned lamellar state and a defect free state, it is easier for our model to use two different paths, i.e. a path from a mixed state to a lamellar state and a path from a mixed state to a defective state.

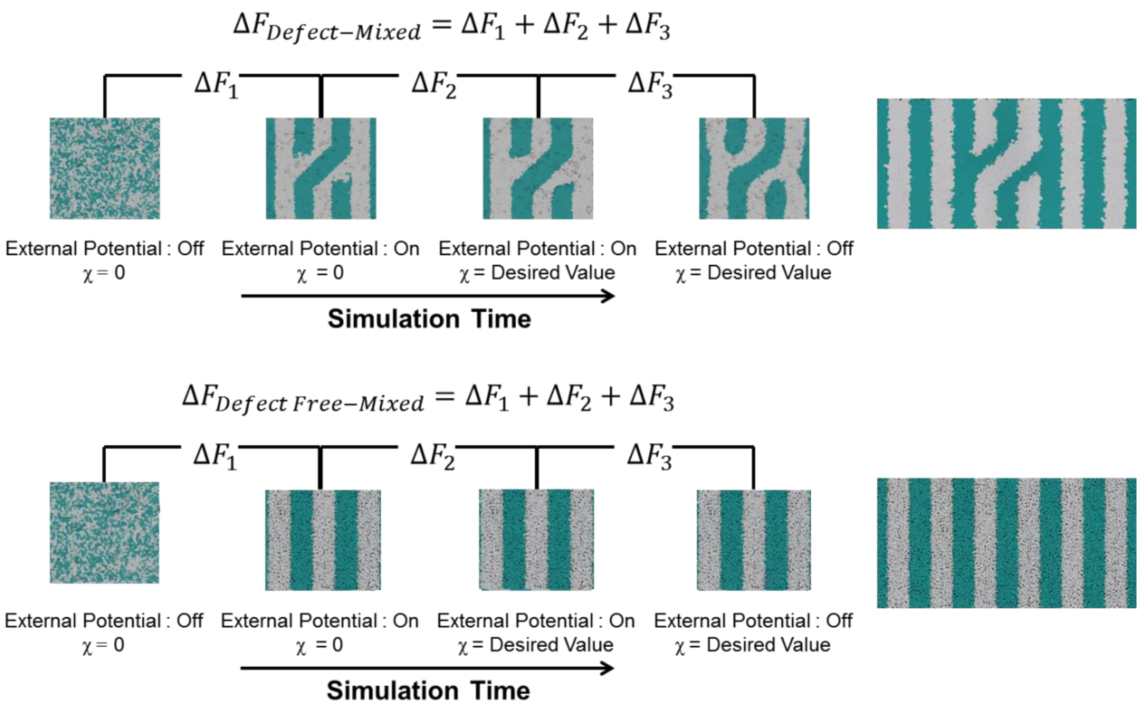
$\Delta F_{Defect-Mixed} = \Delta F_1 + \Delta F_2 + \Delta F_3$
ΔF_1
ΔF_2
ΔF_3
External Potential : Off
$\chi = 0$
External Potential : On
$\chi = 0$
External Potential : On
χ = Desired Value
External Potential : Off
χ = Desired Value
Simulation Time
$\Delta F_{Defect\,Free-Mixed} = \Delta F_1 + \Delta F_2 + \Delta F_3$
ΔF_1
ΔF_2
ΔF_3
External Potential : Off
$\chi = 0$
External Potential : On
$\chi = 0$
External Potential : On
χ = Desired Value
External Potential : Off
χ = Desired Value
Simulation Time

Figure 8.2. Schematic of the method used to calculate the defect free energy. Two simulations are run: one from the mixed to the defective state, and one from the mixed to the defect free state. Each of these simulations yields the free energy difference between the mixed state and the corresponding final state. The difference between the free energies calculated in each simulation is the free energy difference between the defect and the defect free state. Each simulation contains three branches over which a free energy difference is calculated. The first branch orders the system from the mixed state using an external potential, the second changes χ, and the third turns off the external potential.

Both $\Delta F_{\text{Defect – Mixed}}$ and $\Delta F_{\text{Defect-Free – Mixed}}$ were calculated using three branches of the MD simulation. The first branch is used to order the mixed polymers into the desired morphology. This was done using an external potential which assigns an energy to beads based on their type and position within the simulation. In the case of the defect free state, the external potential energy was described by:

$$U_{def-free} = A^{*}\tanh\left(\frac{\cos\left(\frac{2\pi x}{L}\right)}{2\pi w}\right) \tag{8.4}$$

where *A* is the strength of the potential, *x* is the position in the x axis of the bead, *w* is the width of the interface of the potential, and *L* is the repeat distance of the potential. The defect potential is created using the same equation, except the center portion is rotated 45 degrees as shown in Figure 8.3 and Equations 9.1 through 9.3.

$$U_{def} = \begin{cases} U_{in} & -0.75L_0 < x < 0.75L_0 \\ & -0.5L_0 < y < 0.5L_0 \\ U_{out} & otherwise \end{cases} \tag{8.5}$$

$$U_{in} = A\tanh\left(\frac{\cos\left(\frac{2\pi[x\cos(\pi/4) - y\sin(\pi/4)]}{L_0}\right)}{2\pi w}\right) \tag{8.6}$$

$$U_{out} = A\tanh\left(\frac{\cos\left(\frac{2\pi x}{L_0}\right)}{2\pi w}\right) \tag{8.7}$$

This produces the dislocation pair defect found in both our simulations and in published experimental results. The integral from Equation 8.2 was carried out where the reversible path (*u*) is defined by changes in the strength of the external potential, *A*. This integral, which yields ΔF_1 from Figure 8.2, is shown in Equations 8.8 and 8.9 for the defect free case.

$$\Delta F_1 = \int_0^{A_{max}} \left\langle \frac{\delta U_{def-free}}{\delta A} \right\rangle dA = \int_0^{A_{max}} \left\langle \frac{U_{def-free}}{A} \right\rangle dA \qquad 8.8$$

$$\Delta F_1 = \int_0^{A_{max}} \left\langle \tanh\left(\frac{cos\left(\frac{2\pi x}{L}\right)}{2\pi w} \right) \right\rangle dA \qquad 8.9$$

where A_{max} is 2.6. The defective case is identical except that U_{def} is substituted for $U_{def-free}$.

The integral was evaluated by numerically increasing *A* in 100 even steps from 0 to *A_{max}*, which in this case was 2.6. At each step, an MD simulation is run at the new value of *A* until the simulation has equilibrated, and the average value at equilibrium is taken and used in integrating Equation 8.9. In order to determine the amount of time required to run the simulation at each step in the ramp up of *A*, multiple simulations were run for various lengths and the free energy integration was performed, as is shown in Figure 8.4. Short times showed significant deviations from the results at long times, because a short integration time does not allow the system sufficient time to equilibrate, making the path irreversible. At long times the simulations are able to reach equilibrium at each step, and therefore the path is reversible and the measured free energy approaches a constant value. A value of 320,000 timesteps per step in *A* was found to be sufficient and therefore was chosen to be used for the remainder of the paper. In Figure 8.4 initially the value of the integrand is close to zero while the system is not well ordered. As the system phase separates due to the increasing strength of the external potential, the value of the integrand begins to approach a constant value. Figure 8.4 shows a sharp bend at *A*

~ 0.4. At this point the system is mostly already phase separated, and the remainder of the simulation primarily consists of decreasing the interfacial roughness of the BCP.

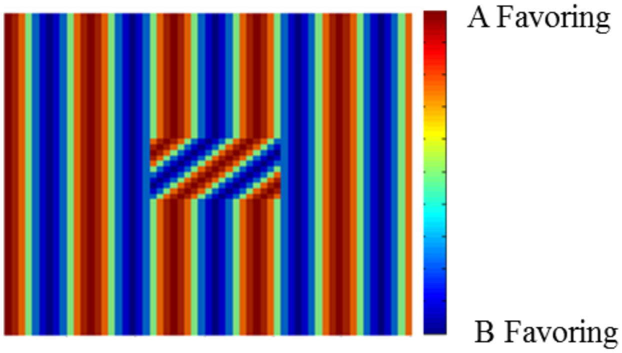

Figure 8.3 External potential used to make defect in branch 1 of the thermodynamic integration simulation. The potential is the same as the well aligned lamellae, except that a region in the center 1.5*L_0* by 0.75*L_0* is rotated 45 degrees. This rotation gives a good matching to spontaneously formed dislocation pair defects and is easily formed. The B potential is the negative of the A potential.

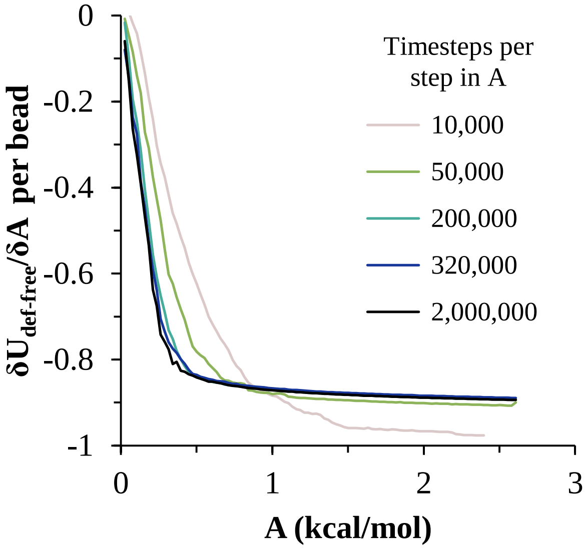

Figure 8.4. Plot of the Integrand of Equation 8.9 as A is increased. As the number of timesteps per step in A is increased, the curves converge. A value of 320,000 was used to ensure accuracy and reasonable simulation times.

Once the BCP has been ordered in the first branch of the simulation, χ (which was initially kept at zero during the first branch by setting $\varepsilon_{AB} = \varepsilon_{AA} = \varepsilon_{BB}$) must be increased. The starting condition had a χ of 0 so that the initial equilibrium state of the system was a well-defined, well mixed state. In our model, χ is controlled by changing only ε_{AB}, so ε_{AB} - was varied from 0.5 kcal/mol ($\chi = 0$) to whatever value was desired, allowing the defect free energy to be calculated as a function of χ. Equation 8.2 was then integrated where *u* is now ε_{AB}, resulting in Equation 8.10. This results in ΔF_2 from Figure 8.2.

$$\Delta F_2 = \int_{0.5}^{\varepsilon_{AB\_Final}} \left\langle \frac{\delta U_{Non-Bonded}}{\delta \varepsilon_{AB}} \right\rangle d\varepsilon_{AB}$$

$$= \int_{0.5}^{\varepsilon_{AB\_Final}} \left\langle \frac{U_{Non-Bonded}}{\varepsilon_{AB}} \right\rangle d\varepsilon_{AB} \qquad 8.10$$

$$\Delta F_2 = \int_{0.5}^{\varepsilon_{AB\_Final}} \left[\left(\frac{\sigma_{AB}}{r}\right)^8 - 2\left(\frac{\sigma_{AB}}{r}\right)^4 \right] \delta\varepsilon_{AB} \qquad 8.11$$

$U_{Non\text{-}bonded}$ is used because χ is changed via ε_{AB} and the non-bonded potential is the portion of the Hamiltonian in which ε_{AB} appears. The value ε_{AB_Final} is the value of ε_{AB} that yields the desired χ. This value will be less than the value of $\varepsilon_{AB} = 0.5$, which yields $\chi = 0$. The number of timesteps per step in ε_{AB} was varied and the integrand measured as for branch 1. The results are found in Figure 8.5. In this case, even very low numbers of timesteps per step in ε_{AB} yield the same result as very long runs. This is because there is little to no overall morphological change in this branch as there was in branch 1. This integration was done in 50 steps and run for 40,000 ps for each step in ε_{AB}.

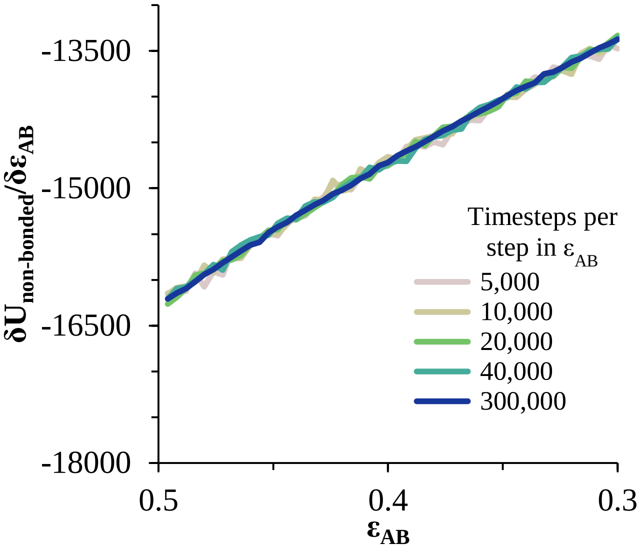

Figure 8.5 Plot of the Integrand of Equations 8.10 and 8.11 as ε_{AB} is increased. All values of timesteps per step in ε_{AB} yield the same integrand.

The third and final branch of each simulation gradually turns off the external potential. Equation 8.2 was then integrated where u is A as A decreases from 2.6 to 0. This is described in Equation 8.12.

$$\Delta F_3 = \int_{A_{max}}^{0} \left\langle \tanh\left(\frac{cos\left(\frac{2\pi x}{L}\right)}{2\pi w}\right)\right\rangle dA \qquad 8.12$$

This is the same as Equation 8.9 except that the integration limits have been switched. The same analysis as was done in Figure 8.4 is performed, the results of which are shown in Figure 8.6. The integrand of Equation 8.12 was calculated as a function of A as A was decreased for various numbers of timesteps per step in A. Very low values of timesteps per step in A show significant deviations, but values of 20,000 and greater all produce the same integrand. This makes sense because the amount of morphological change is in between that of the first and second branches. The first branch was changed from a mixed state to a clear ordered state while the second branch underwent almost no morphological change as χ was increased. This third branch, where the external potential is removed but χ is kept high, undergoes some minor morphological change as the small inaccuracies of the external potential are fixed. This integration was done in 50 steps and run for 40,000 ps for each step in A.

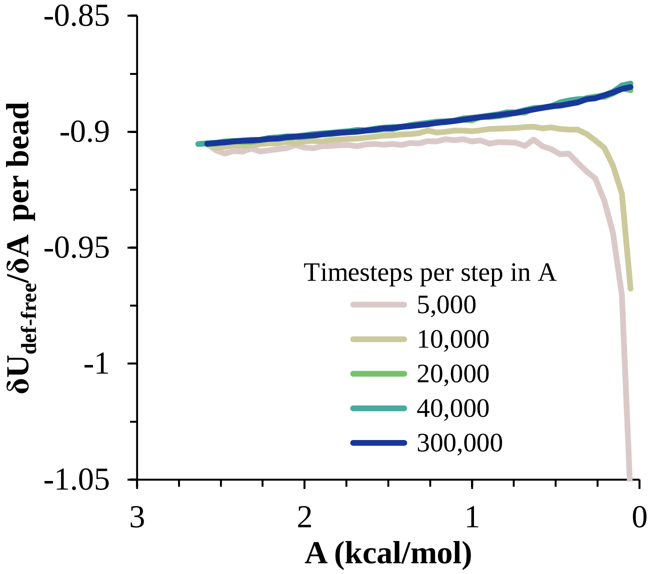

Figure 8.6. Plot of the Integrand of Equation 8.12 as A is decreased. Values of 20,000 timesteps per step in A and higher yielded the same integrand.

The free energies of each of these branches for both the mixed to defect and mixed to defect free simulations were calculated. ΔF_1, ΔF_2, ΔF_3, are summed together to yield $\Delta F_{\text{Defect - Mixed}}$ and $\Delta F_{\text{Defect Free – Mixed}}$ as in Equation 8.3.

8.3. Results and Discussion

8.3.1. Free energy of dislocation pair defects

In order to decide upon a simulation size for determining the free energy of dislocation pairs, various simulation sizes were simulated and the free energies were calculated. Box sizes in the x direction, the dimension perpendicular to the aligned lamellae, were restricted to multiples of L_0 to preserve periodicity and commensurability with the natural pitch of the block copolymer lamellae. Whenever this dimension dropped to $3L_0$ or less, then the defect became severely distorted and free energy could not be calculated. Similar distortions occurred when the y dimension drops to very low dimensions. Once the dimensions of the periodic box were greater than or equal to $5L_0$ in the x dimension and $3L_0$ in the y dimension, there did not seem to be a dependence of defect free energy on simulation area as shown in Figure 8.7. This is very similar to box sizes required in the work of Nagpal and coworkers.[7]

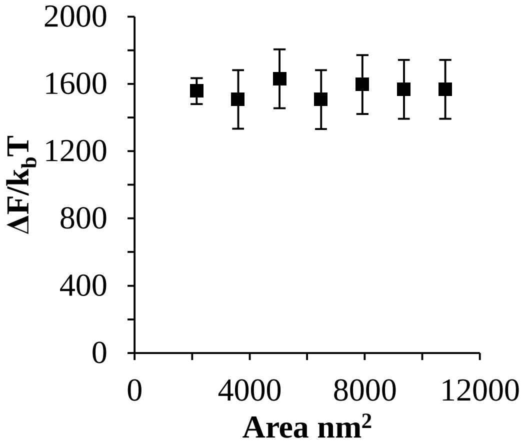

Figure 8.7. Free energy of dislocation pair defect as a function of simulation size. Smaller simulation sizes resulted in deformed defects and made it impossible to calculate defect free energy. As long as the box size was at least $5L_0$ by $3L_0$ (area = 2160 nm^2), the defect free energy did not seem to differ greatly.

In order to determine the effect of N and χ on the free energy of dislocation pairs, fully periodic simulations were run with box dimensions of $5L_0$ by $3L_0$ in x and y dimension by 15 nm in the film depth dimension. L_0 dimensions varied from ~8.3 nm to ~23.1 nm (because of variations in N and χ). N was varied from 64 monomers to 192 monomers at various χ values. The results are plotted as a function of χN in Figure 8.8. Defect free energy is usually investigated and reported as a function of χN, as is done by Takahashi and coworkers.[6] However, as can be seen in this work, when both N and χ are varied the defect free energies do not fall onto a single curve as a function of χN, but in fact show great disparities in defect free energy at a single χN. When the same data is plotted as a function of χ (i.e. instead of a function of χN) as in Figure 8.9, the data seems to collapse and be better described by a χ dependence only and not χN.

Linear extrapolations of the data in Figure 8.8 yields intercepts (where the free energy of the defect and defect free state are equal) of χN ~ 2 to ~11, but the data is fairly noisy. In addition, value of χN in this work generally stay above a χN of 20, in part because defects very near the ODT had a tendency to very quickly heal themselves because of the very small barriers to defect healing.[14,15]

In order to produce smaller features, higher χ materials will have to be produced. Such materials will likely operate at similar χN values as larger featured processes. At a similar χN value but with a lower N and a larger χ, the defect free energy will increase and intrinsic defects will decrease. This means that future generations of DSA will likely suffer from fewer defect problems for similar quality underlayers. Comparing the calculations here to defect densities for a known BCP may be useful. Processes using polystyrene-b-poly(methyl methacrylate) (PS-b-PMMA), the most commonly studied BCP, have obtained defect densities on the order of 1 defect cm^{-2}.[16] Extrapolating a fit to the data in Figure 8.9 to a χ value of 0.04 (approximately the χ for PS-b-PMMA[17]) and using Equation 8.1, a defect density of ~ 0.001 defects per cm^2 is obtained. However, this calculation does not account for imperfect guiding layers or imperfect BCPs, both of which will decrease defect free energy and increase defectivity, both of which can increase defect density by orders of magnitude.[7] Accounting for imperfect guiding layers and polymer and given state of the art achieved defect densities, and the noise in this data, this intrinsic defect density of PS-PMMA seems reasonable. Because the dependence of defect density on free energy is so strong, even a slight increase in χ and therefore in defect free energy results in defect densities that are essentially zero.

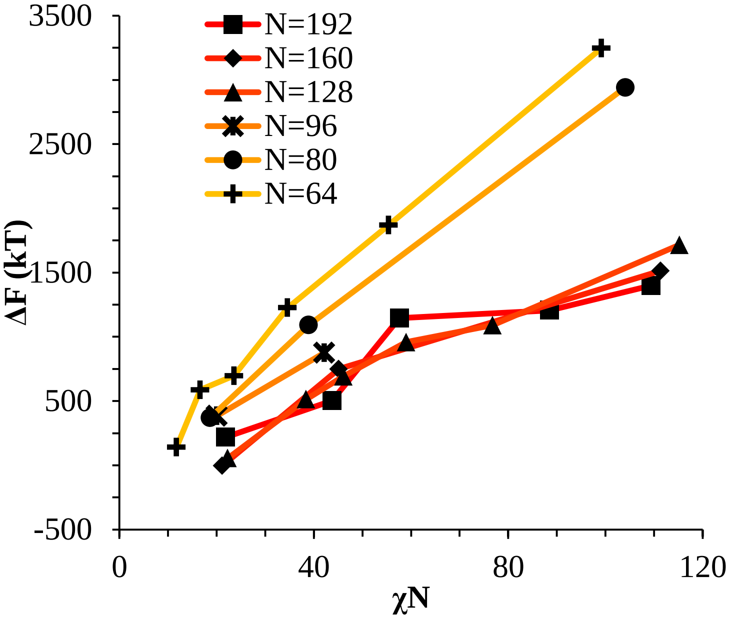

Figure 8.8 The defect free energy as a function of χN. Overall, ΔF increases with χN, but there is a significant change with N. Defect free energy approaches 0 as χN approaches the ODT.

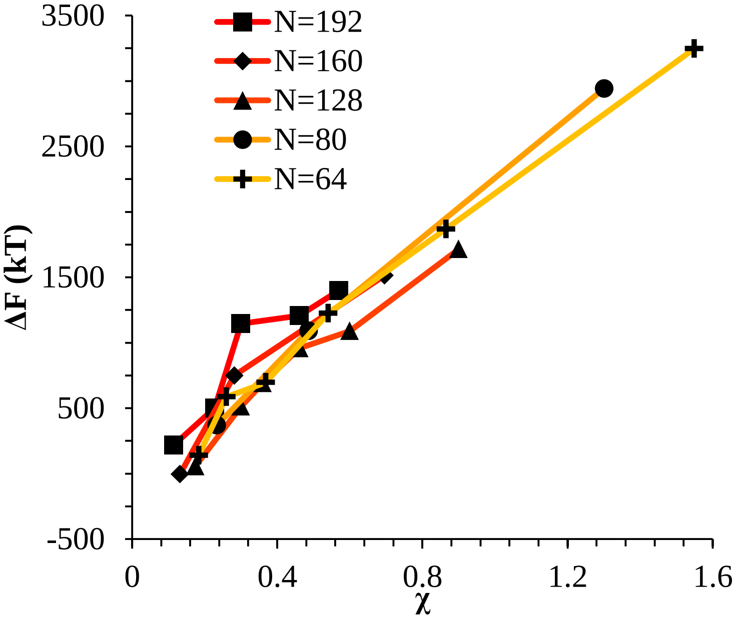

Figure 8.9. The defect free energy as a function of χ. Defect free energy scales very well with χ with little dependence on N.

The above results are obtained using periodic simulations so that the results are independent of guiding pattern. In order to explore the effect of guiding layers on defect free energy, thin film simulations were run. The effect of defect placement relative to the guiding pattern and the composition of the background region in the guiding pattern was measured. An underlayer with 2x density multiplication, or a ratio of pinning stripe width to background region width of 1:3 was used. These underlayers are composed of a pinning stripe that is preferential to one block and is 0.5 L_0 wide and a background region that is 1.5 L_0 wide. The LiNe process uses a similar pattern.[3] The dislocation pair defect can occur at three places on such an underlayer as shown in Figure 8.10. The “1-3A” defect is centered on the pinning stripe. The “1-3B” defect has the pinning stripe on the edge of the defect. The pinning line is shown under the left side of the defect in Figure 8.10, but because the defect is symmetric this is identical to putting the stripe under the right side of the defect. The “1-3C” defect has the pinning stripes adjacent to both sides of the defect but not directly under the defect. Though the pinning stripes change from the B block to the A block to the B block in Figure 8.10, the A and B blocks are energetically identical so it is merely an expedient to keep the defect unchanged and centered in the simulation volume. Defect free energies were calculated on these underlayers through various background compositions and the results are shown in Figure 8.11 for $N = 64$, $\chi N = 30$, and a film thickness of L_0.

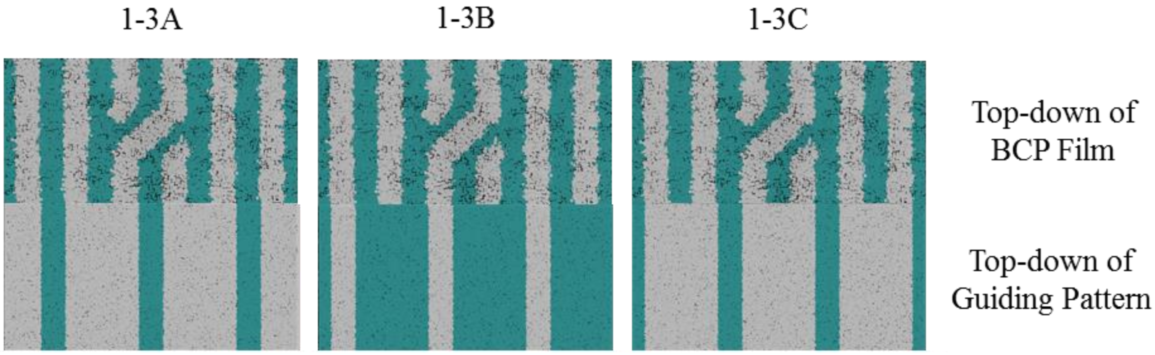

Figure 8.10. Image of the three possible defect locations on a 1-3 guiding pattern.

The defect location relative to the pinning stripes makes a significant difference in the measured free energy. When the pinning stripe is under the center of the defect ("1-3A" location), the free energy penalty is highest, followed by the pinning stripe being under one side of the defect ("1-3B" location) and finally pinning stripes that surround the defect ("1-3C" location). This effect can be explained by looking at how many lines the pinning stripe is influencing. For the "1-3A" case, the pinning stripe interacts directly with one line (the line above it) and indirectly with the two adjacent lines. On the other hand, while "1-3B" still directly interacts with one line, it only indirectly interacts with one adjacent line which decreases the influence of the pinning stripe on the defect free energy. Finally, "1-3C" does not directly influence any lines participating in the defect, but indirectly influences two adjacent lines, which further lowers the free energy of the defect. The effect of background region composition on the free energy is unclear. Different defect types appear to show different dependences but the cause is unclear. There is perhaps a subtle effect of background region composition, however this is hidden it what appears to be fairly noisy measurements. Regardless, the large differences in free energy as a function of defect placement relative to the underlayer (~ 100 kT) on average means that the vast majority of defects will occur between pinning stripes ("1-3C") and not over top of them, though it appears that defects may begin to occur with one edge over the pinning stripe ("1-3B") in appreciable numbers on higher background compositions. At every background composition the defect have very large penalties to form directly over the pinning stripe ("1-3A"). It should also be pointed out that these simulations have defect free energies less than half that of their periodic simulation counterparts (Compare Figure 8.11 with *N* = 64 and χ*N* = 35 in Figure 8.8). The appearance of the film-underlayer interface and the film-vacuum interface play an important role in defect free energy. This may also mean that film thickness plays an important role in defect free energy, but more study is necessary.

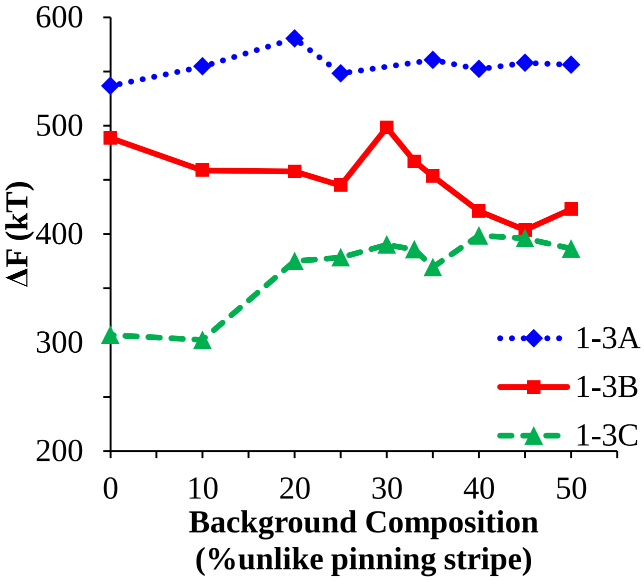

Figure 8.11. Defect free energy as a function of background composition and defect location relative to the underlayer for N = 64, χN = 35, and a film thickness of L_0.

All simulations to this point were run with a PDI of 1, but in practice all BCPs have some polydispersity. While it is expected that PDI can increase the defectivity of a BCP film, this effect has not been explored. Therefore, the effect that PDI had on defect free energy was measured. Simulations using the "1-3B" type underlayer were built for various PDI using a Wesslau distribution with chains randomly dispersed through the simulation. Each chain was forced to have a volume fraction of 50% A and B. The resulting defect free energies are shown in Figure 8.12. There is a significant reduction in free energy with increasing PDI, to the extent that the defect free energy may approach or cross 0 if PDI were increased further, implying the defective state is as likely ($\Delta F = 0$) or more likely ($\Delta F < 0$) than the defect free state at very high PDI. At more commonly used PDI values (PDI = 1.1 or 1.2) the drop is still significant. At A PDI of 1.2 the defect free energy has dropped almost 40% and would correspond to an orders of magnitude increase in defect density.

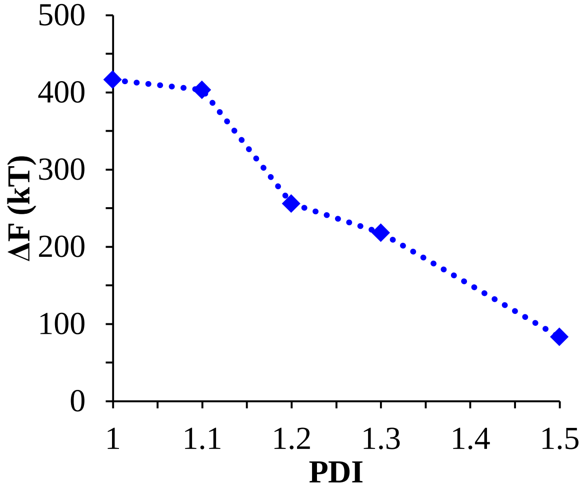

Figure 8.12. Defect free energy as a function of PDI for N = 64 and χN = 35. The "B" defect location was used.

Two factors have been neglected that should be discussed: 1) The effect of variation in volume fraction on each chain has been neglected and may contribute significantly to defect free energy and 2) the distribution of long and short chains is throughout the simulation volume is somewhat restricted. The effect of volume fraction variation is unclear, but it likely that such variations would likely only serve to further decrease the defect free energy. Variations in volume fraction have been shown to occur at bends in lamellae, and a similar effect may serve to stabilize line ends such as is found in this defect and thus stabilize the defect.[18] The external potential restricts almost all movement between lines so that chains are restricted to their original lines. They can move along an interface easily, but moving across an interface would be a very rare event. If the concentration of one length of chain is different near the defect as compared to far away from the defect, this concentration will not be properly sampled. However, in order for that effect to be important it must lower free energy, so the calculated free energy can be viewed as a maximum. This means that the values calculated in Figure 8.12 are likely over estimates of the true defect free energy, and the true free energy difference may be even less than shown here. There is reason to believe that long chains congregate to the defect center and help stabilize the defect. Figure 8.13 shows a representative image of the distribution of long ($N > X_N$) and short ($N < X_N$) chains for the PDI = 1.5 simulation from Figure 8.12. The longer chains seem to concentrate at the center of the defect. However, the method used to calculate free energy here prevents any movement across interfacial boundaries. The external potential inhibits all such motion that each line has the same distribution of chain length. If this restriction were removed then it is possible that more long chains would concentrate at the defect and further stabilize it. While this restriction cannot be directly removed, the initial distribution of chains can be manipulated. Two extra cases were studied: one where long chains ($N > X_N$) were initially placed preferentially in the rectangular region containing the defective structure, and one where long chains where initially place outside that same rectangular region. The region is defined in Figure 8.14. The other chains are randomly distributed throughout the simulation. This does create a density gradient, but a running a short simulation in the mixed state before starting calculation eliminates this. This will create two cases, one where the long chains are more concentrated around the defect, and one where they are less concentrated.

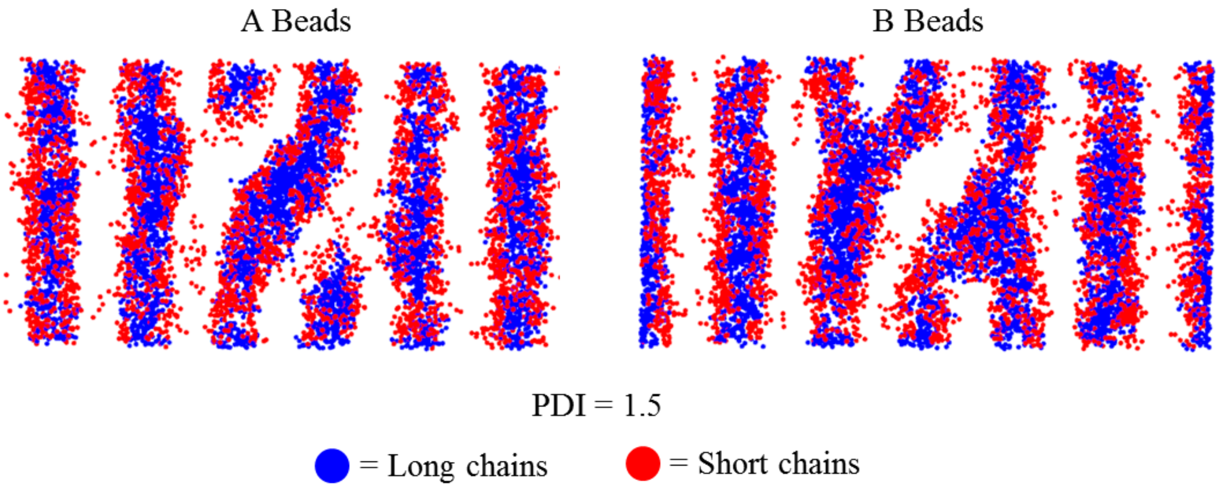

Figure 8.13. Distribution of chain lengths for PDI = 1.5, N =64, and χN = 35. The long chains tend to congregate near the defect.

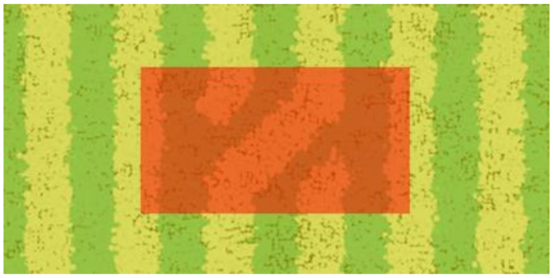

Figure 8.14. Image of locations where long chains ($N > X_N$) were built. When initialized near the defect they are placed within the red rectangle. When initialized away from the defect they are placed within the yellow region outside the red rectangle.

Figure 8.15 shows the defect free energies of the two cases where the distribution of chains lengths was manipulated alongside the results from Figure 8.12. The results are close to expected. The simulations where large chains were built away from the defect resulted in generally higher defect free energies while the simulations that concentrated large chains near the defect resulted in defect free energies similar to or less than the randomly place large chain simulations. Thus, large chains near the defect seem to be stabilizing the defect resulting in near 0 defect free energies as PDI approaches 1.5 for this particular case. How this affects simulations as a function of χ could be an important question to answer as root causes for defectivity in BCP-DSA are still not fully understood. A more systematic study of the effect of the congregation of long chains near the defect and of the effect of volume fraction variation in a polydisperse system are also warranted.

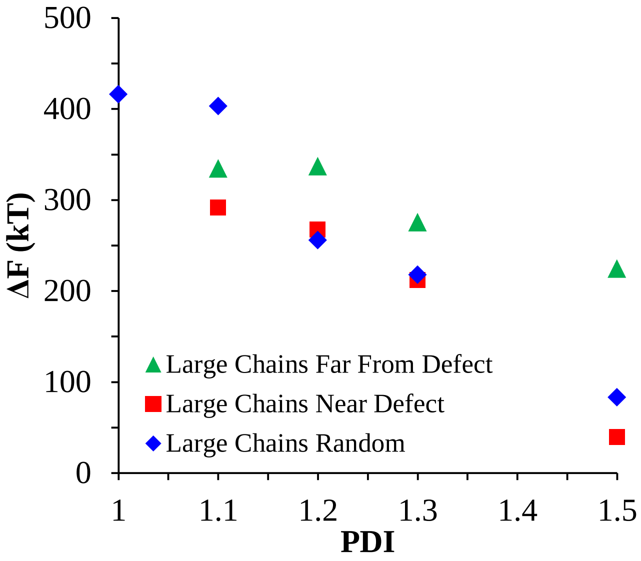

Figure 8.15. Defect free energy as a function of PDI and long chain placement. When the long chains are placed near the defect the defect free energy is equal to or lower than the simulations where they were randomly placed. When the chains are placed far away from the defect, defect free energy is generally higher.

8.4. Conclusions

The defect free energy of a dislocation pair or jog defect is calculated via thermodynamic integration using a coarse grained molecular dynamics model as a function of χ and N. It is found that χN is not the best predictor of defect free energy and that a single χN value can yield vastly different free energies when χ and N are different (though their product is identical). This means that higher χ systems that are being produced to allow for smaller feature size DSA will likely have a lower equilibrium intrinsic defect density. Measurements of defect densities are reasonable for the oft-studied PS-PMMA. Defect free energies were measured as a function of defect placement relative to the underlayer and as a function of background composition. The effect of background composition was unclear but the defect free energy was highly dependent on defect location relative to the underlayer. Free energy differences ~ 100 kT were found between the three possible defect locations on a 1-3 guiding pattern. The effect of PDI on defect free energy was also studied. It was found that PDI significantly reduced defect free energy. Extrapolating form PDI up to 1.5 suggests that the defect will occur in equal proportions with a PDI of around 1.6 for this system. It was found that long chains tended to concentrate near the defect and stabilize the defect.

8.5. References

1 Stoykovich, M. P.; Nealey, P. F. "Block copolymers and conventional lithography" Materials Today 2006, 9, 20.

2 Hawker, C. J.; Russell, T. P. “Block Copolymer Lithography: Mergin “Bottom-Up” with “Top-Down” Processes” MRS Bulletin 2005, 30,952.

3 Liu, C. C.; Nealey, P. F.; Raub, A. K.; Hakeem, P. J.; Brueck, S. R. J.; Han, E.; Gopalan, P. " Integration of block copolymer directed assembly with 193 immersion lithography" Journal of Vacuum Science and Technology B 2010, 28, C6B30.

4 Kim, J.; Yin, J.; Cao, Y.; Her, Y.; Peterman, C.; Wu, H.; Shan, J.; Tsutsumi, T.; Lin, G. " Toward high-performance quality meeting IC device manufacturing requirements with AZ SMARTTM DSA process" Proc. SPIE 2015, 9423, 94230R.

5 Kasahara, Y.; Seino, Y.; Kobayashi, K.; Kanai, H.; Sato, H.; Kubota, H.; Tobana, T.; Minegishi, S.; Miyagi, K.; Kihara, N.; Kodera, K.; Shiraishi, M.; Kawamonzen, Y.; Nomura, S.; Azuma, T. " RIE challenges for sub-15 nm line-and-space patterning using directed self-assembly lithography with coordinated line epitaxy (COOL) process" Proc. SPIE 2015, 9428, 94280S.

6 Takahashi, H.; Laachi, N.; Delaney, K. T.; Hur, S.-M.; Weinheimer, C. J.; Shykind, D.; Fredrickson, G. H. "Defectivity in Laterally Confined Lamella-Forming Diblock Copolymers: Thermodynamic and Kinetic Aspects" Macromolecules 2012, 45, 6253.

7 Nagpal, U.; Müller, M.; Nealey, P. F.; de Pablo, J. J. "Free Energy of Defects in Ordered Assemblies of Block Copolymer Domains," ACS Macro Letters 2012, 1, 418-422.

8 Laachi, N.; Takahashi, H.; Delaney, K. T.; Hur, S.-M.; Shykind, D.; Weinheimer, C.; Fredrickson, G. H. "Self Consistent Field Theory of Directed Self-Assembly in Laterally Confined Lamellae-Forming Diblock Copolymers," Proceedings of SPIE 2012, 8323, 83230K.

9 Bencher, C.; Yi, H.; Zhou, J.; Cai, M.; Smith, J.; Miao, L.; Montal, O.; Blitshtein, S.; Lavi, A.; Dotan, K.; Dai, H.; Cheng, J. Y.; Sanders, D. P.; Tjio , M.; Holmes, S. "Directed self-assembly defectivity assessment. Part II," Proc. SPIE 2012,8323, 83230N.

10 Millward, D. B.; Lugani, G. S.; Light, S. L.; Niroomand, A.; Hustad, P. D.; Trefonas, P.; Quach, D.; Ginzburg, V. V. " Graphoepitaxial and chemoepitaxial methods for creating line-space patterns at 33nm pitch: comparison to a HVM process" Proc. SPIE 2015, 9423, 942304.

11 Toner, J.; Nelson, D. R. “Smectic, cholesteric, and Rayleigh-Benard order in two dimensions,” Phys. Rev. B 1981, 23, 316.

12 Hammond, M. R.; Cochran, E.; Fredrickson, G. H.; Kramer, E. J., "Temperature dependence of order,disorder, and defects in laterally confined diblock copolymer cylinder monolayers" Macromolecules 2005, 38, 6575.

13 Müller, M; Daoulas, K. C. "Calculating the free energy of self-assembled structures by thermodynamic integration," J. Chem. Phys. 2008, 128, 024903.

14 Li, W.; Nealey, P. F.; de Pablo, J. J.; Müller, M. "Defect Removal in the Course of Directed Self-Assembly is Facilitated in the Vicinity of the Order-Disorder Transition" Physical Review Letters 2014, 113, 168301.

15 Peters, A. J.; Lawson, R. A.; Nation, B. D.; Ludovice, P. J.; Henderson, C. L. " Coarse-grained molecular dynamics modeling of the kinetics of lamellar BCP defect annealing" (Submitted 2015)

16 B. T., Lee, Y., Look, L. V., Cao, Y., Her, Y., Lin, G., Harukawa, R., Nagaswami, V., D'Urzo, L., Somervell, M. and Nealey, P., " Defect reduction and defect stability in IMEC's 14nm half-pitch chemo-epitaxy DSA flow," Proc. SPIE 9049, 904905 (2014).

17 Zhao, Y.; Sivaniah, E.; Hashimoto, T. " SAXS Analysis of the Order-Disorder Transition and the Interaction Parameter of Polystyrene-block-poly(methyl methacrylate)" Macromolecules 2008, 41, 9948, 9951.

18 Stoykovich, M. P.; Müller, M.; Kim, S. O.; Solak, H. H.; Edwards, E. W.; de Pablo, J.J.; Nealey, P. F. " Directed Assembly of Block Copolymer Blends into Nonregular Device-Oriented Structures" Science 2005, 308, 1442.

CHAPTER 9

THE KINETICS OF LAMELLAR BCP DEFECT ANNEALING

Directed self-assembly of block copolymers (BCPs) is a process that has received great interest in the field of nano-manufacturing in the past decade, and great strides towards forming high quality aligned patterns have been made. But state of the art methods still yield defect densities orders of magnitude higher than is necessary in semi-conductor fabrication even though free energy calculations suggest that equilibrium defect densities are much lower than is necessary for economic semi-conductor fabrication. This disparity suggests that the main problem may lie in the kinetics of defect removal. This work uses a coarse-grained model to study the rates, pathways, and dependencies of healing a common defect to give insight into the fundamental processes that control defect healing and give guidance on optimal process conditions for BCP-DSA. It is found that infinitely thick films yield an exponential drop in defect heal rate above $\chi N \sim 30$. Below $\chi N \sim 30$, the rate of transport was similar to the rate at which the transition state was reached so that the overall rate changed only slightly. The energy barrier in periodic simulations increased with 0.31 χN on average. Thin film simulations show no change in rate associated with the energy barrier below $\chi N \sim 50$, and then show an increase in energy barrier scaling with $0.16\chi N$. Thin film simulations always begin to heal at either the free interface or the BCP-underlayer interface where the increased *A*-*B* contact area associated with the transition state will be minimized, while the infinitely thick films must start healing in the bulk where the *A*-*B* contact area is increased. It is also found that cooperative chain movement is required for the defect to start healing.

9.1. Introduction

Directed self-assembly of block copolymers (BCPs) is a process that has received great interest in the field of nano-manufacturing in the past decade.[1-4] Surface features in a pre-patterned underlayer are used to guide BCPs into arrangements with long range order at scales as low as 5 nm.[5] By augmenting existing 193 nm and coming EUV lithographic technologies, BCP directed self-assembly can convert large pitch patterns into a much smaller feature size. The conventional lithographic techniques would be used to pattern a guiding layer, defined either by a chemical contrast (chemoepitaxy[6-8]) or topographical contrast (graphoepitaxy[9-11]), to which the BCP would align. These types of patterns and processes have been widely studied, but problems still abound. One major problem that still exists is that of defects in the final BCP pattern, even after great effort has gone forth into reducing defects.[12] The defect goal is less than 0.01 defects per cm^2 but state of the art techniques still produce BCP based defects orders of magnitude higher than this goal.[12,13] Such high defectivity could be the result of an equilibrium defectivity given a particular BCP and guiding pattern, but various models indicate that the equilibrium defectivity is, for perfect conditions, orders of magnitude lower than is currently being achieved.[14,15] Though the effects of processing conditions and various imperfect underlayers still requires more study, this disparity may point to the fundamental issue being dynamic in nature.[16-20]

While the driver for eliminating defects (the free energy difference between the defective and the defect free state) increases with χ,[14] the mobility of BCP chains generally decreases as χN increases. Specifically, in the direction perpendicular to the A-

B interface, the diffusion constant scales with $e^{-\alpha\chi N}$.[21,22] These two competing factors would likely lead one to the expectation that χ and χN may have an optimal value at some intermediate value between the extremes of very weak incompatibility between the two blocks coupled with very high mobility, and very high incompatibility between the two blocks coupled with very low mobility; some intermediate χ and χN value might be best. This work will use a coarse-grained model to study the rates, pathways, and dependencies of healing a common defect to give insight into the fundamental processes that control defect healing and give guidance on optimal process conditions for BCP-DSA.

9.2. Methods

9.2.1. Defect Annealing Simulations

Defects were modeled both in simulations periodic in all three dimensions (fully periodic), which models an infinitely thick film, and in a thin film on a neutral underlayer. In order to analyze the healing rate of defects, a large number of defects (≥13, generally ≥ 20) for a variety N and χ values were built and simulated. The time to defect annihilation was calculated for each defect and then a rate assigned to that particular set of χ, N and simulation type (fully periodic or thin film).

Fully periodic simulations were built at five times the natural repeat distance of the BCP in the x dimension, three times the natural repeat distance of the BCP in the y dimension, and at one times the natural repeat distance of the BCP in the z dimension. Previous studies have shown that for similar defects, the energy of the defect is not affected at dimensions smaller than those chosen here, that is, the simulation box we use is large enough that it does not affect the free energy of the defect.[14,15] The initial system was built by placing beads at the equilibrium angle and bond length in the simulation volume. The first bead placed on a chain was placed randomly in the simulation volume. Two minimization steps were used. The first minimization step slowly moves apart beads that were randomly placed too close together, and thus have a very strong repulsive interaction. The σ_{AA}, σ_{BB}, and σ_{AB} values were initialized at a very small value and then a brief minimization was run using the FIRE minimizer in HOOMD. The σ values were then increased in small steps with a short minimization run at each step, until the desired value of σ_{AB} (1.26 nm in this case) was reached. Any beads that were too close together were thus gently moved apart as the interaction distance between them increases. Once this step was complete, a second, longer minimization was run. From here, the defect was built using an external potential running in the NVT ensemble. At this point in the simulation χ was set to 0 (by setting ε_{AB} equal to ε_{AA} and ε_{BB}) because inherent phase separation in the BCP can work against the ordering caused by the external potential. The potential is described by Equations 9.1 - 9.3.

$$U_{ext} = \begin{cases} U_{in} & -0.75L_0 < x < 0.75L_0 \\ & -0.5L_0 < y < 0.5L_0 \\ U_{out} & otherwise \end{cases} \qquad 9.1$$

$$U_{in} = A\tanh\left(\frac{\cos\left(\frac{2\pi[x\cos(\pi/4) - y\sin(\pi/4)]}{L_0} \right)}{2\pi w} \right) \qquad 9.2$$

$$U_{out} = A\tanh\left(\frac{\cos\left(\frac{2\pi x}{L_0}\right)}{2\pi w}\right) \tag{9.3}$$

U is the potential energy, *A* scales the potential strength, L_0 is the natural pitch of the BCP system, and *w* is the width of the *A*-*B* interface relative to the pitch. U_{out} approximately matches the shape of the density profile of one of the blocks in a lamellae forming BCP. A value of 0.053 is used for *w* because it approximately matches the interfacial width for the BCP systems used here. U_{in} is simply a 45° clockwise rotation of the U_{out} potential with the central region of the simulation. It is this portion of the potential that gives rise to the defect. The simulation was run with the external potential for 150,000 timesteps with $\chi = 0$, and then for 100,000 timesteps with χ at some positive value of interest, resulting in a defect as shown in Figure 9.1. If the step where $\chi = 0$ was omitted, then the overall time to the desired morphology was increased. A higher χ restricts the movement of beads through unlike sections, increasing the time for the beads to move to the correct location under the influence of the external potential.

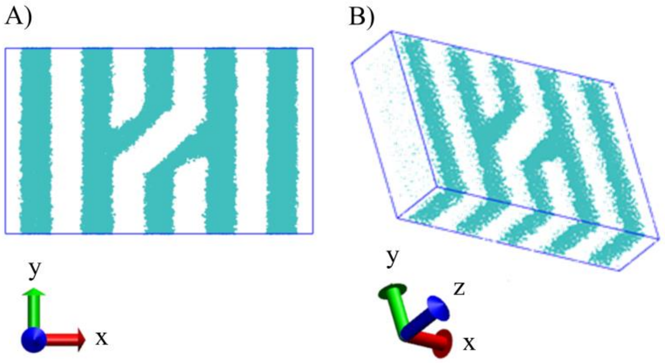

Figure 9.1. Views of a representative periodic simulation. Periodic simulations were periodic in all three dimensions. The defect was built using the external potential described by Equations 9.1 – 9.3.

Thin film simulations were built in a similar fashion at six times the natural repeat distance of the BCP in the *x* dimension, three times the natural repeat distance of the BCP in the *y* dimension, and various thicknesses in the *z* dimension. The simulation boxes are periodic in the *x* and *y* dimensions, simulating an infinitely wide and long film, but not in the *z* dimension, allowing a finite thickness and a free interface at the top of the film. The underlayer is built using the same beads that comprise the film. It is built to model a brush underlayer; an underlayer where short polymer chains are grafted to a hard substrate. The bottommost bead in each chain that is part of the underlayer is fixed in space, as if it were bonded to a silicon substrate. Full details regarding the underlayer can be found elsewhere.[23,24] The initial system was built by placing beads at the equilibrium angle and bond length in the simulation volume. The first bead placed on a chain was placed randomly in the simulation volume restricted to some volume of the simulation box 20 or 40 nm tall just above where the underlayer will be built. The resulting system is then placed over an underlayer as seen in Figure 9.2. A wall potential is used at the top of the film to encourage the film to make contact with the underlayer, and to prevent topography in the film. This potential uses the same form as the non-bonded bead to bead potential described in Chapter 2. The distance *r* is defined as the distance from a bead to the “wall” at the top of the film. This potential is removed once the external potential is turned off.

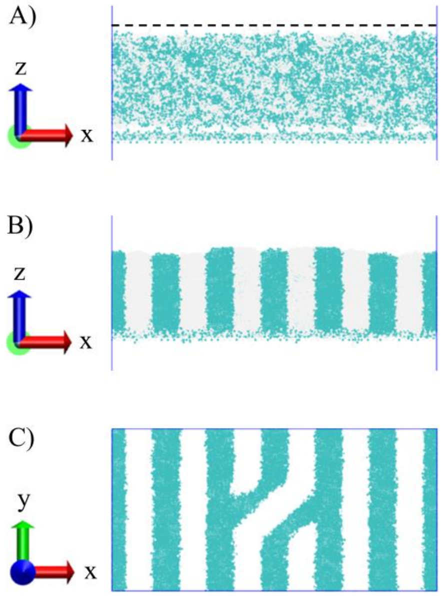

Figure 9.2. Views of a representative thin film simulation. Thin film simulations were periodic in the *x* and *y* dimensions, but not in the *z* dimension. A) A film is built above an underlayer. This film is then made to form a defect using the external potential described by Equations 9.1 through 9.3. The dotted line shows the location of the wall potential used to help the film adhere to initially adhere to the underlayer and to keep the film flat during the initial stages. B) and C) show the film adhered to the underlayer in the defective state.

This system is then minimized in the same manner as the periodic simulation and simulated for 100,000 timesteps with no external potential and $\chi = 0$. This allows the film to remove any high energy states and adhere to the underlayer before the defect is made. The external potential is then turned on and the simulation is run for 100,000 timesteps, and then χ is set to the desired value and the simulation is run for another 100,000 timesteps. The external potential does a better job of making the defect with $\chi = 0$ initially because it is not fighting against any forces in the BCP itself. Then, the external potential is turned off and the simulation is run for some set period of time between 50 and 400 ns. Simulations for sets of parameters that yielded slower rates were annealed longer to allow for more defects to heal and better statistics to be obtained, but all simulations for a given data point were run the same length of time.

9.2.2. Calculation of Defect Heal Rate

The alignment fraction (F) of each simulation, as defined in Equation 9.4, was used to identify when the defect had healed.

$$F = \frac{B_{Correct}}{B_{Total}} \qquad 9.4$$

$B_{Correct}$ is the number of beads in the expected location, that is, *A* beads in expected *A* domains and *B* beads in expected *B* domains for a perfect lamellar state with no roughness. B_{Total} is the total number of beads. For aligned lamellae such as at the edge of the simulations in this study, *F* is high because the actual morphology only differs from the expected by some roughness at the *A*-*B* interface. In the center of the simulation containing the defect, *F* is relatively low because there are *A* beads where *B* beads are expected and vice versa. To identify when the defect had healed, *F* was only calculated in the three center lines that actually contain the defect (see Figure 9.3) to decrease noise. Figure 9.3 shows *F* through time for $N = 64$, $\chi N = 45$, and a film thickness of 20 nm. There is a very clear difference between the defective state and the defect free state. The initial drop is caused by an increase in roughness of the line edges that was suppressed by the external potential which is turned off time 0.

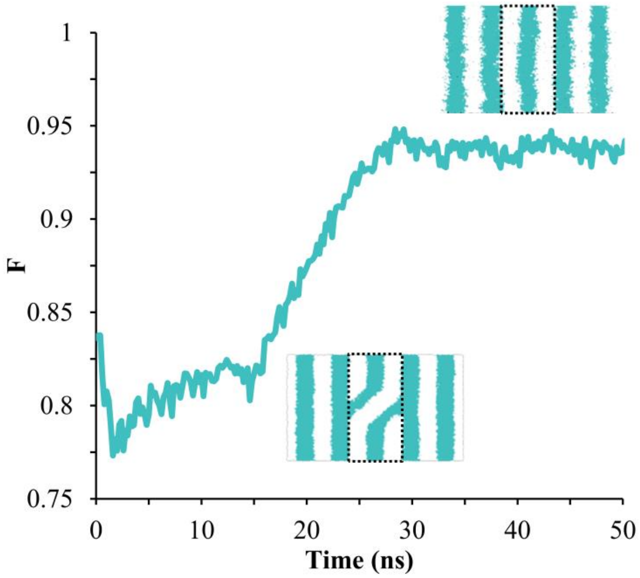

Figure 9.3. Representative plot of the fraction aligned (F) as the defect heals. Only the region in the middle of the simulation designated by the dotted line was used in the calculation. A cutoff value was assigned for each set of N and χN and the defect was deemed annealed when the fraction aligned exceeded that value.

To identify when the defect was annihilated, a cutoff value was used. Because the interfacial roughness varies with χ and N, a different cutoff must be set for each set of χ and N. The cutoff was set to the average of F over the last 3 ns of all the simulations in which a defect healed for that case (that set of χ, N, and simulation type). The heal time was then designated as the first point that exceeded that value.

The defect heal rate was calculated using Equation 9.5:

$$R_{tot} = \frac{F_H}{t_{ave}} \tag{9.5}$$

R_{tot} is a measure of the total rate of defect healing; it includes both the time before the defect begins healing and the time it takes for the defect to heal once the transition has begun. F_H is the fraction of defects healed in the maximum simulation time and t_{ave} is the mean time to heal of the simulations that did heal within the maximum simulation time. In general, F_H is one because all of the defects annealed within the simulation time, so R_{tot} is simply the average rate for these simulations to anneal. For the cases where the lowest rates were measured, F_H is less than one because not all simulations annealed during the maximum simulation time that was used. Since it took a very long time to simulate an appreciable amount of defects healing in those cases, the lower F_H correctly weights the average rate. In particular, high χN periodic simulations showed very low rates and so yielded fewer healed defects. Simulation time was increased up to 400 ns, but the order of magnitude drops in rates still limits the number of defects that healed in the simulation time. The lowest rates had at least 25% of their simulations heal, but generally, even in the cases where not all simulations healed, >50% of them did.

In Figure 9.3, there appear to be two timescales: one timescale over which F is relatively flat and which describes the time to pass the transition state (approximately 0 to 15 ns in Figure 9.3), and one which over which F continuously increases which describes the time to completely heal the defect once the transition state has been passed (approximately 15 to 28 ns in Figure 9.3). We find that the first time scale varies significantly within a single set of parameters, as it is determined by the energy barrier, while the second timescale is relatively constant for a single set of parameters. We will differentiate these two timescales by fitting the fraction defective over time (F_d) to an exponential decay as given in Equation 9.6.

$$F_d(t) = e^{-k(t-\tau_1)} \qquad 9.6$$

This is plotted in Figure 9.4 for a representative series of simulations. The aforementioned time it takes for a defect to heal once healing has started is described by the parameter τ_1 (see insets in Figure 9.4), while the time to begin healing is described by the factor k, in in terms of a time scale, $1/k$ or τ_k. The timescale τ_1, while important, is likely to be of less interest because it will likely be similar to or less than the time it takes a disordered BCP film to order, and therefore unlikely to contribute to large numbers of metastable defects in BCP systems. This allows us to separate the two relevant timescales involved in the healing of these defects. This allows the rate of healing defects to be separated into the two relevant timescales. Assuming there are a large enough number of defects, one defect will reach its transition state immediately therefore the entirety of the time that particular defect heals is equivalent to the time required for the system to progress from the transition state to the defect free state, τ_1. If no defect begins to heal initially, then this unanticipated lag will increase the value of τ_1 but will have little effect on the value of k.

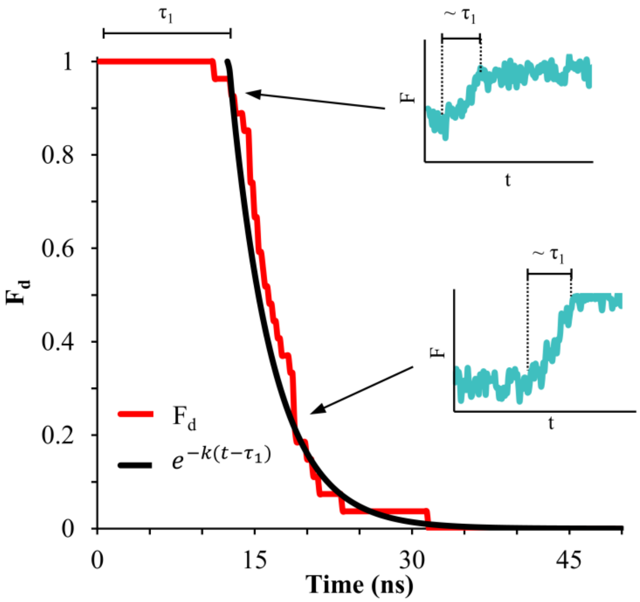

Figure 9.4. Fraction defective (F_d) over time for $\chi N = 35$, $N = 64$ for a film thickness of 20 nm.

9.3. Results and Discussion

9.3.1. Fully Periodic Simulation

Fully periodic simulations were run to calculate defect anneal rates for various χ and N values. The fully periodic simulations are similar to those done by Takahashi et al.[25] in that the effect of the BCP-vacuum and BCP-underlayer interfaces are essentially neglected. In this work there are no such interfaces, while in Takahashi et al., the calculations are done in two dimensions and extrapolated to three dimensions, assuming no variation through depth.[25] Figure 9.5A plots the kinetic rates calculated using Equation 9.5 as a function of χN and N. Both increased N and χN result in decreased anneal rates. There also seems to be a significant drop in rate starting around $\chi N = 30$

(thought this is clearer in Figure 9.5B). The offset in *N* can be explained by the difference in diffusivity and length scale of the defect as a function of *N*. In order to heal the defect, polymers must diffuse through the domain of unlike type, the size of which is proportional to the natural domain size of the polymer. Diffusivity scales with $1/N$ for Rouse chains (the relatively short polymers used here ensure Rouse dynamics), and the distance polymer chains must diffuse scales with the domain size of the polymer, (See the healing pathway shown in Figure 9.8).

These effects can be accounted for by defining two characteristic timescales: $\tau_{R,}$ a characteristic kinetic timescale, and τ_D, a characteristic transport or diffusive timescale.

$$\tau_R = 1/R_{tot} \qquad 9.7$$

$$\tau_D = {L_0}^2/D \qquad 9.8$$

D is the diffusion constant measured in a simulation of homopolymer via mean squared displacement (MSD). *D* is equal to the slope of the MSD of the beads in the system at long times divided by 6. L_0 is the domain size of the BCP. Figure 9.5B compares the timescale of diffusion (τ_D) to the timescale of defect healing (τ_R). Large values mean that the timescale for diffusion is greater than the timescale of the healing of defects. The three data sets found in Figure 9.5B lie nearly on top of one another, showing that the differences in the timescale of diffusion explains the change in rate with *N* seen in Figure 5A. The $N = 64$ data set does deviate slightly from the other two at low χN, but the difference is small and there is more noise in that data set. This noise is caused by the relatively large interfacial thickness relative to the domain size, which creates noise in measurements of F, and leads to noisy measurements of t_{ave} which ultimately introduces noise in the calculated rate.

The timescale for diffusion can be associated with the time required for a mixed BCP to phase separate and initially order. Therefore, it can be inferred from Figure 9.5B that at χN values less than about 30, when the timescale for diffusion is larger than the timescale for the healing of a defect, the energy barrier to defect healing is not important. This is because the time to order the BCP from the initial mixed state is longer than the time to remove a defect from the simulation, and therefore little extra anneal time is necessary to remove defects, perhaps on the order of the original ordering timescale. As χN increases to ~ 35, the two phenomena are at similar timescales; increased time will be necessary to remove all the defects from the system. The actual time required will depend on the initial concentration of defects after ordering has occurred, which is a difficult number to investigate, but significant reduction in defectivity will require anneal times much longer than the characteristic timescale for diffusion (τ_D). Increasing χN above 35 will cause the necessary annealing time to increase exponentially due to the increase in the energy barrier to healing defects, and therefore probably prevent viability. What the initial concentration of defect is, and what it depends on is an important and interesting question for BCP researchers, and one that requires more attention in the future. If this number is orders of magnitude higher than the desired defectivity, then even when defect healing timescales are relatively short, significant anneal time will be required to remove them. If, on the other hand, such concentrations are relatively small, then lower defect heal rates may be viable. However, even after some optimization of anneal time, currently achievable defect densities are still significantly higher than the desired density, and the initial density cannot be lower than the final density, so it is unlikely that initial defect concentrations are in fact low. How high these initial concentrations of defects truly are, and what affects them, remains an important question.

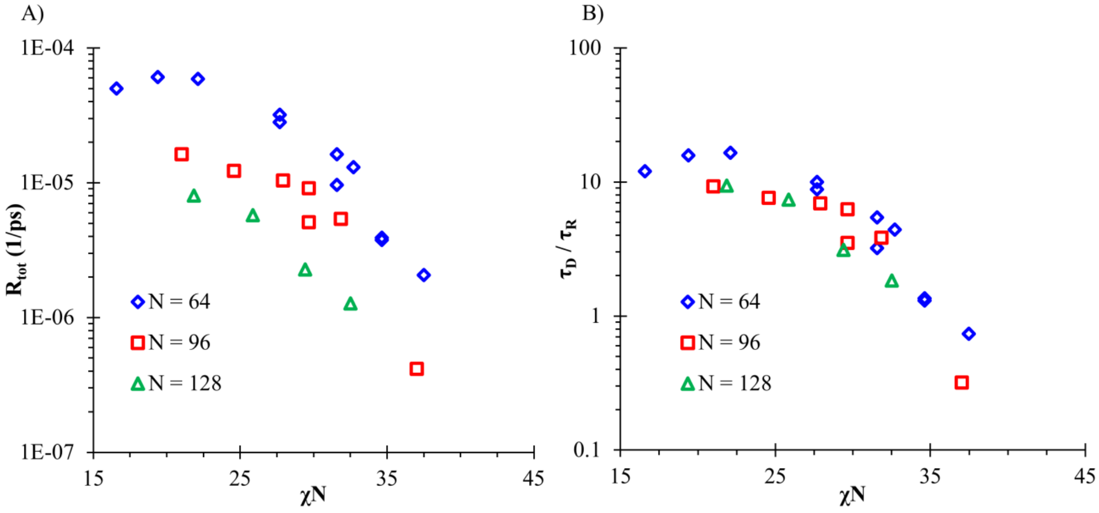

Figure 9.5. Defect heal rates as a function of χN and N for the periodic simulations. A) plots the raw rates. B) plots rates normalized by D/L_0^2.

The relatively sharp change in slope in Figure 9.5B at $\chi N \sim 30$ is interesting and the cause for this is not necessarily clear at first. R_{tot} confounds the time for a defect to begin annealing with the time it takes for a defect to finish anneal once it has started; the first is primarily associated with an energy barrier, while the second is primarily determined by transport. While this overall rate is certainly useful, there is a lot to learn from separating out the two effects.

By fitting Equation 9.6 to F_d, two parameters, k and τ_1, are found. These two parameters correlate to the two timescales relevant in this process. $1/k$ (or τ_k) is associated with the characteristic time to pass over the energy barrier, and τ_1 is associated with the characteristic time to complete healing process once begun, that is, transport. Separating the two portions out results in a clearer look at what the two components, the energy barrier and transport limitations, are doing in the process of defect healing. To consider the relative importance of the two timescales, Figure 9.6 plots τ_1/τ_k as a function of χN. Values above 1 indicate that τ_1 is greater than τ_k, and so transport dominates the overall rate, while values below 1 indication that τ_k is greater than τ_1 and so the energy barrier dominates the overall rate. Values near 1 indicate both are similarly important. At low χN, τ_1/τ_k is slightly above 1 but begins to decrease such that it passes 1 at about $\chi N = 25$ and drops well below 1 soon after. This tracks with the change in slope found in Figure 9.5, where the slope start to rapidly decrease at $\chi N \sim 30$, the same approximate value at which τ_1/τ_k start to become much less than 1 and the rate begins to be dominated by the energy barrier.

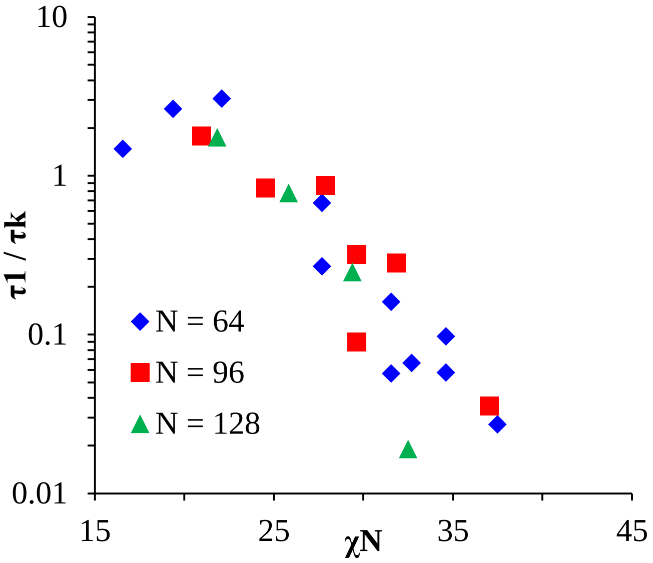

Figure 9.6 Comparison of the characteristic timescales τ1 and τk. Values above 1 indicate that transport has a greater impact on the overall time to defect annihilation, whiles values less than 1 indicate that the energy barrier has a greater impact.

Though comparing both timescales is useful to understand the rates obtained in Figure 9.5, *k* by itself is also of interest because it gives more direct information about the energy barrier. In addition, it is this portion that will be the primary cause for increased anneal time aimed at reducing defectivity. This is because τ_1 is likely to be equal to or less than the timescale of bulk phase separation and ordering present in any BCP-DSA process, since τ_1 requites smaller amounts of transport to anneal the defect than the large scale transport required to order the bulk BCP. This is seen in our simulations where bulk alignment takes longer than the time required to anneal the defect once the energy barrier is overcome. However, the time required to overcome the energy barrier (characterized by τ_k) is often much longer than both.

Figure 9.7 plots k as a function of χN. Instead of the change in slope found in Figure 9.5, the decrease in rate occurs at all χN and is approximately constant because the effects of the two timescales, τ_1 and τ_k that were convoluted in R^*_{tot}, are now separated such that we only see the effects of τ_k, the timescale associated with overcoming the energy barrier. This rate exponentially decreases with χN over almost all χN, with the exception of the $\chi N = 16.6$ point for the $N = 64$ series. This might be explained either by the increased noise close to the ODT caused by large interfacial roughness that obscures the measurement of F, and therefore of the rates, or by the fact multiple simulations spontaneously formed extra defects that had to be removed before the simulation was to be considered defect free. As can be seen in Figure 9.7, the rates scale with $e^{-0.31\chi N}$, $e^{-0.29\chi N}$, and $e^{-0.32\chi N}$ for the $N = 64$, 96, and 128 data sets respectively. Since all these are run at constant temperature, these values tell how the activation energy for defect annealing changes with χN. Given how close these values are to one another, it appears that this change in activation energy is constant with N with a value of $0.31\chi N$.

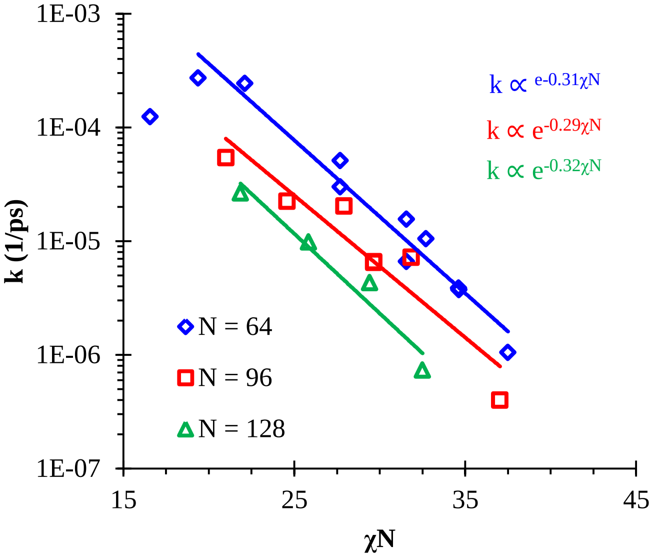

Figure 9.7. Rates calculated using exponential fit with exponential fits shown. Exponential fit for N = 64 excludes χN = 16.6.

While these results are limited to this particular polymer and more work would need to be done to extend this to the variety of polymers being used for these purposes, this relation allows researchers to directly consider the effect of χN on defect annealing rate when they are designing and optimizing their processes. A significant increase in the energy barrier as a function of χN is found, such that an order of magnitude drop in rate is found with an increase in χN of less than 10 (For R_{tot}, this is true for $\chi N > 30$ [Figure 9.5] and true at all χN for k [Figure 9.7]), highlighting the need to keep χN low to increase defect healing rates. However, in the case of this particular polymer, the energy barrier is still sufficiently small at $\chi N <$ ~30 that the rate is still largely controlled by the timescale of polymer rearrangement. The applicability of this fact to other polymers still needs to be studied, as these timescales may be different relative to one another in different polymer systems.

Figure 9.8 shows a series of representative snapshots from a periodic defect simulation through time where N = 64 and χN = 31.6. Only the *A* domains in the center region of the simulation are shown for clarity. The defect starts to heal by forming a branch of *A* across the *B* domain, shown in Figure 9.8B. Defects always began to heal by forming a bridge from the *A* domain to the *A* domain, not from the *B* domain to the *B* domain, but they did not appear to favor the left or right side of the defect as the defect is symmetric. This is not due to any chemical difference between the *A* and *B* blocks, as the parameters that guide them are identical, but because of the specific shape of the defect, the two lines on the edge of the defect begin healing first and they are composed of *A* beads in this instance. This bridge corresponds to an increase in interfacial area between the *A* and *B* domains. Figure 9.8 shows this first bridge as forming in the middle of the *z* dimension, but this bridge formed at a variety of points in the *z* dimension, as the original defect as determined by the external potential does not vary in that dimension. The time at which this first branch formed also varies significantly, as is expected in a stochastic process such as this. As χN increases, the energy penalty for this extra interfacial area increases, and as that penalty increases the occurrence of the bridge becomes less and less likely, and so the rate decreases at higher χN. Once the first bridge is formed the defect starts to heal outward from that point on that side of the defect. Typically around the same time, though at high χN there is a fairly large delay, a bridge on the other side of the defect forms, shown in Figure 9.8C. Finally, the middle strip begins to heal with a *B* to *B* domain bridge forming which appears as a hole in the *A* domain shown as in Figure 9.8D. The order of these events is consistent across all periodic simulations, including those above and below χN ~ 30, though those at very low χN will often form multiple branches between the same domains before the defect is fully healed.

The formation of this first bridge seems to be associated with the transition state of the defect healing pathway. Once this branch has formed, the defect always progressed towards healing. However, if this branch had not yet formed there was no obvious way to predict when a defect would heal. Occasionally, combinations of χN and N that exhibited lower rates (high χN and high N) would get stuck in a smaller defective state where one side of the defect had begun to anneal; the simulation apparently reached a metastable state at a smaller defect. It may be that there are two energy barriers, but the energy barrier of forming the first branch is higher than the energy barrier of forming the second branch that finally anneals the whole defect, so that this metastable state where an intermediate defect exists is rare. This metastable state may become more apparent and more important in large N and χN cases. In some cases, very low χN simulations formed larger defects before finally removing the defect. The rates of different sizes of defects and the pathways between them could be an important part of the overall defect healing picture that deserves more study.

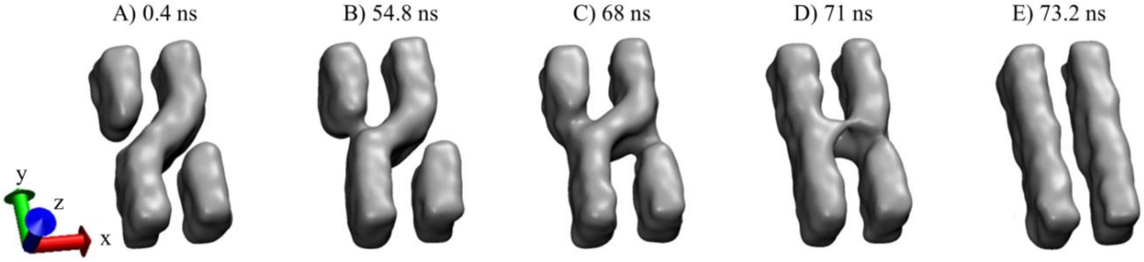

Figure 9.8. Views of a representative defect through time as the defect anneals (N = 64 and χN = 31.6). Only the A domain in the center region is shown for clarity. First a branch forms across one side of the defect, and then as that line propagates outward the other side forms a branch and soon after a hole forms in the center region. The branches thicken as the hole widens until the defect is healed.

9.3.2. Thin Film Simulations

In the periodic simulations, it was clear that the rate decreased quickly with increasing χN, even after accounting for changes in diffusion and in the size of the defect healed. However, it is possible that the interfaces present in thin films play an important role in the process of defect healing, so thin films on neutral underlayers were simulated. The value of k as function of χN was calculated and is plotted in Figure 9.9A for both thin film simulations and periodic simulations. Thin film simulations and periodic simulations show similar rates at low χN (χN ~20), but very different rates at high χN. While the periodic simulations drop rapidly even at χN values just above 20, the thin film simulations are more or less constant until χN ~ 50, above which they drop fairly rapidly, which means there is little to no dependence of the energy barrier on χN until χN ~ 50, after which the energy barrier increases with χN. Fitting an exponential to the thin film rates above χN ~ 50 yields a slope of -0.16 and -0.15 for N = 64 and N = 96 respectively, about half that of the periodic simulations which yielded a slope of -0.31 on average, indicating that the time to overcome this energy barrier increases with increasing χN at about half the rate in the thin film situation as compared to the periodic simulations. As in the periodic case, larger N have a lower rate at which the energy barrier is overcome. 40 nm thick films (3 – 4 L_0) do not overcome the energy barrier at substantially different rates as compared to 20 nm (1.5 – 2 L_0) thick films. However, as shown by Figure 9.9B, the time to heal once the defect has started healing does increase with film thickness. There are only two data points for each set, but it would be reasonable to assume that τ_1 would be proportional to film thickness. This data is consistent with this hypothesis because the τ_1 values at 40 nm are close to twice that of the τ_1 values at 20 nm. Practically, real BCP DSA systems that operate at a $\chi N < 50$, which encompasses nearly all systems that operate at the length scales of interest ($L_0 < \sim 25$ nm), will see similar defect removal rates, and there is no need to go to very low χN values. In applications that require much thicker films (orders of magnitude thicker), τ_1 values will potentially grow so large that this time scale dominates the anneal time such that the total anneal time could be much higher, even though k is constant.

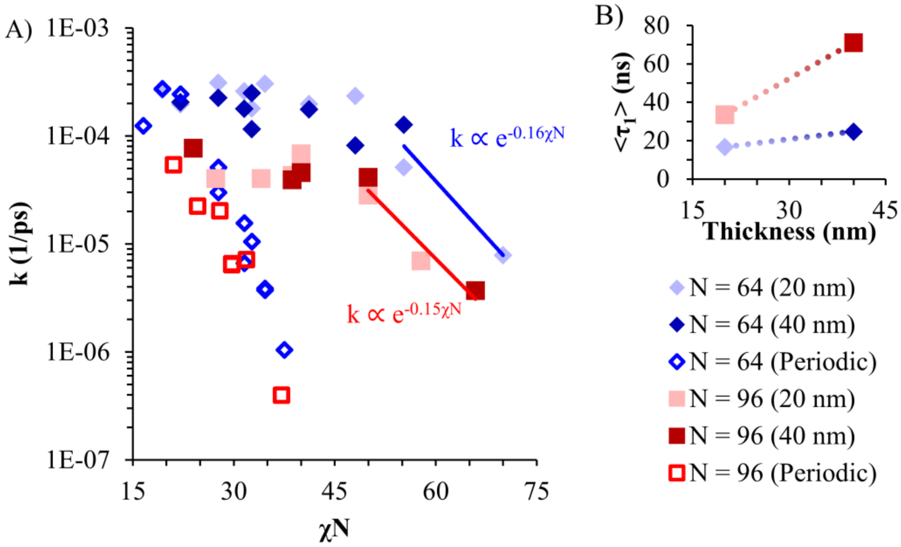

Figure 9.9. A) Defect healing rates for the thin film simulations plotted alongside the periodic simulation rates. Rate are calculated using an exponential fit as in Figure 9.4. B) Average τ_1 values (time to heal defect once the transition state has occurred) as a function of film thickness.

The cause for the change in rate between periodic and thin film simulations can be understood by viewing the defect heal pathway in Figure 9.10. The thin film defect heals similarly to the periodic defect, except that the bridges form at the surface of the film. In all thin film simulations the bridges form at either the free interface or the film-underlayer interface. If the bridges were to form in the center of the film, the bridges would be completely surrounded by unlike beads, but at the free interface or the film-underlayer interface, only half of the interfacial area of the bridge is now in contact with unlike beads, lowering the energy penalty. The fact that the extra interfacial area associated with the branch is about half of what it is in the periodic case may account for the fact that the increase in energy barrier with χN in the thin film case is about half that of the periodic case. The energy penalty scales with χN, and would be expected to scale with the added interfacial area, so when that area drops, so does the increase with χN. This reduction in the energy penalty yields an apparently constant rate until very high χN values are reached at which point it halves the rate at which the barrier increases.

Figure 9.10 displays the defect healing pathway from beginning to end, but Figure 9.11 (not the same simulation as Figure 9.10) takes a closer look at the initial formation of the bridge as it forms initially. Figure 9.11A and Figure 9.11B are shown to aid the viewer in understanding the orientation of the view in Figure 9.11C. Only the BCP film is shown, but the underlayer is located beneath the BCP. One side of the defect is viewed at an angle such that there is a clear gap between the two parts of the defect that first connect in the healing process. This allows a clear view of the width of this gap, and of the formation of the first branch as shown in Figure 9.10B. Initially, the interfaces that form the sides of the gap are fairly parallel and they will typically stay this way for some time. Eventually, one side of the gap will slowly creep towards the other side. There will still be a region of *B* beads between the *A* domains that are nearing each other. It is clear that this is not a single chain, but the cooperation of chains that causes the narrowing of the gap near the BCP-underlayer interface, or BCP-vacuum interface, though the final formation of the branch may be composed primarily of a single chain as seen in Figure 9.11C at 31.8 ns. It is also not uncommon for one side of the wall to remain fairly straight until the last moment while the other wall bends substantially towards the corresponding interface.

It should be pointed out that only unpatterned underlayers have been used in this study, but even on a patterned underlayer, defects are most likely to occur between the pinning stripes, not on top of them, or in the case of graphoepitaxy, near the center of the trench, not near the walls. If a pinning stripe is located directly beneath a formed defect, the rate at which it heals would certainly be significantly increased so that the defects that will be of interest will generally be those that are not located directly over a pinning stripe. Most existing techniques for chemoepitaxial or topographic BCP alignment, include fairly wide areas between guiding features[26-29] (at least three domains wide, usually five or more) that will allow plenty of area free of pinning stripes for defect formation.

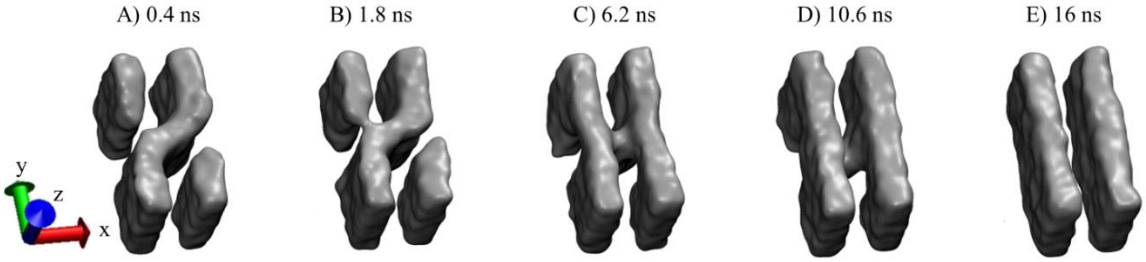

Figure 9.10. Views of a representative defect through time as the defect anneals in a thin film (N = 64 and $\chi N = 45$ with a thickness of 20 nm). Only the A beads in the center region are shown for clarity. The pathway is similar to that of the periodic simulation, except that the branches that initialize the healing in each domain always occur at either the free interface or the BCP-underlayer interface.

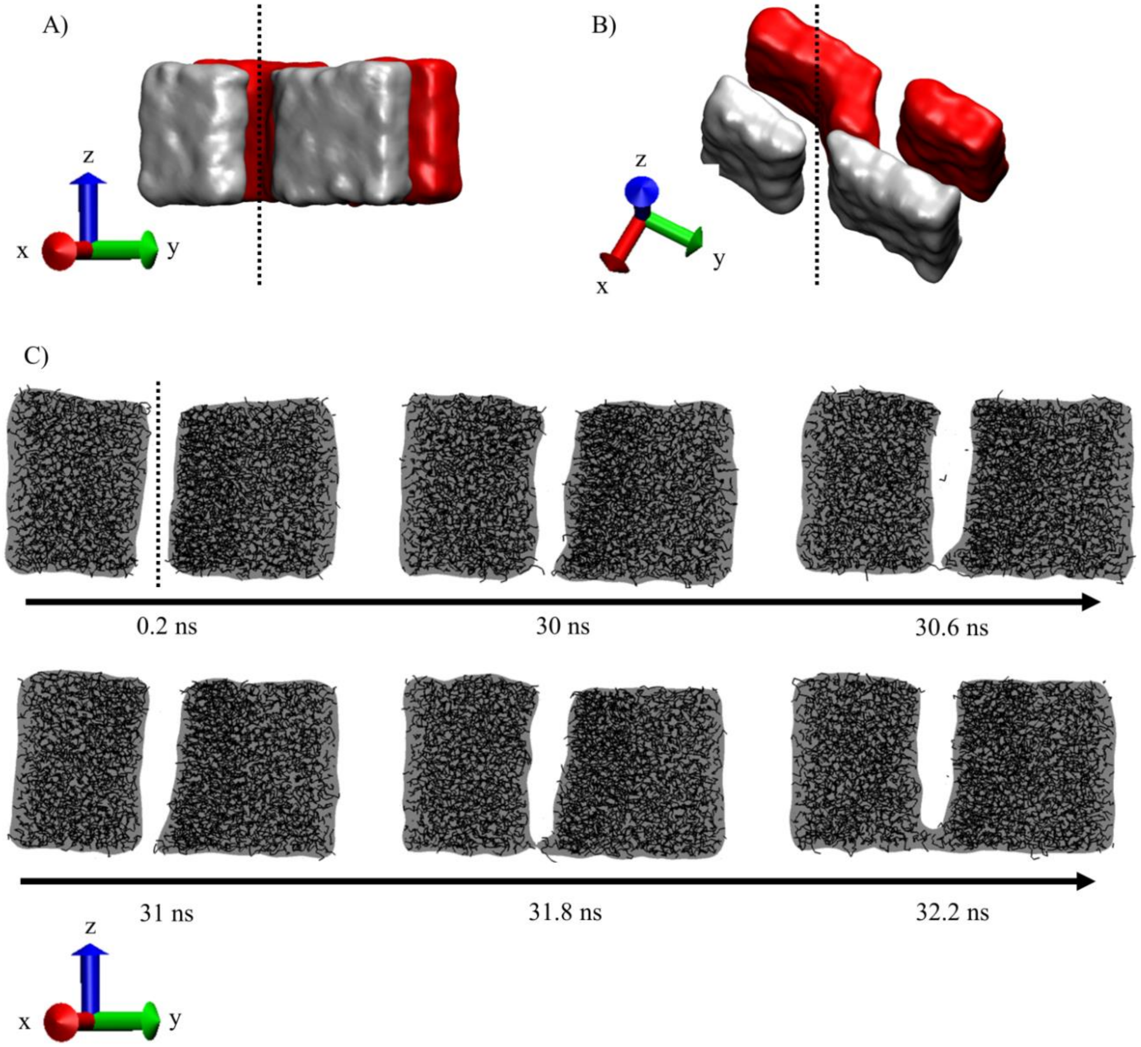
A)
B)
C)
z
x
y
z
x
y
0.2 ns
30 ns
30.6 ns
31 ns
31.8 ns
32.2 ns
z
x
y

Figure 9.11. Images of the formation of the initial branch in a thin film simulation (N = 96, $\chi N = 45$, and thickness = 20 nm). A) and B) are included to give the viewer a clear idea of the view used in C). A) Uses the same rotation and C), while B) gives a better view of the defect as a whole. Only the A domains are shown, and the portions highlighted in red are excluded from C) in order to make the formation of the branch clearer.

9.4. Conclusions

A coarse grained molecular dynamics model was used to study the rates and pathways of defect healing in lamellar block copolymer thin films. Periodic simulations showed a sharp decrease in rate as a function of χN for χN > ~30. A universal rate curve for this particular polymer and defect was found when the characteristic time scale for diffusion was divided by the characteristic timescale for defect healing. After separating the measured rate into contributions from the kinetic limitations to crossing energy barrier and transport limitations by fitting an exponential curve to the data, the energy barrier was found to increase with $0.31\chi N$ on average. Thin film simulations were also run, and it was found that the rate contribution from the energy barrier was independent of χN below χN ~ 50. Above that value the energy barrier increased at approximately $0.16\chi N$ on average, about half that of the periodic case. In the case of the thin film simulations, the defects always began healing at either the free interface or the BCP-underlayer interface. In these regions the formation of the initial branch would interact with approximately half of the unlike beads that it would in the absence of such interfaces, probably accounting for the shift in the appearance of the energy barrier away from low χN and for the change in slope of the energy barrier as a function of χN. It is also found that cooperative chain motion is necessary for this first branch to form and it is the penalty for this motion that is responsible for setting the rate at which the energy barrier for defect healing increases.

9.5. References

1 Bencher, C.; Smith, J.; Maio, L.; Cai, C.; Chen, Y.; Cheng, J. Y.; Sanders, D. P.; Tjio, M.; Truong, H. D.; Holmes, S.; Hinsberg W. D. "Self-Assembly Patterning for sub-15nm Half-Pitch: A Transition from Lab to Fab," Proc. SPIE 2011, 7970, 70700F.

2 Cheng, J. Y.; Rettner, C. T.; Sanders, D. P.; Kim, H. C.; Hinsberg, W. D., "Dense Self-Assembly on Sparse Chemical Patterns: Rectifying and Multiplying Lithographic Patterns Using Block Copolymers," Adv. Mater. 2008, 20, 3155-3158.

3 Kim, H. C.; Hinsberg, W. D. "Surface patterns from block copolymer self-assembly," J. Vac. Sci. Technol. A. 2008, 26, 1369.

4 Detcheverry, F. A., Nealey, P. F., de Pablo, J. J., Pike, D. Q., and Nagpal, U., "Theoretically informed coarse grain simulations of block copolymer melts: method and applications," Soft Matter 5, 4858-4865 (2009).

5 Cushen, J. D.; Otsuka, I.; Bates, C. M.; Halila, S.; Fort, S.; Rochas, C.; Easley, J. A.; Rausch, E. L.; Thio, A.; Borsali, R.; Wilson, C. G.; Ellison, C. J. "Oligosaccharide/Silicon-Containing Block Copolymers with 5 nm Features for Lithographic Applications" ACS Nano 2012, 6, 3424-3433.

6 Kim, S. O.; Solak, H. H.; Stoykovich, M. P.; Ferrier, N. J.; de Pablo, J. J.; Nealey, P. F. " Epitaxial self-assembly of block copolymers on lithographically defined nanopatterned substrates" Nature 2003, 424, 411.

7 Stoykovic, M. P.; Kang, H.; Daoulas, K. C.; Liu, G.; Liu, C.; de Pablo, J. J.; Müller, M.; Nealey, P. F. " Directed Self-Assembly of Block Copolymers for Nanolithography: Fabrication of Isolated Features and Essential Integrated Circuit Geometries" ACS Nano 2007, 1, 168.

8 Ruiz, R.; Kang, H.; Detcheverry, F. A.; Dobisz, E.; Kercher, D. S.; Albrecht, T. R.; de Pablo, J. J.; Nealey, P. F. " Density Multiplication and Improved Lithography by Directed Block Copolymer Assembly" Science 2008, 321, 936.

9 Segalman, R. A.; Yokoyama, H.; Kramer, E. J. "Graphoepitaxy of Spherical Domain Block Copolymer Films" Adv. Mater 2001, 13,1152.

10 Segalman, R. A. " Patterning with block copolymer thin films," Mater. Sci. Eng. 2005, 48, 191.

11 Cheng, J. Y.; Mayes, A. M.; and Ross, C. A. "Nanostructure engineering by templated self-assembly of block copolymers," Nat. Mater. 2004, 3, 823.

12 Gronheid, R.; Delgadillo, P. R.; Pathangi, H.; Heuvel, D.; Pafnell, D.; Chan, B. T.; Lee, Y.; Look, L. V.; Cao, Y.; Her, Y.; Lin, G.; Harukawa, R.; Nagaswami, V.; D'Urzo, L.; Somervell, M.; Nealey, P. "Defect reduction and defect stability in IMEC's 14nm half-pitch chemo-epitaxy DSA flow" Proc. SPIE 2014, 9049, 904905.

13 "International technology roadmap for semiconductors," 2013, < http://www.itrs.net/> February 2015.

14 Peters, A. J.; Lawson, R. A.; Nation, B. D.; Ludovice, P. J.; Henderson, C. L. "Understanding defects in DSA: calculation of free energies of block copolymer DSA systems via thermodynamic integration of a mesoscale block-copolymer model" Proc. SPIE 2014, 9049, 90492E.

15 Nagpal, U.; Müller, M; Nealey, P. F.; de Pablo, J. J. "Free Energy of Defects in Ordered Assemblies of Block Copolymer Domains," ACS Macro Lett. 2012, 1, 418-422.

16 Campbell, I. P.; Hirokawa, S.; Stoykovich, M. P. “Processing Approaches for the Defect Engineering of Lamellar-Forming Block Copolymers in Thin Films” Macromolecules 2013, 46, 9599-9608.

17 Campbell, I. P.; Lau, G. J.; Feaver, J. L.; and Stoykovich, M. P. “Network Connectivity and Long-Range Continuity of Lamellar Morphologies in Block Copolymer Thin Films” Macromolecules 2012, 45, 1587-1594.

18 Jeong, J. W.; Hur, Y. H.; Kim, H.; Kim, J. M.; Park, W. I.; Kim, M. J.; Kim, B. J.; Jung, Y. S. " Proximity Injection of Plasticizing Molecules to Self-Assembling Polymers for Large-Area, Ultrafast Nanopatterning in the Sub-10-nm Regime" ACS Nano 2013, 7, 6747-6757.

19 Son, J. G.; Change, J. B.; Berggren, K. K.; and Ross, C. A. "Assembly of Sub-10-nm Block Copolymer Patterns with Mixed Morphology and Period Using Electron Irradiation and Solvent Annealing" Nano Lett. 2011, 11, 5079-5084.

20 Li, W.; Nealey, P. F.; de Pablo, J. J.; Müller, M. "Defect Removal in the Course of Directed Self-Assembly is Facilitated in the Vicinity of the Order-Disorder Transition" Phys. Rev. Lett. 2014, 113, 168301.

21 Lodge, T. P.; Hamersky, M. W.; Milhaupt, J. M.; Kannan, R. M.; Dalvi, M. C.; Eastman, C. E. "Diffusion in microstructured block copolymer melts," Macromol. Symp. 1997, 121, 219.

22 Lodge, T. P.; Dalvi, M.C. "Mechanisms of Chain Diffusion in Lamellar Block Copolymers," Phys. Rev. Lett. 1995, 75, 657.

23 Lawson, R. A.; Peters, A. J.; Ludovice, P. J.; Henderson, C. L.; "Coarse grained molecular dynamics model of block copolymer directed self-assembly" Proc. SPIE 2013, 86801, 86801Y.

24 Peters, A. J.; Lawson, R. A.; Ludovice, P. J.; and Henderson, C. L. "Detailed molecular dynamics studies of block copolymer directed self-assembly: Effect of guiding layer properties" J. Vac. Sci. Technol. B 2013, 31, 06F302.

25 Takahashi, H.; Laachi, N.; Delany, K. T.; Hur, S. M.; Weinheimer, C. J.; Shykind, D.; Fredrickson, G. H. "Defectivity in Laterally Confined Lamella-Forming Diblock Copolymers: Thermodynamic and Kinetic Aspects," Macromolecules 2012, 45, 6253.

26 Liu, C.; Nealey, P. F.; Raub, A. K.; Hakeem, P. J.; Brueck, S. R.; Han, E.; Gopalan, P. "Integration of block copolymer directed assembly with 193 immersion lithography" J. Vac. Sci. Technol. B 2012, 28, C6B30.

27 Dammel, R. R. "Cost-Effective Sub-20 nm Lithography: Smart Chemicals to the Rescue," J. Photopolym. Sci. Technol. 2011, 24, 33-42.

28 Jeong, S.; Moon, H.; Kim, B. H.; Kim, J. Y.; Yu, J.; Lee, S.; Lee, M. G.; Choi, H.; Kim, S. O. "Ultralarge-Area Block Copolymer Lithography Enabled by Disposable Photoresist Prepatterning" ACS Nano 2010, 4, 5181-5186.

29 Cheng, J. Y.; Sanders, D. P.; Truong, H. D.; Harrer, S.; Friz, A.; Holmes, S.; Colburn, M.; Hinsberg, W. D. "Simple and Versatile Methods To Integrate Directed Self-Assembly with Optical Lithography Using a Polarity-Switched Photoresist" ACS Nano 2012, 4, 4815-4823.

CHAPTER 10

PROTRACTED COLORED NOISE DYNAMICS FOR POLYMER SYSTEMS

Block copolymer (BCP) systems are often studied using mean field or self consistent field theories because of the comparatively large scales, both in time and space, involved. A method for increasing the efficiency of sampling activated states in molecular dynamics simulations of polymer systems is described. By applying a time correlated random force along the backbone of the polymer chain, chain movement is encouraged without significant perturbation of the free energy of the system. This method is applied to a coarse-grained MD model in the context of defect healing in an aligned thin film system. It was found that PCND increased defect heal rate by 4 orders of magnitude. Diffusion is also increased by about an order of magnitude. An investigation of the limits of the parameters that describe the random force was undertaken, and a set of parameters that both significantly decrease defect heal time and have little effect on system properties such as natural pitch and chain statistics was found. A comparison to increased temperature annealing was undertaken and it was found that the correlated random force was much more effective at sampling over energy barriers.

10.1. Introduction

Block copolymer (BCP) systems are often studied using mean field or self consistent field theories because of the comparatively large scales, both in time and space, involved.[1-4] Diffusion in polymer systems is orders of magnitude lower than that of many systems based around small molecules requiring large simulation times, and the relatively large dimensions of the polymer chains require simulation sizes to be significantly larger than those of small molecules. In the past 5-10 years, various coarse grained Monte Carlo and molecular dynamics models have been developed to handle the shortcoming of the various mean field theories that have been used for decades, namely the lack of fluctuations which is known to be important near the order disorder transition and in applications such as BCP directed self assembly (DSA).[1,5] However, such models are still severely limited in the time and length scales they can achieve. Even relatively short BCPs at realistic χN values often take days or weeks of simulation time to anneal a single defect. To anneal a whole array of defects at currently used N and χ values would require months or even years of simulation time, an unusable timescale in the study of BCP directed self assembly (DSA). Even in other fields, an atomistic or coarse grained model of a polymer that can be used on very long time and/or length scales would be very useful.

PCND is a method that increases the fluctuations in a system using time correlated stochastic forces in order to increase sampling over energy barriers. Such a method, if applied to polymer systems in an intelligent manner, should significantly reduce the simulation time required when studying slow transitions such as defect removal in BCP systems. PCND has already been developed for use in a Lennard Jones glass system. This work applies the ideas behind the LJ-glass version of PCND to polymer systems.

10.1.1. PCND and Langevin Dynamics

Paul Langevin developed the original Langevin equation in the early 20th century.[6] It was designed to describe Brownian motion, that is, the random motion of a particle in a fluid caused by random collisions with other particles. It is based on the idea that the mean kinetic energy of a particle should in thermal equilibrium should have a value of *nkT/2*, where n is the number of degrees of freedom for that particle, and that there should be two forces acting on a particle of mass *m*: a fluctuating or random force that represents the continuous impacts of molecules of the fluid on the particle, and the second which is essentially a viscous drag. The first force should be random but over long time average to zero, that is, it should not impart a net force on the particle. Combining these two forces into an equation gives the simplified Langevin Equation[6,7].

$$m\frac{d^2x(t)}{dt^2} = \eta(t) - m\zeta\frac{dx(t)}{dt} \qquad 10.1$$

Equation 10.1 is the simplified Langevin Equation in one dimension, but it can be extended to multiple dimensions easily. In Equation 10.1 $\eta(t)$ is the random force, while ζ is the frictional coefficient corresponding to the viscous drag. The particle has a position of $x(t)$ and a mass of m. The inclusion of a random force (and therefore a random variable) is the first example of a stochastic differential equation in literature[7].

The generalized Langevin equation was developed in 1960 by Zwanzig[8-10] who did so based on the idea of removing rapidly varying degrees of freedom. Mori later refined the derivation.[11,12] The generalized Langevin equation (GLE) is given in Equation 10.2 where $\eta(t)$ is again a stochastic force and which satisfies Equations 10.3 and 10.4.

$$m\frac{d^2x(t)}{dt^2} = \eta(t) - m\int_0^t \zeta(t-s)\frac{dx(s)}{dt}ds \qquad 10.2$$

$$\langle\eta(t)\rangle = 0 \qquad 10.3$$

$$\langle\frac{dx(0)}{dt}\eta(t)\rangle = 0 \qquad 10.4$$

That is, the average of $\eta(t)$ over all time is zero and the correlation between the initial velocities and the random force is zero. ζ(t) is a viscous drag coefficient as before and is related to $\eta(t)$ by Equation 10.5.

$$\zeta(t) = \frac{\langle\eta(t)\eta(0)\rangle}{mkT} \qquad 10.5$$

This relationship is sometimes described as the second fluctuation-dissipation theorem.[13] The generalized Langevin equation can be reduced to the simplified Langevin equation by assuming the stochastic forces have an infinitely small correlation time.

The degree to which this equation can increase fluctuations, and increase phase space sampling, is limited. It is the connection between the drag coefficient and the random force that limits stochastic fluctuations. The distribution of the random forces can be increased by increasing the drag coefficient (see Equation 10.5). Though the average of the random force is zero, large rapid forces can be utilized by increasing the width of the distribution. However, increasing the drag coefficient too much will result in an over damping of the system and ultimately reduce fluctuations.

Protracted colored noise dynamics (PCND) decouples the friction coefficient (ζ) and the variance of the stochastic force distribution. This significantly increases fluctuations and allows viscous or highly constrained systems to sample phase space much more quickly. Instead of mimicking a solvent using stochastic fluctuations, PCND increases phase space sampling. By combining this approach with the used of colored stochastic noise (that is, not white noise, or noise that does not equally sample all frequencies in Fourier space), many different system types, especially systems where activated processes are important, can be sample more efficiently.

The most common type of random force is a Gaussian random force, commonly referred to as white noise. This noise can be described by Equations 10.6 and 10.7.

$$\langle \eta(t) \rangle = 0 \tag{10.6}$$

$$\langle \eta(t_1)\eta(t_2) \rangle = 2\delta(t_1 - t_2) \tag{10.7}$$

Equation 10.6 means that the average of $\eta(t)$ over time is zero, while Equation 10.7 describes the variance of the Gaussian distribution and states that there is no time correlation for such noise. This white noise is a time uncorrelated force, but in a colored noise a time correlated force, can also be used.

PCND as used by Jenkins,[7] uses an exponentially time correlated noise ($\varepsilon(t)$) using the differential equation described by Equation 10.8 with properties as described by Equations 10.9 and 10.10.

$$\dot{\varepsilon(t)} = \frac{\Omega^{1/2}\eta(t) - \varepsilon(t)}{\tau} \qquad 10.8$$

$$\langle\varepsilon(t)\rangle = 0 \qquad 10.9$$

$$\{\langle\varepsilon(t)\varepsilon(s)\rangle\} = \frac{\Omega}{\tau} e^{-\frac{|t-s|}{\tau}} \qquad 10.10$$

η(t) is the Gaussian white noise as described in Equations 10.6 and 10.7. The curly brackets denote averaging over the distribution of initial conditions, the importance of which is highlighted by Fox et al.[14] The root mean square magnitude of the forces are given by Ω/τ and the correlation time is given by τ. The distribution of initial values (ε_0) is given by Equation 10.11.

$$P(\varepsilon_0) = \frac{1}{\left(\frac{2\pi\Omega}{\tau}\right)} e^{\left[-\frac{\varepsilon_0{}^2}{\left(\frac{2\Omega}{\tau}\right)}\right]} \qquad 10.11$$

These forces were generated, both by Jenkins and in the rest of this work, using the algorithm of Fox et al.[14] The algorithm generates an initial condition ε_0 by using the Box Mueller algorithm.[15]

$$\varepsilon_0 = \left[-\frac{2\Omega}{\tau}\ln(a)\right]^{1/2} \cos(2\pi b) \qquad 10.12$$

The variables a and b are uniformly distributed random numbers between 0 and 1. The noise is then integrated through time using Equations 10.13, 10.14, and 10.15.

$$E = e^{-\frac{\Delta t}{\tau}} \qquad 10.13$$

$$h = \left[-\frac{2\Omega(1-E^2)}{\tau}\ln(a)\right]^{1/2}\cos(2\pi b) \qquad 10.14$$

$$\varepsilon_{t+\Delta t} = E \cdot \varepsilon_t + h \qquad 10.15$$

Again, a and b are uniformly distributed random numbers between 0 and 1. These uniformly distributed random numbers are generated every timestep for all atoms/beads/spheres/chains for which the stochastic force is being applied.. For the simulations in this work, random numbers are generated using a Mersenne Twister[16] algorithm for each instance. The algorithm is seeded at the beginning of the simulation with the current time in seconds from midnight January 1, 1970 UTC.

The random force is generated using this algorithm ($\varepsilon(t)$) is substituted into the Langevin Equation for the $\eta(t)$ term. The Nosé-Hoover temperature controller is used for all simulations.

This method has been applied to a Lennard-Jones glass where it was shown to drastically reduce the time an LJ-glass took to reach the crystalline state. After a brief optimization of parameters, it was shown that using PCND can reduce the system relaxation time by a factor of about 3000, while less optimal parameters showed a reduction in relaxation time by a factor of about 10, as shown in Figure 10.1 from Jenkins.[7] To estimate this decrease in relaxation time a linear model is assumed in the decrease in potential energy for the simulation with no stochastic noise in Figure 10.1 to the known crystalline potential energy.[7] In this case, both parameter sets shown caused an increase in potential energy before dropping the energy significantly. Though it is not clear for the data set where $\tau = 5$ in Figure 10.1, the author claims such in the text.[7] The final energy level is constant for both, though the PCND does add a slight offset that scales with the input parameters, increasing the final energy state with higher Ω/τ and τ values. It is suggested that a brief simulation without PCND, or a stepping down of PCND parameters would remove this offset in energy altogether. Once the crystalline state has been reached, the stochastic noise continues to increase fluctuations in the system, increase potential energy, but because the system is still in the crystalline state, removing these fluctuations should quickly restore the overall system state and potential energy to the true value for the crystalline state.

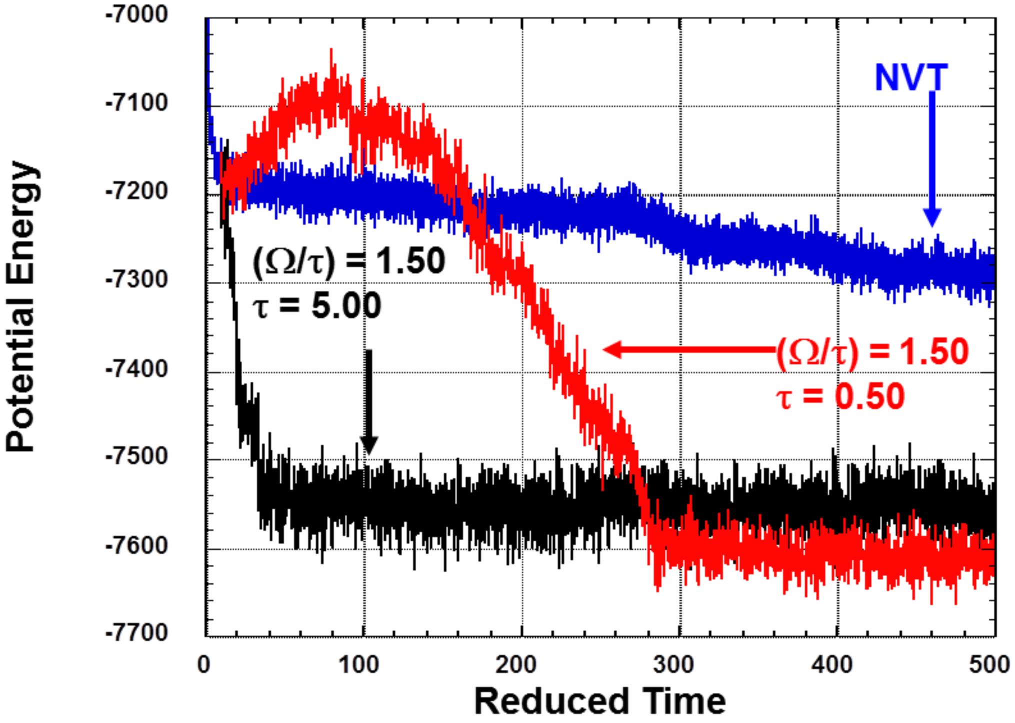

Figure 10.1. From Jenkins[7]. Plot of reduced potential energy vs. reduced time for two simulations with different PCND parameters and one simulation run without PCND. The simulations with PCND reach the equilibrium state significantly faster than the simulation without.

10.2. Protracted colored noise for polymer systems

The LJ-glass version increased the intensity and the time correlation of thermal fluctuations, but the immediate application of this increase in fluctuations to the polymer system may not be useful. Applying an exponentially correlated force on every atom in a polymer (or bead in a coarse grained polymer) would increase fluctuations, but perhaps not in a way that would ultimately increase diffusivity. Unless all the atoms in the chain by chance happened to fluctuate in the same direction, the stochastic forces may simply act on the internal bond and angle energies of the polymer instead of moving the polymer through space. Apply the force identically to all atoms or beads in a chain might work better, but would result in unrealistic motion, especially in the case of entangled chains. In the limit of many entanglements, it may not move the chains at all and again only act on the internal energy of each polymer. Instead, it could be envisioned that applying the force along the backbone of the polymer would result in the most realistic movement of the chain; essentially the force would encourage a reptation like motion. This work will describe PCND for polymer systems and demonstrate its effectiveness in a BCP-DSA context, though the results should be useful for any similar polymer system.

The same coarse grained molecular dynamics model that has been used throughout this thesis has been used here. As described earlier, NVT simulations have been run using the Nosé-Hoover thermostat algorithm. A stochastic force was applied using Equation 10.11 through Equation10.15, which culminate in Equation 10.16 where U(x) is the potential energy, ε is the stochastic force, and ζ is the drag associated with the temperature controller.

$$m\frac{d^2x(t)}{dt^2} = -\nabla U(x) + \varepsilon(t) - \zeta(t)\frac{dx(t)}{dt} \qquad 10.16$$

The stochastic force $\varepsilon(t)$ is calculated via Equations 10.11 through 10.15. This force was applied to every interior bead on a chain in the direction of the backbone of the chain. This direction was calculated by taking the vector between the two adjacent beads in the chain as shown in Figure 10.2. Every interior bead in a single chain experiences a force of equal magnitude, but the direction of this force is rotated such that the direction of the force is along the backbone of the chain. While the positive direction of the backbone is always from the A end of the chain to the B end of the chain, the force can be negative, which is the same as applying a positive force in the reverse direction. The end bead did not experience any stochastic force due to PCND. The timescale over which the force changes values is determined by the parameter τ, or the correlation time. The root mean square of the force is determined by the parameter Ω/τ. The effect of τ is visualized in Figure 10.3 where various series of forces are calculated through time for various τ values. The series are offset for clarity. When τ is zero, the noise is completely random, and as τ increases, the correlation time of the force increases, that is, the force changes directions more gradually. The stochastic force algorithm was programmed into HOOMD-blue[17,18] by modifying the existing code. The random numbers are calculated at every timestep using Mersenne Twister[19] algorithm for each instance at each timestep, specifically the MT19937 implementation. The algorithm is seeded with the current time in seconds from midnight January 1, 1970 UTC.

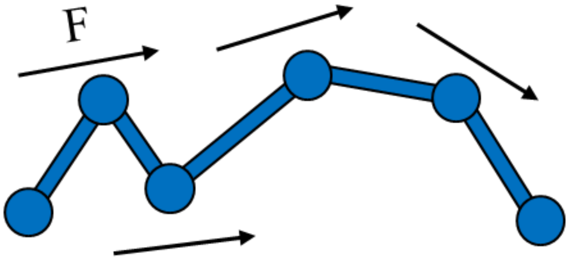

Figure 10.2. Visualization of how the stochastic forces are applied in polymer PCND. The forces are applied along the backbone of the chain, that is, the force on an interior bead is applied along the vector between the two adjacent beads. The magnitude of the force is the same for every bead on the chain and can change sign with time.

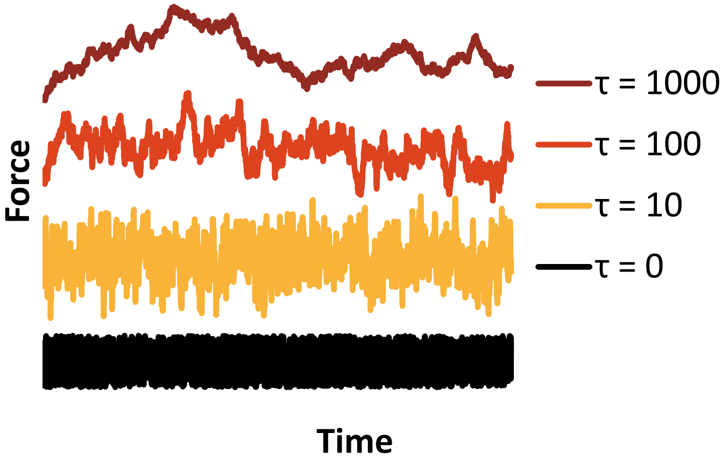

Figure 10.3. Representative plot of the magnitude of the force over time for a single chain at various values of τ. As τ increases, the force magnitude is correlated over longer times. The various τ series are offset for clarity.

The effect that PCND has on the fluctuations in the system can be visualized by plotting energy histograms. Figure 10.4 plots energy histograms for simulations with PCND (Ω/τ = 0.1 kcal/mol and τ = 1000 ps) and without PCND at two different temperatures. Adding PCND to the system keeps the average energy constant, (as is required to keep the temperature constant) but the width of the distribution is increased. This increase in width results in more high energy beads and polymers, which translates into better phase space sampling, that is, energy barriers are sampled over more efficiently. Interestingly, the effect of temperature is much greater than the effect of PCND on the amount of high energy beads. This might suggest that increasing the temperature for a short period of time may be a way to sample over energy barriers, however it will be shown later that this is not as effective as PCND.

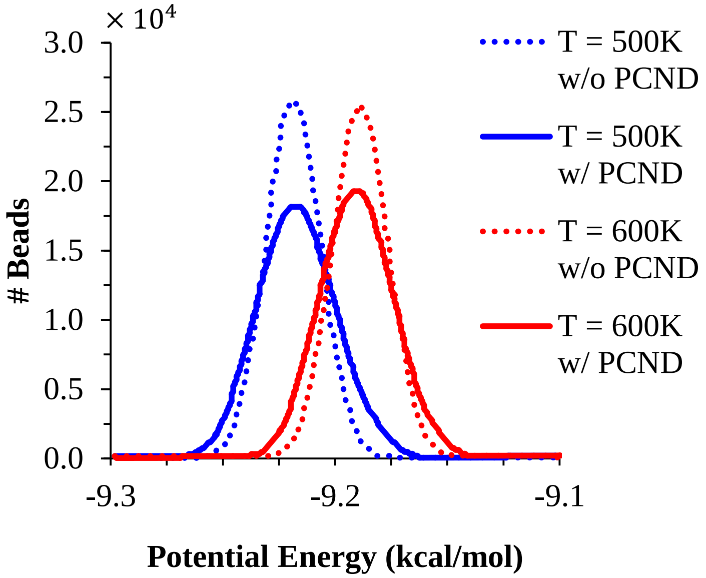

Figure 10.4. Histogram of the potential energy of beads with and without PCND at 500K and 600K. The inclusion of PCND slightly widens the energy distribution.

10.3. Applications of PCND for polymer systems

10.3.1. Increased Diffusion

The effect of PCND on diffusion was measured. It is expected that increased τ and Ω/τ values would increase diffusion. This was measured for homopolymers for which $N = 64$ using the same potential set as used throughout this work for various τ and Ω/τ and the results are shown in Figure 10.5. Diffusion as a function of τ seems to fit a power law of about $\tau^{0.29}$. Small values of τ give significant increases in diffusion but larger values yield diminishing returns. The effect of Ω/τ looks to be much more linear. Figure 10.6 shows the coefficient of the fits shown in Figure 10.5 as a function of Ω/τ, and these points seems to fall along a line, but more points are necessary to confirm. PCND clearly provides increased diffusivity. Increasing more than an order of magnitude would require very large parameters.

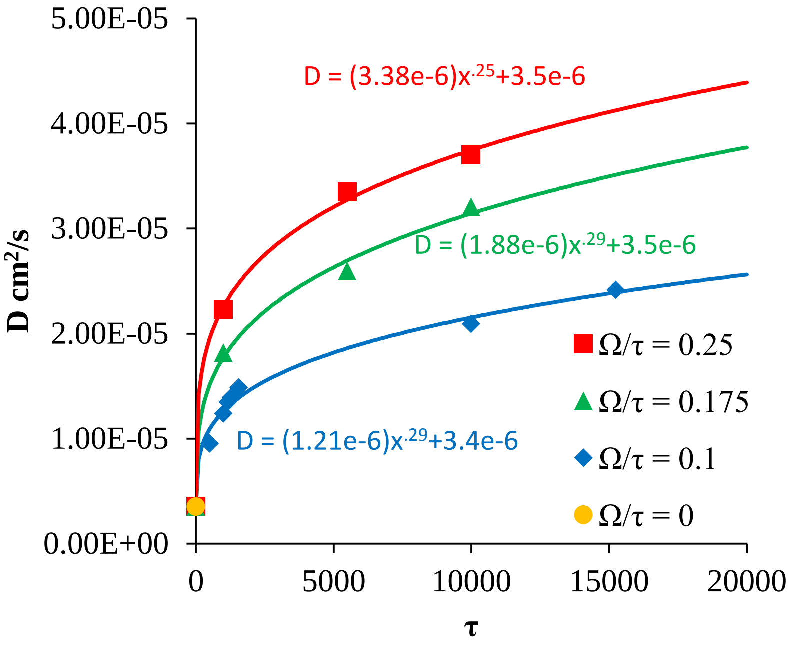

Figure 10.5. Plot of diffusion constant as a function of τ for various Ω/τ for N = 64. Diffusion appears to scale with $\tau^{0.29}$ at various values for Ω/τ.

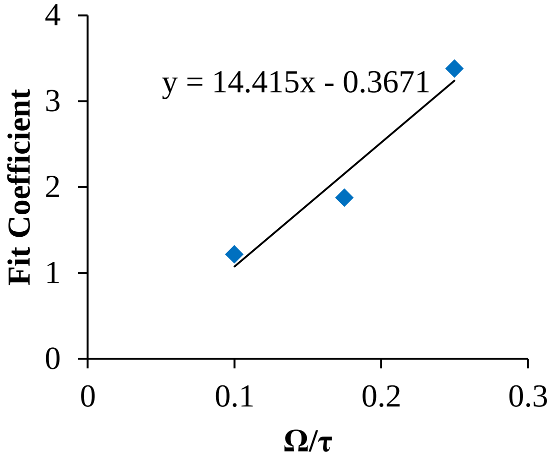

Figure 10.6. Plot of the fit coefficients from Figure 10.5 as a function of Ω/τ. The coefficients, and thus diffusion, appears to scale linearly with Ω/τ.

The stochastic force (ε(t), as described by the parameters Ω/τ and τ) force (along with thermal energy) moves the polymer through the bulk, but the non-bonded potential opposes this motion, essentially imposing a drag force. Ω/τ would be considered high when it is large compared to the non-bonded interaction strength of the homopolymers. However, the strength of Ω/τ is confounded with τ and the length of the polymer chain (*N*). Because every bead on the chain experiences the Ω/τ force, the total force on a chain scales with the number of beads. What would be considered a large τ is less clear. Previously, a range of τ values were used to find what values would work best,[7] but presumably τ could be compared to the relevant relaxation times of the polymer of interest.

10.3.2. Increased defect heal rate

Defect healing rate is used as a measure of the effectiveness of PCND. The defect rate was measured using the method described in Chapter 9, but a brief description will be given here. A defect was built using an external potential in a fully periodic simulations were built at five times the natural repeat distance of the BCP in the *x* dimension, three times the natural repeat distance of the BCP in the *y* dimension, and at one times the natural repeat distance of the BCP in the *z* dimension. The defect heal rate was calculated using Equation 10.17:

$$R_{sim} = \frac{F_H}{t_{ave}} \qquad 10.17$$

R_{sim} is a measure of the rate of defect healing in the simulation; it includes both the time before the defect begins healing and the time it takes for the defect to heal once the transition has begun. This rate should change in response to PCND, but this does not indicate a change in the true rate of the modeled system, only in rate recorded in the simulation. Without PCND these rates are identical, but because PCND is applied with the intention of reducing simulation time, and therefore increase simulation rate, R_{sim} will differ from the intrinsic defect heal rate. F_H is the fraction of defects healed in the maximum simulation time and t_{ave} is the mean time to heal of the simulations that did heal within the maximum simulation time. In general, F_H is one because all of the defects annealed within the simulation time, so R_{sim} is simply the average rate for these simulations to anneal. In the case of T = 600K and T = 700K for χN = 55 and no PCND, no simulation healed in 500,000 ps.

In order to demonstrate the usefulness of PCND for polymer systems, the effect on defect anneal rate was measured and compared to simulations without PCND. The results of defect anneal rate without PCND are taken from the chapter 9.Defect heal rates for a jog defect are plotted as a function of χN for N = 64. The rate is relatively constant for $\chi N < 30$ because, as explained in the chapter 9 the simulations in this region are limited by the diffusion of mass into the already healing defect, not the initialization of the healing process. Above this value, the rate decreases exponentially. In order to clearly show the effect that PCND had on the rate of defect healing, defects were run with PCND at a χN of 55. Extrapolating the results of the simulations without PCND gives a rate of approximately $5x10^{-9}$ defects / ps. As shown in Figure 10.7A, running the same simulations with the addition of PCND with parameters of various Ω/τ for $\tau = 500$ ps, the rate of defect healing was drastically increased. In the best case the rate increased more than 10,000 times over the extrapolated rate without PCND. Increasing Ω/τ increases defect rate because larger Ω/τ values sample more efficiently. It is possible that further increase of in Ω/τ would reduce the defect rate even further, but at that point there is likely to be deviation in the natural pitch, as will be discussed later. It is worth noting that the maximum rate achieved using PCND is very similar to the maximum rate achieved at low χN without PCND.

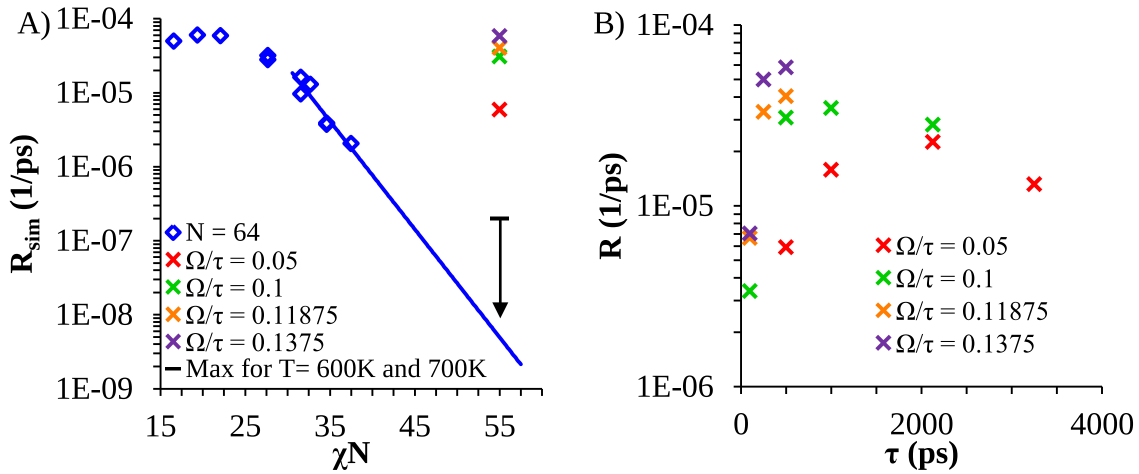

Figure 10.7 Plots of the simulated rate of defect healing as a function of χN and PCND parameters for N = 64. A) shows defect heal rates as a function of χN without PCND alongside rates using PCND at various Ω/τ values for τ = 500 ps and maximum rates at elevated temperatures. All PCND sets show a massive increase in rate, ~200 times faster than the extrapolated rates that do not use PCND. Increasing temperature does not increase the rate as much as PCND does. No defect healed in the given time frame for the elevated temperatures and the rate shown is likely higher than the real rate. B) shows the defect heal rates as a function of τ and Ω/τ. Rate is not sensitive to PCND parameters, though they do look to drop as τ nears zero, as would be expected.

Figure 10.7B plots defect heal rates as a function of τ for various Ω/τ. It appears that there may be some peak rate in τ. Larger τ values increase sampling over energy barriers and therefore increase defect heal rate, but if that value is too large then pathways that do not lead to a healed defect are probed for too long, so time is wasted and the rate decreases. It appears that the peak in defect heal rate decreases with increasing Ω/τ, but more data is needed. This would make sense because at larger Ω/τ values the time required for a certain pathway to be properly probed is decreased, and so τ can be decreased so that more pathways are probed more quickly, ultimately reducing the time for a defect to heal.

One obvious alternative to implementing the PCND process is to temporarily increase the temperature of the simulation. As mentioned regarding Figure 10.4, increasing the temperature has a greater effect on the number of high energy beads in the system. In addition, increasing temperature temporarily is very easy and all platforms are capable of doing so with no extra work. However, increasing temperature does not work nearly as efficiently as using PCND. Simulation sets were run at three temperatures, 600K, 700K and 1000K and the rates were measured as before using the same initial defects (as would be found in a 500K system) as in the PCND case. The goal is to remove the defect and reach the final defect free state. The defect is one that would occur in a 500K system, and occurs at the natural pitch of a 500K system. The pitch of the guiding layer and the natural pitch polymer used to build the defect is not adjusted to accommodate for the changes in pitch associated with temperature. This is because the increase in temperature is would be a temporary one used to quickly sample over energy barriers in the annealing process. Once the polymer has been able to cross the energy barriers, the temperature would then be returned to the base temperature or 500 K. The 600 and 700K simulations did not produce any measurable results within 500,000 ps. The point shown in Figure 10.7 for T = 600 and T= 700 refers to the rate that would be measured if each had one defect heal at 500,000.05 ps, that is, one timestep past the end of the run. This theoretically would be the maximum rate unless a cascade of defects began to heal soon after the end of the run which is unlikely. Even with the cascade healing though, the measured rate would only be slightly higher. Regardless, the theoretical rate for these simulations is far lower than the rate of the PCND simulations.

Simulations were also run at 1000K, but the change in pitch was so immense at this temperature that a completely different structure was formed. Instead of healing the defect, all of the lines buckled in order to match the significantly lower natural pitch of the high temperature simulation, as shown in Figure 10.8. The 600K and 700K simulation also showed a slight slanting because of the incommensurability of the natural pitch at the elevated temperature as compared to the natural pitch at the original temperature. The simulation with PCND shows more fluctuations (as seen in the rougher line edges) than the systems without PCND, which is to be expected, but the overall pitch is nearly identical and no slanting or buckling can be detected, as seen in Figure 10.8. By including PCND with parameters that do not significantly affect the equilibrium state, the rate at which defects are sampled over is increased by 4 orders of magnitude.

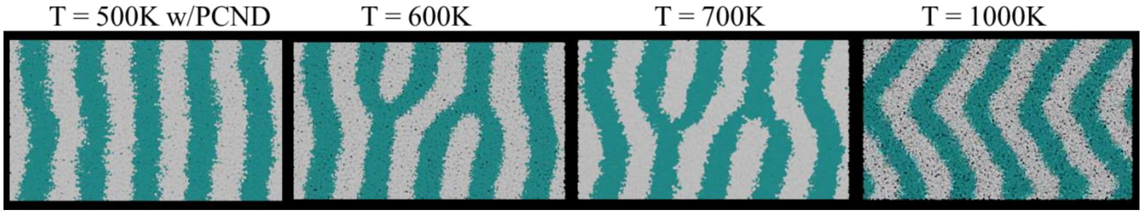

Figure 10.8. Images of end states of representative simulations. The elevated temperatures cause a decrease in pitch which results in a tilt in the lamellae. At T = 1000K the tilt is so extreme the lines buckle. At 500K under PCND (Ω/τ = 0.1 kcal/mol, τ = 500 ps) there is no tilting because the natural pitch remains unchanged. There is increased interfacial roughness due to the increased fluctuations.

The increase in temperature is not as effective as PCND because in PCND all the beads on a chain experience a force in a particular direction that is correlated along the length of the chain, resulting in one increased mode of movement (reputation). On the other hand, the higher energy states reached by increasing temperature increases translation in all directions randomly as well as increasing bond vibrations, resulting in less useful fluctuations. PCND's motions specifically creates that concerted motion and moves individual chains.

10.3.3. Efficiency of the PCND algorithm

The effect of PCND on the overall calculation time was also computed. A simulation of 15,900 beads in chains 1000 beads long was run and the time spent on each part of the calculation was computed using HOOMD's built in profile option and the results are shown in Figure 10.9. The PCND calculation is about 5% of the overall calculation time, indicating a relatively efficient process. The other columns in Figure 10.9 refer to the bond force and energy calculation, the angle force and energy calculation, the integration, the Lennard Jones neighbor list calculation, the Lennard Jones force and energy calculation, and the overhead of memory transfers and other process required by HOOMD's algorithms. This time will depend on the chain length because the force magnitude is calculated once for each chain length; smaller chains will take a longer time than longer chains. Fortunately, longer chains will probably benefit more since they will generally have larger energy barriers and generally slower kinetics. More optimization is probably possible, as this was simply done by a modification of existing code and not programmed from scratch. Even in this current method though, PCND is fairly efficient.

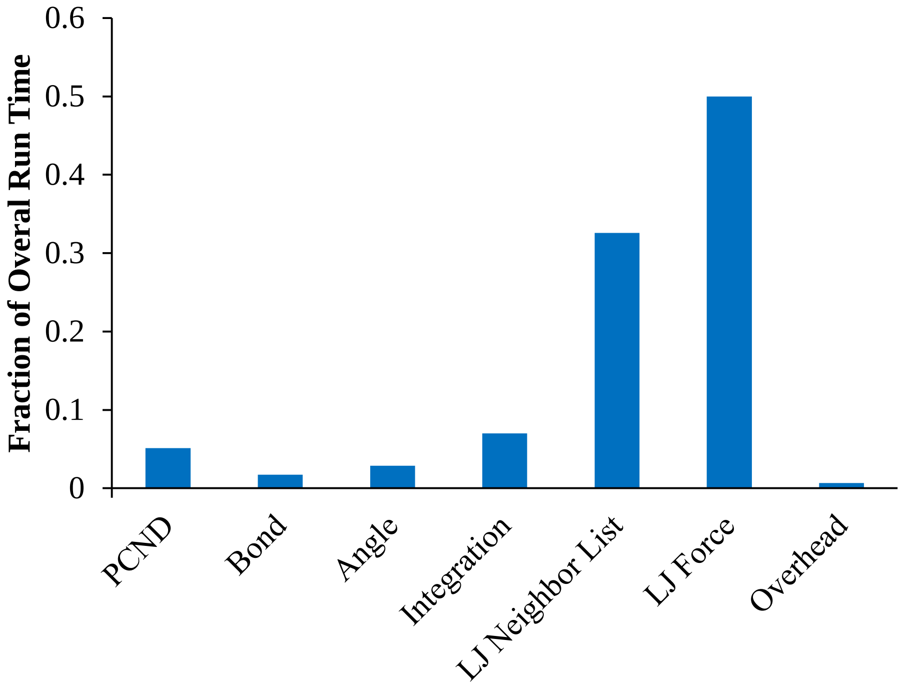

Figure 10.9. Time spent for various calculations during MD simulation in HOOMD. PCND account for approximately 5% of the overall calculation time when N = 1000. Smaller N will result in an increase in the relative time spent calculating the PCND force.

10.4. Limits of PCND parameters

PCND parameters in the previous sections were chosen to highlight the advantages of PCND. However, the effect that parameters have on the system as a whole is an important question. One way to determine what values of τ and Ω/τ are appropriate and what values are too large is to find the point at which a BCP loses cohesion under the influence of PCND. This point was found for BCPs with a degree of polymerization of 64, 96 and 128 for a non-bonded interaction strength between unlike beads (ε_{AB}) of 0.3. This transition is measured using the structure factor with a Lorch window function as calculated using Equation 10.18. [20,21] This method was also used to measure the natural pitch of the BCP systems as described in Chapter 1.

$$S(q) - 1 = 4\pi\rho_0 \int_0^R \frac{sin\,qr}{qr}[g(r) - 1]\frac{sin(\pi r/R)}{\pi r/R}dr \qquad 10.18$$

The structure factor is essentially equivalent to the result of a scattering experiment, which are often used to measure the ODT is experimental systems.[22-25] As order is lost, there is a significant change in peak height of the scattering intensity, specifically to lower peak heights. Here, the structure factor was measured as a function of τ for a given Ω/τ for N = 64, 96 and 128. Simulations were run for ~ 50 ns. When there was a significant decrease in the peak height, the simulation was considered to have undergone a a disordering transition. The structure factor results for N = 64 and Ω/τ = 0.1 kcal/mol are shown in Figure 10.10. Adding PCND shrinks the peak of the structure factor due to the increase fluctuations, but significant changes in τ show little effect on the scattering peak height. However, the small increase from τ = 15,000 ps to τ = 15,250 ps shows a very large decrease in peak height. At this point, the cohesion of a single lamellar phase is lost and fluctuations dominate, as is corroborated by Figure 10.11. In Figure 10.11, the orientation of the lamellae changes, but otherwise the changes are relatively small as τ increases to 15,000 ps, but as τ reaches 15,250 ps, the lamellae are clearly beginning to disintegrate. This is not the same as a ordered to mixed transition as occurs when χN drops too low, but is a different type of transition where the lamellae are constantly fluctuating and reorienting, but the phase separation remains. This transition is not common in the study of BCP systems and so more work is required to fully understand the nature of this transition. For the work described here it is only important to point out that a BCP dominated by fluctuations will be largely useless and so this transition can be considered an upper limit of usefulness.

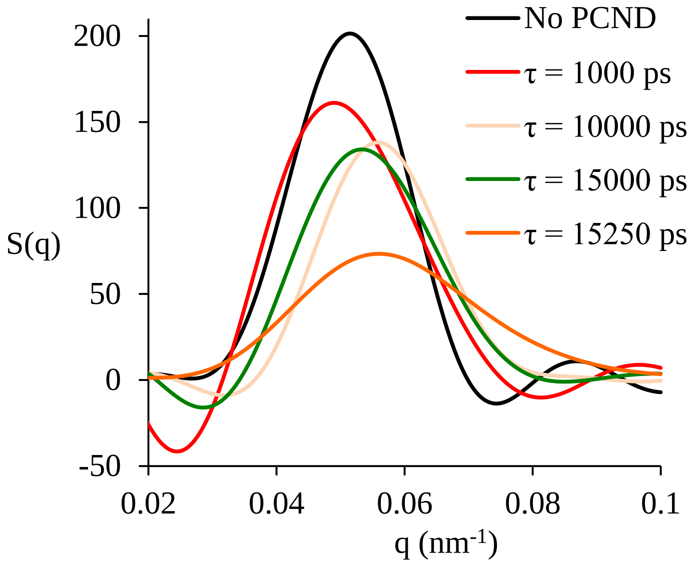

Figure 10.10. Representative plot of the structure factor (S(q)) for various values of τ for Ω/τ for N = 64. At low τ values, the size and location of the peak changes little with τ. However, the small jump from τ = 15,000 ps to τ = 15,250 ps results in a sharp decrease in peak height. This sudden drop is associated with the ODT and means the BCP is now mixing.

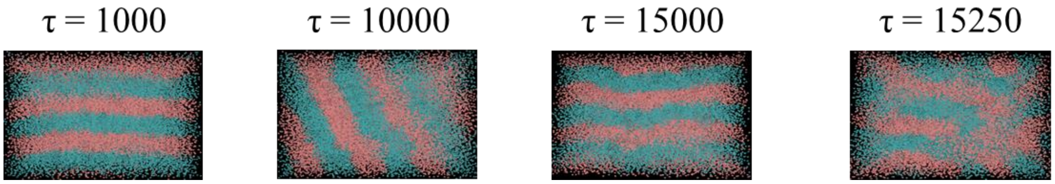

τ = 1000

τ = 10000

τ = 15000

τ = 15250

Figure 10.11. Images of the simulations for which the structure factor was calculated in Figure 10.10. Rotations and increases in interfacial roughness can be seen as τ increases for τ ≤ 15,000 ps, but when τ reaches 15,250 ps the simulation has started to mix.

This transition as a function of Ω/τ and τ is found in Figure 10.12A. Everything to the upper right of the lines shown mix, while everything to the lower right still order at this value of χ. Large Ω/τ values require smaller τ values to induce mixing. A short, strong force is not enough to mix the system, as it does less work and ultimately applies less energy towards mixing the system than a strong force applied over time. This leads to the result that the mixing curves in Figure 10.12A are dependent on both τ and Ω/τ. It is the work done by the stochastic force that causes mixing. As mentioned before increasing N increases the total force on the chain because each bead receives the same force. Figure 10.12B plots the mixing curve as N · Ω/τ vs. τ. Plotting in this way, the transition for each N has very similar values. The small discrepancies may be improved by using finer differences in parameters. By scaling Ω/τ by N, the plot is then the overall force on the chain vs. the time the force is applied. It is the overall force on the chain that appears to be important, not the force on any given bead. The effect of τ on the mixing curve seems to be smaller as τ increases, similar to the diffusion curves. Diffusion increases slowly at large τ, which suggests that the ultimate drive to mix may have a similar dependence at large τ. More work is required to fully understand the dependence of this mixing curve on τ, Ω/τ and N but this gives an idea of the relevant operating range for a simple study on the usefulness of PCND for polymers.

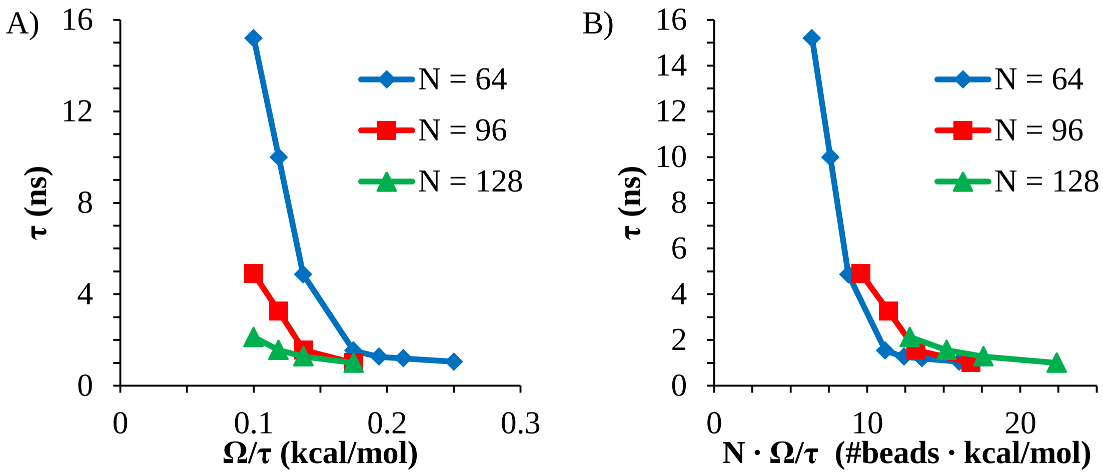

Figure 10.12. Plot of the disorder transition (but not ordered to mixed transition) of a polymer as a function of τ and A) Ω/τ or B) N· Ω/τ for various N. Parameters above and to the right of the curves, the BCP simulation mixes, while parameters below and to the left of the curves the BCP simulation phase separated.

The results in Figure 10.12 only give the absolute limit of parameters that could be used. Any values at this limit or beyond will only mix the system and ultimately produce useless results, but what effect does this have on the free energy of the system at values to do not mix the system? A direct free energy calculation is time consuming and fairly difficult, but a proxy, like the effect of PCND parameters on the natural pitch of the BCP, is both easier and quicker than the full free energy calculation. The effect that PCND had on the natural pitch of the system was measured using the structure factor in Equation 10.18. The location of the peak gives the plane to plane repeat distance of the polymer as described in Chapter 1. For a lamellar morphology, the plane to plane repeat distance is equivalent to the natural pitch of the BCP. The natural pitch of a $N = 64$ lamellae forming BCP is shown in Figure 10.13 as a function of τ for various Ω/τ . The black line refers to the natural pitch found without PCND and is plotted at all τ values for comparison. When τ is low compared to the τ that caused mixing (the points shown go up to the largest τ that did not cause mixing), the pitch is only minorly disturbed compared to the no PCND case. For example, when τ is ~2000 or below, the measured pitch of the Ω/τ is within 3% of the simulation without PCND except at the largest Ω/τ. Larger values of Ω/τ have similar behaviors. At higher τ values the deviation is more significant. Simulations using PCND should be operated in the region where the pitch is minimally affected. The effect that χN has on pitch significantly more than the effect that PCND has on pitch. As χN varies from 70 to 10.5 (the ODT), the natural pitch varies from 6.6 nm to 13.3 nm, far greater than the change in pitch due to PCND shown in Figure 10.13.

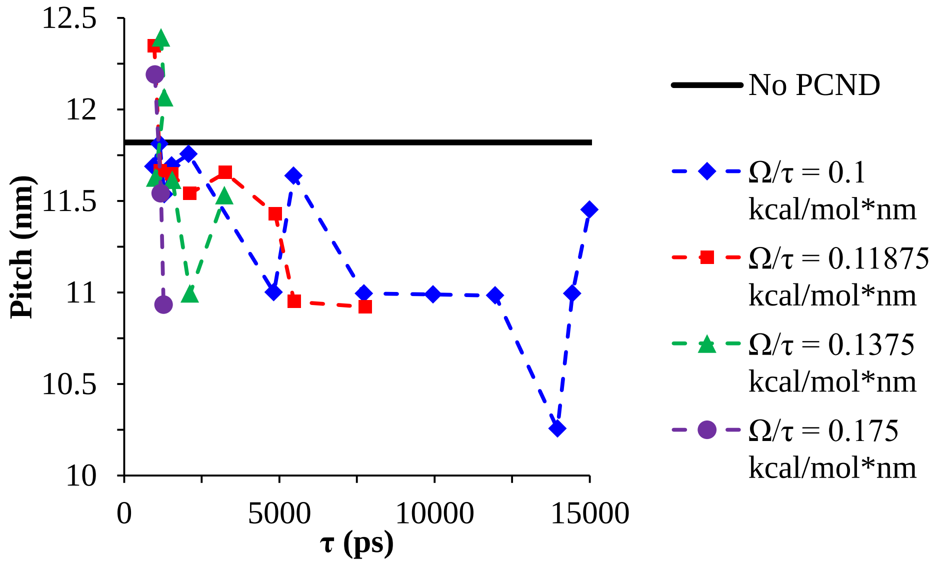

Figure 10.13. Plot of measured natural pitch as a function of τ and Ω/τ for N = 64. At low values of τ, PCND does not perturb the natural pitch. Higher values yield a slight perturbation in pitch.

The results shown for the kinetic healing rates were chosen as to optimize heal rate without significantly perturbing the system as described in Figure 10.12 and Figure

10.13. The extra fluctuations in such simulations can be quickly removed by simulating without PCND.

Radius of gyration (R_g), end to end distance (r_0), bond length, and bond angle were measured for various PCND parameters that did not greatly perturb the natural pitch and the results are found in Figure 10.14. Including PCND for the modest parameters chosen has a negligible effect on the statistics shown.

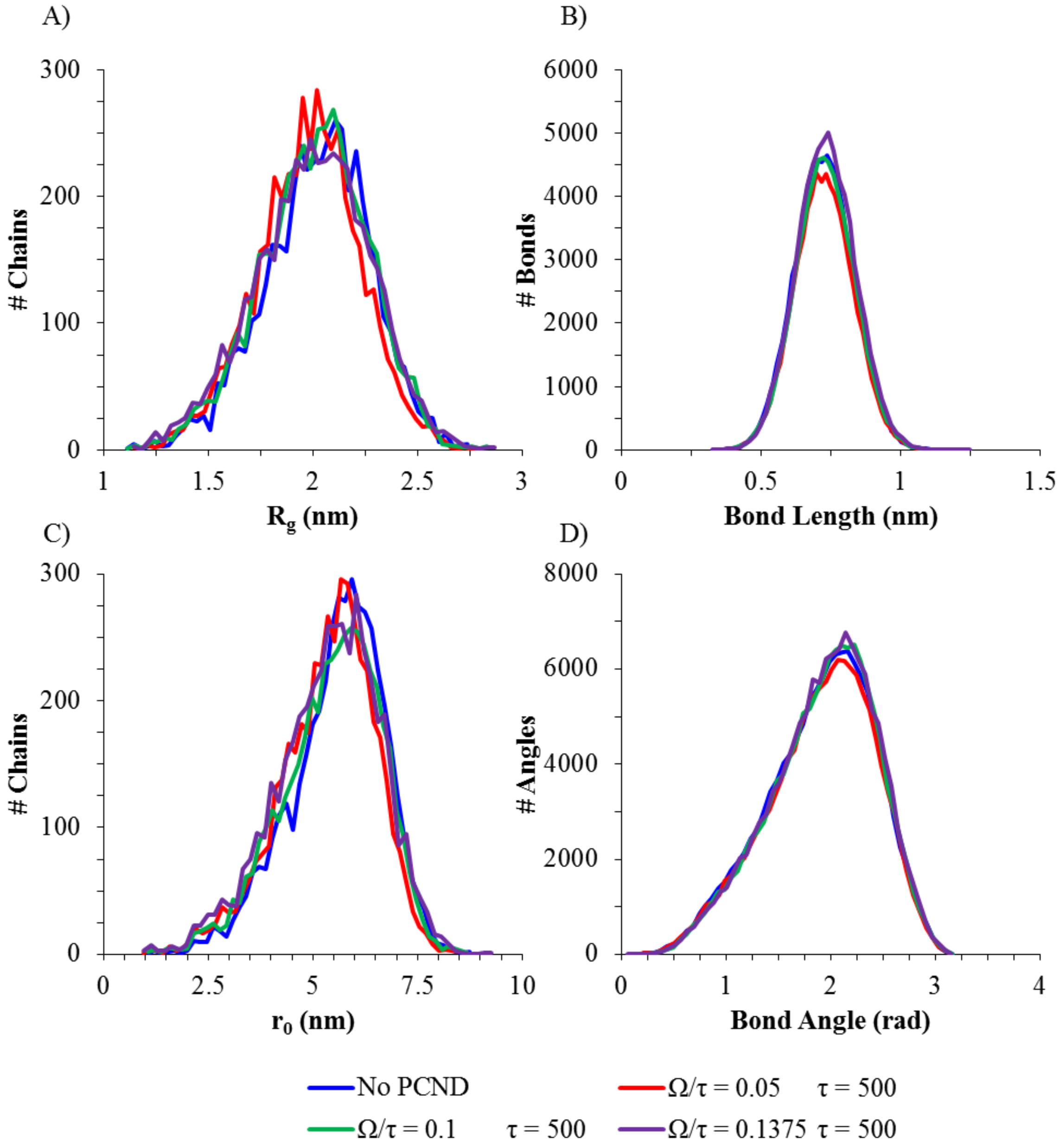

Figure 10.14. Histograms of A) radius of gyration (R_g), B) bond length, C) end to end distance (r_0), and D) bond angle for N = 64. PCND makes little difference on these statistics for the parameters shown here.

10.5. Conclusions

PCND was adapted for use in a polymer system. Instead of applying an independent stochastic force to every bead or atom in a simulation, the stochastic forces applied were the same for a given chain, and applied in the direction along the backbone of the chain. Some preliminary studies on the effects of PCND and its parameters on energy distributions, diffusion, and equilibrium state were done. As expected, a slight widening of the distribution of energy was found. It was also found that diffusion increased following a power law as τ increased, and apparently linearly as Ω/τ increased. An order-disorder transition curve for PCND parameters was generated for BCP's with degrees of polymerization of $N = 64$ and $N = 96$. It was found that a combination of τ and Ω/τ were required to induce mixing and that the effect of Ω/τ scales with N. The product of Ω/τ and N that induces mixing in the system is a constant for a given τ. This indicates that it is the force on the overall chain that is important for mixing, not the force on the individual. The effect on equilibrium domain size was measured as a proxy for PCND's effect on equilibrium states. There exists a set of parameters that has little to no effect on the equilibrium domain size of the polymer system for the systems studied here. As the mixed state is approached, there is found to be a decrease in pitch, approximately 12 % of the overall pitch at worst. Defect healing rates were calculated as a function of χN. Compared to previous results at high χN, PCND increased heal rates by a factor of ~ 10,000 even for very small parameters for PCND. Larger Ω/τ increased this rate but there appeared to be an optimal τ value away from which rate decrease. However, even at non-optimal values significant increases in rate as compared to the simulation without PCND were found. A comparison was made to defect heal rate with temperature increase. It was found that temperature did not increase heal rates nearly as fast as PCND, and the effect on equilibrium morphology was greater indicating that PCND is a better tool for sampling over energy barriers and better sampling phase space. PCND, as implemented in HOOMD, was found to be a relatively efficient process in terms of total CPU (or GPU) time.

10.6. References

1 Detcheverry, F. A.; Pike, D. W.; Nagpal, U.; Nealey, P. F.; de Pablo, J. J. “Theoretically informed coarse grain simulations of block copolymer melts: methods and applications” Soft Matter (2009), 5, 4858.

2 E. Helfand, J. Chem. Phys., 1975, 62, 999.

3 M. Matsen, J. Phys.: Condens. Matter, 2002, 14, R21.

4 G. H. Fredrickson, The Equilibrium Theory of Inhomogeneous Polymers, Clarendon Press, Oxford, 2006.

5 Lawson, R. A.; Peters, A. J.; Ludovice, P. J.; Henderson, C. L. " Coarse grained molecular dynamics model of block copolymer directed self-assembly ", Proc. SPIE 8680, Alternative Lithographic Technologies V, 86801Y (2013).

6 Langevin, P.; Comptes. Rendues. (1908), 146: p. 530.

7 Jenkins, J. “Novel Efficient Simulation Techniques for use in Molecular Modeling“. Dissertation, Georgia Institute of Technology. Atlanta, Georgia. July 2000.

8 Zwanzig, R.; Journal of Chemical Physics. (1960), 33: p. 1338-41.

9 Zwanzig, R.; "Statistical Mechanics of Irreversibility; Lectures in Theoretical Physics"; (eds. W. E. Brittin, B. W. Downs, and J. Downs); v. 3; Interscience Publishers; New York; (1961).

10 Zwanzig, R.; Physical Review. (1961), 124: p. 983-92.

11 Mori, H.; Progress in Theoretical Physics. (1965), 33: p. 423-55.

12 Mori, H.; Progress in Theoretical Physics. (1965), 34: p. 399-416.

13 Kubo, R.; Reports on the Progress in Physics. (1966), 29: p. 255-284.

14 Fox, R. R; Gatland, I. R.; Roy, R.; Vemuri, G.; Physical Review A. (1988), 38: p. 5938-40.

15 Knuth, D. E.; "The Art of Computer Programming." Addison-Wesley; Reading MA; volume 2; (1969).

16 Matsumoto, M.; Nishimura, T. "Mersenne twister: a 623-dimensionally equidistributed uniform pseudo-random number generator". ACM Transactions on Modeling and Computer Simulation 8 (1): 3–30 (1998).

17 HOOMD-blue web page: http://codeblue.umich.edu/hoomd-blue

18 J. A. Anderson, C. D. Lorenz, and A. Travesset. „General purpose molecular dynamics simulations fully implemented on graphics processing units“ Journal of Computational Physics 2008, 227(10), 5342-5359

19 Matsumoto, M.; Nishimura, T. "Mersenne twister: a 623-dimensionally equidistributed uniform pseudo-random number generator". ACM Transactions on Modeling and Computer Simulation 8 (1): 3–30 (1998).

20 Lorch E A 1969 J. Phys. C: Solid State Phys. 2 229

21 Du, J.; Benmore, C. J.; Corrales, R.; Hart, R. T.; Webler, J. K. R."A molecular dynamics simulation interpretation of neutron and x-ray diffraction measurementson single phase" Y2O3–Al2O3 glasses, 2009 J. Phys.: Condens. Matter 21 205102

22 Takahashi, Y.; Kitade, S.; Noda, M.; Ochiai, N; Noda, I; Imai, M; Matsushita, Y. “Order-Disorder Transition of Symmetric Poly(styrene-b-2-vinylpyridine) in Bulk and Solution” Polymer Journal 1998, 30,388.

23 Bates, F. S.; Rosedale, J. H.; Fredrickson, G. H. “Fluctuation effects in a symmetric diblock copolymer near the order–disorder transition” J. Chem. Phys. 1990, 92, 6255.

24 Hasegawa, H.; Sakamoto, N.; Takeno, H.; Jinnai, H.; Hashimoto, T.; Schwahn, D.; Frielinghaus, H; Janβen, S.; Imai, M.; Mortensen, K. “Small-angle neutron scattering studies on phase behavior of block copolymers” J. Phys. Chem. Solids 1999, 60, 1307.

25 Maurer, W. W.; Bates, F. S.; Lodge, T. P.; Kristoffer, A.; Mortensen, K.; Fredrickson, G. H. “Can a single function for χ account for block copolymer and homopolymer blend phase behavior?” J. Chem. Phys. 1998, 108, 2989.

CHAPTER 11

STUDY ON LINEAR A-B MULTIBLOCK PITCH, ODT, AND CHAIN CONFORMATIONS

11.1. Introduction

Block copolymers (BCPs) have been used in a variety of applications, including adhesive tape, upholstery foam, asphalt additives, and recently, nano-lithography for semi-conductor fabrication.[1] Decades of study have provided great advances in the understanding of block copolymers, especially in the case of linear diblock copolymers, the simplest form of block copolymer.[1-6] By using various computer simulation methods, including a variety of mean-field theories[7-10], Monte Carlo methods[11], and molecular dynamics methods[12], great insight has been made into linear diblock copolymers. Some of the more extensively studied topics include the order-disorder transition[13], order-order transitions between various morphologies, the repeat distance between morphological units such as cylinders, spheres, or lamellar sheets, the thickness of the interfaces between domains[9]. Thin films BCPs have enjoyed extra focus within the past decade or so because of their many applications in nanolithography, nano templating, nanoporous membranes, and ultra-high density storage media.[3] While linear dibock copolymers have been studied in great detail, and extensions made into triblock copolymers, few have focused on multiblock copolymers. The sheer number of possible configurations of multiblocks makes studying the entire space a significant challenge. This paper will consider simulations of one small subclass of multiblock copolymers, namely, multiblocks formed by the linking together of linear diblock copolymers. Applications will focus on those in the semiconductor manufacturing field.

For diblock copolymers, the order-disorder transition (ODT) is determined by the product of χ (the Flory-Huggins interaction parameter) and N, the degree of polymerization. Mean-field predictions place the order-disorder transition for a linear diblock copolymer at a χN of 10.5.[7] The repeat distance of the phase separated domains scales with $N^{2/3}$, and scales with $\chi^{1/6}$ when χN is high. When χN is low, these scaling powers increase, but the dependence on N is always 0.5 larger than χ.[9] In the field of semi-conductor fabrication a small repeat distance is desirable so that smaller features and therefore smaller transistors can be made. The focus of this paper is on linear multiblock copolymers containing two types of monomer, *A* and *B* types. Higher order block copolymers of the type studied here are made by linking smaller order block copolymers together. As seen in Figure 11.1, a triblock copolymer (A-B-B-A) is made of two di-block copolymers (A-B), and a tetrablock copolymer (A-B-B-A-A-B) is a triblock copolymer (A-B-B-A) linked with a diblock copolymer (A-B). Intuitively, this design prevents domain size from scaling with *N* as in diblock copolymers, as the domains will be limited by the size of the limited length of like sections in the polymer. This is has been shown to be true in the case of such tri-block copolymers experimentally. At the same time, increasing *N* may cause the system to remain above the ODT, even at pitches that would normally impossible with a traditional diblock BCP system. The effectiveness, or lack thereof of this idea, as well as insightful information into the configurations of chains in the phase separated lamellar state will be shown.

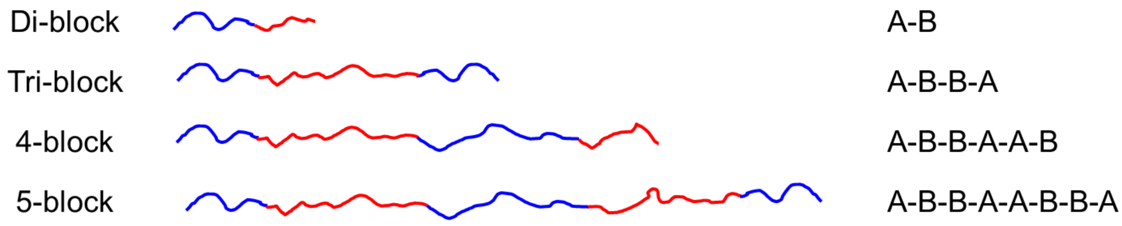

Figure 11.1. Types of block copolymers simulated in this work. Diblock copolymers are typically used in BCP-DSA, but other polymers may allow smaller domain sizes by depressed in the effective ODT.

11.2. Model

11.2.1. Coarse Grained Model

A coarse grained molecular dynamics model as used elsewhere is used here.[12] The polymers are coarse grained by representing four monomers (which corresponds to a statistical segment length) as a single bead. Four monomers was chosen because it approximately corresponds to the statistical segment length of polystyrene and poly(methyl methacrylate) as measured by atomistic simulations. Grouping a different number of monomers were grouped together into a single bead allows for different statistical segment lengths, and therefore different chain flexibilities to be modeled. Each bead experiences three different potentials: a nonbonded potential, a harmonic bond potential, and a harmonic angle potential. The non bonded potential is similar to a Lennard-Jones potential, but made softer and broader by using an 8-4 potential. It uses the form

$$E(r) = \varepsilon\left[\left(\frac{\sigma_{ij}}{r}\right)^8 - 2\left(\frac{\sigma_{ij}}{r}\right)^4\right] \qquad 11.1$$

where ε_{ij} refers to the strength of the interaction between beads of type i and j, r refers to the distance between the bead, and σ_{ij} refers to the point of lowest energy in the potential. Any two beads undergo this potential as long as they do not also participate in a bond or angle potential. Two bead types were used as shown in Figure 1, and are referred to as type *A* and type *B*, each representing a different arbitrary monomer. The potential function parameters for these tow bead types were set to reproduce properties similar to typical BCPs such as polystyrene and poly(methyl methacrylate) and the χ value of the system was manipulated via the ε_{AB} parameter. The relationship between χ and ε_{AB} was determined by assuming the ODT occurred at a χN of 10.5 as calculated by Liebler.[7] By measuring the ODT for a series of chain lengths, a relation between ε_{AB} and χ can be found. This is analogous to what is done experimentally by several other researchers who have measured the different ODT temperatures for different N and used this data to extract the χ-T relationship.[14-16] The full explanation and details of the relation can be found elsewhere.[17] The relation used here is found in Equation 11.2.

$$\chi = -7.845\varepsilon_{AB}{}^2 + 4.442\varepsilon_{AB} - 0.2426 \qquad 11.2$$

The same potential values as used elsewhere were also used here.[12,17] For the bond potential, the spring constant (k_{str}) used was 100 kcal/(mol*nm^2) and the equilibrium length used was 0.82 nm. For angle potential, the spring constant (k_{ang}) used was 5 kcal/(mol*nm^2) and the equilibrium angle used was 120°. For the nonbonded potential,

ε_{AA} and ε_{BB} were both set at 0.5 kcal/mol. All r values (σ_{AA}, σ_{BB} and σ_{AB}) were set at 1.26 nm.

11.2.2. Measurement of ODT

The SAXS peak intensity has been previously used experimentally to determine ODT temperature for different molecular weights of poly(oxyethylene)-poly(oxybutylene) diblock copolymers.[14] Data from this study is shown in Figure 2.15. In the experimental study, the peak intensity was studied as a function of temperature. At high temperatures, the system is mixed and as the sample is cooled: χ increases with decreasing temperature. The peak intensity is a nearly constant at temperatures where the system is mixed, but rapidly jumps to a much larger value at the ODT as the sample is cooled. Further cooling the sample in the ordered state shows a slowly increasing peak intensity as χ further increases. Identification of the ODT temperature by the rapid jump in scattering intensity was shown to give equivalent results to identification of the ODT temperature by conventional rheological measurements. The structure factor S(q*) (defined in Equation 11.3) provides equivalent information to the pattern observed in a small-angle scattering experiment and so the peak intensity of the structure factor should therefore give equivalent accuracy for identification of the ODT with changing interaction strength in simulation.[18-20]

$$S(q) - 1 = 4\pi\rho_0 \int_0^\infty r^2 \frac{\sin qr}{qr}[g(r) - 1]dr \qquad 11.3$$

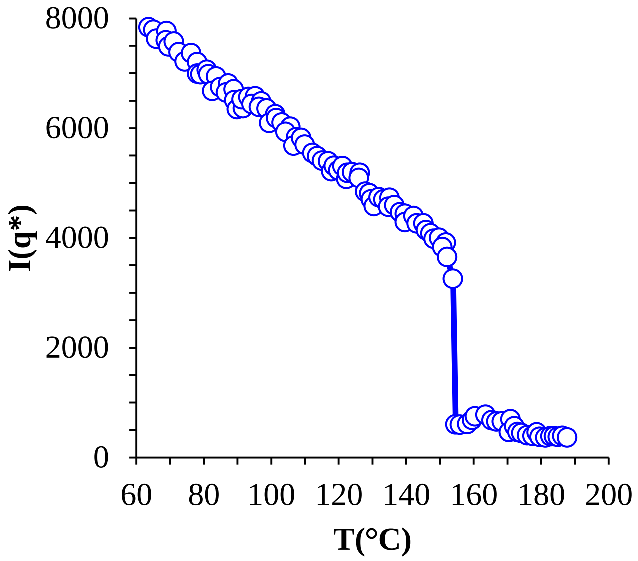

Figure 11.2. Changes in the scattering peak height for poly(oxyethylene)-poly(oxybutylene) diblock copolymers. A sharp increase in peak height is seen at the ODT. Data from Mai et al.[14]

The structure factor for a BCP simulation with N = 32 at different values of ε_{AB} is shown in Figure 2.16; these results are directly extracted from the simulations shown in Figure 2.14. Figure 2.16a shows the full structure factor while Figure 2.16b shows just the peak intensity S(q*). The full structure factor shows the expected behavior. The well separated structures at small ε_{AB} show strong sharp peaks corresponding to the domains of the BCP. As the interaction strength between A and B segments increases, the peaks become weaker and broader as the interface between domains becomes more diffuse. Peaks are still observed below the visual ODT of $\varepsilon_{AB} = 0.37$ (Figure 2.14) because of the correlation hole effect[7] and become very weak nearing the homogeneously mixed state. Considering the change in peak intensity in Figure 2.16b, there is an obvious jump in S(q*) as the system crosses the ODT (between $\varepsilon_{AB} = 0.36$ and $\varepsilon_{AB} = 0.37$)and a slowly increasing peak intensity in the ordered phase as the AB interaction decreases; both results are fully consistent with the experimental results. What appears different from the experimental result is that there is a reasonable increase in the peak intensity even in the disordered phase at $\varepsilon_{AB} = 0.37$ and below.

The increase in intensity in the disordered phase is fully consistent with Leibler theory[7] , and so should not be unexpected. The major difference between the experiment and our simulation results is likely due to the small system size in our simulation. The experimental scattering is the result of measurements over a volume that is likely microns to millimeters in length, while our experiments are only run on simulations that are nanometers in length. The radial pair distribution function can only be evaluated up to a distance r that is the smallest simulation box dimension divided by the square root of two. As a result, the upper limit on the integral in Equation 11.3 used to calculate the structure factor is limited to this same r value. Since the integration is only over a few periods (10-20 nm), the intensity of the scattering peak is relatively small, while in the experiment the periodicity may persist for microns and is included in the scattering spectra. This causes the ODT to be significantly sharper when measured experimentally as compared to computationally. However, the transition is still clearer seen in Figure 2.16b and the results match those found visually in Figure 2.14.

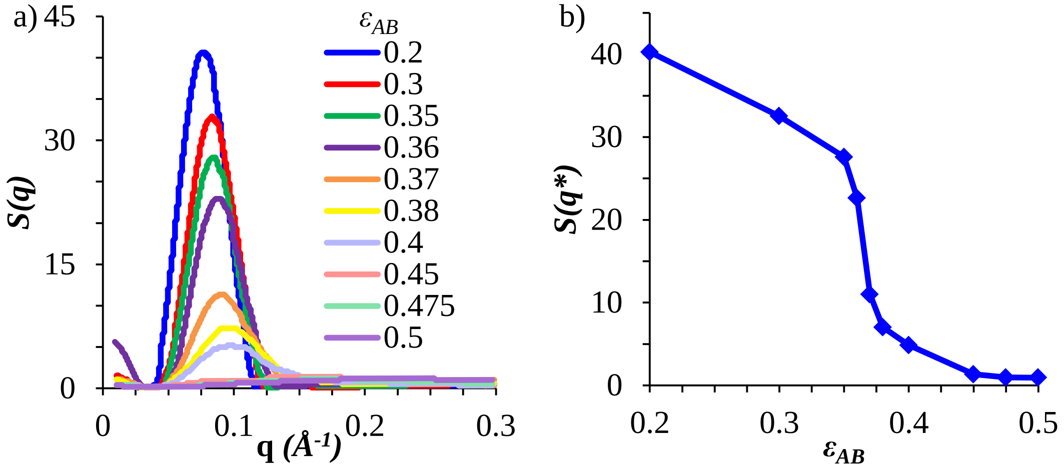

Figure 11.3. Changes in the structure factor for a BCP with N = 32 for different values of the AB interaction strength ε_{AB} (A) the full structure factor; (B) the peak intensity of the structure factor S(q*).

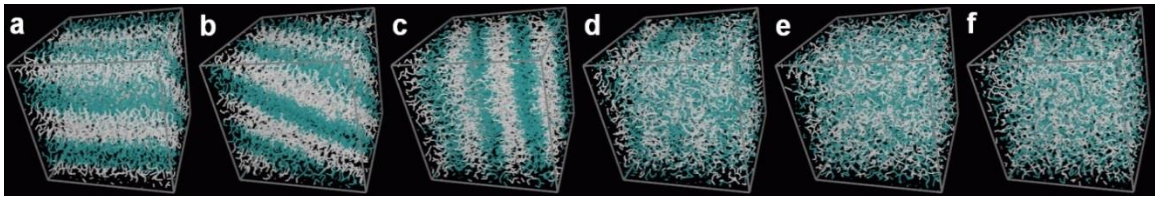

Figure 11.4. Bulk BCP structure after 100 ns simulation time for increasing ε_{AB} (decreasing χ), (a) $\varepsilon_{AB} = 0.2$, (b) $\varepsilon_{AB} = 0.3$, (c) $\varepsilon_{AB} = 0.36$, (d) $\varepsilon_{AB} = 0.37$, (e) $\varepsilon_{AB} = 0.4$, (f) $\varepsilon_{AB} = 0.5$, $\chi = 0$.

11.2.3. Calculation of Chain Orientation and Statistics

The radius of gyration (R_g) is commonly used to describe the size of chains in polymer systems, but the eigenvalues of the radius of gyration tensor (S) as described by Equation 11.4 can provide much more information about the shape and orientation of polymer chains in a system.[21]

$$S = \frac{1}{n}\sum_{i=1}^{n} \boldsymbol{s_i}\boldsymbol{s_i^T} = \begin{bmatrix} \overline{x^2} & \overline{xy} & \overline{xz} \\ \overline{xy} & \overline{y^2} & \overline{yz} \\ \overline{xz} & \overline{yz} & \overline{z^2} \end{bmatrix} \qquad 11.4$$

s_i is the position vector of a coarse-grained bead and the overbar denotes averaging over all backbone atoms in the chain. The center of mass of the chain is defined as the origin so that s_i describes coordinates away from the center of mass. Transforming S to a principal axis diagonalizes S, and a principal axis system can be chosen such that:

$$S = \begin{bmatrix} \overline{X^2} & 0 & 0 \\ 0 & \overline{Y^2} & 0 \\ 0 & 0 & \overline{Z^2} \end{bmatrix} \qquad 11.5$$

$$\overline{X^2} \geq \overline{Y^2} \geq \overline{Z^2} \qquad 11.6$$

The radius of gyration R_g is then equalk to the square root of the sum of squares of the eigenvectors of S, $\overline{X^2}$, $\overline{Y^2}$, and $\overline{Z^2}$.

$$R_g = \sqrt{\overline{X^2} + \overline{Y^2} + \overline{Z^2}} \qquad 11.7$$

The values of the eigenvalues of S can give us an idea of the shape of chains in the system. For example, if $\overline{X^2}/\overline{Y^2}$ is large, then the chain is extended along a single axis. In a phase separated BCP system this is generally an axis fairly perpendicular to the A-B interface. Similarly, $\bar{X}, \bar{Y}$, and $\bar{Z}$ then describe the size of the chain along is most extended axis, along the most extended axis perpendicular to the first, and along the axis perpendicular to those two axes respectively. This is shown in Figure 11.5 for a triblock (A-B-B-A) copolymer shown in two dimensions.

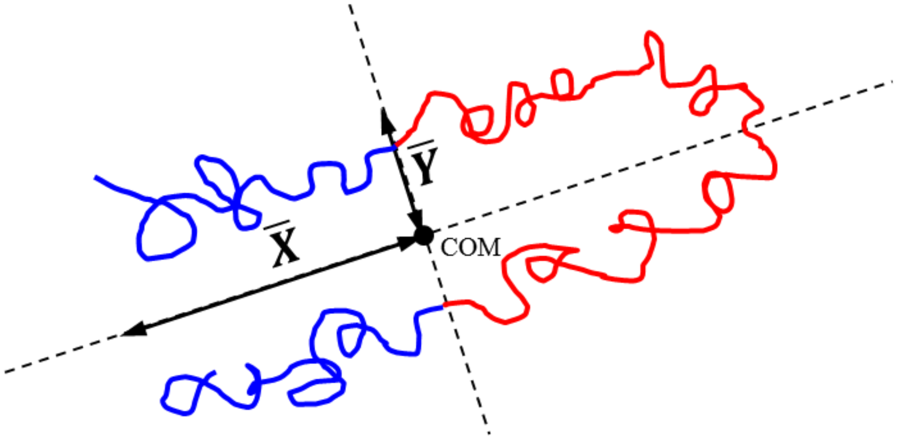

Figure 11.5. Diagram of the $\overline{X}$ and $\overline{Y}$ components of the radius of gyration.

11.3. Results and Discussion

11.3.1. Multiblock BCP domain size

The domain size of BCPs with various numbers of blocks, at various χ values, and at two different block lengths were measured. BCPs with 2, 3, 4, and 5 blocks were used with block lengths in the diblock of 16 and 32 monomers. As can be seen in Figure 11.6, the number of blocks in a polymer chain does not significantly affect the domain size of the BCP, consistent with experimental results. A priori it is conceivable that the decreased entropy from the extra bonds that the domain size would be slightly increased in the larger block systems. The fact that this does not have a significant effect means that if this ODT is depressed for BCPs with more blocks, then a smaller pitch would be achievable with those BCPs with more blocks. This results has been confirmed experimentally in polystyrene-b-poly(metyl methacrylate).

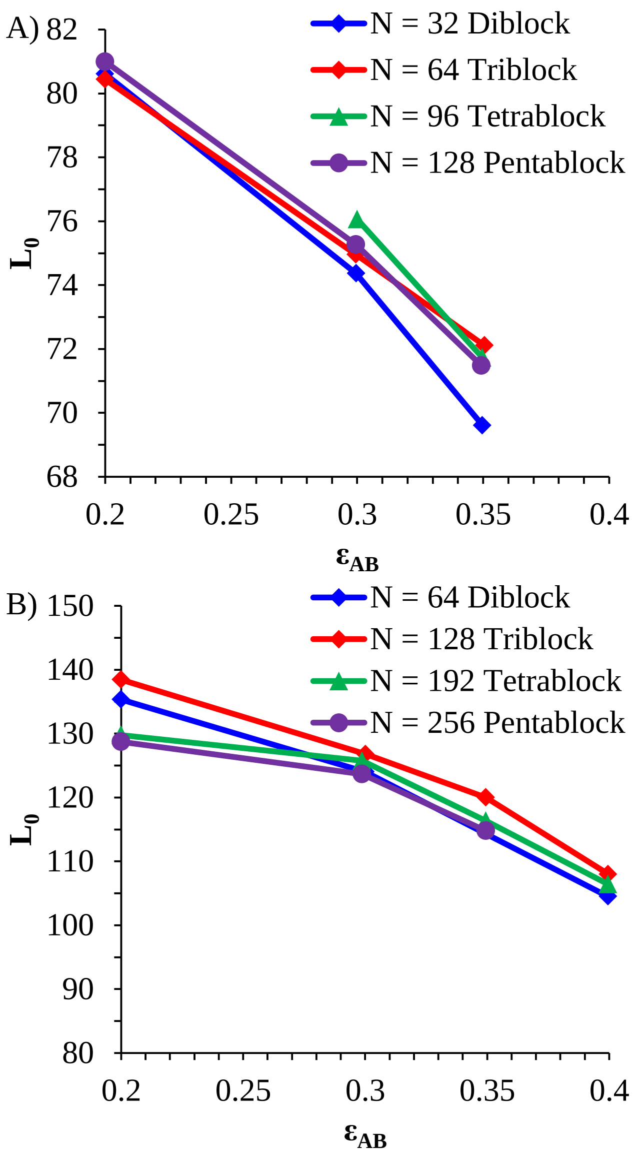

Figure 11.6. Plot of measured natural pitch (L_0) as a function of ε_{AB} and number of blocks. (A) shows the results using a diblock of 32 monomers and polymers composed of linked N = 32 diblocks. (B) shows the same for a diblock of 64 monomers.

11.3.2. Effect of Multiplicity of blocks on ODT

The order-disorder transition was measured via the structure factor for a number of N for a number of multiblock polymers. As can be seen in Figure 11.7a, the χN at the

ODT increases as the number of blocks increase. However, this is not the value that is of greatest concern. In order to determine if the ODT limited pitch in diblock systems can be beaten by using triblock (A-B-B-A) or high order multiblock copolymer, a diblock equivalent χN must be defined. Instead of using the N for the entire chain, the N for the equivalent diblock, that is the length of the first block and half of the second block in a triblock or high order multiblock copolymer, is used. This results in:

$$N_{eq} = \frac{N}{b-1} \tag{11.8}$$

where N_{eq} is the diblock equivalent N for a BCP with b blocks. Because a triblock copolymer as used here is simply two diblocks linked together, the diblock equivalent N_{eq} is half of the true N. A tetrablock copolymer is composed to 3 diblocks linked end to end and so the N_{eq} is 1/3 of the true N. This is most clearly seen in Figure 11.1. Bly plotting χN_{eq} as a function of b, the number of blocks per chain, a fair comparison between blocks of different length can be made. As seen in Figure 11.7b, there is a drop of ~ 1.5 in χN_{eq} when a triblock is used, but negligible change after that. This is a very small depression of the ODT and will result in a very modest change in ODT limited pitch for a given BCP, thus using such polymers is not recommended. The effect of multiblock copolymers on other important properties, such as defectivity, are not studied here,, but may be worthy of study. Whatever the effect of multiblock copolymers on equilibrium defect density, defect will surely heal out much more slowly than the equivalent diblock systems both because N is longer, reducing diffusion, and the length of chain that must be pulled through an unlike region is significantly larger than in the diblock case. By decreasing the rate at which defects heal, the measured defectivity may increase above the diblock equivalent.

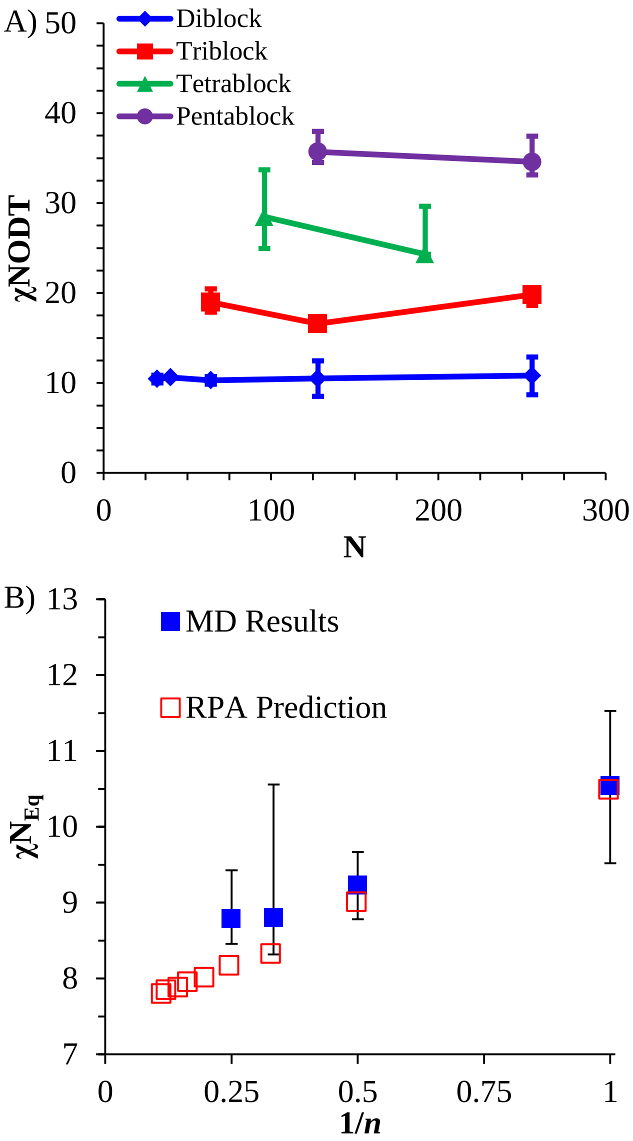

Figure 11.7. A) Plot of χN_{ODT} (χN at the ODT) as a function of N and blocks per chain. B) Plot of χN_{Eq} (N_{eq} is the diblock equivalent N) as a function of blocks per chain.

11.3.3. Chain Conformations

Diblock copolymers only have one basic conformation in a phase separated state as seen in Figure 11.8a. The chain is basically perpendicular to the A-B interface with half of the chain in adjacent domains. Triblock copolymers though have two different conformations: one that extends across three domains and one that loops back and only inhabits two domains. This is shown in Figure 11.8b. The distributions of these two conformations is probed by measuring the shape of the chains.

The shape of the chains in diblock and multiblock systems was measured using the eigenvalues of the radius of gyration tensor as described above. $\bar{X}$ describes the size of the chain along is most extended axis; $\bar{Y}$ describes the size of the chain along the most extended axis perpendicular to the first, and $\bar{Z}$ describes the size of the chain along the axis perpendicular to those two axes respectively. This is shown in Figure 11.5 for a triblock (A-B-B-A) copolymer.

Two chain descriptors, the end to end distance (r_0) and $\bar{X}$are plotted normalized by the pitch in Figure 11.9. Because the diblock copolymers only have one basic conformation, there is a single peak. The triblock copolymers have two peaks because they have two basic conformation: the first peak corresponds to the loop conformation, while the second corresponds to the extended conformation. The end to end distance of such a conformation is small because the two chain ends end up relative close. The extended conformation is represented by the peak around $r_0/L_0 = 0.9$. These chains span approximately a full domain from the center of one domain to the center of the other and this is reflected in their end to end distance relative to the pitch. By using $\bar{X}/L_0$ instead of

r_0/L_0, similar information is gained, but in perhaps a more intuitive way. Instead of considering chains ends (for which peaks become confounded with higher order multiblock polymers), $\bar{X}/L_0$ uses the shape of the whole chain which is more intuitive and easier to distinguish with longer chains. When plotted this way, the two peaks are still represented, but this time, the diblock peak and the looped triblock peak occur at the same value, which makes sense because the take up approximately the same space perpendicular to the A-B interface.

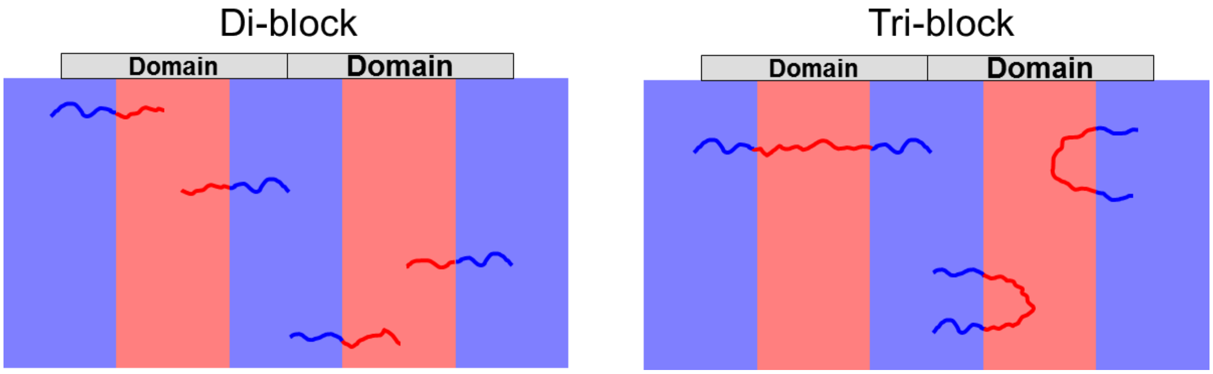

Figure 11.8. Diagram of conformations of Diblock and Triblock copolymers. The Diblock only has one conformation, while the Triblock has two, an extended and a loop conformation.

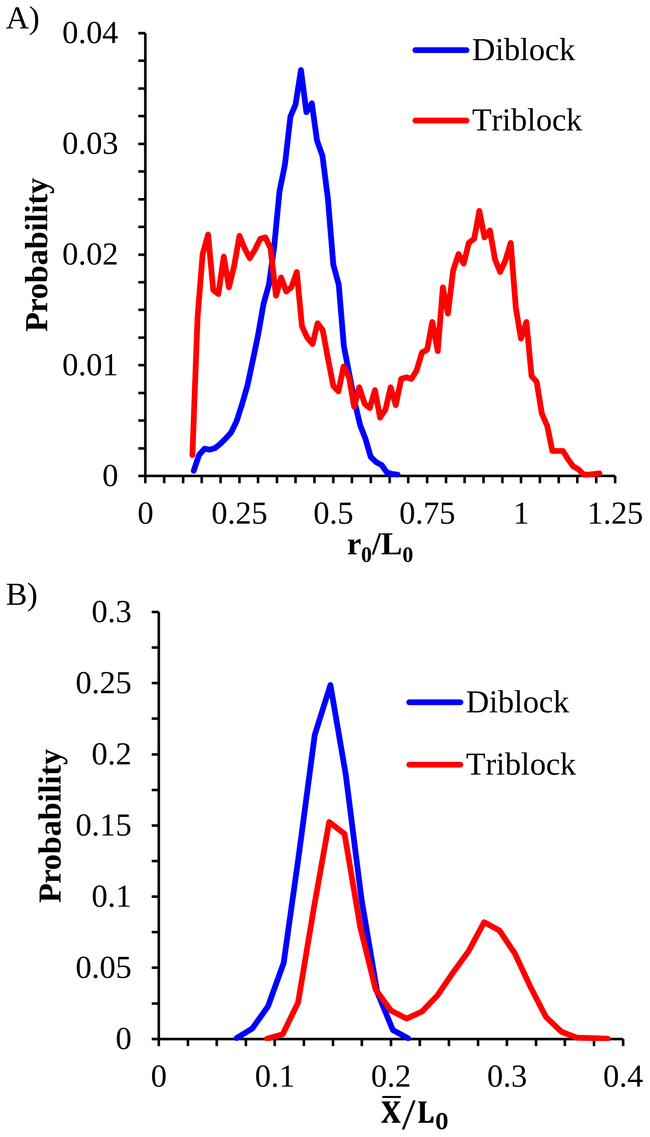

Figure 11.9. Histograms of chain shape for both Diblock and Triblock copolymers based on a diblock of 32 monomers ($N_{Eq} = 32$) at an ε_{AB} of 0.3 kcal/mol. A) plots probability as a function of end to end distance (r_0) over L_0 while B) plots probability as a function of $\bar{X}/L_0$.

The same analysis was performed for tetrablock and pentablock copolymers using the $\bar{X}/L_0$ descriptor. Because tetrablock and pentablock copolymers have 3 and 4 possible conformations respectively (see Figure 11.10), these polymers have 3 and 4 peaks respectively and are plotted alongside the diblock and triblock results in Figure 11.11.

The area under each peak corresponds to the fraction of each conformation exists in our simulations. The area under each of these peaks is shown in Figure 11.12. The area is taken from minimum to minimum. As the number of blocks increases, the area under the peaks in the middle of the distribution increases relative to the outlying peaks. One might conjecture that the relative occurrences of each of the conformations is caused by the number of possible configurations of each conformation. In the tetrablock case there are 3 conformations: *extended* which spans 1.5 domains, *single loop* which spans 1 domain, and *double loop* which spans 0.5 domains. The extended and double loop conformations can only exist in one way, that is, one configuration. The single loops conformation has two different places in which the loop can occur: the interior B block or the interior A block. Using just the number of possible configurations for each conformation, one might expect that the tetrablock conformations would occur at a ratio of 1:2:1 for the extended, single, and double loops respectively. However, the extended and double look conformations don’t occur to the same degree; in fact the double loop conformation occurs twice as often as the extended conformation. Similarly, the pentablock copolymers have 4 configurations: extended, single, double and triple loop which span 2, 1.5, 1, and 0.5 domains respectively. These would be expected to occur in a ratio of 1:3:3:1 (ratios of high order BCPs would continue to follow ratios as given by Pascal’s triangle), however, the single and double loop conformations, which should occur in equal proportion if the number of occurrences of each conformation are driven by the number of possible configurations of each conformation, occur at a ratio of 1:3, a significant deviation.

The proportions as calculated using the number of configurations for each conformation is compared with the simulation results in Figure 11.12. It seems that conformations with more loops (spanning fewer domains) are favored over equaled expected, more extended domains. Two possibilities seem probable. One, the simulation has simply not equilibrated. This possibility is currently being investigated. Two, it may be that more extended configurations suffer an entropic penalty for spanning the domain, thus reducing their occurrence. When a block loops back on itself and causes the chain to cross the dame interface an additional time, there are a wide variety of locations this second intersection can occur. While it cannot move too far away from the original intersection, it can deviate from that location in the plane of the A-B interface. However, when a block is extended across an A or B domain, the second A-B intersection must occur very close in the A-B interfacial plane to the original A-B intersection, or stretch the block in order to accommodate any difference. This results in reduced entropy for the extended conformation and a relative favoring of the conformations with more loops. The increased entropy of multiple configurations for a single conformation and reduced entropy from extended blocks results in the ultimate distribution found in Figure 11.11 and Figure 11.12.

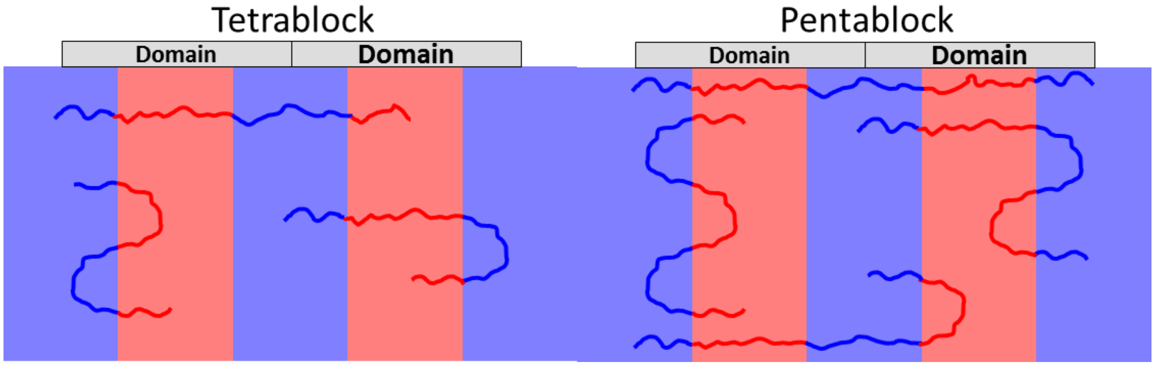
Tetrablock
Domain
Domain
Pentablock
Domain
Domain

Figure 11.10. Diagram of the possible conformation of tetra and pentablock copolymers.

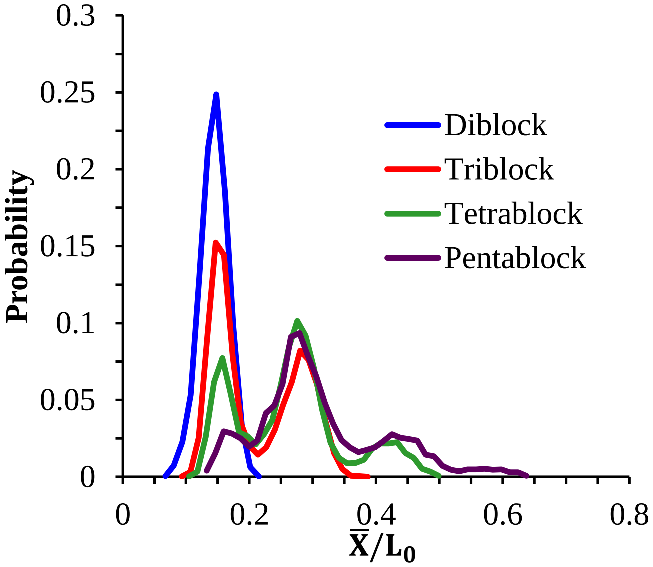

Figure 11.11. Histogram of $\bar{X}/L_0$ for di, tri, tetra, and pentablock copolymers for N_{Eq} = 32 and ε_{AB} = 0.3 kcal/mol. Each plot has a peak corresponding to the possible conformations in Figure 11.10.

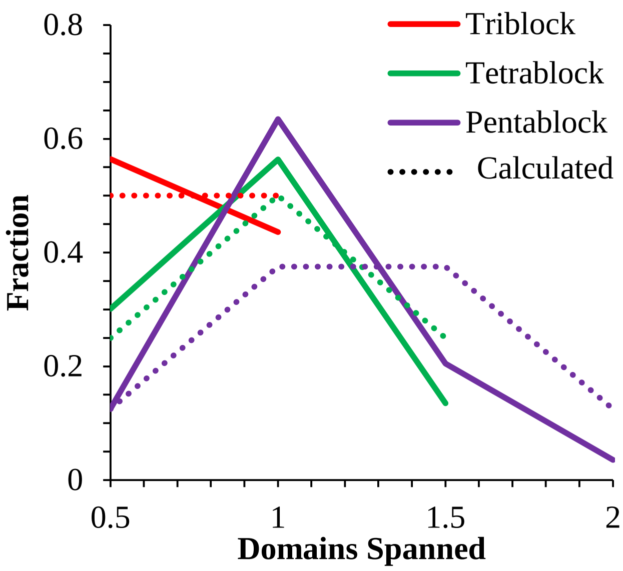

Figure 11.12. Comparison of the calculated fraction of each conformation with the measured fraction in simulation for N_{Eq} = 32 and ε_{AB} = 0.3 kcal/mol.

11.4. Conclusions

Simulations of multiblock BCPs created by linking diblock BCPs together end to end are run. It is found that increasing multiplicity has no effect on domain size. Increasing multiplicity decreases χN (equivalent to the diblock) at the ODT, but the decrease is small. This calculation is in agreement with previous RPA predictions. The distribution of chain conformations as a function of multiplicity is investigated using the eigenvalues of the radius of gyration tensor. The fraction of chains in a particular conformation (described by the number of time a chain loops back and intersection the same interface) scale with the configurational entropy of each conformation, but are skewed towards more looped conformations.

11.5. References

1 Bates, F. S.; Fredrickson, G. H. "Block Copolymers – Designer Soft Materials" Physics Today 1999, 52, 32.

2 Stoykovich, M. P.; Nealey, P. F. "Block copolymers and conventional lithography" Materials Today 2006, 9, 20.

3 Hawker, C. J.; Russell, T. P. “Block Copolymer Lithography: Mergin “Bottom-Up with “Top-Down” Processes” MRS Bulletin 2005, 30, 952.

4 Matsen, M. W. “The standard Gaussian model for block copolymer melts” Journal of Physics: Condensed Matter 2002, 14, R21.

5 Klok, H. A.; Lecommandoux, S. "Supramolecular Materials via Block Copolymer Self-Assembly" Advanced Materials, 2001, 13, 1217.

6 Rösler, A.; Vandermeulen, G. W. M.; Klok, H. A. "Advanced drug delivery devices via self-assembly of amphiphilic block copolymers" Advanced Drug Delivery Reviews 2012, 64, 270.

7 Leibler, L Macromolecules, 1980, 13, 1602-1617.

8 Matsen, M. W.; Bates, F. S. "Unifying Weak- and Strong-Segregation Block Copolymer Theories," Macromolecules 1996, 29, 1091-1098.

9 Shull, K. R."Mean-Field Theory of Block Copolymers: Bulk Melts, Surfaces, and Thin Films," Macromolecules 1992, 25, 2122-2133.

10 Semenov, A. N. Macromolecules 1993, 26, 6617.

11 Detcheverry, F. A.; Nealey, P. F.; de Pablo, J. J.; Pike D. Q.; Nagpal, U. "Theoretically informed coarse grain simulations of block copolymer melts: method and applications" Soft Matter 2009, 24, 4858-4865.

12 Peters, A. J.; Lawson, R. A.; Ludovice, P. J.; Henderson, C. L. “Detailed Molecular Dynamics Studies of Block Copolymer Directed Self-Assembly: Effect of Guiding Layer Properties” J. Vac. Sci.Technol. B 2013, 31, 06F302.

13 Fredrickson, G. H.; Helfand, E. " Fluctuation effects in the theory of microphase separation in block copolymers" J. Chem. Phys. 1987, 87, 697.

14 Mai, S.; Fairclough, J. P. A.; Hamley, I. W.; Matsen, M. W.; Denny, R. C.; Liao, B.; Booth, C.; Ryna, A. J. „Order−Disorder Transition in Poly(oxyethylene)−Poly(oxybutylene) Diblock Copolymers“ Macromolecules 1996, 29, 6212-6221.

15 Mai, S.; Fairclough, J. P. A.; Terrill, N. J.; Turner, S. C.; Hamley, I. W.; Matsen, M. W.; Ryan, A. J.; Booth, C. “Microphase Separation in Poly(oxyethylene)-Poly(oxybutylene) Diblock Copolymers,” Macromolecules 1998, 31, 8110-8116.

16 Schulz, M. F.; Khandpur, A. K.; Bates, F. S.; Almdal, K.; Mortensen, K.; Hajduk, D. A.; Gruner, S. M. “Phase Behavior of Polystyrene−Poly(2-vinylpyridine) Diblock Copolymers,” Macromolecules 1996, 29, 2857-2867.

17 Lawson, R. A.; Peters, A. J.; Ludovice, P. J.; Henderson, C. L. “Coarse grained molecular dynamics model of block copolymer directed self-assembly” Proc. SPIE 2013, 8680, 86801Y.

18 Takahashi, Y.; Kitade, S.; Noda, M.; Ochiai, N; Noda, I; Imai, M; Matsushita, Y. “Order-Disorder Transition of Symmetric Poly(styrene-b-2-vinylpyridine) in Bulk and Solution” Polymer Journal 1998, 30,388.

19 Bates, F. S.; Rosedale, J. H.; Fredrickson, G. H. “Fluctuation effects in a symmetric diblock copolymer near the order–disorder transition” J. Chem. Phys. 1990, 92, 6255.

20 Hasegawa, H.; Sakamoto, N.; Takeno, H.; Jinnai, H.; Hashimoto, T.; Schwahn, D.; Frielinghaus, H; Janβen, S.; Imai, M.; Mortensen, K. “Small-angle neutron scattering studies on phase behavior of block copolymers” J. Phys. Chem. Solids 1999, 60, 1307.

21 Theodorou D. T.; Suter, U. W. "Shape of Unperturbed Linear Polymers: Polypropylene" Macromolecules 1985, 18, 1206.

CHAPTER 12

CONCLUSIONS AND RECOMMENDATIONS

12.1. Conclusions

As IC fabrication requires smaller and smaller features, the insertion point of BCP-DSA comes ever nearer. For it to ever be implemented, a fuller understanding of BCP-DSA in general and the specific problems it faces is critical. This work used a coarse-grained polymer model and molecular dynamics simulations to study the effects of materials and guiding layer properties on line roughness and defect density in BCP-DSA. Also included were basic studies necessary to use the model, a new technique which applied PCND to polymer systems to enable enhanced phase space sampling of energetically restricted systems, and a brief study on extending the minimum pitch of a BCP-DSA process through the use of multiblocks.

Chapter 2 introduced the coarse-grained model and some tools necessary for its use. The coarse grained model used here treated a number of monomers (equivalent to the statistical segment length) as a single point. These beads were bonded together using a harmonic bond potential, a harmonic angle potential, and a Lennard-Jones like non-bonded potential. This method, along with the use of GPUs, decreased simulation time by 4 orders of magnitude or more as compared to a simple atomistic system. Chapter 2 also covered techniques to measure the pitch of a BCP system, measure χ in a BCP system, measure the ODT of a BCP system, and compared results to well established mean field results.

Chapter 3 considered some of the implications of using a finite periodic box to simulation an ordered system. When using a lamellae forming BCP (or anything else that forms similar layered structures) only a finite number of repeat distances are allowed. A simple equation was derived to describe all possible allowable distances. It was found that using more elongated boxes generally produced more allowable pitches for a given simulation volume. The calculations were demonstrated using our BCP model.

Chapter 4 explored the effect of guiding layer properties and errors on resulting directed self-assembly (DSA) pattern properties produced in block copolymer (BCP) thin films. Guiding patterns that are non-commensurate to the natural BCP pitch were considered, as were guiding lines that have correlated or anti-correlated line edge deviations. The process window was detailed for non-commensurate line widths. Guiding lines with various correlated and anti-correlated roughnesses showed that under the high χ conditions used here, very significant guiding roughness was required to have any effect on the BCP film, and most of the guiding roughness was damped out within 5 nm of the bottom surface of the BCP film. Also, pitch sub-division patterns (where the BCP natural periodicity is some integer multiple smaller than the guiding pattern periodicity) damped out guiding line roughness more easily than pitch replicating patterns where a guiding pattern exists for each line formed in the BCP film.

Chapter 5 studied the thin film self-assembly and resulting pattern properties of block copolymer (BCP) systems with various molecular weight polydispersities. Effects of the polydispersity index (PDI) on feature pitch and interfacial roughness, which are critical lithographic parameters that have a direct impact on integrated circuit performance, were simulated. It was found that for a realistic distribution of polymer molecular weights, modeled by a Wesslau distribution, both line edge roughness (LER) and line width roughness (LWR) increase approximately linearly with increasing PDI, up to ~ 45% of the monodisperse value at PDI = 1.5. Mechanisms of compensation for increase A-A and B-B roughness were considered. It was found that long and short chain positions were not correlated, and that long chains were significantly deformed in shape. The increase in LWR was due to the increase in LER and a constant correlation between the line edges. Unaligned systems showed a correlation between domain width and local molecular weight, while systems aligned on an alternating pattern of A and B lines did not so any correlation. When the volume fraction of individual chains was allowed to vary, similar results were found when considering the PDI of the block as opposed to the PDI of the entire system.

Chapter 6 studied the effect of χN on the block domain interfacial roughness and block domain width variation. The domain interfacial roughness was characterized in terms of line edge roughness (LER) at the A-B lamellar domain interface as defined by bead density mapping. The block domain width variation was characterized in terms of a line width roughness (LWR) of the A and B domains again as defined by bead density mapping of the aligned BCP films. These two parameters were chosen and quantified since they are particularly important for the potential application of block copolymer directed self-assembly in semiconductor manufacturing as an enhancement to current optical lithography techniques. LER and LWR behavior at low χN values received particular attention in this work because of the lack of prior studies in this area. Previously, the behavior of LER and LWR at high χN values has been probed using analytical techniques based on mean-field Leibler, Ohta, and Kawasaki (LOK) models, but these models use assumptions that limit their accuracy in the low χN regime.[1,2] Using a coarse grained molecular dynamics model, this low χN region was explored. A sharp increase in LER and LWR in aligned BCP patterns is found for low χN values. Other models underestimate roughness at low χN. Using guiding stripes with programmed roughness instead of idealized straight guiding stripes does not change the dependence of BCP LER and LWR on χN.

Chapter 7 described a technique to measure free energy differences between states called thermodynamic integration and applied it to variations in pitch and to measurements of the ODT. The minimum free energy occurred at a pitch that corresponded to the calculated natural pitch from scattering calculations. The penalty for pitches lower than the natural pitch was found to scale with χ and the proportional decrease in pitch, indicating a purely enthalpic driving force and resulting in a universal energy penalty curve. The penalty for pitches larger than the natural pitch is entropically driven and requires more complex calculations. The entropic and enthalpic terms must be separated to investigate such behavior. The ODT was also measured in a manner similar to Müller et al.[3] by calculating the free energy in the mixed state and of the demixed state. The intersection of these curves is the ODT. The measured ODT depends on the pitch used in the demixed calculation. If the pitch is too large, then the χN at the ODT will be over estimated. The measurement was taken as a function of pitch and found to approach the expected ODT of 10.5 when smaller pitches were used, thus correcting the work by Müller et al.[3]

Chapter 8 applied the previously mentioned thermodynamic integration to measurement of defect free energies of a defect commonly found in BCP-DSA. By measuring this free energy, the concentration of defects, and what affects that concentration, at equilibrium can be found. Because defect density is one of the most important hurdles yet to be overcome in BCP-DSA for IC fabrication, understanding what affects this free energy is critical. It is found that χN is not the best predictor of defect free energy and that a single χN value can yield vastly different free energies when χ and N are different (though their product is identical). This means that higher χ systems that are being produced to allow for smaller feature size DSA will likely have a lower equilibrium intrinsic defect density. Measurements of defect densities are reasonable for the oft-studied PS-PMMA. Defect free energies were measured as a function of defect placement relative to the underlayer and as a function of background composition. The effect of background composition was unclear but the defect free energy was highly dependent on defect location relative to the underlayer. Free energy differences ~ 100 kT were found between the three possible defect locations on a 1-3 guiding pattern. The effect of PDI on defect free energy was also studied. It was found that PDI significantly reduced defect free energy. Extrapolating form PDI up to 1.5 suggests that the defect will occur in equal proportions with a PDI of around 1.6 for this system. It was found that long chains tended to concentrate near the defect and stabilize the defect.

In addition to equilibrium defect density, the kinetics of defect healing are important to understanding final defectivity in a real BCP-DSA process. Chapter 9 considers the kinetic of healing the defect studied in chapter 8. It is found that infinitely thick films yield an exponential drop in defect heal rate above χN ~ 30. Below χN ~ 30, the rate of transport was similar to the rate at which the transition state was reached so that the overall rate changed only slightly. The energy barrier in periodic simulations increased with 0.31 χN on average. Thin film simulations show no change in rate associated with the energy barrier below $\chi N \sim 50$, and then show an increase in energy barrier scaling with $0.16\chi N$. Thin film simulations always begin to heal at either the free interface or the BCP-underlayer interface where the increased *A*-*B* contact area associated with the transition state will be minimized, while the infinitely thick films must start healing in the bulk where the *A*-*B* contact area is increased. It is also found that cooperative chain movement is required for the defect to start healing.

The large energy barriers found at high χN in chapter 9 suggest a need for a method to increase the sampling efficiency of MD calculations in systems with large activation energies. Such a method is developed by applying PCND to polymer systems. By applying a time correlated random force along the backbone of the polymer chain, chain movement is encouraged without significant perturbation of the free energy of the system. This method is applied to a coarse-grained MD model in the context of defect healing in an aligned thin film system. It was found that PCND increased defect heal rate by 4 orders of magnitude. Diffusion is also increased by about an order of magnitude. An investigation of the limits of the parameters that describe the random force was undertaken, and a set of parameters that both significantly decrease defect heal time and have little effect on system properties such as natural pitch and chain statistics was found. A comparison to increased temperature annealing was undertaken and it was found that the correlated random force was much more effective at sampling over energy barriers.

Chapter 11 considered a slightly different problem, that a given polymer with a given χ has a minimum pitch that can be achieved before the ODT is reached. The pitch can be reduced by decreasing N, the degree of polymerization, but when χN drops too low, the polymer will mix. By using multiblock copolymers where A and B are linked together to form longer chains but block size is retained, this limit can be decreased. The diblock equivalent χN at the ODT can be reduced such that the minimum pitch possible for that combination of A and B is reduced beyond the diblock limit. However, the gain is minimal. The distribution of chain conformations is also studied.

12.2. Recommendations for future work

While chapter 3 considers the effect of box size on allowable lamellar repeat distances, cylinder repeat distances are also of interest in the BCP community. A similar approach could be taken to derive an equation, or set of equations, that describe allowable repeat distances of cylinders. This is a more complicated problem because: 1) there is an extra dimension around which the cylinders can rotate, and 2) the penalty for producing cylinders that are not hexagonally packed or have some other morphology is low compared to analogous defect in lamellae forming systems. Using a limited box size may favor forming a defect over adopting one of the allowable repeat distances for perfect hexagonally packed cylinders.

Chapter 4 presents interesting data regarding a BCPs ability to accommodate defective underlayer patterns, but these results are not generalized. Large defects in the underlayer are required to perturb the overlying BCP, but what determines how large the defect must be? A systematic study of exactly how large such a defect must be, and how that varies with properties like χ would be worthwhile.

Line edge roughness was measured as a function of polydispersity, χ and N, and some underlayer properties. Other properties, such as differences in cohesive energy density or differences in stiffness between block could be studied. This is an area that is completely unstudied, and in fact would be very difficult to study using conventional simulation techniques. Our model would excel at elucidating such effects. In chapter 6, using more accurate interfacial width calculations or results may modify Semenov's theory to better match the data found here.

Defect free energy calculations are shown in chapter 8 and provide good insight into what properties are important when optimizing BCP-DSA materials and properties. However, a great many underlayer properties have not been considered. Various types of guiding layers will produce different defects, but only one such defect and guiding layer has been studied here. Processes such as the COOL[4] process or the SMART™[5] process have different underlayers that may affect defect density. What approach is best? What effect does topography, which is present in the COOL and SMART™ approaches and perhaps unintentionally in other approaches, have of defect density? Thermodynamic integration could be used to study these processes. Additionally, the defects that may be present may be different than those in pure chemoepitaxial processes. The types of defects that occur, especially near topography in the underlayer, could be easily studied using our model, but very difficult to study experimentally. Studies similar to those found in chapter 9 on the kinetics of such defect healing could also be carried out for the various defects and underlayers for which equilibrium defect density is studied. Additionally, the effect of chain distribution on defect free energy as a function of χN could be more fully studied. Two approaches could be envisioned: 1) the approach used here where various distributions are forced and the defect free energy is measured, and 2) a defect is forced (perhaps via a defect in the guiding layer) and the chains are allowed, over a very long period of time, to adopt their preferred distribution. Light PCND could help with sampling time, but care would have to be taken to preserve the defect.

Protracted colored noise dynamics for polymer systems, while introduced here, has not been fully studied. A full study on the effect that PCND has on the free energy of a system would be worthwhile. If PCND does affect the relative free energies of various states significantly, then understanding how that happens is crucial. Alternatively, if PCND generally does not, then it is necessary to know that before making conclusions from simulations involving PCND in some cases. Preliminary studied suggest the effect is small, but what that effect is like under different conditions has not been studied. In addition, a detailed study on choosing parameters that best fit a system and purpose is worth pursuing. Here, a wide range of parameters are considered to find the optimal range. However, if this is necessary for every new system, PCND's useful would be significantly hampered. PCND has only been applied to short chains. Longer chains which are thoroughly entangled may have very different behavior under the influence of PCND. Such systems are almost never studied using MD because of the exceedingly long simulation times required. PCND may allow such systems to be studied in greater detail, but this has not been considered.

Solvent annealing, or processes that involve both solvent and thermal annealing, are becoming more common. Adapting this model to include solvent-polymer interactions would be a worthwhile undertaking. The effects that solvent annealing have on χ, pitch, chain mobility and effects on morphology and orientation are not fully understood, especially when considering the concentration gradients that can occur and which have been shown to affect alignment orientation.[6] Simulations can consider these gradients more easily than experiments and the effects can be more clearly elucidated. When combined with rapid thermal annealing, these processes only get more complicated.[7] Effects of solvent mixing may be an important topic in the future, especially as solvents will partition into various block differently.[8] The effect that this has is not fully understood and could benefit from simulation.

This work has only used BCPs that were symmetric, that is, each block had the same homopolymer parameters. However, no real BCP systems exist in this state. In fact, high χ materials often have a very asymmetric nature and it is often this fact that creates the large χ. One estimation of the χ value of a BCP uses the differences in the solubility parameters which derive from the cohesive energy density of the homopolymers. If these are the same, then χ is calculated as zero, but if they are very different then a high χ is calculated. While this method is not very accurate, it does demonstrate how an asymmetry in a BCP gives rise to χ. Because of this fact, the impact of asymmetries will likely increase as more high χ materials are used, thus study of such system may become increasingly important. In fact it has already been demonstrated that BCP asymmetry is a cause for the formation of horizontal lamellae (lamellae that lay parallel to the underlayer), which are largely useless in semi-conductor fabrication.[9] Traditional mean-field models are currently largely incompatible with these asymmetries, but the coarse-grained model used here can be easily adapted to model BCPs who blocks have different densities, cohesive energy densities, stiffnesses, etc. The effect of asymmetry on the various aspects of BCP-DSA shown here, an on more fundamental BCP phase separation would be very useful.

12.3. References

1 Patrone, P. N.; Gallatin, G. M. Macromolecules 2012, 45, 9507.

2 Semenov, A. N. Macromolecules 1994, 27, 2732.

3 Müller, M.; Daoulas,K. C. "Calculating the free energy of self-assembled structures by thermodynamic integration," J. Chem. Phys. 2008, 128, 024903.

4 Kasahara, Y.; Seino, Y.; Kobayashi, K.; Kanai, H.; Sato, H.; Kubota, H.; Tobana, T.; Minegishi, S.; Miyagi, K.; Kihara, N.; Kodera, K.; Shiraishi, M.; Kawamonzen, Y.; Nomura, S.; Azuma, T. " RIE challenges for sub-15 nm line-and-space patterning using directed self-assembly lithography with coordinated line epitaxy (COOL) process" Proc. SPIE 2015, 9428, 94280S.

5 Kim, J.; Yin, J.; Cao, Y.; Her, Y.; Peterman, C.; Wu, H.; Shan, J.; Tsutsumi, T.; Lin, G. "Toward high-performance quality meeting IC device manufacturing requirements with AZ SMART^{TM} DSA process" Proc. SPIE 2015, 9423, 94230R.

6 Albert, J. N. L.; Young, W.-S.; Lewis III, R. L.; Bogart, T. D.; Smith, J. R.; Epps III, T. H. " Systematic Study on the Effect of Solvent Removal Rate on the Morphology of Solvent Vapor Annealed ABA Triblock Copolymer Thin Films" ACS Nano 2012, 6, 459-466.

7 Gotrik, K. W.; Ross, C. A. "Solvothermal Annealing of Block Copolymer Thin Films" Nano Letters 2013, 13, 5117-5122.

8 Gotrik, K. W.; Hannon, A.F.; Son, J. G.; Keller, B.; Alexander-Katz, A.; Ross, C. A. " Morphology Control in Block Copolymer Films Using Mixed Solvent Vapors" ACS Nano 2012, 6, 8052-8059.

9 Lawson, R. A.; Peters, A. J.; Nation, B.; Ludovice, P. J.; Henderson, C. L. “Simulation study of the effect of differences in block energy and density on the self-assembly of block copolymers” J. Micro Nanolithogr. MEMS MOEMS 2014, 13, 031308.